University of Bielefeld

Doctoral Thesis

Strong Coupling Lattice QCD in the Continuous Time Limit

Author:
Marc Andre Klegrewe
University of Bielefeld

Supervisor:
Dr. Wolfgang Unger
Dr. Olaf Kaczmarek
University of Bielefeld

A thesis submitted in partial fulfillment of the requirements for the degree of Doctor rerum naturalium

in the

High Energy Physics Group
Department of Physics

May 2020

Acknowledgements

My PhD position was funded by the Deutsche Forschungsgemeinschaft (DFG) through the Emmy Noether Program under Grant No. UN 370/1. Additionally, I was supported through the CRC-TR 211 'Strong-interaction matter under extreme conditions'– project number 315477589 – TRR 211. My numerical simulations were mainly performed on the OCuLUS cluster at PC2 (Universität Paderborn). I'm very pleased that all these institutions and collaborations supported my work.

I would like to thank Dr. Wolfgang Unger for supervising my PhD thesis. I'm extremely grateful that he was always available for many fruitful discussions. He successfully guided me through the different stages of my PhD and strongly encouraged me to pursuit a scientific career. Sorry for that 😜.

Apart from spending my time in Wolfgang's office, I was always enjoying the company of Thilo Siewert. I can't think of any better office buddy. After more than four years, our office turned out to be a pretty solid 3d printer factory with an attached snack bar. Who can say that?

Thank you to Dr. Hauke Sandmeyer for providing the AnalysisToolBox and explaining its functionality. I appreciate our monthly night shifts in medieval city building activities. After eight years of practice we mastered the craft quite well.

Furthermore, I'm grateful of having awesome parents who invited me for dinner every sunday evening such that I was always well fed for the upcoming week. Also, I had to stack up on nutella every other weekend and therefore it was quite essential for me to come by.

Finally, thank you Lisa for being there for me 💏.

Strong Coupling Lattice QCD in the Continuous Time Limit

Marc Andre Klegrewe

Abstract

Lattice methods are the essential tool to study QCD in its non-perturbative framework. At finite baryon densities, Monte Carlo simulations are most severely hindered by the sign problem. Thus, a finite density analysis of thermodynamic observables is limited, and the exploration of the QCD phase diagram via lattice QCD requires new ideas to tackle the sign problem.

Within the strong coupling limit of lattice QCD (SC-LQCD), a dual formulation is known which suffers only from a mild sign problem, allowing studies at finite baryon densities. Moreover, the continuous time framework is employed, which exhibits many assets compared to standard discrete time analysis such as a faster sampling of configurations, the avoidance of extrapolations in N_τ as well as a smoother treatment of observables on anisotropic lattices. On top of that, its feature of having static baryons removes the sign problem completely.

The measurement of the critical temperature T_c at $\mu_B = 0$ or the determination of physical quantities such as the pion decay constant F_π directly in the continuous time limit significantly removes uncertainties due to extrapolations in discrete time studies. The featured continuous time algorithm allows for a straightforward study of temporal correlators at zero and finite baryon density. Pole masses are extracted using correlated fits and the temperature dependence is analyzed. A Taylor expansion in the pressure allows to compare the finite density phase transition with the radius of convergence. The temperature dependence of Taylor coefficients is inspected and the pressure from finite density Monte Carlo simulations is reconstructed.

The continuous time limit within the SC-LQCD framework turns out to be highly promising for future projects such as studies with multiple flavors, at finite quark masses as well as at finite gauge coupling. Within the scope of this thesis, evidence is provided that the continuous time limit is well defined and suited to study QCD thermodynamics. This is illustrated with various applications.

Table of Contents

Preface

It is the most fundamental goal of physics to describe the states and interactions of matter based on a minimal set of hypotheses which lead to theories that characterize phenomena taking place on microscopical scales to cosmological distances. This scale dependence was not immediately apparent, as classical physics rooted in the *mechanics* of Galileo Galilei and Isaac Newton, the study of *electromagnetism* by Michael Faraday and James Maxwell or *thermodynamics* discussed by Ludwig Boltzmann and Hermann von Helmholtz is based on macroscopic observations. In fact, by the end of the 19^{th} century it was widely assumed that the insights from the mentioned fields account for all physic phenomena known by then [1].

It was Planck's theory on the black-body radiation [2] giving finally rise to the idea of quantization which is fundamental for the study of microscopic theories. While it was widely believed that the quantization of radiation could be a property of the emitting and absorbing object, the discovery of the photoelectric effect [3] stating that the energy quantization is in fact a property of the electromagnetic radiation itself corrected this believe. Apart from light, the concept of quantization was successively introduced in the description of nuclear matter as well. While the interaction of photons with electrons gave rise to the first of the three fundamental microscopical interactions, a further exploration of the substructure of the atomic nucleus was necessary for the others to emerge. While the nucleus was first believed to be constituted merely out of protons [4], it took till the 1930's to discover the neutron [5]. With the arising studies of nuclear fission processes the weak force as an interaction for explaining nuclear decays started to thrive. A further exploration of the substructure of protons and neutrons was strongly enhanced by collider experiments in the 1950s which led to the discovery of innumerable many new resonances in the particle spectrum (often referred to as particle zoo). As these could not be all be elementary particles, it dates back to Gell-Mann in 1961 [6] and his classification according to the Eightfold Way which took the field a giant leap forward. This structured way of organizing hadrons gave rise to the quark-model in 1964 [7, 8]. The associated interaction is the strong force which binds quarks together into colorless objects called mesons and baryons and dominates over the electric repulsion of its constituents on short distances.

This completes the set of three classes of fundamental interactions acting on microscopical scales - the strong, weak and electromagnetic interaction - which are formulated as Quantum Field Theories that comprise the frameworks of quantum mechanics and special relativity. The only exception is gravity, which represents the fourth fundamental interaction and acts

on macroscopic scales.

Within this dissertation the Quantum Field Theory of quark interactions mediated by massless non-abelian gauge vector fields (so-called gluons) is discussed which is known as Quantum Chromodynamics (QCD). It is because of this strong force why quarks are bound together into hadrons. Apart from gluons being able to self-interact, a particular interesting feature of QCD is the energy dependence of its coupling constant. At large energies the coupling decreases and finally vanishes resulting in what is called asymptotic freedom [9]. Quarks and gluons are then forming a state of matter referred to as Quark-Gluon Plasma (QGP) [10]. On the contrary, the strong coupling regime reveals a state denoted as confinement where quarks form bound, colorless objects referred to as hadrons. As perturbation theory breaks down in this regime, alternative methods have to be applied to describe these states of matter. While confinement is not yet proven by analytic studies, it is predicated by lattice QCD [11] where a discretization of Euclidean space-time is used to perform studies typically on a $3+1$ dimensional grid. In addition to the lattice acting as a non-perturbative regularization scheme where no infinities arise at finite lattice spacing a, there is the advantage to perform lattice QCD calculations on a computer using Monte Carlo methods. Even though lattice QCD is nowadays a well-established tool, it still suffers a very crucial limitation. Simulations at finite baryon chemical potential fail due to the infamous sign problem that is manifested in a complex integrand which cannot be interpreted as a probability weight. Therefore, Monte-Carlo methods require an infinite amount of statistics to yield reasonable results. As the sign problem is representation dependent, it can be circumvented by finding a suitable set of dual variables. In the strong coupling limit of QCD such a formulation is known which renders the sign problem mild. While this limit exhibits important similarities to full QCD such as chiral symmetry breaking, it also offers an unobstructed view on lattice QCD at finite densities [12]. Within this thesis the strong coupling limit framework is enhanced by performing studies directly in the continuous time limit [13]. Hence, extrapolations in N_τ can be avoided while the algorithm allows a faster sampling of configurations. The sign problem vanishes completely in the continuous time limit and the expressions for the calculation of dual observables simplify significantly.

This thesis is structured into six chapters. The first chapter 1 comprises an introduction to the theory of Quantum Chromodynamics and its formulation on a discrete lattice. Symmetries are studied and the staggered formulation of fermions is introduced. Finally, the partition function for the strong coupling limit is derived and the new degrees of freedom are discussed. This chapter is followed by the formulation of the continuous time limit (chapter 2). In particular, the step-by-step derivation of the continuous time partition function from the discrete version expressed in terms of a Hamiltonian, is the central element of this chapter. A

Worm type algorithm is presented which samples configurations according to the continuous time partition function (see chapter 3). This algorithm is used to perform first measurements which validate the correct performance of the algorithm (chapter 4). Furthermore, various thermodynamic observables are extracted at zero temperature $T = 0$ as well as at finite temperatures. A comparison to results from discrete time simulations and extrapolation in N_τ highlights the significance of an algorithm that directly samples in the continuous time limit. The last chapters deal with two major topics in the field of QCD.
In chapter 5 meson correlators are studied with the main intention to analyze their behavior at finite densities and temperatures in the chiral limit. Pole masses for various particles are extracted from correlated fits [14] of temporal correlators that decay in time. A sophisticated fit procedure is presented which is essential for a reasonably extended mass plateau and therefore, the ground state mass extraction. Multiple state fits are discussed which deal with correlators being in general spoiled by infinitely many states especially at short distances [15]. The continuous time formulation is a key concept to yield an almost arbitrary discretization in temporal direction for an exceptional ground state analysis.
In the final chapter 6 the Taylor expansion method is explored which is a well-established tool in full QCD to study the finite density phase diagram and locate the critical endpoint [16–18]. In the strong coupling limit the phase diagram is already settled due to the mild sign problem. Hence, this framework allows to test the range of validity of a Taylor expansion of some thermodynamic variable in powers of μ_B about $\mu_B = 0$. Taylor coefficients for an expansion in the pressure are discussed under the assumption that the system is homogeneous. The continuous time framework in combination with a histogram method allows to extract the first six orders of Taylor coefficients. These expansion coefficients are used to construct the radius of convergence which locates the nearest non-analyticity, i.e. the phase boundary with its tri-critical point in the chiral limit. Finally, the pressure itself is reconstructed which requires to account for the non-homogeneity of the system. Thus, a Taylor expansion based on the spatial dimer density is performed.

Chapter 1

Theoretical Framework

1.1 The Theory of Quantum Chromodynamics

From all the elementary particles contributing to the Standard model of modern physics (cf. Fig. 1.1), the theory of Quantum Chromodynamics (QCD) deals with the quarks and gluons. Latter are the massless gauge bosons mediating the strong force and they are the reason for the interaction of quarks. Furthermore, as gluons themselves carry the color charge, it is possible for them to self-interact.

QCD is a non-Abelian gauge theory based on the color gauge symmetry $SU(3)$ described by the Lagrangian density in Minkowski space-time [20]

$$\begin{aligned}\mathcal{L}^{\mathrm{M}}_{QCD} =& \mathcal{L}_{\mathrm{F}} + \mathcal{L}_{\mathrm{YM}} \\ =& \sum_{f=1}^{N_f} \sum_{a,b=1}^{N_c} \sum_{\alpha,\beta=1}^{4} \bar{\psi}_f^{a\alpha}(x)(\not{D}_{\alpha\beta}^{ab} - m_f\delta_{ab}\delta_{\alpha\beta})\psi_f^{b\beta}(x) - \sum_{a=1}^{N_c^2-1} \frac{1}{4} F^a_{\mu\nu}(x)F_a^{\mu\nu}(x),\end{aligned} \tag{1.1}$$

with the six flavors of quarks $f = u, d, s, c, b, t$ featured in nature coming in three colors N_c. The color indices a, b and spinor indices α, β are dropped in the following to shorten the upcoming expressions. Additionally, the flavor index is neglected as this dissertation focuses on systems with a single flavor of quarks $N_f = 1$ only. The Dirac operator and the field strength tensor incorporated in Eq. (1.1) read

$$\begin{aligned}\not{D} \equiv& \gamma^\mu(\partial_\mu + igA_\mu) \\ F_{\mu\nu} \equiv& \partial_\mu A_\nu - \partial_\nu A_\mu - ig[A_\mu, A_\nu],\end{aligned} \tag{1.2}$$

with the gluonic gauge field $A_\mu = \sum_{a=1}^{N_c^2-1} \frac{\lambda^a}{2} A^a_\mu$ and the Gell-Mann matrices λ^a as generators of $SU(3)$ [20]. These gluon fields describe a vector with $N_c^2 - 1 = 8$ components which are used to express all traceless Hermitian matrices within the gauge group.

In order to draw a connection between Quantum Field Theory and Statistical Physics, an analytic continuation to imaginary (Euclidean) time is performed by $t \to -i\tau$ [21]. This gives

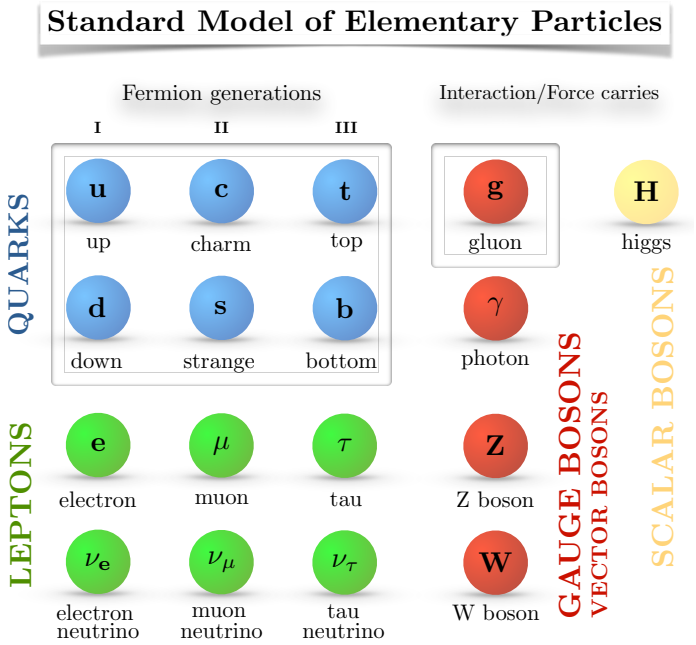

Figure 1.1: *The Standard Model of elementary particles in contemporary physics (inspired by [19]). The quarks are the fermionic contribution to QCD while the gluon is the gauge particle mediating the strong force. Additionally, the photon is depicted as the carrier of the electromagnetic force which acts on the charged particles, which includes all quarks and the first leptonic row. The W and Z boson complete the set of gauge particles. These mediate the weak interaction and all fermions as well as the Higgs particle are affected by this force.*

rise to the Euclidean action

$$\begin{aligned} S^{\mathrm{E}}_{\mathrm{QCD}}[A_\mu, \bar{\psi}, \psi, g, m] &= \int_0^\beta d\tau \int_V d^3\mathbf{x}\ \mathcal{L}^{\mathrm{E}}_{QCD}[A_\mu, \bar{\psi}, \psi, g, m] \\ &= \int_0^\beta d\tau \int_V d^3\mathbf{x}\ \bar{\psi}(x)(\not{D}^{\mathrm{E}} + m)\psi(x) + \frac{1}{4}F_{\mu\nu}(x)F^{\mu\nu}(x), \end{aligned} \tag{1.3}$$

with the covariant derivative given as $\not{D}^{\mathrm{E}} \equiv \gamma^\mu(\partial_\mu + igA_\mu)$. Note that due to the Wick rotation the inverse temperature $\beta = 1/T$ and the Euclidean time τ are matched. This relation can be stressed by writing the QCD partition function as an Euclidean path integral with the Boltzmann weight given by the Euclidean action $S^{\mathrm{E}}_{\mathrm{QCD}}$ in Eq. (1.3)

$$\mathcal{Z} = \mathrm{Tr}[e^{-\beta H}] = \int \mathcal{D}A_\mu \mathcal{D}\bar{\psi}\mathcal{D}\psi e^{-S^{\mathrm{E}}_{\mathrm{QCD}}[A_\mu, \bar{\psi}, \psi, g, m]}. \tag{1.4}$$

The partition function is by all means essential for the calculation of any thermodynamic quantity. Note that the dependency on the bare input parameters g, m is dropped in the following. Furthermore, the expression Eq. (1.4) can be simplified by analytically integrating

over the Grassmann-valued fermionic part $\int \mathcal{D}\bar{\psi}\mathcal{D}\psi$ (see Appendix (B))

$$\mathcal{Z}_F = \int \mathcal{D}\bar{\psi}\mathcal{D}\psi e^{-S_F[A_\mu,\bar{\psi},\psi]} = \det M[A_\mu] \tag{1.5}$$

by means of the Matthews-Salam formula Eq. (B.5).
Finally, thermal expectation values of some observable $\mathcal{O}$ can be written in terms of Eq. (1.4) and Eq. (1.5) as

$$\langle \mathcal{O} \rangle = \frac{1}{\mathcal{Z}} \int \mathcal{D}A_\mu \mathcal{D}\bar{\psi}\mathcal{D}\psi \mathcal{O} e^{-S^{\mathrm{E}}_{\mathrm{QCD}}[A_\mu,\bar{\psi},\psi]} \tag{1.6}$$

$$= \frac{1}{\mathcal{Z}} \int \mathcal{D}A_\mu \mathcal{O}_F[A_\mu] e^{-S_{YM}[A_\mu]} \det M[A_\mu] \tag{1.7}$$

where $\mathcal{O}_F[A_\mu]$ is given by [22]

$$\mathcal{O}_F[A_\mu] = \frac{\int \mathcal{D}\bar{\psi}\mathcal{D}\psi \mathcal{O}[A_\mu,\bar{\psi},\psi] e^{-S_F[A_\mu,\bar{\psi},\psi]}}{\int \mathcal{D}[\bar{\psi}\psi] e^{-S_F[A_\mu,\bar{\psi},\psi]}} \tag{1.8}$$

In Section 1.3 these fundamental relations of QCD are formulated on a four-dimensional lattice.

1.2 Symmetries of QCD

This section covers a discussion on the symmetries of the QCD Lagrangian. Especially the introduction of a mass term will give rise to various scenarios. Since the breaking of certain symmetries is strongly related to the phase structure of QCD a short review on the expected phase diagram is given.
Within QCD the color charge is a conserved quantity characterized by the local symmetry group $SU(N_c)$ which is the defining local gauge group for the strong interactions. Global symmetries are of interest in order to study the dynamics of fermions coupled to gauge fields where the hierarchy of hadron masses is explained through the spontaneous breaking of symmetries giving rise to Goldstone bosons.

1.2.1 Chiral Symmetry

The non-interacting part of the QCD Lagrangian that contains the quark fields exhibits the symmetry properties of interest. For simplicity the Euclidean Lagrangian with massless quarks $m_q = 0$ is considered which yields the gauge invariant fermionic action

$$S_{\mathrm{F}} = \int d^4x \, \left(\bar{\psi}(x)\gamma_\mu[\partial_\mu + igA_\mu(x)]\psi(x) \right). \tag{1.9}$$

Based on the chiral projectors [23]

$$\begin{aligned} P_R &= \frac{\mathbb{1}+\gamma_5}{2}, \quad P_L = \frac{\mathbb{1}-\gamma_5}{2} \\ \text{with} \quad P_R P_L &= 0, \quad P_R^2 = P_R, \quad P_L^2 = P_L \quad \text{and} \quad P_R\gamma_\mu = \gamma_\mu P_L, \end{aligned} \tag{1.10}$$

the quark fields can be projected onto states of definite chirality

$$\begin{aligned} \psi_R &= P_R\psi, \quad \psi_L = P_L\psi, \quad \psi(x) = \psi_L(x) + \psi_R(x), \\ \bar{\psi}_R &= \bar{\psi}P_R, \quad \bar{\psi}_L = \bar{\psi}P_L, \quad \bar{\psi}(x) = \bar{\psi}_L(x) + \bar{\psi}_R(x). \end{aligned} \tag{1.11}$$

This decomposition allows to split up the fermionic action in a left and right-handed contribution

$$S_{\mathrm{F}} = \int d^4x \left(\bar{\psi}_L(x)\gamma_\mu[\partial_\mu + igA_\mu(x)]\psi_L(x) + \bar{\psi}_R(x)\gamma_\mu[\partial_\mu + igA_\mu(x)]\psi_R(x)\right), \tag{1.12}$$

such that also the Lagrangian $\mathcal{L} = \mathcal{L}_L + \mathcal{L}_R$ decouples into two independent terms. Therefore, the massless Lagrangian is invariant under independent left- and right-handed transformations. The symmetry group decomposition for massless quarks reads

$$SU(N_f)_V \otimes SU(N_f)_A \otimes U(1)_V \otimes U(1)_A, \tag{1.13}$$

where the indices denote vector ($L = R$) and axial-vector ($L = R^\dagger$) transformations. From the symmetry in Eq. (1.13) the $U(1)_A$ contribution is broken by quantum effects, also denoted as the axial anomaly, such that $SU(N_f)_V \otimes SU(N_f)_A \otimes U(1)_V$ remains, with $U(1)_V \equiv U(1)_B$ comprising the conservation of the Baryon number.

In case of finite quark masses, the introduction of a respective mass term mixes states of different chirality

$$S_{\mathcal{M}}[\bar{\psi}, \psi] = \int d^4x \, (\bar{\psi}_R \mathcal{M} \psi_L + \bar{\psi}_L \mathcal{M} \psi_R). \tag{1.14}$$

such that the $SU(N_f)_A$ is explicitly broken. In case of degenerate masses, the symmetry group is broken down to

$$SU(N_f)_V \otimes U(1)_V, \tag{1.15}$$

with the still intact $SU(N_f)_V$ vector subgroup. However, if non-degenerated masses $m_u \neq m_d \neq \ldots$ for the quark fields are assumed, also this part is explicitly broken down to

$$SU(N_f)_V \to \bigotimes_{f=1}^{N_f} U(1)_f = U(1)_u \otimes U(1)_d \otimes \cdots \otimes U(1)_{N_f}. \tag{1.16}$$

On the lattice the number of flavors is typically $N_f = 1, 2$ or $2 + 1$. The latter notation emphasizes that two light flavors (u and d) and a heavier quark (s) are considered. In nature the explicit breaking of chiral symmetry is very small in case of the two lightest quarks such that $SU(2)_L \otimes SU(2)_R$ is a very reasonable symmetry. By including the strange quark there are $\sim 10\%$ effects leading to a more strongly broken $SU(3)_L \otimes SU(3)_R$ symmetry [22].

1.2.2 Spontaneous Breaking of Chiral Symmetry

In theory, the QCD Lagrangian follows a symmetry of $SU(N_f)_L \otimes SU(N_f)_R \otimes U(1)_V$ for massless quarks. Compared with the continuum, the chiral symmetry $SU(N_f)_L \otimes SU(N_f)_R$ is present for $N_f = 2$ where isospin multiplets can be formulated for hadrons which then transform under $SU(2)_I = SU(2)_V$. For three flavors this symmetry is more approximate but still clearly visible in the spectrum.
However, mass degenerated parity doublets are missing in the spectrum of hadrons as expected if the full symmetry would be valid. For example the proton and neutron have masses of about 938 MeV while their parity partner has a mass of $\sim$ 1535 MeV [24]. Furthermore, the occurrence of light pseudo-scalar pions (π^+, π^-, π^0) as well as heavier but still light pseudo-scalar kaons (K^+, K^0, $\bar{K}^0$, K^-) and the η-meson has to be explained. A comparison with experimental data indicates that this significant mass difference must be due to a spontaneously broken symmetry. Physically, the spontaneous symmetry breaking in the confined phase can be understood by quarks polarizing the gluonic medium. This leads to the formation of a gluon cloud which gives the quarks an effective mass [10]. This mass also holds in case massless quarks are considered. If a continuous symmetry such as the chiral symmetry spontaneously breaks, it generates massless Goldstone bosons in the spectrum. The number of particles to be generated is stated by Goldstone's theorem as the difference of the number of generators of the full symmetry group and the subgroup that remains unbroken. Hence, for the chiral symmetry group there are $N_f^2 - 1$ massless Goldstone bosons to be expected as $SU(N_f)_L \otimes SU(N_f)_R \to SU(N_f)_V$. For $N_f = 2$ these are the three pions, while for $N_f = 3$ this yields the following eight particles [23]: the three pions, the four kaons, and the η-meson (c.f. Fig. C.1:Left).
In nature the particles associated with the Goldstone bosons do have finite, non-degenerated quark masses since the chiral symmetry is explicitly broken by the mass term. Either way, they can be seen as pseudo-Goldstone bosons which stay light due to u and d quark masses being much smaller than the QCD scale Λ_{MS} and the mass of the strange quark being of the order of the scale [23].

1.2.3 QCD Phase Diagram

In analogy with confinement, chiral symmetry and its breaking is another phenomenon that has not been proven analytically but can be observed in the non-perturbative framework

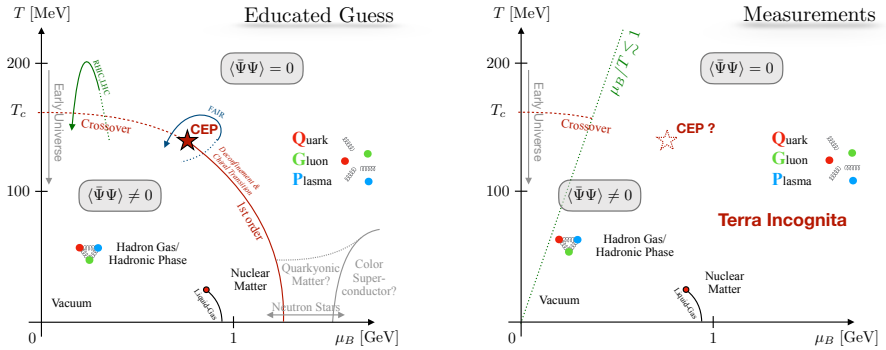

Figure 1.2: *Phase diagram of full QCD in terms of temperature T and baryon chemical potential μ_B.* ***Left:*** *It is expected that hadronic phase and the Quark Gluon Plasma are separated by a first order line at small temperatures and large densities. This line ends in a critical point (CEP) as a crossover region is connected to it at small densities and temperatures around T_c. The chiral restoration and deconfinement transition match and the chiral condensate $\langle\bar{\chi}\chi\rangle$ can be used as an order parameter.* ***Right:*** *In fact, only small portions of the phase diagram are settled. While the nuclear matter transition and a crossover region around T_c are verified, little is known about the rest of the finite density phase diagram from actual measurements. However, there are many heavy ion colliders probing the essential regions.*

accessible by lattice QCD. The order parameter is the chiral condensate [10]

$$\langle\bar{\psi}\psi\rangle = \langle 0|\bar{\psi}(x)\psi(x)|0\rangle = \langle 0|\bar{\psi}_R(x)\psi(x)_L + \bar{\psi}_L(x)\psi(x)_R|0\rangle \tag{1.17}$$

which is invariant under simultaneous (vector) transformations but not under general chiral rotations. If the chiral symmetry is restored, the chiral condensate vanishes. Otherwise, it has a non-zero expectation value $\langle\bar{\psi}\psi\rangle \neq 0$. Surprisingly, it is observed that the deconfinement phase transition and the chiral transition seem to coincide [21]. This is unexpected as these are related to two distinctly different physical effects. In other words, the chiral transition can indicate at what temperatures quarks and gluons deconfine and transition from the hadronic phase to a Quark-Gluon Plasma. At zero chemical potential the transition temperature is 156.5(1.5) MeV[25]. The main features of the expected phase diagram of full QCD are depicted in Fig. 1.2. In terms of thermodynamic quantities the chiral condensate and the chiral susceptibility are given by

$$\langle\bar{\psi}\psi\rangle = \frac{T}{V}\frac{\partial \ln \mathcal{Z}}{\partial m_q}, \quad \chi_{m_q} = \frac{\partial}{\partial m_q}\langle\bar{\psi}\psi\rangle. \tag{1.18}$$

While the condensate vanishes if the chiral symmetry is restored, the susceptibility forms a peak. Whether the chiral condensate drastically drops to zero when slowly increasing the temperature or if a smooth transition is expected depends on the type of phase transition that takes place. In the same manner the chiral susceptibility can diverge or stay finite depending

on the nature of the phase transition.
There are different schemes that classify the nature of a phase transition. The **modern classification** scheme distinguishes between two broad categories:

1. First-order, discontinuous phase transitions that involve a latent heat due to a fixed amount of energy being absorbed or released. The solid→liquid and liquid→gas transitions are of this category.

2. Second-order, continuous phase transitions that have no associated latent heat. These transitions are associated with critical phenomena and characterized by critical exponents. Systems that are filed in the same universality class have matching critical exponents [26].

The QCD phase diagram features a "crossover transition" in Fig. 1.2 which ends in a critical end-point (CEP). The existence as well as the exact location of the CEP is still subject to research. The crossover transition is not a real phase transition since there is no non-analyticity for a definite point with a sensitive order parameter. The phases are continuously connected. In case QCD simulations at vanishing quark masses are considered, denoted as the so-called chiral limit, the crossover becomes a second-order transition which terminates in a tri-critical point (TCP). The chiral condensate $\langle\bar{\psi}\psi\rangle$ stays finite along this transition while the susceptibility is divergent. At large chemical potentials both crossover or second-order transition turn into a first-order transition. In addition to this chiral restoration transition, there is the first-order liquid-gas phase transition of nuclear matter which terminates in a CEP. Along a first-order transition, both $\langle\bar{\psi}\psi\rangle$ and χ_q are discontinuous.

1.3 Lattice Quantum Chromodynamics

As in all Quantum Field Theories, also QCD has to deal with ultraviolet divergences which spoil calculations, even though the related physical quantities are well-defined and finite. In order to remove these contributions, it is necessary to "regulate" them, i.e. to remove the divergences such that they stay finite. In the low energy regime of QCD the typical perturbative regularization is useless. However, the replacement of continuous space-time by a hypercubic lattice provides the desired ultraviolet (UV) cutoff. This unphysical regulator must be removed in order for calculations to reproduce results in the continuum.

1.3.1 Lattice Regularization

For the regularization of Euclidean space-time, a hyper-cubic lattice Λ is introduced [22]

$$\begin{aligned}\Lambda \equiv a\{n = (n_1, n_2, n_3, n_4)| \\ \mathbf{n} = (n_1, n_2, n_3) = 0, 1, \ldots N_\sigma - 1;\ n_4 = 0, 1, \ldots N_\tau - 1\}\end{aligned} \tag{1.19}$$

The four-vector n labels all of the $|\Lambda| = \prod_\mu N_\mu = N_\sigma^3 \times N_\tau$ individual sites which are separated with respect to their nearest neighbor by the lattice spacing a. Each lattice site location is therefore addressed as

$$x \in \Lambda, \quad x_\mu = an_\mu, \quad n_\mu \in [0, N_\mu - 1] \;\; \forall\, \mu = 1, 2, 3, 4. \tag{1.20}$$

and consequently, the following replacements have to be taken into account

$$\begin{aligned} x &\to x = na \\ \int d^4x &\to a^4 \sum_{x \in \Lambda}. \end{aligned} \tag{1.21}$$

Applied on a function in the momentum this means

$$f(p_\mu) = \int dx_\mu e^{-ip_\mu x_\mu} f(x_\mu) \to a \sum_{x_\mu} e^{-ip_\mu x_\mu} f(x_\mu) \tag{1.22}$$

where the periodicity in the exponential

$$f\left(p_\mu + \frac{2\pi}{a} e_\nu\right) = \sum_{x_\mu} e^{-ip_\mu x_\mu} e^{-2\pi i n_\nu} f(x_\mu) = f(p_\mu) \tag{1.23}$$

constraints the momenta to a finite Brillouin Zone as $n_\nu \in \mathbb{Z}$. The maximum momentum of $p \sim 1/a$ acts as the mentioned regulator to render lattice QCD ultraviolet save.
Typically, the spatial volume is considered to be isotropic with $N_\sigma^3 = N_1 \cdot N_2 \cdot N_3$. In general it will deviate from the temporal extent $N_\sigma \neq N_\tau$.
In the following, lattice sites host quark fields

$$\psi(x), \bar{\psi}(x), \quad x \in \Lambda \tag{1.24}$$

while the gluon gauge fields will be placed on the links connecting two adjacent sites. They are represented by the link variables $U_\mu(x)$, interconnecting site x with its neighbor in direction $ae_\mu = \mu$.
The main errors in lattice QCD arise from discretization effects and finite volume effects. These can be improved by choosing the spatial extent much larger than the correlation length $aN_\sigma \gg \xi$ of the particle to be investigated as well as $\xi \gg a$. As ξ is proportional to the inverse of the lightest hadron mass, it can be deduced that discretization effects are small if $aM \ll 1$, while finite volume effects are small for $aMN_\sigma \gg 1$.
Note that due to the lattice discretization, symmetries are violated such as Lorentz symmetry. These are recovered when proceeding towards the continuum limit. This is done by first extrapolating in the volume $V = N_\sigma^3 \to \infty$ denoted as thermodynamic limit and second by removing the lattice spacing $a(\beta) \to 0$. A naïve continuum limit procedure by just sending

$a \to 0$ as presented for the discussion of the gauge and fermion part of the discretized QCD action (see Sections (1.3.2) and (1.3.3)) is not possible, as the only input parameters are bare parameter, namely the bare coupling $g^2 = 2N_c/\beta$ and the bare quark masses $am_u, am_d, \ldots, am_f$. Instead of referring to the continuum limit by $a \to 0$, the relation $\beta \to \infty$ is used because of $\beta \propto g^{-2}$ and $g \to 0$. Discussions on the functional dependence of $g(a)$ via the Renormalization Group Equation (RGE) (or Callan–Symanzik equation) can be found in [22, 27] and [20].

1.3.2 A Naïve discretization - Gluons

First the Yang-Mills contribution comprising the gluon propagation term of QCD is formulated in terms of lattice degrees of freedom. Such studies where the quarks are considered as infinitely heavy, static objects is referred to as quenched limit with only gluons being the dynamic variables. Due to the requirement of gauge invariance according to $SU(3)$ transformations, a gluon field is required to be represented by an appropriate lattice version which is an element of the color gauge group as well. These lattice degrees of freedom are the so-called link variables $U_\mu(x)$. As indicated by their name, the link variables connect two sites which are required to be nearest neighbors. For the construction of loops it is useful to note that link variables showing in backward direction $U_{-\mu}(x)$ are given as

$$U_{-\mu}(x) = U_\mu(x-\mu)^\dagger. \tag{1.25}$$

In order to reconstruct the gauge invariant gluonic part of the continuum action $S_{\mathrm{G}}^{\mathrm{Cont.}} = \frac{1}{4}\int d^4x F_{\mu\nu}F^{\mu\nu}$ up to some order in the lattice spacing a, the smallest closed loop build from links on the lattice is considered, the so-called plaquette (see Fig. 1.3)

$$U_{\mu\nu}(x) \equiv U_\mu(x)U_\nu(x+\mu)U_\mu^\dagger(x+\nu)U_\nu^\dagger(x) = \square_{\mu\nu}(x). \tag{1.26}$$

Its traced real part is gauge invariant. In fact, the trace of any path ordered product of link variables which forms a closed loop is gauge invariant. Based on the plaquette the Wilson gauge action is formulated [11]

$$S_{\mathrm{G}}(U) = \beta \sum_x \sum_{\mu<\nu} \left(1 - \frac{1}{N_c}\mathrm{Re}\,\mathrm{Tr}\,U_{\mu\nu}(x)\right), \tag{1.27}$$

with the lattice coupling β being related to the bare coupling g via $\beta = \frac{2N_c}{g^2}$. This is the discrete expression for the continuum gauge action contribution.

In order to ensure that the correct continuum limit can be recovered, the limit $a \to 0$ has to be performed. To do so, the relation of gauge fields $A_\mu(x) = \sum_{a=1}^{N_c^2-1} \frac{\Lambda^a}{2} A_\mu^a(x)$ and link

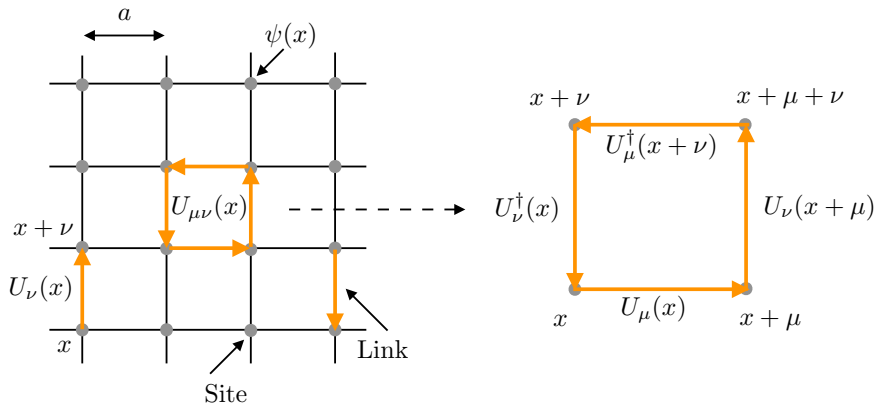

Figure 1.3: ***Left:*** *An isotropic hypercubic lattice. Sites x denote where the quark fields $\psi(x)$ are placed at. These are connected by links $U_\mu(x)$ which have an orientation μ and represent the gauge degrees of freedom. The lattice spacing a denotes the shortest distance between two neighboring sites.* ***Right:*** *The smallest loop on a lattice, the plaquette $U_{\mu\nu(x)}$ consisting of four links. Its trace is gauge invariant.*

variables in terms of the parallel transporter is recalled

$$U_\mu(x) = \mathcal{P} e^{iag\int_x^{x+\mu} dx_\mu A_\mu(x)} \approx e^{iagA_\mu(x)}, \tag{1.28}$$

with $\mathcal{P}$ denoting the path-ordering. The parallel transporter shifts color from a point x on the lattice to the adjacent one in direction μ. The plaquette in terms of the gauge field variables reads

$$U_{\mu\nu}(x) = e^{iagA_\mu(x+\mu/2)} e^{iagA_\nu(x+\mu+\nu/2)} e^{-iagA_\mu(x+\nu+\mu/2)} e^{-iagA_\nu(x+\nu/2)}. \tag{1.29}$$

By utilizing the Baker-Campell Hausdorff formula $e^A e^B = e^{A+B+\frac{1}{2}[A,B]} + \ldots$ yields

$$U_{\mu\nu}(x) = e^{ia^2 g(\partial_\mu A_\nu(x) - \partial_\nu A_\mu(x) + ig[A_\mu(x), A_\nu(x)]) + \mathcal{O}(a^3)} = e^{ia^2 g F_{\mu\nu} + \mathcal{O}(a^3)}, \tag{1.30}$$

with the field strength tensor $F_{\mu\nu}(x) = \partial_\mu A_\nu(x) - \partial_\nu A_\mu(x) - ig[A_\mu(x), A_\nu(x)]$ defined just as the continuum version. Finally, an expansion in the lattice spacing a results in

$$U_{\mu\nu}(x) = 1 + ia^2 g F_{\mu\nu} - \frac{a^4 g^2}{2} F_{\mu\nu} F^{\mu\nu} + \mathcal{O}(a^6) \tag{1.31}$$

which is inserted into the Wilson action Eq. (1.27) with the real part of the trace removing the $\mathcal{O}(a^2)$-term of Eq. (1.31). The Wilson action becomes

$$S_\mathrm{G} = \frac{a^4}{4} \sum_x \sum_{\mu<\nu} \mathrm{Tr}\, F_{\mu\nu} F^{\mu\nu} + \mathcal{O}(a^2). \tag{1.32}$$

In the continuum limit the order $\mathcal{O}(a^2)$ cut-off effects become irrelevant as they vanish for $a \to 0$. In order to approach the continuum limit faster, there are strategies incorporating larger gauge invariant loops in the formulation of the gauge action.

1.3.3 A Naïve Discretization - Fermions

This section covers the naïve lattice discretization of the quark fields. For the sake of simplicity, the interacting contribution is disregarded for this discussion such that free fermion fields are described. Therefore, it is the goal to find a formulation for the continuum fermion action

$$S_{\mathrm{F}}^{\mathrm{free}}[\psi, \bar{\psi}] = \int d^4x \, \left(\bar{\psi}(x)[\gamma_\mu D_\mu + m]\psi(x)\right) s \tag{1.33}$$

in terms of the discretized degrees of freedom, with the covariant derivative $D_\mu = \partial_\mu + igA_\mu$. While the prescription from Eq. (1.21) dictates how to convert the space-time integral to a finite sum over lattice sites, the quark fields are placed on the lattice sites according to Eq. (1.24). For the naïve fermion formulation, the derivatives of the quark fields have to be replaced by finite differences. For a symmetric discrete derivative scheme

$$\partial_\mu \psi(x) \to \frac{1}{2a}(\psi(x+\mu) - \psi(x-\mu)), \tag{1.34}$$

a lattice version of the free fermion action reads

$$S_{\mathrm{F}}^{\mathrm{free}}[\psi, \bar{\psi}] = a^4 \sum_{x\in\Lambda} \bar{\psi}(x) \left(\gamma_\mu \frac{\psi(x+\mu) - \psi(x-\mu)}{2a} + m\psi(x)\right). \tag{1.35}$$

This expression is not gauge invariant yet when applying the transformations

$$\psi(x) \to \psi' = \Omega(x)\psi(x), \tag{1.36}$$

$$\bar{\psi}(x) \to \bar{\psi}' = \bar{\psi}(x)\Omega^\dagger(x) \tag{1.37}$$

on the finite difference quark field term, with $\Omega(x)$ being an element of $SU(3)$. A gauge invariant formulation is obtained by introducing the link variables $U_\mu(x)$ from Sec. 1.3.2 which transform according to

$$U_\mu(x) \to U'_\mu(x) = \Omega(x)U_\mu(x)\Omega^\dagger(x+\mu). \tag{1.38}$$

Thus, the naïve action for fermions in an external gauge field U reads

$$S_{\mathrm{F}}[\psi, \bar{\psi}, U] = a^4 \sum_{x\in\Lambda} \bar{\psi}(x) \left(\gamma_\mu \frac{U_\mu(x)\psi(x+\mu) - U_{-\mu}(x)\psi(x-\mu)}{2a} + m\psi(x)\right) \tag{1.39}$$

$$= a^4 \sum_{x,y\in\Lambda} \bar{\psi}(x) M(x,y) \psi(y). \tag{1.40}$$

In the last line the bilinear structure was identified, with the naïve lattice Dirac operator (or fermion matrix) given as

$$M(x,y) = \frac{1}{2a}\sum_{\mu}\gamma_\mu[U_\mu(x)\delta(x+\mu,y) - U_\mu^\dagger(x-\mu)\delta(x-\mu,y)] + m\delta(x,y). \tag{1.41}$$

For $a \to 0$, the link variables from Eq. (1.28) are Taylor expanded

$$\begin{aligned} U_\mu(x) \approx& 1 + iagA_\mu(x) + \mathcal{O}(a^2) \\ U_{-\mu}(x) \approx& 1 - iagA_\mu(x-\mu) + \mathcal{O}(a^2) \end{aligned} \tag{1.42}$$

and inserted in the action Eq. (1.39)

$$\begin{aligned} S_F[\psi,\bar{\psi},U] =& a^4\sum_{x\in\Lambda}\bar{\psi}(x)\left[\sum_{\mu=1}^{4}\gamma_\mu\left(\frac{\psi(x+\mu)-\psi(x-\mu)}{2a}\right.\right. \\ &\left.\left. + \frac{iagA_\mu(x)\psi(x+\mu) + iagA_\mu(x-\mu)\psi(x-\mu)}{2a}\right) + m\psi(x)\right] + \mathcal{O}(a) \\ =& a^4\sum_{x\in\Lambda}\bar{\psi}(x)\left[\gamma_\mu(\partial_\mu + igA_\mu(x))\psi(x) + m\psi(x)\right] + \mathcal{O}(a). \end{aligned} \tag{1.43}$$

In the last line it is used that $\psi(x \pm \mu) = \psi(x) + \mathcal{O}(a)$ and $A_\mu(x-\mu) = A_\mu(x) + \mathcal{O}(a)$. Additionally, the continuum derivative is already reintroduced to highlight the similar structure to Eq. (1.33).

In comparison, the fermionic part of the action provides an error in the lattice spacing of order $\mathcal{O}(a)$ while for the gauge part it is $\mathcal{O}(a^2)$. Note that the naïve discretization scheme is only one choice to reproduce the continuum action.

The final partition sum, taking into account the gauge-invariant measure on the lattice reads

$$\mathcal{Z} = \int\prod_{x\in\Lambda} d\bar{\psi}(x)d\psi(x)\int\prod_{x\in\Lambda}\prod_{\mu=0}^{3} dU_\mu(x)e^{-S_F[U,\bar{\psi},\psi]}e^{-S_G[U]} \tag{1.44}$$

The naïve lattice discretization introduces a major drawback in the form of the doubler problem which is explored hereafter.

1.3.4 Doubling Problem

In the following, the doubling problem is explored that hinders the use of the naïve fermion discretization. For the free fermion action, i.e. $U_\mu(x) = \mathbb{1}$, the Dirac operator Eq. (1.41) in momentum space reads

$$\tilde{M}(p) = m\cdot\mathbb{1} + \frac{i}{a}\sum_{\mu=1}^{4}\gamma_\mu\sin(p_\mu a) \tag{1.45}$$

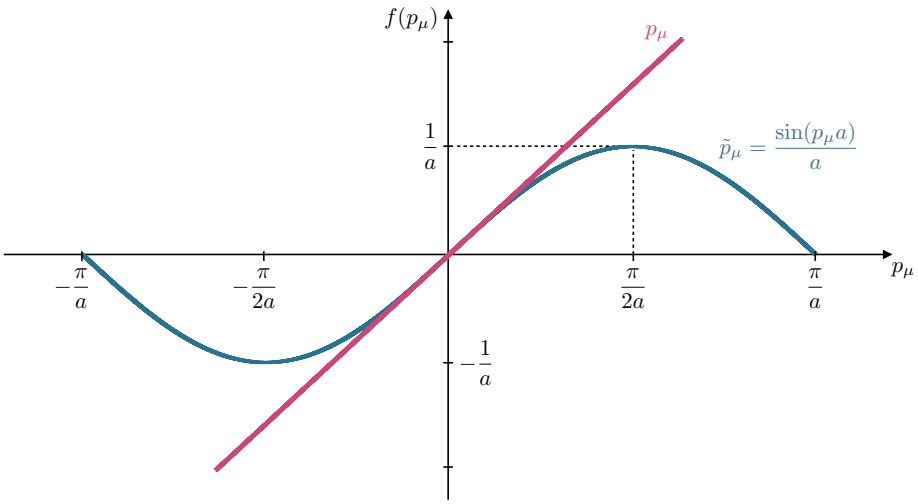

Figure 1.4: *The naïve lattice discretization gives rise to the momentum* $\tilde{p}_\mu = \sin(p_\mu a)/a$ *which becomes zero at additional locations* $\pm\pi/2$ *within the Brillouin Zone. In comparison, the continuum momentum* p_μ *has a simple zero at* 0*. In four dimensions this gives rise to* 16 *poles or so-to-say* 15 *unwanted doublers. (Figure inspired by [20])*

which has to be inverted in order to give rise to the fermion propagator [20]

$$\tilde{M}(p)^{-1} = \frac{m - i\sum_\mu \gamma_\mu \tilde{p}_\mu}{m^2 + \sum_\mu \tilde{p}_\mu^2}, \tag{1.46}$$

where $\tilde{p}_\mu$ is given by $\tilde{p}_\mu = \sin(p_\mu a)/a$ (see Fig. 1.4). For $\tilde{p}_\mu \to p_\mu$ the continuum propagator is obtained

$$\underset{a\to 0}{\overset{m=0}{\Rightarrow}} \frac{-i\sum_\mu \gamma_\mu p_\mu}{p^2}. \tag{1.47}$$

This propagator has a single particle pole at $p_{\text{Phys}} = (0,0,0,0)$ for massless fermions. However, the discrete lattice version does not just have a single pole at zero momentum but it is spoiled by the Sine-function which introduces additional contributions. Within the Brillouin Zone there are 15 additional locations where the Sine-function becomes zero for $p_\mu = \pi/2$. These correspond to the edges of the Brillouin Zone

$$p_{\text{Edge}} = \{(\pi/2,0,0,0),(0,\pi/2,0,0),\ldots,(\pi/2,\pi/2,\pi/2,\pi/2)\} \tag{1.48}$$

with a doubling in the number of particles with each dimension. In four dimension there are $2^d = 15 + 1 = 16$ poles, 15 unphysical and a single physical relevant one.
Thus, the naïve discretization produces $N_f \cdot 2^d$ particles which do not vanish in the limit $a \to 0$. This is the motivation for the use of different fermion actions, such as the staggered formulation, which try to cancel out the doublers with additional contributions. These

contributions are required to vanish in the continuum limit as well. A limitation concerning the construction of lattice fermion formulations is given by the Nielsen–Ninomiya theorem. This theorem states that there is no fermion action without doublers that has all the following properties [28]:

- Continuum chiral symmetry ($\{D, \gamma_5\} = 0$) in massless case
- Locality of the fermion operator
- Correct continuum limit

Hence, there are various approaches to discretize fermions in order to tackle the doubling problem. For Wilson fermions all doublers are removed, however, chiral symmetry is explicitly broken. In contrast, the idea of staggered fermions is to reduce the number of doublers by a factor of four, such that doublers will remain in the continuum, however, also chiral symmetry is partly kept restored.
The fermion doubling phenomenon is strongly related to the existence of the chiral anomaly. While in the continuum the anomaly arises from the chiral non-invariance of the path integral measure [23], for the lattice version it is the non-invariance of the Lagrangian.

1.3.5 Staggered Fermions

In order to work towards the staggered formulation, a symmetry of the naïve action is utilized which reduces the number of doublers by a factor four. This four-fold degeneracy is obtained by a local transformation of the fermion fields (spin-diagonalization)

$$\psi(x) \to \Omega(x)\psi'(x), \quad \bar{\psi}(x) \to \bar{\psi}'(x)\Omega^\dagger(x), \tag{1.49}$$

with a total of sixteen different transformation matrices Ω defined as [29]

$$\Omega(x) = \gamma_0^{x_0}\gamma_1^{x_1}\gamma_2^{x_2}\gamma_3^{x_3} \text{ and } x_\mu \in (0, 1). \tag{1.50}$$

This transformation is used to remove the γ_μ dependence from the naïve fermion description by applying

$$\begin{aligned} \eta_\mu(x) \equiv \Omega^\dagger(x)\gamma_\mu\Omega(x) =& (-1)^{x_0+x_1+x_2+x_3} \\ \Omega^\dagger(x)\Omega(x) =& \mathbb{1}. \end{aligned} \tag{1.51}$$

The newly introduced staggered phases $\eta_\mu(x)$ take over the role of the γ_μ matrices such that the whole action S will be diagonal in Dirac space. The phases are constraint by

$$\begin{aligned} \eta_\mu(x)\eta_\nu(x+\mu)\eta_\mu^\dagger(x+\nu)\eta_\nu^\dagger(x) =& -1 \\ \Rightarrow \eta_\mu(x) =& (-1)^{\sum_{\nu<\mu} x_\nu}. \end{aligned} \tag{1.52}$$

Finally, the fermion action acquires the form

$$S = \sum_{x\in\Lambda}\sum_{\alpha=0}^{3}\left[\bar{\psi}_\alpha(x)\sum_{\mu=0}^{3}\left(\eta_\mu(x)\frac{U_\mu(x)\psi_\alpha(x+\mu)-\psi_\alpha(x-\mu)U_\mu^\dagger(x-\mu)}{2a}\right)+m\bar{\psi}_\alpha(x)\psi_\alpha(x)\right] \tag{1.53}$$

Each component of the Dirac spinor labeled by α yields the same term. Because of being diagonal, three of the four components can be discarded and the one-component field χ is introduced. This reduces the number of Dirac particles in the continuum from 16 to four. In order to distinguish these four continuum quark flavors, the term *taste* is introduced. With the newly defined one-component fields χ the gauge invariant staggered action reads

$$\begin{aligned} S_{\text{stagg}}(\mu) = \sum_{x\in\Lambda}\frac{1}{2a}\Big[&\eta_0(x)\gamma\bar{\chi}(x)\left(e^{a_\tau\mu_q}U_0(x)\chi(x+0)-\chi(x-0)e^{-a_\tau\mu_q}U_0^\dagger(x-0)\right)\\ &+\sum_{i=1}^{d}\eta_i(x)\bar{\chi}(x)\left(U_i(x+0)\chi(x+i)-\chi(x-i)U_i^\dagger(x-0)\right)+m\bar{\chi}(x)\chi(x)\Big] \end{aligned} \tag{1.54}$$

where it is incorporated that general lattice simulations with staggered fields are performed on anisotropic lattices $a_\sigma \neq a_\tau$, thus, accounting for the bare anisotropy parameter γ. Furthermore, a quark chemical potential contribution is incorporated.

There are a total of 16 one component fields, each with a different phase factor, corresponding to the sites of a 2^4 hypercube. Each such staggered fermion with its 16 components can be seen as four tastes of continuum fermions each with four Dirac components. Note that the taste-symmetry of rotations is broken by a discrete lattice leading to a mass splitting of the taste multiplets [30].

In contrast to Wilson fermions, the staggered formulation keeps a remnant chiral symmetry. This is stressed by considering the transformation of γ_5. According to Eq. (1.49) this is given by [22]

$$\bar{\psi}(x)\gamma_5\psi(x) = \eta_5(x)\bar{\psi}(x)'\psi(x)'. \tag{1.55}$$

Thus, the site-dependent staggered phase $\epsilon(x) \equiv \eta_5 = (-1)^{x_0+x_1+x_2+x_3}$ substitutes γ_5. In the chiral limit the staggered action is then invariant under continuous transformations

$$\chi(x) \to e^{i\alpha\epsilon(x)}\chi(x), \quad \bar{\chi}(x) \to \bar{\chi}e^{i\alpha\epsilon(x)}. \tag{1.56}$$

This is the global chiral symmetry for the staggered quark degrees of freedom that are distributed over the hypercube.

A further reduction of the number of doublers can be achieved by applying the rooting procedure where the quartic (square) root is taken from the four-flavor staggered determinant

$\det[M]$ yielding one (two) flavors.
Within this dissertation, staggered fermions based on the action Eq. (1.54) are used.

1.3.6 Finite Temperature and Density

Lattice studies at finite temperature and density are of interest in order to investigate QCD matter in the early stages of the universe and the condensation of hadrons during the cooling process [22].

Finite Temperature The infinite space-time volume limit corresponds to QCD at zero temperature. However, as implied by the continuum discussion of Equations (1.3) and (1.4) a non-zero temperature is achieved by restricting the physical extent of time to β while the spatial volume is still be considered in the infinite volume limit. The corresponding fields are periodic (bosons) or anti-periodic (fermions) in time. While the spatial contribution is still considered in the infinite volume limit, the Euclidean lattice time extent is associated with

$$\beta = aN_\tau = \frac{1}{T}. \tag{1.57}$$

The limit $\beta \to \infty$ corresponds to $T \to 0$. At finite spatial volume and finite temperature the continuum limit is achieved by $a \to 0$ while aN_σ and aN_τ are kept fixed.

Finite Density For QCD matter the net quark number density is non-vanishing. This is accounted for by considering a non-zero quark chemical potential which yields the grand canonical ensemble

$$\mathcal{Z}(T, \mu) = \mathrm{Tr}\left[e^{-\beta(H-\mu_q N_q)}\right], \tag{1.58}$$

with the quark number N_q. Alternatively, the baryon number $N_B = N_q/3$ and the baryon chemical potential $\mu_B = 3\mu_q$ can be used. Since N_q and N_B are integer valued, the grand canonical partition function can be expanded in a power series

$$\mathcal{Z}(T, \mu) = \sum_n \left(e^{\mu_q/T}\right)^n \mathcal{Z}(T). \tag{1.59}$$

This expansion is referred to as fugacity expansion with the fugacity variable $e^{\mu_q/T}$ and the quark number $n \in \mathbb{Z}$ [22].
The finite density sign problem arises when integrating out the fermionic contribution to the partition function which results in the fermion determinant Eq.(1.5) which depends on the chemical potential. For $\mu = 0$ the fermion matrix exhibits γ_5 hermicity which leads to

$$\det M^\dagger = \det(\gamma_5 M \gamma_5) = \det M = (\det M)^*, \tag{1.60}$$

i.e. the determinant is real. However, for non-zero μ the determinant becomes complex [31]

$$M^\dagger(\mu) = \gamma_5 M(-\mu^*)\gamma_5. \tag{1.61}$$

This prevents Monte Carlo methods from using the fermion determinant as a probability measure for finite, real chemical potentials.

1.4 Strong Coupling Limit

QCD suffers from a severe sign problem when considering calculations at finite chemical potential due to the fermion determinant becoming complex. A possible solution to this problem is to consider a dual formulation which is an established method and has been applied to many models in the past (a more detailed review can be found in [32]). To obtain a dual formulation the original degrees of freedom are integrated out and replaced by discrete ones that encode nearest neighbor interactions. These can be expressed as unoriented occupation numbers which are usually referred to as monomers and dimers as well as oriented fluxes [32]. Both, occupation numbers and fluxes, are restricted by constraints which are enforced by the original symmetries of the system.

In the strong coupling limit of QCD the dual degrees of freedom result in a sign problem that becomes mild [33, 34]. Note that enforcing the strong coupling limit $g \to \infty$ alone, will not solve the sign problem but the dual degrees of freedom are essential. Furthermore, it is possible for a model to have several dual representations with different sign problems.

1.4.1 Dual Representation of Strong Coupling QCD

Within the strong coupling limit the Wilson plaquette action $S_G[U]$ vanishes from Eq. (1.44) as $\beta = 0$. By considering a staggered fermion action $S_F = S_{\text{stagg}}$ (cf. Eq. (1.54)) the QCD partition function reads

$$\begin{aligned} Z &= \int \prod_x \left(d\bar{\chi}(x) d\chi(x) e^{2am_q \bar{\chi}(x)\chi(x)} \prod_\mu \left[dU_\mu(x) e^{\eta_\mu(x)\left(\bar{\chi}(x)U_\mu(x)\chi(x+\mu) - \bar{\chi}(x+\mu)U_\mu^\dagger(x)\chi(x)\right)} \right] \right) \\ &= \int \prod_x \left(d\bar{\chi}(x) d\chi(x) e^{2am_q \bar{\chi}(x)\chi(x)} \prod_\mu z(x,\mu) \right), \end{aligned} \tag{1.62}$$

where the sum over the lattice points x and directions μ factorizes into respective products. For a finite chemical potential μ_q as well as an anisotropic lattice the temporal links $U_{\pm 0}(x)$ are weighted with the factor $\gamma \exp(\pm a_\tau \mu_q)$. The last line of Eq. (1.62) features the one-link

integral $z(x,\mu)$ over the Haar measure for $U(N_c)$ or $SU(N_c)$ which is of the form [30, 33]

$$z(x,y) = \int dU e^{\bar{\chi}(x)U\chi(y) - \bar{\chi}(y)U^\dagger\chi(x)}. \tag{1.63}$$

The staggered phase factor as well as the additional weight factor of the temporal link variable component can be absorbed in a redefinition of the χ fields to match the form of Eq. (1.63). The only contributions from this integral that arise must have equal powers in U and $U^\dagger$ modulo N_c. For the different gauge groups the integration yields [30, 33]

$$z(x,y) = \sum_{k=0}^{N_c} \left[\alpha_k \left(\rho(x,y)^2 \bar{\chi}(x)\chi(x)\bar{\chi}(y)\chi(y)\right)^k\right] \tag{1.64}$$

$$+\frac{\kappa}{N_c!}\left[(\tilde{\rho}(x,y)\bar{\chi}(x)\chi(y))^{N_c} + (-1)^{N_c}(\tilde{\rho}(y,x)\bar{\chi}(y)\chi(x))^{N_c}\right], \tag{1.65}$$

where

$$\alpha_k = \frac{(N_c-k)!}{N_c!k!} \quad \text{and} \quad \kappa = \begin{cases} 0, & U(N_c) \\ 1, & SU(N_c) \end{cases} \tag{1.66}$$

follows from an integration over $\int d\bar{\chi}(x)d\chi(x)e^{\bar{\chi}(x)\chi(x)}$ of Eq. (1.63) and likewise Eq. (1.64)

$$\begin{aligned} \int d\bar{\chi}(x)d\chi(x)e^{\bar{\chi}(x)\chi(x)}\left[\int dU e^{\bar{\chi}U\chi - \bar{\chi}U^\dagger\chi}\right] &= e^{\bar{\chi}(y)\chi(y)} = \sum_{k=0}^{\infty}\frac{1}{k!}(\bar{\chi}(y)\chi(y))^k \\ \int d\bar{\chi}(x)d\chi(x)e^{\bar{\chi}(x)\chi(x)}\left[\sum_{k=0}^{N_c}\alpha_k(\bar{\chi}(x)\chi(x)\bar{\chi}(y)\chi(y))^k\right] &= \sum_{k=0}^{N_c}\alpha_k\frac{N_c!}{(N_c-k)!}(\bar{\chi}(y)\chi(y))^k, \end{aligned} \tag{1.67}$$

and a matching of the coefficients of $\bar{\chi}(y)\chi(y)$ [30, 33]. Note that the factor $\rho(x,y)$ in Eq. (1.64) had to be neglected to match the form of the one-link integral Eq. (1.63). The factors $\rho(x,y)$ and $\tilde{\rho}(x,y)$ summarize the contributions from the phase factor, the anisotropy and the chemical potential

$$\rho(x,y) = \eta_\mu(x)\gamma^{\delta_{0,\mu}} \quad \text{and} \quad \tilde{\rho}(x,y) = \eta_{y-x}(x)\begin{cases} \gamma\exp(\pm a_\tau\mu_q), & (y-x)_0 = \pm 1 \\ 1, & \text{otherwise.} \end{cases} \tag{1.68}$$

Equation (1.64) comprises the result for the $U(N_c)$ gauge group, i.e. $\kappa = 0$, where the combinations of $M(x) \equiv \bar{\chi}(x)\chi(x)$ represent the bosonic ("mesonic") degrees of freedom. These come in pairs of two $M(x)M(y)$ with a so-called mesonic link connecting them. For the $SU(N_c)$ gauge group an additional term, i.e. $\kappa = 1$, yields the fermionic ("baryonic") degrees of freedom $B(x) \equiv \frac{1}{N_c!}\epsilon_{i_1\ldots i_N}\chi_{i_1}(x)\ldots\chi_{i_N}(x)$ which are oriented fluxes connecting to sites $B(x)\bar{B}(y)$. The quark chemical potential affects the baryonic contribution where the mild sign problem is still hidden such that $SU(N_c)$ simulations are affected by it. The one-link

integral in terms of mesons and baryons reads

$$z(x,y) = \sum_{k=0}^{N_c} \left[\alpha_k(\rho(x,y)^2 M(x)M(y))^k\right] \tag{1.69}$$

$$+\kappa \left[\tilde{\rho}(x,y)^{N_c}\bar{B}(x)B(y) + (-1)^{N_c}\tilde{\rho}(y,x)^{N_c}\bar{B}(y)B(x)\right]. \tag{1.70}$$

Finally, after the link variables are integrated out, the Grassmann integral is evaluated. Note that interchanging the order of integration is possible due to the absent plaquette contribution for $\beta(g) = 0$. An integration of the exponential in Eq. (1.62) yields [27, 33]

$$\int \prod_x d\bar{\chi}(x)d\chi(x)e^{2am_q\bar{\chi}(x)\chi(x)} = (2am_q)^{N_c}, \tag{1.71}$$

which follows when expanding the exponential as $1 + 2am_q\bar{\chi}(x)\chi(x)$. Due to the nilpotency of Grassmann variables this series terminates after the second term (see Appendix Sec. B). The full Grassmann integral including the mesonic contributions yields integrals of the form

$$\int \prod_x d\bar{\chi}(x)d\chi(x)e^{2am_q\bar{\chi}(x)\chi(x)}(\bar{\chi}(x)\chi(x))^k = \frac{N_c!}{n_x!}(2am_q)^{n_x}, \quad n_x = N_c - k. \tag{1.72}$$

The integration generates constraints on possible configurations as well as on the mix of degrees of freedom occupying a lattice site. There are three contributions [33, 35]:

Dimers The mesonic contribution comes from the one-link integral term $(M(x)M(y))^k$. This comprises a mesonic hopping between the sites x and y which is non-oriented. The number k is the dimer or link occupation number taking values $k \in \{0, 1, \dots N_c\}$. It states how many dimers are attached to a specific link connecting sites x and y.

Monomers These contributions arise from the Grassmann integration over the Boltzmann factor involving the quark mass m_q. The monomer number n_x is constraint to $n_x \in \{0, 1, \dots N_c\}$. While a baryonic contribution excludes monomers from a site, a mesonic contribution yields a reduction in the total monomer number

$$n_x = N_c - \sum_{\mu=\pm 0,\dots,\pm d} k_\mu(x) \tag{1.73}$$

which is the so-called Grassmann Constraint for monomers and dimers.

Baryon Loops The baryonic degrees of freedom occur in the one-link integration for a gauge group $SU(N_c)$. These form directed pairs $\bar{B}(y)B(x)$ located at different sites with $B(x)$ exploiting N_c staggered fields $\chi_{i_1}(x)\dots\chi_{i_N}(x)$ and $\bar{B}(y)$ exploiting the fields $\bar{\chi}_{i_1}(x)\dots\bar{\chi}_{i_N}(x)$. This leaves the baryonic contribution $\bar{B}(x)$ at site x and $B(y)$ at site y which will also connect to a nearest neighbor to form a pair $\bar{B}(x)B(z)$ or $\bar{B}(\tilde{z})B(y)$

respectively. Thus, baryons will form a closed, self-avoiding loop with single chain elements $\bar{B}(y)B(x)$. A baryonic link variable $b_\mu \in \{-1, 0, 1\}$ assigns to all links connected to site x a value of 1 for an incoming baryon line, -1 for an outgoing line and 0 when no baryon line occupies the link. Since there is no baryon source or sink the constraint reads

$$\sum_{\mu=\pm 0,\ldots,\pm d} b_\mu(x) = 0. \tag{1.74}$$

Furthermore, the Grassmann Constraint for a system of monomers, dimers and baryon loops is given as

$$n_x + \sum_{\mu=\pm 0,\ldots,\pm d} k_\mu(x) + \sum_{\mu=\pm 0,\ldots,\pm d} \frac{N_c}{2}|b_\mu(x)| = N_c. \tag{1.75}$$

In the following baryon loops are denoted by ℓ. The final expression after the gauge field and Grassmann integration for the partition function in the strong coupling limit reads

$$\mathcal{Z}(\gamma, N_\tau, m_q, \mu_q) = \sum_{\{k,n,\ell\}} \left(\prod_{x,\mu} \frac{(N_c - k_\mu(x))!}{N_c! k_\mu(x)!} \gamma^{2k_\mu(x)\delta_{0,\mu}} \prod_x \frac{N_c!}{n_x!} (2am_q)^{n_x} \prod_\ell w(\ell, \mu_q) \right), \tag{1.76}$$

where the very first sum runs over all configurations k, n, ℓ yielding non-zero contributions based on the dimer (k) and monomer (n) occupation numbers as well as the baryon loops ℓ. The first term describes the mesonic hoppings, while the second comprises the monomer contribution. The final term describes the baryon loop where the quark chemical potential is hidden in the weight

$$w(\ell, \mu_q) = \sigma(\ell)\gamma^{N_c \sum_x |\ell_0(x)|} \exp\left(N_c N_\tau \omega(\ell) a_\tau \mu_q\right), \tag{1.77}$$

with ℓ_0 the number of lattice sites on a baryon loop in temporal direction. The sign $\sigma(\ell)$ depends on the geometry of the baryon loop [35]

$$\sigma(\ell) = (-1)^{\omega(\ell)+N_-(\ell)+1} \prod_{b=(x,\mu)\in\ell} \eta_\mu(x) \tag{1.78}$$

and comprises the sign problem in this dual formulation. The winding number $\omega(\ell)$ in Eq. (1.78) counts the number of boundary crossings in forward or backward temporal direction ($\omega(\ell) \in \mathbb{Z}$) and $N_-(\ell)$ sums up the number of links which are oriented in negative temporal direction [35]. The mildness of the sign problem at finite μ_q was discussed in [30]. It is a result of the change of integration order which leads to the introduction of mesonic and baryonic color-singlet degrees of freedom after the gauge integrals are fully integrated out. Interestingly the sign problem does not vanish even at zero quark chemical potential $\mu_q = 0$ but a polymer

resummation presented by Karsch and Mütter [35] can resolve this issue. As baryons will become static in the continuous time limit, the loop geometry becomes trivial as they are only oriented in temporal direction without any spatial baryon hoppings. As presented later the sign then becomes $\sigma(\ell) = 1$ as $(\omega(\ell) \in \pm 1)$ and $N_{-}(\ell)$ is even.

1.4.2 High Temperature Limit

At various temperatures around T_c, configurations generated by the partition function Eq. (1.76) exhibit a very diverse structure. Therefore, it is only possible to evaluate these systems analytically for the smallest volumes. An exception is the limiting case of large temperatures where the static limit of purely temporal meson and baryon lines is approached. Thus, in discrete and continuous time, baryons form one-dimensional objects that can be resummed as

$$\exp(\mu_B/T) + \exp(-\mu_B/T) = 2\cosh(\mu_B/T). \tag{1.79}$$

Furthermore, there are $N_c + 1$ possible states for a static mesonic line. Their respective weight is 1 such that the total one-dimensional partition function is given by

$$\mathcal{Z}_{\text{static}} = (\mathcal{Z}_{\text{1d}})^{V_\sigma} = ((N_c + 1) + 2\cosh(\mu_B/T))^{V_\sigma}. \tag{1.80}$$

The spatial volume is either defined as $V_\sigma \equiv V_{\text{DT}}$ or $V_\sigma \equiv V_{\text{CT}}$ depending on the respective type of algorithm in use.

Discussion Within the strong coupling limit regime it is possible to perform simulations of Eq. (1.76) at finite baryon density. Based on discrete time results, the phase diagram and the location of the tri-critical point (TCP) in the chiral limit is well known [36]. There are efforts to include finite β-corrections in order to make sure that features from the strong coupling limit are maintained. However, a connection to the continuum limit is not possible (yet). Within the strong coupling limit the lattices are as coarse as possible with a lattice spacing which cannot be specified. Therefore, there is no chance to set a scale and ratios of physical observables have to be considered in order to compare values. Furthermore, due to the coarse lattice spacing the mentioned mass splitting of taste multiplets (cf. Sec. 1.3.5) is maximal for the strong coupling limit.

1.5 Numerical Approaches and Statistics

For the calculation and evaluation of observables in lattice QCD it is necessary to solve high-dimensional integrals over gauge and quark fields as in Eq. (1.4) which is analogous to

the partition functions solved in statistical mechanics

$$\langle \mathcal{O} \rangle = \frac{1}{\mathcal{Z}} \sum_{\text{states}} \mathcal{O}(x) e^{-\beta H}. \tag{1.81}$$

As mentioned in Sec. 1.1, the Boltzmann weight can be identified with the exponential of the Euclidean action $S^{\mathrm{E}}_{\mathrm{QCD}}$. Thus, it is the goal to numerically sample configurations according to the weight e^{-S}. The number of possible states grows exponentially with an increasing number of degrees of freedom. These are typical numerical integration problems addressed by Monte Carlo methods based on generating successive configurations according to the Boltzmann weight which build up the so-called Markov Chain.

1.5.1 Markov Chain Monte Carlo

Within a Monte Carlo simulation a sequence of configurations is generated

$$[s^{(1)}] \to [s^{(2)}] \to \cdots \to [s^{(N)}], \tag{1.82}$$

which is referred to as Markov Chain. The strategy of acceptance or rejection of certain configurations according to some procedure was formulated by Metropolis in 1953 [37]. A new configuration $[s^{(i+1)}]$ is obtained by suggesting modifications on the current configuration $[s^{(i)}]$ leading to a different weight. With a certain transition probability this new configuration is accepted. If this acceptance test fails, the configuration is rejected such that $s^{k+1} = s^k$ is also a valid update. This choice is related to the main concept of the Markov process which is to visit configurations of a larger Boltzmann weight more often than others. The transition probability

$$P(s^{(i+1)} = U' | s^{(i)} = U) = T(U'|U) \tag{1.83}$$

only depends on the current configuration U and its successor but not on the location within the Markov Chain. In general it is necessary for a probability to fulfill

$$0 \leq T(U'|U) \leq 1, \quad \sum_{U'} T(U'|U) = 1. \tag{1.84}$$

In order for a Markov process to sample configurations according to the Boltzmann weight it is required for the algorithm to be ergodic. This means that the Markov Chain is able to reach any configuration in a finite number of steps. In other words, there exists an n such that $T^n(U'|U)$ is positive. Ergodicity is ensured by enforcing the detailed balance condition

$$T(U'|U)P(U) = T(U|U')P(U') \tag{1.85}$$

which contains only successive configurations as in the Markov Chain. The equilibrium distribution is approximated by using importance sampling that satisfies detailed balance. Starting from an initial configuration $s^{(1)}$, a thermalization process equilibrates the system. Depending on the complexity of the problem this might require already a large number M of Monte Carlo iterations. Statistical quantities are then measured on a chain of equilibrated configurations. The chance for a certain configuration $[s^{(i)}]$ to occur is defined by the probability measure given by the Boltzmann weight in Eq. (1.81). An approximation for the statistical mechanic average $\langle A \rangle$ is obtained from averaging $A[s]$ over a large number of configurations N which yields

$$\langle \mathcal{O} \rangle = \lim_{N \to \infty} \frac{1}{N - M} \sum_{i=M+1}^{N} \mathcal{O}[s^{(i)}]. \tag{1.86}$$

In the limit $N \to \infty$ the calculation becomes exact. In lattice QCD gauge field configurations are constructed according to the respective probability distribution which allows to consider only the most significant contributions from the path integral. This is called importance sampling. Note that while the exponential factor does not occur anymore explicitly in Eq. (1.86), it is implicitly included as the configurations occur with the respective probability. In order to make sure that configurations are distributed according to the Boltzmann weight it is necessary to have an ergodic algorithm that fulfills detailed balance as presented before.

1.5.2 Error Analysis

The use of a Markovian process requires a more detailed error analysis due to correlations in the data set. Although a new configuration $[s^{(i+1)}]$ can be extracted fully from its predecessor $[s^{(i)}]$, it will be strongly related to a certain extent to the subsequent time-series of generated configurations. This is expressed by the autocorrelation of data in terms of a non-vanishing autocorrelation function [22]

$$C_{\mathcal{O}}(t) = \langle \mathcal{O}_i \mathcal{O}_{i+t} \rangle \langle \mathcal{O}_i \rangle - \langle \mathcal{O}_{i+t} \rangle \tag{1.87}$$

for an observable $\mathcal{O}$. The problem that arises is that fluctuations in the data appear smaller than they are since in fact the correlation leads to a reduction of the number of independently sampled events which should be considered in error estimation. In order to account for such a temporal correlation, different methods such as blocking are enforced.

Jackknife Method The Jackknife Method is applied to estimate and reduce the biases of sample statistics [38] and to estimate variances [39]. For this method a data set $X = \{x_i | i = 1, 2, \dots N\}$ of N random variables is divided into N_b disjoint blocks. These are required to be of equal size $n = N/N_b$ which can result into dropping a few data points. The average value

is calculated based on a sample from $N_b - 1$ blocks which is achieved by banishing each of the $j = 1, 2, \ldots N_b$ subsets X^j exactly once. This results in N_b average values J_k which are used to calculate the standard mean value

$$\bar{J} = \frac{1}{N_b} \sum_{k=1}^{N_b} J_k. \tag{1.88}$$

The jackknife bias according to Quenouille [38] is simply given by $(N-1)(\bar{J} - \bar{X})$ where $\bar{X}$ is the mean value calculated on the original data set. A bias-corrected jackknife estimator then follows by constructing the N pseudo-values [40–42]

$$\tilde{J}_k \equiv N_b \bar{J} - (N_b - 1) J_k, \tag{1.89}$$

which are treated as if they are independent random variables. These reduce the bias from the original data set from $\mathcal{O}(N^{-1})$ to $\mathcal{O}(N^{-2})$ [40]. These pseudo-values Eq. (1.89) can be used to construct unbiased mean value and variance estimators for the Jackknife method [39]

$$\bar{f} = \frac{1}{N_b} \sum_{k=1}^{N_b} f_k, \quad \sigma(\bar{f}) = \sqrt{\frac{1}{N_b(N_b-1)} \sum_{k=1}^{N_b} (f_k - \bar{f}_k)^2}, \tag{1.90}$$

with $f_k = f(\tilde{J}_k)$. Compared to the Bootstrap method, the Jackknife is computationally more efficient for small samples. It typically fails to describe statistics that are not smoothly changing such as the median [41]. In general, the Jackknife is considered to be a linear approximation to the Bootstrap method [43].

Bootstrap Method Within a data set of size N there are $2^N - 1$ possible ways to construct non-empty subsets. The jackknife method is restricted to utilize a small fraction of this. The aim of the Bootstrap Method is to improve on the used statistics by incorporating more subsets [44]. Within this method blocks of size n are constructed by drawing random samples from the original data set X with replacement. The total number of blocks N_b that is drawn is not affected by the size of the original ensemble and can be chosen reasonably large to get better statistics depending on the computational resources that are invested. On each of these individual blocks the mean value $\bar{f}_b$ is calculated. These N_b observations shape a distribution, which resembles the distribution of data in the original data set. A bias-corrected bootstrap estimate is obtained when calculating the mean value of all $N_b \cdot n$ resampled data points $\mathfrak{f}$ which results in [41, 44]

$$\tilde{f}_b \equiv \mathfrak{f} - \frac{1}{N_b} \sum_{b=1}^{N_b} (\bar{f}_b - \mathfrak{f}) = 2\mathfrak{f} - \frac{1}{N_b} \sum_{b=1}^{N_b} \bar{f}_b. \tag{1.91}$$

The unbiased mean value and variance of an observables is calculated by

$$\bar{f} = \frac{1}{N_b} \sum_{b=1}^{N_b} \tilde{f}_b, \quad \sigma_f = \sqrt{\frac{1}{N_b} \sum_{b=1}^{N_b} (\tilde{f}_b - \bar{f})^2}. \tag{1.92}$$

In case of measuring the variance of an observable, the jackknife method is often preferred as it requires fewer calculations. On the other hand, bootstrapping yields not just the variance but first estimates the complete distribution which is useful for further analysis. Both methods can be used to determine statistical errors for fitted quantities.

Chapter 2

Continuous Time Limit

Based on the infinite coupling limit the continuous time limit is formulated. First, the anisotropy parameter is discussed which finally leads to the motivation and definition of the CT limit (cf. Sec. 2.1). This particular joint limit is applied to the strong coupling partition function Eq. (1.76) for a step-by-step derivation of $\mathcal{Z}_{\mathrm{CT}}$ (cf. Sec. 2.2). Within this derivation first insights on the benefits of the CT limit are given (see e.g. Sec. 2.2.2) and meson occupation numbers are introduced as new degrees of freedom (cf. Sec. 2.3). This chapter concludes by formulating the CT partition function in terms of a Hamiltonian which will be most helpful for the construction of a suitable algorithm to sample such a partition function (see Sec. 2.4).

2.1 Definition of the Continuous Time Limit

For studying the continuous time limit it is crucial to be able to change the temperature continuously. That's why the bare anisotropy γ was introduced to the staggered action (see Eq. (1.54)). It is also part of the dual formulation where the bare anisotropy is included in the weights of mesonic and baryonic hoppings as implied by the $\rho(x,y), \tilde{\rho}(x,y)$ factors in Eq. (1.68). Hereafter, it is pointed out why the bare anisotropy is essential for the derivation of the CT limit.

The main objective of SC-LQCD is to study thermodynamic properties. Since $\beta = 0$, the only way to change the temperature $T = 1/(N_\tau a(\beta))$ is by means of the temporal lattice extent N_τ, as the lattice spacing cannot be varied in the strong coupling limit. In the staggered formulation the smallest temporal lattice extent is $N_\tau = 2$ such that the highest possible temperature to be addressed is limited to $1/2$. However, the chiral transition region is located at much higher values such that simulations are always placed in the chirally broken phase. In order to solve this limitation, an anisotropy parameter is included in the Dirac operator to favor fermions temporal direction. In contrast to the chemical potential, there is no favoring of forward or backward direction but both are treated equally. The temperature can be expressed in terms of this anisotropy parameter

$$T = \frac{1}{a_\tau N_\tau} = \frac{\xi(\gamma)}{a_\sigma N_\tau} \qquad \text{with} \qquad \xi(\gamma) \equiv \frac{a_\sigma}{a_\tau}(\gamma). \tag{2.1}$$

A study of the functional dependence $\xi(\gamma)$ of the ratio of the spatial and temporal lattice spacings on the bare anisotropy is essential. In general, this dependency is not known. There are different approaches such as a weak coupling analysis ($\beta \to \infty$) suggesting $\xi(\gamma) = \gamma$. However, this does not carry over to strong coupling, where quarks are confined on links to color singlets. Another analysis based on a mean field approximation (with $\beta \ll 1$) of SC-LQCD [45] states that $a_\sigma T \propto \frac{\gamma^2}{N_\tau}$. However, the most persuasive approach depends on a non-perturbative determination of the functional dependence of $\xi(\gamma)$ using anisotropic lattices

$$N_\sigma a_\sigma = N_\tau a_\tau, \quad \xi = \frac{N_\tau}{N_\sigma}. \tag{2.2}$$

Here, a bare anisotropy calibration $\gamma(\xi)$ via conserved currents in spatial and temporal direction is performed [36, 46]. It is found that the function $\xi(\gamma)/\gamma^2$ is monotonic decreasing (see Fig. 2(b) in [36]) and there are various choices of fit-functions to describe the functional behavior such as the one parameter ansatz

$$\frac{\xi(\gamma)}{\gamma^2} \simeq \kappa + \frac{1-\kappa}{1+\kappa(\gamma^4-1)}. \tag{2.3}$$

Note that by construction the isotropic case $\xi(1) \stackrel{!}{=} 1$ is covered. In [46] an improved fit ansatz is discussed that drastically reduces the χ-squared error, and which requires four independent fit parameters. So far, the type of fit-ansatz to extract the anisotropy correction factor κ is a choice with unknown systematic error. Therefore, the κ factor will be measured directly in the CT limit in Sec. 4.3.1 via the above-mentioned method of anisotropy calibration with conserved currents. So far, discrete time studies based on Eq.(2.3) suggest [36]

$$\lim_{N_\tau \to \infty} \xi(\gamma) = \kappa\gamma^2, \quad \kappa = 0.7810(8). \tag{2.4}$$

Typically, observables have a strong N_τ dependence, which can even be non-monotonic. Calculations at large N_τ might be necessary to gain control and perform a meaningful extrapolation. Thus, the top goal is to remove both γ and N_τ from the partition function Eq. (1.76) and replace them by just one input parameter, the temperature aT. Taking Eq. (2.1) in combination with the insight of Eq. (2.3) and Eq. (2.4) results in the definition of the CT limit as the joint limit in γ and N_τ

$$aT_{\mathrm{CT}} = \kappa \lim_{\substack{N_\tau \to \infty \\ \gamma \to \infty}} a\mathcal{T}(\gamma, N_\tau), \quad a\mathcal{T} \equiv \frac{\gamma^2}{N_\tau} = const. \tag{2.5}$$

Note that the subscript for the lattice spacing is dropped, $a \equiv a_\sigma$. The second condition implies

that γ diverges as $\sqrt{\acute{a}\mathcal{T}N_\tau}$. Likewise, the chemical potential can be defined unambiguously as

$$a\mu_{B,\mathrm{CT}} = \kappa \lim_{\substack{N_\tau\to\infty \\ \gamma\to\infty}} \acute{a}\mu(\gamma, N_\tau), \quad \acute{a}\mu \equiv N_c a_\tau \mu_q \gamma^2 = const. \tag{2.6}$$

Lattice simulations in continuous time will take the bare temperature $\acute{a}\mathcal{T}$ and chemical potential $\acute{a}\mu$ as input parameters. However, according to Equations (2.5) and (2.6) the correction factor κ has to be included in order to adjust the parameter set as $(\acute{a}\mathcal{T}, \acute{a}\mu) \to (aT_{\mathrm{CT}}, a\mu_{B,\mathrm{CT}})$. The factor κ will be determined later directly in the CT limit at zero temperature.
Within the next section, the joint limit of Eq. (2.5) is applied to the partition function of SC-LQCD Eq. (1.76) in order to derive the partition function in the CT limit.

2.2 Towards the Continuous Time Partition Function

The CT partition function is studied in the chiral limit $m_q = 0$. Since the mass contribution to the partition function comes merely from the monomer sector, the chiral limit is obtained by removing the monomers ($n_x = 0$) . This converts the monomer term to a trivial weight $\prod_x \frac{N_c!}{n_x!}(2am_q)^{n_x} = (N_c!)^V$. The CT partition function in the chiral limit reads

$$\mathcal{Z}_{\mathrm{DT},m_q=0}(\mu_q) = (N_c!)^V \sum_{\{k,\ell\}}^{\mathrm{GC}} \prod_{\mu=0}^{d} \left\{ \left(\prod_{x\in V_M} \frac{(N_c - k_\mu(x))!}{N_c! k_\mu(x)!} \gamma^{2k_\mu(x)\delta_{0\mu}} \right) \right. \tag{2.7}$$

$$\left. \times \left(\prod_{\ell\subset V_B} \frac{1}{N_c!} \sigma(\ell) \prod_{x\in\ell} \gamma^{N_c\delta_{0\mu}} \exp\left(\omega(\ell) N_c N_t a_t \mu_q\right) \right) \right\}, \tag{2.8}$$

with the sign function $\sigma(\ell)$ defined as before (cf. Eq. (1.78)) and the lattice volume $V \equiv V^{\mathrm{DT}} = N_\sigma^3 \times N_\tau$. Inside the curly brackets, the partition function is split up distinctively in a mesonic (Eq. (2.7)) and a baryonic (Eq. (2.8)) contribution. Within each respective sector, the bare anisotropy only couples to the temporal contribution via $\delta_{0\mu}$. In the following, different steps are performed in order to proceed gradually towards the continuous time limit.

2.2.1 Factorization and Grassmann constraint

Each sector is factorized in a temporal and spatial part such that the impact of the bare anisotropy can be studied better:

$$\mathcal{Z}(\gamma, a_t\mu_q, N_\tau) = \sum_{\{k,\ell\}}^{\mathrm{GC}} \left\{ \left(\prod_{x\in V_M} \left(\prod_{i=1}^{d} \frac{(N_c - k_i(x))!}{N_c! k_i(x)!} \right) \frac{(N_c - k_0(x))!}{k_0(x)!} \gamma^{2k_0(x)} \right) \right. \tag{2.9}$$

$$\left. \times \left(\prod_{\ell\subset V_B} \sigma(\ell) \prod_{(x,\mu)\in\ell} \gamma^{N_c\delta_{0,\mu}} \exp\{r(\ell) N_c N_t a_t \mu_q\} \right) \right\}. \tag{2.10}$$

Note that the prefactor $(N_c!)^V$ is canceled by pulling out its inverse from both mesonic $1/(N_c!)^{V_M}$ and baryonic $1/(N_c!)^{V_B}$ volume. The restriction of the configuration sum enforced by the Grassmann Constraint (GC, cf. Eq. (1.75)) can be explicitly incorporated. For the mesonic volume V_M the GC states that configurations need to fulfill $\sum_\mu k_\mu = N_c$. This means that exactly N_c dimers are required to be attached to a single site. The baryonic sector already satisfies the GC by being build up from self-avoiding baryon loops only.

From the Grassmann Constraint it follows:

$$\sum_{x\in V_M,\mu} k_\mu(x) + \sum_{x\in V_B,\mu} \frac{N_c}{2}|b_\mu(x)| = \frac{N_c\cdot V}{2}. \tag{2.11}$$

The factor $1/2$ emerges as each dimer or baryon line connects two adjacent sites. Thus, it contributes twice which has to be compensated for. Based on Eq. (2.11), further modifications can be worked out by distinguishing between spatial and temporal contributions

$$\begin{aligned} N_cV &= \sum_{x\in V_M,\mu} 2k_\mu(x) + \sum_{x\in V_B,\mu} N_c|b_\mu(x)| \\ &= \underbrace{\left(\sum_{x\in V_M} 2k_0(x) + \sum_{x\in V_B} N_c|b_0(x)|\right)}_{\mathcal{G}_0} + \underbrace{\left(\sum_{x\in V_M,i} 2k_i(x) + \sum_{x\in V_B,i} N_c|b_i(x)|\right)}_{\mathcal{G}_i}. \end{aligned} \tag{2.12}$$

As discussed, the bare anisotropy acts only on the temporal contributions as $\gamma^{\mathcal{G}_0} = \gamma^{N_cV-\mathcal{G}_i}$. Thus, by pulling out the factor γ^{N_cV} from Eq. (2.10) changes the partition function to

$$\begin{aligned} \mathcal{Z}(\gamma, a_t\mu_q, N_\tau) = \gamma^{N_cV} \sum_{\{k,\ell\}} \Bigg\{ &\left(\prod_{x\in V_M} \delta_{\sum_\mu k_\mu(x),N_c} \left(\prod_{i=1}^{d} \frac{(N_c-k_i(x))!}{N_c!k_i(x)!}\gamma^{-2k_i(x)}\right) \frac{(N_c-k_0(x))!}{k_0(x)!}\right) \\ &\times \left(\prod_{\ell\subset V_B} \sigma(\ell) \prod_{(x,\mu)\in\ell} \gamma^{-N_c\delta_{i,\mu}} \exp\{\omega(\ell)N_cN_\tau a_\tau\mu_q\}\right)\Bigg\}. \end{aligned} \tag{2.13}$$

Spatial links are now suppressed by a factor of $1/\gamma^2$ for mesons and $1/\gamma^{N_c}$ for baryons.

2.2.2 Carrying out the CT limit

For the limit in the bare anisotropy $\gamma \to \infty$, all subleading terms are supposed to vanish. Since the average contribution per time location is $1/\gamma^2$, this has far-reaching consequences.

Firstly, there are no spatial dimer contributions with occupation numbers $k_i(x) > 1$. The remaining contributions come from static dimer chains and single spatial dimers. Thus, the

spatial mesonic sector changes to

$$\prod_{i=1}^{d} \frac{(N_c - k_i(x))!}{N_c! k_i(x)!} \gamma^{-2k_i(x)} \quad \Rightarrow \quad \delta_{k_i(x),0} + \delta_{k_i(x),1} \frac{1}{N_c} \gamma^{-2}. \tag{2.14}$$

Secondly, spatial baryonic links for models with $N_c \geq 3$ are suppressed. Studies on discrete time lattices but with a restriction on the maximally allowed number of spatial dimers support this truncation [46]. As baryons are purely temporal (i.e. static) the sign $\sigma(\ell) = (-1)^{\omega(\ell)+N_-(\ell)+1}$ becomes strictly one since $\omega(\ell) = \pm 1$ and $N_- \in \{0, N_\tau\}$. Thus, in the continuous time limit there is no sign problem. Each spatial baryonic site comes with a weight $e^{\omega(\vec{x}) N_c N_\tau a_\tau \mu_q}$ with only two distinctively different states: a static baryon line with winding number $\omega(\vec{x}) = +1$ or a static anti-baryon with $\omega(\vec{x}) = -1$.

Finally, for $N_c = 3$ the partition function simplifies to

$$\tilde{\mathcal{Z}}(\gamma, \mu_B/T, N_\tau) = \sum_{\{k\}|_{V_M}} \left(\prod_{x \in V_M} \delta_{\sum_\mu k_\mu(x), N_c} \left(\delta_{k_i(x),0} + \delta_{k_i(x),1} \frac{\gamma^{-2}}{N_c} \right) \frac{(N_c - k_0(x))!}{k_0(x)!} \right) \tag{2.15}$$

$$\times \sum_{\{\omega\}|_{V_B^\sigma}} \left(\prod_{\vec{x} \in V_B^\sigma} \exp\{\omega(\vec{x}) \mu_B/T\} \right). \tag{2.16}$$

Here, the overall prefactor $\gamma^{N_c V}$ is dropped as it treats all sites equally. The baryonic volume is split up into a spatial and temporal part $V_B = V_B^\sigma \times N_\tau$. The exponential of the baryonic weight is rewritten in terms of the ratio of temperature and baryon chemical potential

$$\mu_B/T = a\mu_\mathcal{B}/a\mathcal{T} = N_c N_\tau a_\tau \mu_q. \tag{2.17}$$

While N_τ drops out of the baryonic contribution of the partition function, it is still implicitly incorporated in the product over the mesonic volume $V_M = V_M^\sigma \times N_\tau$.

Note that it does not require large N_τ to make baryons static at a fixed temperature.

2.2.3 Baryon resummation and mesonic vertices

As baryons are static they can loop around the lattice in temporal direction exactly once. Therefore, the set of winding numbers $\{\omega\}|_{V_B^\sigma}$ contains two possible values: $\omega(\vec{x}) = +1$ or -1. As a result, the static (anti-)baryon contribution can be resummed into one combined object, a polymer with site weight $\omega_\mathcal{P} = 2\cosh(\mu_B/T)$. For the full baryonic volume it follows that this weight comes with a power $|V_B^\sigma|$ corresponding to the number of spatial sites within V_B^σ. The mesonic sector is the most part trivial as static lines or segments carry a weight of 1. This can easily be shown by considering a temporal dimer chain consisting of two sites and

bonds and explicitly writing down the weights

$$\sqrt{N_c!}\sqrt{\frac{(N_c-k_i)!}{N_c!k_i!}}\sqrt{N_c!}\sqrt{\frac{(N_c-(N_c-k_i))!}{N_c!(N_c-k_i)!}}=1 \tag{2.18}$$

Due to the staggered even-odd decomposition of the lattice, sites come in pairs and the weights have to be split by taking the square-root. The weight of a mesonic line is only affected by attached spatial dimers. These contributions will be encoded in vertex weights $v_{(\vec{x},\tau)}$ with each vertex having N_c-1 temporal dimers attached to it as well as one spatial dimer. Latter connects two adjacent spatial sites $(\vec{x},\tau)$, $(\vec{x}+i,\tau)$ via the bond $b=(\vec{x},\tau;i)$ such that vertices always come in pairs. In fact, the total number of vertices in a configuration has to be a multiple of four in order to restore the Grassmann Constraint at the boundary.

There are different types of vertices which can be classified according to the number of attached temporal dimers in backward direction $k_0^-\equiv k_0(\vec{x},\tau-1)$ and in forward direction $k_0^+\equiv k_0(\vec{x},\tau)$. Based on this notation the Grassmann constraint simplifies to $k_0^-+k_0^++1=N_c$. Generally, the associated vertex weights are calculated as usual by considering the site weight $N_c!$ as well as three bond contributions belonging to k_0^-, k_0^+ and the single spatial dimer. Thus, the weight follows as

$$v(k_0^-|k_0^+)=N_c!\sqrt{\frac{(N_c-k_0^-)!}{k_0^-!}\frac{(N_c-1)!}{N_c!1!}\frac{(N_c-k_0^+)!}{k_0^+!}}=\sqrt{\frac{(N_c-k_0^-)(k_0^-+1)}{N_c}}. \tag{2.19}$$

As there are N_c-1 temporal dimers distributed among k_0^- and k_0^+, there are N_c different types of vertices. These take values in the range $\{0,1,\dots,N_c-1\}$.

The partition function expressed in terms of static baryons as well as pairs of meson vertices reads

$$\tilde{\mathcal{Z}}(\gamma,\mu_B/T,N_\tau)= \tag{2.20}$$
$$\sum_{\{V_B^\sigma,V_M^\sigma\}}\sum_{\substack{k_0\in\{0,\dots,N_c\}\\ k_i\in\{0,1\}}}^{\mathrm{GC}}\Big\}\Big|_{V_M}\left\{\left(\prod_{\{x|k_i(x)=1\}}\frac{v(k_0^-|k_0^+)_{(\vec{x},\tau)}v(k_0^-|k_0^+)_{(\vec{x}+i,\tau)}}{\gamma^2}\right)(2\cosh(\mu_B/T))^{|V_B^\sigma|}\right\},$$

The N_τ dependence remains as configurations are still implicitly given by discrete dimer-chains. The weights of these configurations are dictated by the shape of the vertices and calculated via Eq. (2.19). Note that in Eq. (2.20) the lattice volume is separated into two distinctive volumes, a mesonic subvolume V_M^σ and a baryonic V_B^σ.

2.2.4 Vertices for $N_c=3$

For $N_c=3$, two general classes are distinguished, **L**-shaped and **T**-shaped vertices. The

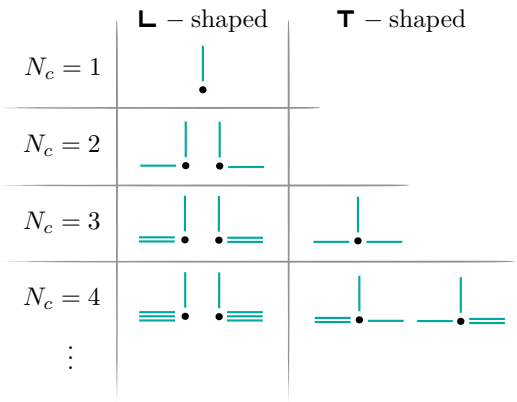

Figure 2.1: *Two different classes of vertices emerge as the number of colors is increased. For $N_c \geq 2$ there are $N_{\mathsf{L}} = 2$ L-shaped vertices and $N_{\mathsf{T}} = N_c - 2$ T-shaped vertices with weights given by Eq. (2.19). For $N_c = 3$ the specific weights are stated in Eq. (2.21).*

specific weights read

$$v_{\mathsf{L}} = v(0|2) = v(2|0) = 1, \qquad v_{\mathsf{T}} = v(1|1) = \frac{2}{\sqrt{3}}. \tag{2.21}$$

There are four key observations:

- For arbitrary N_c, non-trivial weights only occur in the T-shaped class.
- The calculation of vertex weights is independent of their location $(\vec{x}, \tau)$ within the mesonic volume and only the respective number of different vertex types affects the contribution to the mesonic part of the partition function.
- The complete temporal dimer chain can be reconstructed from knowing the dimer occupation number in the first time-slice $k_0(\vec{x}, 0)$ as well as the position of the attached vertices.
- In addition to the requirement of an even number of vertices per spatial site, it is also necessary for vertices to occupy the same number of sites with even and odd parity. Therefore, the number of absorption (even parity) and emission sites (odd parity) is the same $\#\mathcal{E} = \#\mathcal{A}$.

As a result, the mesonic sector of $\mathcal{Z}$ is decomposed in L and T vertex weights coming with respective multiplicities fulfilling

$$\frac{1}{2}\left(\sum_{\vec{x}\in V_M^\sigma}\int_0^{1/d\mathcal{T}} d\tau n_{\mathsf{L}}(\vec{x},\tau) + n_{\mathsf{T}}(\vec{x},\tau)\right) \equiv n_{D_\sigma}, \tag{2.22}$$

with n being the number of attached spatial dimers. The partition function changes to

$$\tilde{\mathcal{Z}}(\gamma, \mu_B/T, N_\tau) = \tag{2.23}$$
$$\sum_{\{V_B^\sigma, V_M^\sigma\}} \sum_{n=0}^{V_M} \sum_{\left\{\substack{k_0(\vec{x},0),\\ n_{\mathsf{L}}, n_{\mathsf{T}}}\right\}|_{V_M}}^{\mathrm{GC}} \left\{ \left(\prod_{\substack{j=1 \\ (\langle \vec{x},\vec{y}\rangle_j, \tau_j)}}^{n} \left(\frac{v_{\mathsf{L}}}{\gamma}\right)^{n_{\mathsf{L}}(\vec{x},\tau)} \left(\frac{v_{\mathsf{T}}}{\gamma}\right)^{n_{\mathsf{T}}(\vec{y},\tau)} \right) (2\cosh(\mu_B/T))^{|V_B^\sigma|} \right\},$$

with the number of spatial dimers being bound by the mesonic volume due to the discretization in temporal direction. The product is over all nearest neighbor pairs $\langle \vec{x}, \vec{y} \rangle$ connected by a spatial dimer.

2.3 Continous Time Partition Function

According to the definition of the continuous time limit Eq. (2.5) it is necessary to replace the γ and N_τ dependence of the partition function Eq. (2.23) by the temperature. This is done by studying the admissible sequence of vertices on an arbitrary mesonic site. As a shorthand notation, vertices are written in terms of meson occupation numbers $v(k|l)$ which are used at this stage merely to label all possible $N_c + 1$ alternating dimer chains. The sequence of successive vertices can then be denoted as $v(k|l|m) \equiv v(k|l)v(l|m)$. The following part focuses on $N_c = 3$ but can be straightforward generalized to arbitrary N_c.

Without considering discrete dimer chains anymore, an interval between two successive vertices can still be classified as even or odd. A sequence of either emission sites $\mathcal{E} - \mathcal{E}$ or absorption sites $\mathcal{A} - \mathcal{A}$ is determined to be even. The meson occupation number is either successively increased or decreased by such a vertex combination

$$\begin{aligned} &v(0|1|2), \qquad v(1|2|3) \\ &v(3|2|1), \qquad v(2|1|0). \end{aligned} \tag{2.24}$$

This corresponds to a combination of L-vertex followed by a T-vertex or vice-versa (for $N_c = 3$). Since the initial and final meson occupation number do not match, such vertex combinations are necessarily followed by further vertices in order to fulfill the GC. As mentioned before, the number of dimers attached to absorption and emission sites has to agree. This is realized by mixed sequences $\mathcal{A} - \mathcal{E}$ and $\mathcal{E} - \mathcal{A}$ corresponding to odd intervals where the occupation numbers are increased (decreased) by one unit and successively decreased (increased)

$$\begin{aligned} &v(0|1|0), \qquad v(1|2|1), \qquad v(2|3|2) \\ &v(3|2|3), \qquad v(2|1|2), \qquad v(1|0|1). \end{aligned} \tag{2.25}$$

In this case, also the vertex type stays unchanged corresponding to two subsequent $\mathbf{L}$-vertices or two subsequent $\mathbf{T}$-vertices.

Considering a set of n oriented spatial dimers to be distributed along the temporal extent of site $\vec{x}$. Multiple spatial dimers are suppressed such that each spatial bond $b(\vec{x},t;i) \in \{0,1\}$ is occupied by maximally one dimer. Due to the Grassmann Constraint the number of oriented dimers attached to an absorption site $\mathcal{A}$ equals the number attached to an emission site $\mathcal{E}$. Thus, the first spatial dimer from one of the subsets has $N_\tau/2$ possible locations. For the second dimer from the same subset there are $N_\tau/2-1$ locations left and the k^{th} dimer has $N_\tau/2-k+1$ options left. For large N_τ this results in

$$\prod_{k=1}^{n/2}\left(N_\tau/2-(k-1)\right) \underset{\substack{| \\ N_\tau \text{ large}}}{\approx} \prod_{k=1}^{n/2}\left(\frac{N_\tau}{2}\right) = \left(\frac{N_\tau}{2}\right)^{n/2}. \tag{2.26}$$

For spatial dimers of arbitrary orientation this leads to a factor $(N_\tau/2)^n$. This means that a single spatial dimer suppressed by γ^{-2} has on average $N_\tau/2$ position to choose from when being attached to a site $\vec{x}$. This factor can be expressed in terms of the temperature

$$\left(\frac{N_\tau}{2\gamma^2}\right)^n = \left(\frac{1}{2a\mathcal{T}}\right)^n, \quad \text{with} \quad N_\tau/\gamma^2 = 1/a\mathcal{T}. \tag{2.27}$$

Note that within this limit the probability of having multiple spatial dimers at the exact same location is zero as the maximal number of spatial dimers is given by the order $\mathcal{O}(\gamma^{-n})$.

Furthermore, time ordering is a global aspect: From all possible $n!$ permutations of n vertices only one is time-ordered. Thus, a respective factor $1/n!$ has to be included and the continuous time partition function follows as

$$\mathcal{Z}_{\text{CT}}(a\mathcal{T},a\mu) = \sum_{\{V_B^\sigma,V_M^\sigma\}}\sum_{\{\omega\}|_{V_B^\sigma}} e^{\omega(\vec{x})\mu_B/T}\sum_{n\in 2\mathbb{N}}\frac{1}{n!}\frac{1}{(2a\mathcal{T})^n}\sum_{\mathcal{G}\in\Gamma_n^{V_M^\sigma}} v_{\mathbf{T}}^{N_{\mathbf{T}}(\mathcal{G})}, \tag{2.28}$$

with $\Gamma_n = \{n_{\mathbf{L}}(\vec{x},\tau), n_{\mathbf{T}}(\vec{x},\tau)\}$ being the set of all valid configurations with a total of n spatial dimers. Since the time direction is compact, it is in theory possible to distribute infinitely many spatial dimers on the lattice such that the sum $\sum_{n\in 2\mathbb{N}}$ is not restricted anymore by the mesonic volume. Moreover, as $v_{\mathbf{L}} = 1$, such contributions can be neglected and only the total number of $\mathbf{T}$-shaped vertices contributes as

$$N_{\mathbf{T}} = \sum_{\vec{x}\in V_M^\sigma}\int_0^{1/a\mathcal{T}} d\tau\, n_{\mathbf{T}}(\vec{x},\tau), \tag{2.29}$$

with an integration over the compact temporal direction.

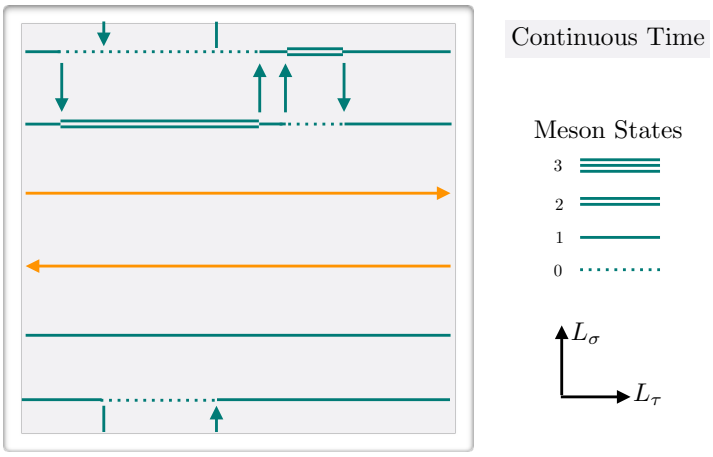

Figure 2.2: *Example for a CT configuration on a two-dimensional lattice. Baryons are static and purely loop in temporal direction. Spatial dimers are located at uniformly distributed temporal position.*

Discussion The expansion in n is an all order high temperature expansion. It will also hold at very low temperatures and it is possible to address zero-temperature phenomena.

When studying the partition function Eq. (2.28), it gives immediately an impression on how configurations in CT look like (see Fig. 2.2). There is a baryonic volume V_B^σ saturated with static (anti)-baryons and a mesonic volume V_M^σ with scattered vertices v_{L} and v_{T}. The number of spatial dimers is a function of the temperature due to the factor $1/(2a\mathcal{T})^n$. At large temperatures the partition function is dominated by configurations that are almost spatial dimer free since the density $\langle n_{D_\sigma} \rangle$ becomes small. On the other hand, in the low temperature regime configurations with large numbers of spatial dimers still contribute. As discussed in Sec. 4.2, the spatial dimer density can be taken as an order parameter for chiral symmetry breaking.

Note that even though spatial dimers are suppressed by $1/\gamma^2$, their number stays finite since the summation is over $\mathcal{O}(\gamma^2)$ sites is compensating for the suppression.

2.4 Hamiltonian Formulation

For analytic studies of the continuous time limit the partition function in Eq. (2.28) is well suited, especially at temperatures above T_c where the series can be truncated at low orders. A main challenge is the determination of the T-vertex multiplicities.

Nevertheless, a formulation in terms of a Hamiltonian composed of operators is also of interest for analytic and numeric studies. Thus, in order to prepare for Quantum Monte Carlo on quantum states, it will be more suitable to reformulate Eq. (2.23) in terms of meson

occupation numbers $\mathfrak{m}$. Instead of referring to a discrete dimer chain by its dimer occupation at $k(\vec{x},0) \equiv k_0(\vec{x})$, this can be replaced by the following assignment

$$k_0(x) \mapsto \mathfrak{m}(x) = \epsilon(x)\left(k_0(x) - \frac{N_c}{2}\right) + \frac{N_c}{2} \tag{2.30}$$

$$\mathfrak{m}(x) \in \{0, 1, \dots N_c\}\,, \tag{2.31}$$

with the parity of a site $\epsilon(x) = \pm 1$ introduced in Eq. (1.56). Note that neighboring sites which feature the exact same dimer chain will have meson states that add up to $m(x)+m(y) = N_c$. A meson occupation number $\mathfrak{m}(x)$ is constant on the interval between attached spatial dimers. As used before, vertices in the dimer number are replaced by the vertices which are characterized by meson occupation numbers

$$v(k_0^-|k_0^+) \mapsto v(\mathfrak{m}^-, \mathfrak{m}^+) \tag{2.32}$$

with k_0^- the number of dimers in temporal backward direction and k_0^+ in forward direction. These new vertices change the meson state by one unit: $\mathfrak{m}^-(x) \mapsto \mathfrak{m}^+(x) = \mathfrak{m}^-(x) \pm 1$ such that the partition function reads

$$\tilde{\mathcal{Z}}(\gamma, \mu_B/T, N_\tau) = \tag{2.33}$$
$$\sum_{\{V_M^\sigma, V_B^\sigma\}} \sum_{n=0}^{V_M} \sum_{\{\mathfrak{m}, b(\vec{x},t;i)\}|_{V_M}} \left\{ \left(\prod_{\substack{j=1 \\ (\vec{x},\tau)\in b_j}}^{n} \frac{v(\mathfrak{m}^-|\mathfrak{m}^+)_{(\vec{x},\tau)}}{\gamma} \frac{v(\mathfrak{m}^-|\mathfrak{m}^+)_{(\vec{x}+i,\tau)}}{\gamma} \right) (2\cosh(\mu_B/T))^{|V_B^\sigma|} \right\},$$

with $b(\vec{x},\tau;i)$ the set of bonds occupied by one spatial dimer at location $(\vec{x},\tau)$ and in direction i. Two vertices connected by a spatial dimer are defined on sites $\vec{x}$ and $\vec{x}+i$ of opposite parity. From the meson state definition (2.30) it follows, that if the quantum number $\mathfrak{m}^-(x)$ is raised (lowered) by a spatial dimer, the associated state $\mathfrak{m}^-(x+i)$ is lowered (raised). Thus, the meson occupation number is a conserved quantum number. The vertices are replaced by meson state lowering/raising operators $\hat{J}^\pm$ and the partition function is further rewritten as

$$\mathcal{Z}_{\mathrm{CT}}(a\mathcal{T}, a\mu) =$$
$$\sum_{\{V_M^\sigma, V_B^\sigma\}} \left\{ \mathrm{Tr}_{\mathfrak{m}|_{V_M^\sigma}} \left[\exp\left(\frac{1}{2a\mathcal{T}} \sum_{\langle \vec{x},\vec{y}\rangle} \left(\hat{J}_{\vec{x}}^+ \hat{J}_{\vec{y}}^- + \hat{J}_{\vec{x}}^- \hat{J}_{\vec{y}}^+ \right) \right) \right] \mathrm{Tr}_{\omega|_{V_B^\sigma}} \left[e^{\hat{\omega}\mu_B/T} \right] \right\}. \tag{2.34}$$

The configuration sum is over all possible volume partitions into a mesonic M and a baryonic B part. There is a trace contribution for the meson states $\mathrm{Tr}_{\mathfrak{m}}$ which are constraint on the spatial mesonic volume and a trace over the winding number that's limited to the baryonic subvolume. The same large N_τ discussion as in Sec. 2.3 makes it possible to write spatial dimer

contributions as an exponential $\exp(x) = \sum_n (x)^n/n!$. The product over bonds occupied by a spatial dimer becomes a summation over nearest neighbors within the exponential. Finally, both sectors can be written as traces of exponentials, where baryons and anti-baryons are considered independently via the baryon winding number operator $\hat{\omega}$. In terms of a joint trace over hadronic quantum states $\mathfrak{h}$ the partition function reads

$$\mathcal{Z}_{\mathrm{CT}}(a\mathcal{T}, a\mu) = \mathrm{Tr}_{\mathfrak{h}}\left[e^{(\hat{\mathcal{H}}+\hat{\Omega}_B a\mu)/a\mathcal{T}}\right], \quad \hat{\mathcal{H}} = \frac{1}{2}\sum_{\langle\vec{x},\vec{y}\rangle}\left(\hat{J}^+_{\vec{x}}\hat{J}^-_{\vec{y}} + \hat{J}^-_{\vec{x}}\hat{J}^+_{\vec{y}}\right), \quad \hat{\Omega}_B = \sum_{\vec{x}}\hat{\omega}_x, \tag{2.35}$$

with the Hamilton operator $\hat{\mathcal{H}}$ and the baryon number operator $\hat{\Omega}_B$ corresponding to meson and baryon exchange respectively. The meson state lowering and raising operators $\hat{J}^{\pm}$ contain the vertices within a $(N_c+1)\times(N_c+1)$ block as well as the diagonal baryon winding number $(2)\times(2)$ block

$$\hat{J}^+ = \left(\begin{array}{cccc|cc} 0 & 0 & 0 & 0 & & \\ v_{\llcorner} & 0 & 0 & 0 & & \\ 0 & v_{\urcorner} & 0 & 0 & & \\ 0 & 0 & v_{\llcorner} & 0 & & \\ \hline & & & & 0 & 0 \\ & & & & 0 & 0 \end{array}\right), \quad \hat{J}^- = (\hat{J}^+)^T, \quad \hat{\omega} = \left(\begin{array}{cccc|cc} 0 & 0 & 0 & 0 & & \\ 0 & 0 & 0 & 0 & & \\ 0 & 0 & 0 & 0 & & \\ 0 & 0 & 0 & 0 & & \\ \hline & & & & 1 & 0 \\ & & & & 0 & -1 \end{array}\right). \tag{2.36}$$

The block diagonal form, here explicitly stated for $N_c = 3$, is due to the Hilbert space being decomposed into invariant subspaces – mesonic states and baryonic states cannot coexist on the same site. Thus, a hadronic quantum state $|\mathfrak{h}\rangle$ can be written as a direct product of a mesonic part $|\mathfrak{m}\rangle$ and a baryonic part $|\mathfrak{b}\rangle$ such that

$$|\mathfrak{h}\rangle = |\mathfrak{m}\rangle \oplus |\mathfrak{b}\rangle = (0, \pi, 2\pi, 3\pi|B^+, B^-)^T, \quad [\hat{H}, \hat{\Omega}_B] = 0, \tag{2.37}$$

with $B^{\pm}$ the (anti-)baryon. The invariance of the two is stressed by the commutation relation of the Hamiltonian and the Baryon number operator. The meson quantum state counts the number of pions which are flavorless for $N_f = 1$.

In the chiral limit the pion current is conserved as vertices come in pairs of opposite parity. Due to this conservation law, spatial dimers cannot be distributed on a lattice that is fully saturated since every site is occupied by N_c pions. Likewise, a configuration with no pions at all cannot develop meson transfers.

There are some more interesting features concerning the creation and annihilation operators. If the additive constant $N_c/2$ is omitted from Eq. (2.30) a particle-hole symmetry emerges. For the $N_c + 1$ mesonic states, half of them behave like particles propagating in forward direction while the other half consists of the opposite directed current. The corresponding algebra has structure of a spin, but it has nothing to do with the spin of the particles. Note,

that the alternating dimer chains just encode the fact that the lattice spacing for staggered fermions is $2a_\tau$ rather than just a_τ.
The Hamiltonian formulation is the starting point for constructing a worm-type algorithm as presented in chapter 3. Interesting symmetries concerning the creating and annihilating operators are accessible from Eq. (2.35). The meson/baryon state occupations numbers occur as quantum numbers of the operators. Within the next chapter it will become evident how a worm-type algorithm changes a configuration gradually by adjusting these occupation numbers.

Chapter 3

Continuous Time Worm Algorithm

Nowadays, continuous time algorithms are widely used in Quantum Monte Carlo (see e.g. [47, 48]), but to my knowledge have not yet been applied to quantum field theories. In this respect global algorithms such as cluster-type algorithms or worm algorithms are of interest as they eliminate the critical slowing down problem in case of performing simulations close to non-analyticities [49]. A worm algorithm works in an extended configuration space with additional configurations that feature two defects, a worm Head and a worm Tail. This algorithm consists of local update schemes which operate at these ends of the worm. For its applicability, the partition function needs to be formulated in terms of bond variables. This is available in a dual representation of lattice QCD based on the strong coupling expansion. Based on the derivation from the previous chapter 2, the CT partition function $\mathcal{Z}_{\mathrm{CT}}$ formulated in terms of a Hamiltonian is used to be sampled by a CT worm algorithm. As discussed, this algorithm will use meson state occupation numbers in order to direct the worm through the lattice.

Within this chapter, the two concepts of an algorithm working in continuous Euclidean time and a worm algorithm are highlighted (see Sec. (3.1)). A combination of the two ideas leads to the CT worm algorithm, which is introduced and applied throughout this dissertation (Sec. (3.3)). It samples the CT partition function Eq. (2.35) for SC-LQCD. A focus is on pointing out the interplay of absorption and emission update procedures guiding the worm through the lattice (Sec. 3.2.1). Finally, the benefits of an algorithm that samples directly in the CT limit is stressed (Sec. 3.4).

3.1 Two essential concepts

The simulation of quantum systems in continuous Euclidean time was first discussed by *Beard* and *Wiese* [47]. They study the 2D Heisenberg model which is obtained by means of the Trotter-Suzuki expansion of a 1D quantum mechanical system which is transformed into a 2D system of classical Ising-like variables. There are three different types of decision processes to be encountered in time that guide through an updating path. These are referred to as “forced continuation”, “forced transition” and “optional decay” [47]. An updating path is characterized by transition times and the states that are interconnected by transitions.

Therefore, for a continuous time algorithm it suffices to store the transition times for each spatial site in addition to the initial state in time-slice $\tau = 0$. In contrast a discrete time algorithm requires to store the state information at each space-time point [47]. While path updates are performed incrementally step-by-step in discrete time, greater leaps are possible in the continuous time version where the transitions are known to be distributed exponentially. The associated Poisson process is described in the next section.
A cluster-type algorithm that satisfies locality was first discussed by Prokofev et al. [49, 50]. The idea of the so-called worm algorithm is to sample closed path configurations which are based on high-temperature expansions such as derived for CT in Eq. (2.28). An update procedure features a disconnected path with two special sites, worm Head and Tail at either end. While the worm Tail remains stationary, the worm Head propagates until reunion denoted as "shift Update" (cf. Alg. 2). With a certain probability p_{shift} the shifting will continue, but with probability $p_{\text{move}} = 1 - p_{\text{shift}}$ worm Head and Tail recombine and a "move Update" suggests a new location (cf. Alg. 1). Note that for a discrete time setup, during the "shift Update" an increase (decrease) in bond occupation number is always balanced by a respective decrease (increase). Likewise, the meson state will be conserved by a continuous time algorithm. During the worm evolution, two-point correlation functions are sampled (cf. Sec. 3.3.2) which give immediately rise to histograms for the temporal correlator analysis and the chiral susceptibility (cf. Sec. 4.2).

3.2 Poisson Process

The weight of a configuration does not depend on the lengths of the segments separating two spatial dimers, but only on the relative ordering. Therefore, spatial dimers should be uniformly distributed with the inter-arrival times $t_{i+1} - t_i$ being exponentially distributed [47]. The probability to locate exactly N spatial dimer emission events within a time interval of Δt is given in terms of a Poisson distribution [51]

$$P(N|\Delta t) = \frac{1}{N!}(\lambda \Delta t)^N e^{-\lambda \Delta t}, \quad \Delta t \in [0, 1]. \tag{3.1}$$

The decay constant λ represents the average number of spatial dimers being emitted per unit time. The compact time interval is rescaled $[0, 1/a\mathcal{T}] \mapsto [0, 1]$ such that the decay constant is temperature dependent. Due to the presence of baryons, the number of possible neighbors to emit to is constraint and λ also becomes space dependent

$$\lambda(T, \vec{x}) = d_M(\vec{x})/(4a\mathcal{T}), \quad d_M(\vec{x}) = 2d - \sum_{\langle \vec{x}, \vec{y} \rangle} |B(\vec{y})|. \tag{3.2}$$

The number of available nearest neighbor mesonic sites is denoted as $d_M(\vec{x})$. Note that in case a site $\vec{x}$ on which the Poisson process operates is fully surrounded by baryons, the decay

constant becomes $\lambda = 0$. In this case, the distance covered by the Poisson process is maximal

$$P(N = 0|\Delta t) = \exp(-\lambda \Delta t)\Big|_{\lambda=0} = 1, \tag{3.3}$$

and a pure temporal propagation is chosen.
The distribution of spatial dimers can be measured in CT Monte Carlo worm simulations on various intervals Δt. A fit of the resulting distributions according to Eq. (3.1) validates the Poissonian shape. By excluding baryons and fixing parameters to their usual values ($N_c = 3$, $d = 4$), the decay probability λ takes the value

$$\lambda_{\text{site}} = \frac{2d}{4\mathcal{dT}} N_c = \frac{18}{4\mathcal{dT}}, \tag{3.4}$$

in case the distribution of spatial dimers over the lattice sites is considered. Based on the results in Fig. 3.1, it becomes evident that the extracted distributions are clearly Poissonian with good agreement. The few percentage mismatch in the decay constant is probably due to the periodic boundary conditions. Usually, a Poisson process is defined on an infinite line and not a circle. Additionally, a mismatch in the fit becomes more distinct at larger temperatures where the distribution is expected to become more peaked shaped and settles towards smaller numbers of vertices per site. Here, static baryons influence the result, as they become more and more common in temperature ranges below, but in close proximity to T_c.

3.2.1 Emission and Absorption Sites

According to the Poisson process, an interval Δt is covered before a pion is transferred from an initial site $\vec{x}$ to a neighbor $\vec{y}$. The site $\vec{x}$ is denoted as emission site $\mathcal{E}$ which reduces the meson occupation number by one unit

$$\text{Emission event:} \quad (\vec{x}, t) \in \mathcal{E}, \quad \mathfrak{m} \mapsto \mathfrak{m} - 1 \tag{3.5}$$

$$\text{Absorption event:} \quad (\vec{y}, t) \in \mathcal{A}, \quad \mathfrak{m} \mapsto \mathfrak{m} + 1. \tag{3.6}$$

In terms of the Hamiltonian representation, the meson state lowering operator $\hat{J}^-$ represents an emission event. Due to the meson number conservation, the emitted meson occupation number unit is transferred via the spatial dimer (pion hopping) and is absorbed at site $(\vec{y}, t) \in \mathcal{A}$, thus called absorption site (cf. Eq. (3.6)). Here, $\hat{J}^+$ raises the respective mesonic quantum state by one unit $\mathfrak{m} \mapsto \mathfrak{m} + 1$. In order to obey the Grassmann Constraint it is necessary to have as many emission sites as absorption sites belonging to the same $\vec{x}$

$$|\{t_i \,|\, (\vec{x}, t_i) \in \mathcal{E}\}| = |\{t_i \,|\, (\vec{x}, t_i) \in \mathcal{A}\}|. \tag{3.7}$$

This resembles the underlying even/odd decomposition structure of staggered lattice sites.

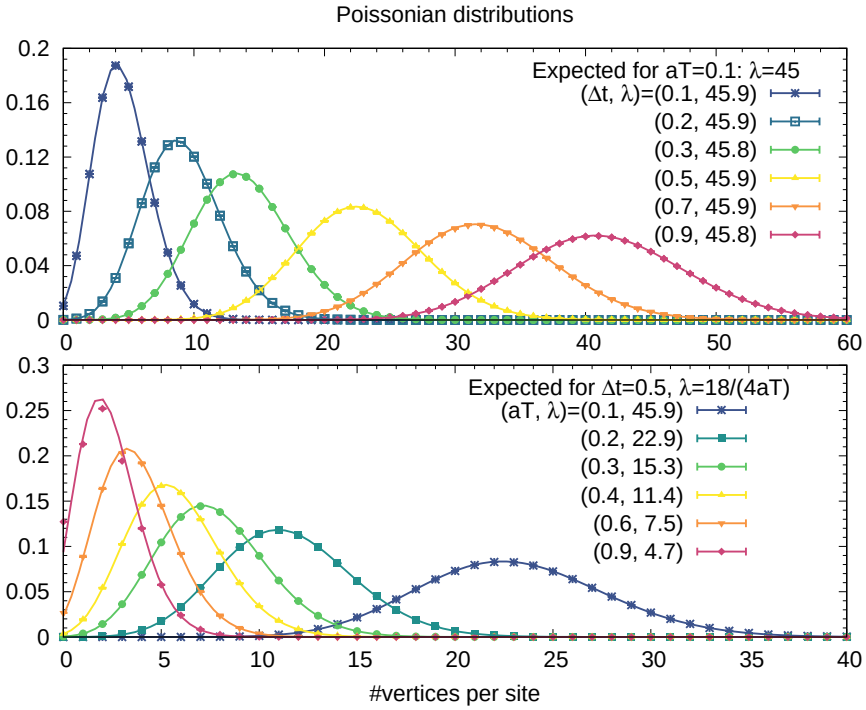

Figure 3.1: ***Top**: Distribution of the number of spatial dimers at fixed temperature in varying interval length Δt. Data are fitted by a Poisson distribution and results compared to the expected value of the decay constant λ. **Bottom:** Distribution of the number of spatial dimers at various temperatures but fixed interval length $\Delta t = 0.5$. Results are Poissonian distributed as validated by the fit.*

Apart from the emission of spatial dimers, a corresponding absorption process is necessary in order to fulfill detailed balance and to obtain an equilibrium distribution of spatial dimers for a certain temperature and chemical potential. This means that the meson state is a conserved quantity throughout the propagation of the worm.

3.3 Algorithm Details

The basic idea for a worm algorithm operating in the strong coupling limit was developed by *Adams* and *Chandrasekharan* [52]. They discussed a discrete time algorithm with staggered fermions in the chiral limit and a $U(N_c)$ gauge group. They excluded dynamic baryons since these could form non-trivial geometries that trap a directed path mesonic worm (see Fig. D.1). For a directed path algorithm, the incoming and outgoing propagation direction of the worm Head have to be different. Such an algorithm is more efficient in updating configurations in contrast to an algorithm which allows for backtracking (incoming and outgoing direction are allowed to match).

Algorithm 1 Select new location to place worm Head and Tail, avoid baryons

```
1: function moveUpdate
2:     do
3:         Hx=irand(V);                          ▷ Choose random spatial site
4:         Ht=drand();                ▷ Choose random temporal location ∈ [0 : 1]
5:     while on baryonic site
6:     return Hx, Ht
```

Algorithm 2 Shift worm Head through lattice until recombination

```
1: function shiftUpdate
2:     Call moveUpdate                ▷ Determine initial Head and Tail location
3:     while Worm not closed do
4:         Call absorptionUpdate                          ▷ Determine direction
5:         if dir=spatial then
6:             if At Worm Tail then
7:                 Close Worm
8:                 break
9:             Move to neighboring site Hx=Hy
10:            dir=Choose temporal direction
11:        Call emissionUpdate                                ▷ Determine Δt
12:        for (t = 0; t < Δt; t++ ) do
13:            Increment Histogram
14:            if Found Absorption site then
15:                Hx=Ha
16:                break
17:        if not at Absorption site then
18:            Add spatial dimer
```

For $SU(N_c)$ gauge theory studies of the continuous time limit, two separate worms are required [30], one sampling the mesonic sector and a second one sampling the baryonic sector. The algorithm is based on a decomposition of the lattice in absorption $\mathcal{A}$ and emission sites $\mathcal{E}$. A new update starts with a moveUpdate where the worm enters the lattice through an absorption site. The worm Tail is fixed at this position until recombination and raises the meson state by one unit $\mathfrak{m} \to \mathfrak{m} + 1$, similar to a monomer source. In order to consider the Grassmann Constraint to be fulfilled at all times the worm Head can be interpreted as a (1) monomer source on emission sites which acts as an absorption site raising the meson state, or (2) a monomer sink at absorption sites which lowers the meson state by one unit.

In general, the worm movement is an alternating succession of Absorption and Emission Update procedures. While an Absorption Update deals with decision processes at absorption sites, the Emission Update covers the handling with emission sites (cf. Alg. (2)).

Algorithm 3 Choose direction to continue worm propagation

```
1: function absorptionUpdate
2:     if Incoming from spatial direction then
3:         dir=Choose temporal direction
4:     if Incoming from temporal direction then
5:         dir=Choose spatial direction or proceed temporal
6:     return dir
```

Algorithm 4 Determine distance to cover in temporal direction

```
1: function emissionUpdate
2:     Calc #AccessibleNeighbors
3:     Calc Δt from exponential distribution
4:     return Δt
```

Absorption Update Whenever located at an absorption site, an Absorption Update is performed which either deletes an absorption site or chooses a temporal direction (see Fig. 3.2). This depends on whether the incoming direction is *spatial*, *temporal* or *the site itself*:

- Coming from a spatial direction μ after spatial dimer emission requires the worm to select a new temporal direction. Due to the new absorption site vertex which raises the meson occupation number by one unit, it is not possible to choose both temporal directions with equal probability due to the Grassmann Constraint. The probabilities are based on the respective occupation numbers

$$P_{(s|\text{-}0)} = \frac{\mathfrak{m}_{\text{-}0}}{N_c - 1}, \quad P_{(s|+0)} = \frac{\mathfrak{m}_{+0}}{N_c - 1}. \tag{3.8}$$

  In case of zero pion current $\mathfrak{m}_{\text{-}0} = 0$ in backward direction, the worm has to continue propagation in forward temporal direction. Vice versa, the emitted absorption site can raise the meson occupation number in forward direction to $\mathfrak{m}_{+0} = N_c + 1$ which requires a temporal backward propagation of the worm.

- Coming from a temporal direction ± 0, the temporal propagation of the worm Head is paused at each absorption site. These are either associated to a spatial dimer or the worm Tail. Either way, both are considered to have an occupation number of $\mathfrak{m} = 1$, i.e. they are identified as a source. It is always an option to delete the spatial dimer or worm Tail respectively, however, a continuation in temporal direction depends on the meson occupation number

$$P_{(\text{-}0|\mu)} = \frac{1}{1 + \mathfrak{m}_{+0}}, \quad P_{(\text{-}0|+0)} = \frac{\mathfrak{m}_{+0}}{1 + \mathfrak{m}_{+0}} \tag{3.9}$$

$$P_{(+0|\mu)} = \frac{1}{1 + \mathfrak{m}_{\text{-}0}}, \quad P_{(+0|\text{-}0)} = \frac{\mathfrak{m}_{\text{-}0}}{1 + \mathfrak{m}_{\text{-}0}}. \tag{3.10}$$

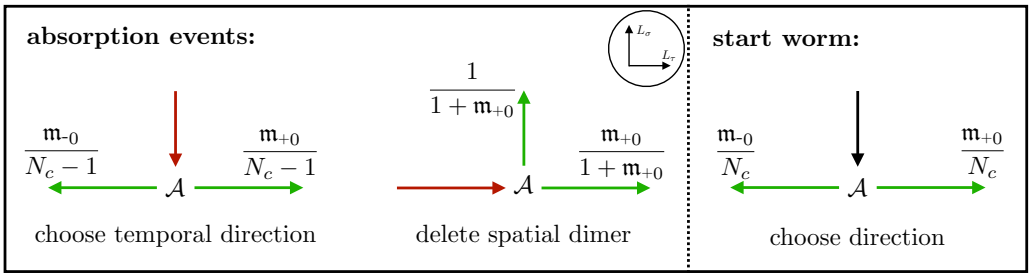

Figure 3.2: *An absorption site is encountered after the emission of a spatial dimer or when deleting a spatial dimer. During worm start the absorption site is entered via the site itself and an immediate recombination is possible.*

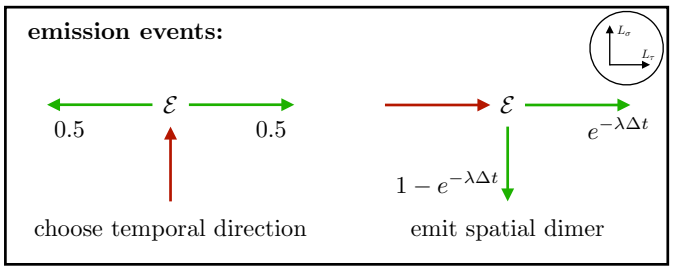

Figure 3.3: *An emission site is removed from the lattice as a consequence of the deletion of a spatial dimer. The distribution of emission sites is controlled by the Poisson process.*

Emission Update Whenever located at an emission site $\mathcal{E}$, an Emission Update is required. Either a spatial dimer is emitted or a new temporal direction is chosen after an emission site was removed (see Fig. 3.3).

- Coming from a temporal direction, the worm propagation is dictated by a Poisson process. The probability to emit a spatial dimer or rather continue in temporal direction is given by

$$P_{(\pm 0|\mp 0)} = e^{-\lambda\Delta t}, \quad P_{(\pm 0|\mu)} = 1 - e^{-\lambda\Delta t}. \tag{3.11}$$

  In case of spatial dimer emission, each spatial direction $\mu = \pm 1, \cdots \pm d$ can be selected with equal probability excluding the ones occupied by baryons. It is impossible that all neighboring sites are baryonic for $\Delta t < 1$. For $\Delta t = 1$ (see Eq. (3.3)) the Poisson process dictates to loop around the lattice in temporal direction to find the absorption site where it started.

  At high temperatures, the decay constant is small $\lambda = \lambda(a\mathcal{T}) \ll 1$ (cf. Eq. (3.2)). Therefore, the worm Head likely covers lager distances in temporal direction before emitting spatial dimers. On the contrary, a small temperature will encourage the spatial

dimer emission such that the worm Head is redirected so frequently resulting in a much larger sequence of updates before recombination. Therefore, the average worm length drastically increases.

- If the incoming direction is spatial, a spatial dimer is removed by an Absorption Update. As a consequence, the attached emission site is removed and the meson state is not modified anymore at the current worm Heads location. Thus, meson occupation numbers are equal in forward and backward temporal direction. Therefore, the probabilities for either direction are equal

$$P_{(s|\pm 0)} = \frac{1}{2}. \tag{3.12}$$

Worm Start Based on the Absorption Update, the start of a worm requires an almost identical discussion to the case when the worm Heads incoming direction is spatial. However, since there was so far no monomer placed at the worm Tails location, the Grassmann constraint is satisfied by the mesonic states in forward and backward temporal direction. The involved probabilities read

$$P_{(s|\text{-}0)} = \frac{\mathfrak{m}_{\text{-}0}}{N_c}, \quad P_{(s|+0)} = \frac{\mathfrak{m}_{+0}}{N_c}, \quad \text{with} \quad \mathfrak{m}_{\text{-}0} + \mathfrak{m}_{+0} = N_c. \tag{3.13}$$

3.3.1 Worm Propagation

After a successful moveUpdate, worm Head and Tail are located on a random mesonic lattice site. The Head finds an outgoing path with a probability that satisfies detailed balance. The maximal propagation distance in temporal direction is given by

$$\Delta t = -\ln(\mathfrak{R}) d_M(\vec{x}) / (4\acute{a}\mathcal{T}), \tag{3.14}$$

with the decay constant from Eq. (3.2) and $\mathfrak{R}$ a random number $\mathfrak{R} \in$ `[0:1]`. Note that it is incorporated in Eq. (3.14) that the inter-arrival times are distributed exponentially. During its movement in temporal direction, the meson states are modified. For each boundary crossing in forward direction, the occupation numbers are raised by one unit and for each crossing in backward direction they are lowered respectively. Two scenarios can occur:

- An absorption site is located within the interval Δt such that the worm stops at its location $\vec{x}$ and an Absorption Update decides on whether to delete the spatial dimer (see Eq. (3.9)).

- No absorption site is found and the full distance is covered in temporal direction. A spatial dimer is emitted and the worm Head is moved to the selected site where an Absorption Update decides on the new temporal direction.

This interplay of Absorption and Emission Update is continued until the worm Tail is removed from the lattice by an Absorption Update corresponding to a recombination of worm Head and Tail.
Measurements of closed loop observables are performed after each update. Furthermore, a certain number of measurements N_{measure} is required to obtain decent statistics. This results in a total of $N_{\text{update}} \cdot N_{\text{measure}}$ worm updates to be carried out for each simulation.

3.3.2 Measurement of Monomer Two-point Functions

In contrast to the vast majority of observables discussed in the next chapter 4, the monomer two-point functions are measured during the worm evolution as worm estimators and not on closed loop configurations. Therefore, a short overview on these specific functions is given here. In the chiral limit where monomers are absent ($n_x = 0$), measurements of monomer two-point functions only include the worm Head and Tail. A measurement is performed when both defects are located at an absorption site which is true after an Emission Update. While the Tail is always considered to be a monomer source, the Head only acts as a monomer sink at absorption sites. The monomer two-point contributions are accumulated in histograms which give rise to correlators.
Due to translational invariance, only the relative lattice vector $z = x_1 - x_2$ is needed. For discrete time configurations the increment reads

$$H_2(z) \mapsto H_2(z) + f(\gamma)\delta_{z,x_{\mathrm{T}}-x_{\mathrm{H}}}, \quad f(\gamma) = \frac{V_{\mathrm{DT}}}{d_{\mathrm{M}}(x_{\mathrm{H}}) + 2\gamma^2} \tag{3.15}$$

with $d_{\mathrm{M}}(x)$ defined in Eq. (3.2) and $V_{\mathrm{DT}} = N_\sigma^3 N_\tau$. In continuous time this is modified to

$$H_2(\vec{z},\tau) \mapsto H_2(\vec{z},\tau) + f(T)\delta_{\vec{z},\vec{x}_{\mathrm{T}}-\vec{x}_{\mathrm{H}}}\delta(\tau - (\tau_{\mathrm{T}} - \tau_{\mathrm{H}})), \quad f(T) = \frac{V_{\mathrm{CT}}}{2a\mathcal{T}} \tag{3.16}$$

with $V_{\mathrm{CT}} = N_\sigma^3$. The connected chiral two-point function $G(\vec{z},\tau)$ is approximated by such accumulated and normalized histograms

$$G(\vec{z},\tau) = \langle \bar{\chi}\chi_0\, \bar{\chi}\chi_{\vec{z},\tau}\rangle \simeq \frac{N_c}{Z} H_2(\vec{z},\tau). \tag{3.17}$$

3.4 Benefits of a Continuous Time Worm Algorithm

It is only reasonable to end this chapter by stressing the benefits of the presented algorithm. An algorithm that operates directly in the Euclidean continuous time limit is strongly motivated:

- There is no necessity to perform multiple simulations at different N_τ - where larger N_τ require more statistics - and an extrapolation to continuous time $N_\tau \to \infty$ becomes

obsolete. Thus, an unnecessary high workload can be avoided which would include an additional fit error estimation.

- Observables have a simpler structure in the CT Limit as it is not necessary to consider the functional dependence on the anisotropy $\xi(\gamma)$ (cf. Sec. 4.1). Especially a non-monotonic behavior makes it harder to deal with the discrete time extrapolation process.

- Baryons are static in CT since spatial hoppings are suppressed for the $\gamma \to \infty$ limit ($N_c \geq 3$). This results in a vanishing sign problem $\sigma(\ell) = 1$, such that no sign reweighting is necessary which introduces noise. A static baryon approximation can also be enforced in DT such that the N_τ extrapolation is much more controlled. The error introduced by this approximation is not too bad.

- The CT algorithm is expected to be faster in many regions of interest, especially around the chiral transition and for large temperatures. In particular, the baryonic update procedure is detached from the mesonic and requires no worm evolution.

As mentioned by the last item, the CT algorithm clearly outperforms the discrete time worm. In a temperature range around the chiral transition line and above this is strongly supported by shorter sampling times (Fig. 3.4). Simulations at large temperatures feature mostly static meson lines as spatial dimers are suppressed. The Poisson process samples time intervals which force the worm to loop around the temporal lattice extent without any emission events. This results in short runtimes as mostly no detours are taken.
At temperatures below the chiral transition the discrete time simulations are affected by saturation effects due to the finite number of spatial dimers that can be placed along the temporal direction. These effects arise at temperatures below $1/N_\tau$ ($\gamma < 1$) where the number of spatial dimers is larger than the number of temporal dimers. Hence, this leads to a limiting value of $N_c N_\tau/2$ for the spatial dimer density in DT. On the contrary, no such limit is present in CT as there is no discretization anymore and dimers can be placed arbitrarily tight. In order to compensate for the saturation effects, it is required to consider larger N_τ for a thermodynamic extrapolation at small temperatures. Therefore, the shorter runtimes in Fig. 3.4 for discrete time algorithms have to be put into perspective to the above discussion. Independently of the temporal discretization, at temperatures below the chiral transition the worm covers rather short distances in temporal direction. Thus, many spatial hoppings are enforced such that the sampling of a configuration takes longer.

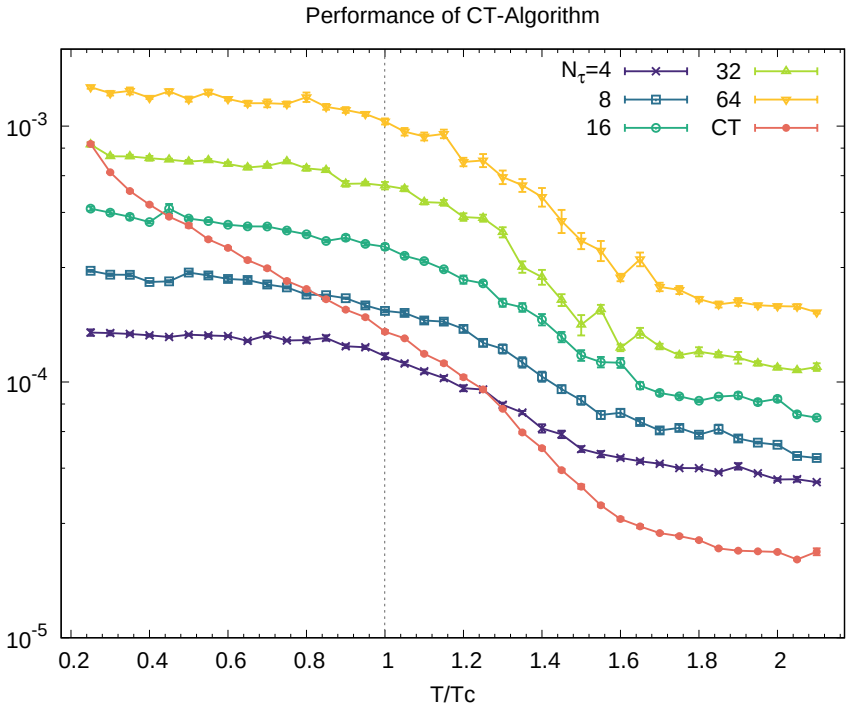

Figure 3.4: *The performance of the continuous time worm algorithm compared to the discrete time algorithm for various N_τ. At and above T_c the CT algorithm even outperforms the $N_\tau = 4$ DT algorithm. Below T_c single DT simulations perform better, however, the range of validity is limited due to saturation effects.*

Chapter 4

Continuous Time Crosschecks and Results

The following section covers a discussion on various observables of interest for this thesis. Crosschecks are performed concerning the reconstruction of results obtained in the CT limit. For that, calculations in discrete time at various N_τ are carried out, in order to compare the extrapolated results in $N_\tau \to \infty$. Features of the CT partition function such as the single spatial dimer approximation are motivated, the Poisson process is further discussed and the κ constant is determined. Finally, zero temperature observables can be measured based on a finite-size analysis and prediction from chiral perturbation theory for the $O(2)$ model.

4.1 Observables in the Dual representation

Within this section various observables are explored which can be constructed from the measurement of dual variables in the strong coupling limit. First, the dual variables and observables for a discrete time formulation are explored before the transition to continuous time is performed.

4.1.1 Discrete Time Observables

There are three main contributions to the partition function Eq. (1.76): Monomers, dimers and baryons.
Since the chiral limit is considered, monomer contributions $N_M = \sum_x n_x$ vanish and are therefore not relevant for further discussions. The chiral condensate is directly related to the monomer density by

$$a^3 \left\langle \bar{\psi}\psi \right\rangle = \frac{\langle N_M \rangle}{2am_q N_\sigma^3} = \frac{\langle n_M \rangle}{2am_q}. \tag{4.1}$$

Thus, the chiral condensate is zero when measured in terms of dual variables in the chiral limit. However, it can be extracted from chiral perturbation theory as discussed in Sec.4.3.3. Dimer contributions are distinguished for temporal and spatial directions

$$\begin{aligned} \text{Temporal Dimers:} \quad N_{D_\tau} &= \sum_x k_{x,0}, \\ \text{Spatial Dimers:} \quad N_{D_\sigma} &= \sum_x k_{x,i}, \end{aligned} \tag{4.2}$$

while baryonic contributions are extracted from baryon loops winding around the temporal lattice extent as

$$\text{Baryons:} \quad N_B = \sum_{\ell} \Omega_B(\ell). \tag{4.3}$$

Latter gives immediately rise to the calculation of the baryon density

$$a^3 n_B = a^3 \frac{T}{V} \frac{\partial \ln \mathcal{Z}}{\partial \mu_B}\bigg|_{V,T} = \frac{\langle \Omega_B \rangle}{N_\sigma^3} = \langle \omega \rangle \,. \tag{4.4}$$

Two more involved observables are the energy density $a^4\epsilon$ and the pressure $a^4 p$. These are closely related when formulated in terms of dual variables:

$$\text{Energy density:} \quad a^4\epsilon = a\mu a^3 n_B - \frac{a^3}{V} \frac{\partial \ln \mathcal{Z}}{\partial (a\mathcal{T})^{-1}}\bigg|_{V,\mu_B} = \frac{\xi}{\gamma} \frac{\partial \gamma}{\partial \xi} \frac{\langle 2N_{D_\tau} + N_c N_B \rangle}{N_\tau N_\sigma^3}, \tag{4.5}$$

$$\text{Pressure:} \quad a^4 p = -a^3 a\mathcal{T} \frac{\partial \ln \mathcal{Z}}{\partial V}\bigg|_{T,\mu_B} = a^4 \frac{\epsilon}{3} + \frac{\langle n_M \rangle}{3N_\tau}. \tag{4.6}$$

These relations are derived in [53] by evaluating the temperature and volume derivative of $\log \mathcal{Z}$ as

$$\frac{\partial \log \mathcal{Z}}{\partial (a\mathcal{T})^{-1}}\bigg|_{V} = \frac{1}{N_\tau \mathcal{Z}} \left(\frac{\partial \xi}{\partial a_\tau} \frac{\partial \gamma}{\partial \xi} \frac{\partial Z}{\partial \gamma}\bigg|_{a} + \frac{\partial \mathcal{Z}}{\partial a_\tau}\bigg|_{\gamma} \right) \tag{4.7}$$

$$\text{and} \quad \frac{\partial \log \mathcal{Z}}{\partial V}\bigg|_{T} = \frac{1}{3a^2 N_\sigma^3 \mathcal{Z}} \left(\frac{\partial \xi}{\partial a} \frac{\partial \gamma}{\partial \xi} \frac{\partial \mathcal{Z}}{\partial \gamma}\bigg|_{a_\tau} + \frac{\partial \mathcal{Z}}{\partial a}\bigg|_{\gamma} \right). \tag{4.8}$$

In the chiral limit energy density and pressure can be obtained simultaneously since the monomer density vanishes. In this specific case these observables differ just a factor of 3. This results in the interaction measure to vanish [10, 53]

$$\Theta_\mu^\mu = a^4(\epsilon - 3p) = -\frac{\langle N_M \rangle}{a_\tau N_\tau a^3 N_\sigma^3} \underset{\text{chiral limit}}{\to} 0. \tag{4.9}$$

Finally, the chiral susceptibility $a^6 \chi_q$ is of interest. It is measured as a worm estimator, which means it is an observable that is directly accumulated as the worm propagates through the lattice. Contributions arise after each Emission Update, such that both Head and Tail are located at absorption sites. The relative offset in time of the worm Head with respect to the Tail is measured. Yet, the spatial offset has to be accounted for as well, since temporal correlators are being projected to zero momentum (see Sec. 5.1.1).

The chiral susceptibility is defined as the integrated monomer two-point function

$$a^6\chi_q = a^4 \frac{\partial^2 \ln \mathcal{Z}}{\partial (2m_q)^2}\bigg|_{m_q=0} \tag{4.10}$$

As discussed in Sec. 3.3.2 this function is measured in terms of a histogram.

4.1.2 Continuous Time Observables

In the continuous time limit the calculation of dual observables simplifies. Without any spatial baryon hoppings, it is necessary for a baryon attached to a spatial site $\vec{x}$ to occupy all temporal locations τ_i. Hence, the winding number $\omega_{\vec{x}}$ can be used to state whether a site is

$$\begin{aligned} \text{mesonic:} \quad & \omega_{\vec{x}} = 0 \\ \text{anti-baryonic:} \quad & \omega_{\vec{x}} = -1 \\ \text{baryonic:} \quad & \omega_{\vec{x}} = +1. \end{aligned} \tag{4.11}$$

Therefore, a measurement of the baryon density $a^3 n_B$ reduces to counting the number of baryons (B) and anti-baryons (A) on the lattice yielding

$$a^3 n_B = \frac{\langle B - A \rangle}{N_\sigma^3} = \langle \omega \rangle \,. \tag{4.12}$$

The final expression agrees with the one for discrete time simulations, however, the way of calculating this observable simplified.

Concerning the pressure and energy density, a slightly deeper analysis has to be performed. In the CT limit it is not possible to specify the number of temporal dimer segments N_{D_τ} as there is no discretization in time anymore. Therefore, the temporal contributions are rewritten in terms of spatial number densities

$$\langle 2N_{D_\tau} + N_c N_B \rangle = \langle N_c N_\tau N_\sigma^3 - 2N_{D_\sigma} \rangle. \tag{4.13}$$

The first term $N_c N_\tau N_\sigma^3$ resembles the Grassmann Constraint on a lattice with $N_\tau N_\sigma^3$ sites and is related to the factor $\gamma^{N_c V}$ which was pulled out of the partition function Eq. (2.15) as it weights all sites equally. The second term $2N_{D_\sigma}$ accounts for all lattice sites that have a spatial dimer attached. Another simplification arises in continuous time for dimensionless thermodynamic observables where the anisotropy dependence reads

$$\frac{\xi(\gamma)}{\gamma}\frac{d\gamma}{d\xi} = \frac{\kappa\gamma^2}{\gamma}\frac{1}{2\kappa\gamma} = \frac{1}{2}, \quad \text{with } \xi(\gamma) = \kappa\gamma^2 \text{ and } \frac{d\gamma}{d\xi} = \frac{1}{2\sqrt{\kappa\xi}} = \frac{1}{2\kappa\gamma}. \tag{4.14}$$

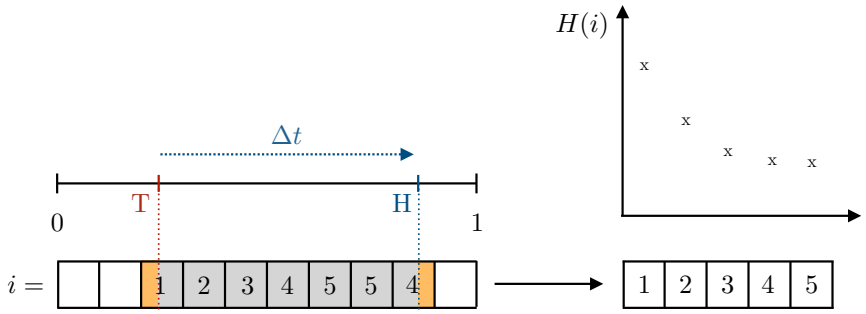

Figure 4.1: *Example for a discretization in time with* 10 *bins. The worm Head is moved away from the Tail by the distance* Δt*. The index* i *states which histogram bins are accumulated since the relative offset in time is measured. Due to symmetry of the correlator only half of the bins* $i = 1, 2, \ldots, N_\tau/2$ *are required.*

This leads to the energy density and the pressure formulated in CT dual variables

$$a^4\epsilon = k\mathcal{a}\mathcal{T}(C - \langle n_{D_\sigma}\rangle), \tag{4.15}$$

$$a^4 p = k\frac{\mathcal{a}\mathcal{T}}{3}(C - \langle n_{D_\sigma}\rangle). \tag{4.16}$$

Thus, both quantities are extracted from a measurement of the spatial dimer density. The additive constant $C = N_c N_\tau N_\sigma$ ensures that both quantities are positive and encodes the Grassmann Constraint.

Finally, the measurement of the chiral susceptibility requires the introduction of an artificial discretization in CT for the histogram accumulation. Two histograms are measured which distinguish the parity of the offset between worm Head and Tail (even or odd). Combinations of these histograms are used to reconstruct continuous time temporal correlation functions (see Fig. 4.1). Note that this offset would be trivial if only the temporal displacement is considered as correlators are always accumulated when Head and Tail have opposite parity. However, temporal correlators are being projected to zero momentum (see Sec. 5.1.1) such that the 4-d parity has to be accounted for. Therefore, an even (odd) site histogram is accumulated whenever the *spatial* distance is odd (even). Due to this update rule there is always only one of the two histograms which is updated.

4.2 Crosschecks

The discussed dual observables are measured both in discrete and continuous time and results are matched. The crosschecks are performed for a vanishing baryon chemical potential $\mu_B = 0$.

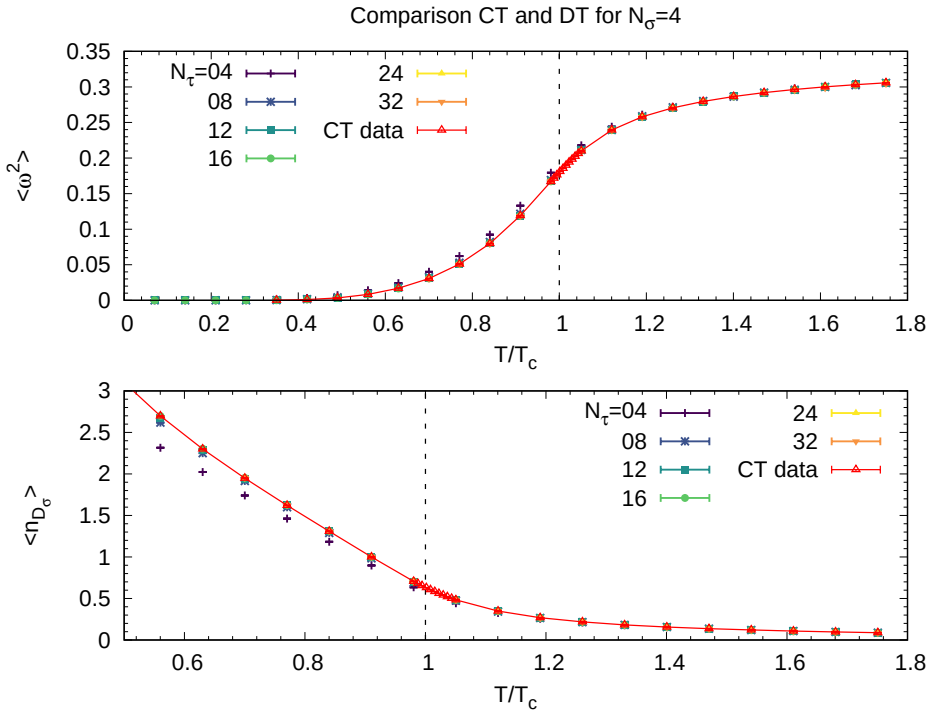

Figure 4.2: ***Top:*** *Temperature dependence of the baryon density susceptibility measured in DT, in direct comparison with the results from CT.* ***Bottom:*** *Temperature dependence of the spatial dimer density measured in DT, in direct comparison with the results from CT.*

Baryon Fluctuations At zero chemical potential, the odd moments $n \pmod 2 = 1$ in the winding number density $\langle \omega^n \rangle = 0$ vanish. There is no preference between baryons and anti-baryons as their weights match at all temperatures $w_{B/A}(\mu_B/T) = e^{\pm \mu_B/T}|_{\mu_B=0} = 1$. Therefore, the second moment in the winding number density ω^2 is considered which gives rise to the baryon susceptibility

$$\chi_B = \langle \omega^2 \rangle - \underbrace{\langle \omega \rangle}_{=0}^2. \tag{4.17}$$

This function monotonically increases with temperature (see Fig. 4.2:Top). The discrete time values converge towards the continuous time curve for each single temperature. There is a strong T_c dependence as static baryons are suppressed below T_c while they are common above T_c. At large temperatures a limiting value of $1/3$ is reached which is obtained when calculating the second moment of the winding number density Eq. (4.4) based on the partition function from one-dimensional QCD (see Eq. (1.80)).

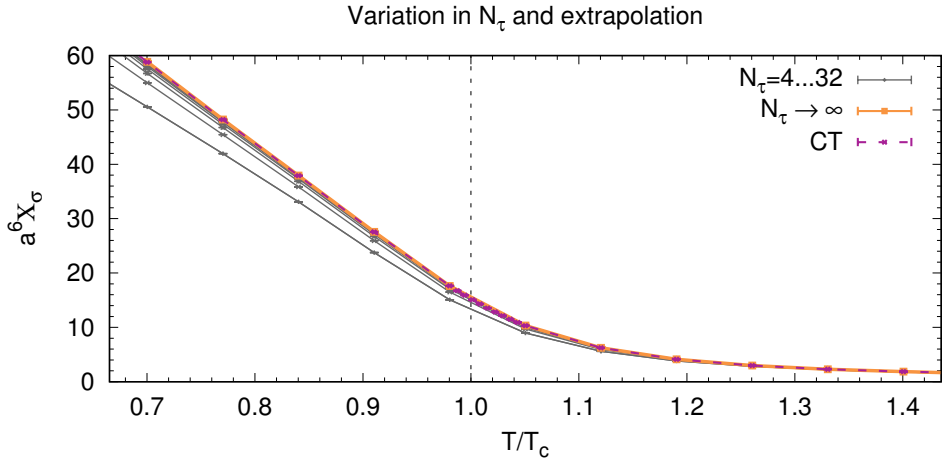

Figure 4.3: *Chiral susceptibility for various N_τ measures on $4^3 \times N_\tau$ lattices. It is a monotonically decreasing function in temperature. There is a clear imprint of the chiral transition. An extrapolation in N_τ shows agreements with $a^6\chi_\sigma$ measured in CT.*

Energy density and pressure Both energy density and pressure follow from the measurement of the spatial dimer density (cf. Fig. 4.2). Spatial dimers are most prominent below T_c where the worm performs many detours due to short temporal intervals sampled by the Poisson process and therefore many spatial hoppings. On the contrary, at large temperatures the static limit is approached where hoppings become more and more unlikely and so the dimer density becomes small. In total, over the whole temperature range the spatial dimer density decreases as the temperature is increased. This also means that pressure and energy density are constantly increasing quantities. Note that the definition of the pressure in Eq. (4.6) is distinctively different from

$$a^4 p' = a^3 \kappa \frac{a\mathcal{T}}{V} \ln \mathcal{Z}, \tag{4.18}$$

which is valid for homogeneous systems. However, while the identity $p = p'$ holds in the continuum it is not true on the lattice. Thus, the Taylor expansion has to be performed in $\langle n_{D_\sigma} \rangle$ (cf. Sec. 6.6).

Chiral Susceptibility The integrated two-point function in Eq. (4.10) measures the susceptibility χ_σ for the σ meson. Further susceptibilities for other mesons can be addressed by weighting the histogram increments with phase factors which are related to the kernel in spin$\otimes$taste space (cf. Sec. 5.2).

At temperatures below T_c, the worm performs many detours due to the emission of spatial dimers. Its chance to find and recombine with the worm Tail is low. Above T_c there are almost no spatial dimers and the worm purely loops in temporal direction resulting in a fast

recombination. Since the chiral susceptibility χ_σ is a measure of the length of the worm path, it is a monotonic decreasing function with temperature (see Fig. 4.3 and Fig. 4.8). The chiral susceptibility exhibits finite N_τ effects which clearly extrapolate towards simulation results from CT (Fig. 4.3). It shows an imprint of the chiral transition at T_c. The impact of spatial dimers on the worm length is strong, with increasing volume a clear kink evolves. (Fig. 4.8).

4.3 Results at $T = 0$

4.3.1 Determination of κ

Lattice simulations at strong coupling are typically performed on anisotropic lattices in order to address temperature ranges of interest. In DT simulations it is necessary to analyze the running of $\frac{1}{\xi}\frac{d\xi}{d\gamma}$, which is a strong coupling analogue of Karsch's coefficients [54, 55]. The anisotropy calibration procedure is discussed for anisotropic lattices at strong coupling and DT in [56] and [36] in detail. In CT this procedure simplifies to the determination of the proportionality factor $\kappa = \lim_{\xi\to\infty} \frac{\xi(\gamma)}{\gamma^2}$ which then defines the temperature and chemical potential (see Eq. (2.5) and Eq. (2.6)). An estimate for κ directly from CT is obtained from the variance of the pion current. In the chiral limit, the pion current for DT

$$j_\mu(x) = \epsilon(x)\left(k_\mu(x) - \frac{N_c}{2}|b_\mu(x)| - \frac{N_c}{2d}\right) \tag{4.19}$$

is conserved

$$\sum_{\hat{\mu}}(j_\mu(x) - j_\mu(x-\hat{\mu})) = 0. \tag{4.20}$$

Likewise, in CT the meson occupation numbers (see Eq. (2.30)) are the corresponding currents

$$\begin{aligned}\mathfrak{m}(\vec{x},\tau) &\equiv j_0(\vec{x},\tau) = \epsilon(\vec{x},\tau)k_0(\vec{x},\tau),\\ \mathfrak{m}_i(\vec{x},\tau) &\equiv j_i(\vec{x},\tau) = \epsilon(\vec{x},\tau)k_i(\vec{x},\tau),\end{aligned} \tag{4.21}$$

which follow the conservation law

$$\mathfrak{m}(\vec{x},\tau) + \sum_{i=1}^{3}\Big(\mathfrak{m}_i(\vec{x},\tau) - \mathfrak{m}_i(\vec{x}-\hat{i},\tau)\Big) = 0. \tag{4.22}$$

Note that the baryonic contributions as well as the constant are dropped as they do not contribute to the pion current.

The temporal and spatial charges are calculated as

$$Q_0 = \sum_{\vec{x}} \mathfrak{m}(\vec{x},\tau) \equiv \mathfrak{M}, \tag{4.23}$$

$$Q_i = \sum_{\vec{x}\perp\vec{e}_i} \int_0^{1/a\mathcal{T}} d\tau\, \mathfrak{m}_i(\vec{x},\tau) \equiv \mathfrak{M}_i, \tag{4.24}$$

Their expectation values

$$\langle\mathfrak{M}\rangle = \frac{N_c}{2}, \quad \langle\mathfrak{M}\rangle_0 = \langle\mathfrak{M}\rangle - \frac{N_c}{2} \quad \text{and} \quad \langle\mathfrak{M}_i\rangle = 0, \tag{4.25}$$

follow from simple considerations:

1) Since meson occupation numbers take values $\mathfrak{m} \in (0, 1, \ldots, N_c)$, it immediately follows that the expectation value $\langle\mathfrak{M}\rangle$ yields $N_c/2$

2) As emission and absorption sites come in pairs, meson state changes due to spatial dimers are always compensated such that the expectation value $\langle\mathfrak{M}_i\rangle$ vanishes.

The variances are however temperature dependent. In case temporal and spatial variances are equal, this indicates that the lattice is physically isotropic

$$L = \frac{1}{T} \quad \Rightarrow \quad N_\sigma = \frac{1}{aT} = \frac{1}{\kappa a\mathcal{T}}. \tag{4.26}$$

Thus, in order to measure κ, a scan in the bare temperature $a\mathcal{T}$ around the crossing point is necessary for each lattice with different spatial extent N_σ. The temperature $a\mathcal{T}_0$ at the crossing point

$$\left\langle\mathfrak{M}^2\right\rangle_0 = \left\langle\mathfrak{M}^2\right\rangle - \frac{N_c^2}{4} \stackrel{!}{=} \left\langle\mathfrak{M}_i^2\right\rangle \tag{4.27}$$

gives immediately rise to $\kappa = 1/(N_\sigma a\mathcal{T}_0)$. An example for an anisotropy calibration is shown in Fig. 4.4. The range in $a\mathcal{T}$ is taken very narrowly in order to approximate a linear slope. The results for κ for various volumes are shown in Tab. 4.1 and the thermodynamic extrapolation $N_\sigma \to \infty$ is depicted in Fig. 4.5:Left. The latter coincides with the zero-temperature extrapolation, and since the calibration is performed at $a\mu = 0$, static baryons are virtually absent. Therefore, there is no reason to distinguish between κ values for gauge groups $U(3)$ and $SU(3)$. Note that this is not valid at finite ξ (finite a_τ).
There is a 2% mismatch when comparing the CT result with the DT extrapolation $\xi \to \infty$ performed in [36]. In this DT study uncertainties in the determination of κ arise, since the extrapolation is based on a limited range of values $\xi \leq 8$. Furthermore, the extrapolation strongly depends on the used fit ansatz for the function ξ/γ^2 [46]. To avoid such disambiguates it is reasonable to measure κ directly in the CT limit.

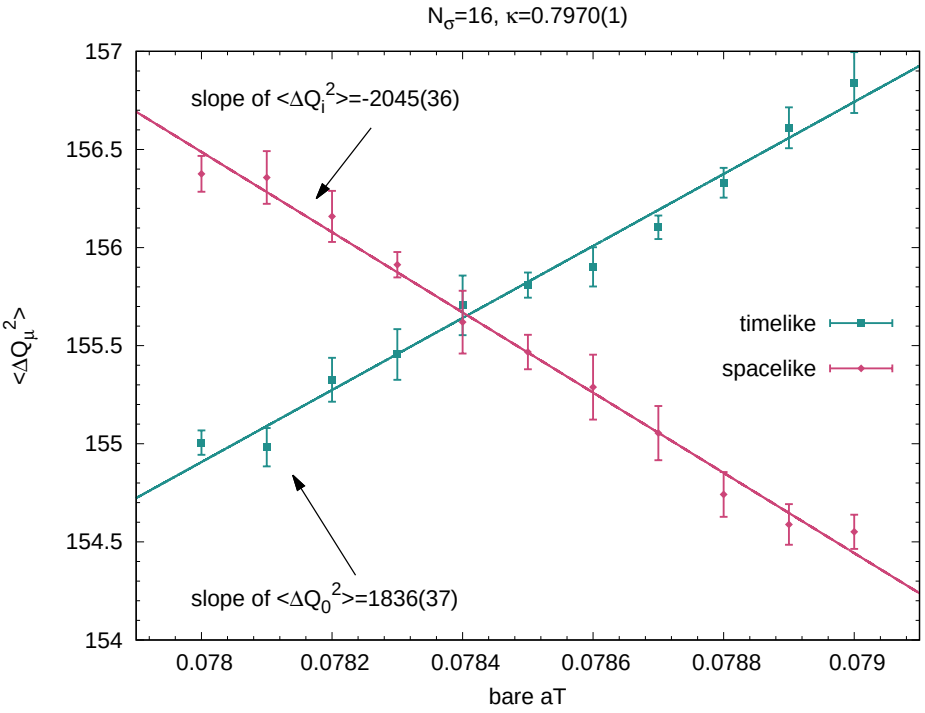

Figure 4.4: *Results on the spatial and temporal charges. The crossing point defines the temperature $a\mathcal{T}_0$ for the determination of κ as well as the charge $\langle\mathfrak{M}\rangle_0$ which gives rise to the helicity modulus and hence the pion decay constant F_π.*

Table 4.1: *Data from the anisotropy calibration on various volumes N_σ^3. The crossing point $(a\mathcal{T}_0, \langle\mathfrak{M}^2\rangle_0)$ gives rise to the calculation of the CT constant κ as well as the helicity modulus $a^2\Upsilon$.*

N_σ	$a\mathcal{T}_0$	$\langle\mathfrak{M}^2\rangle_0$	κ	$a^2\Upsilon$
4	0.31388(1)	9.724(1)	0.7965(1)	0.6078(1)
6	0.20911(1)	21.88(1)	0.7970(1)	0.6079(1)
8	0.15680(1)	38.91(1)	0.7972(1)	0.6080(1)
12	0.10457(1)	87.51(1)	0.7969(1)	0.6077(1)
16	0.07841(1)	155.65(1)	0.7970(1)	0.6080(1)
∞			0.7971(3)	0.6080(1)

Note that the anisotropy calibration can also be performed at finite quark mass [57] as well as at finite coupling β. These results indicate that it is possible to formulate the CT limit unambiguously at finite m_q and β, with $\kappa = \kappa(m_q, \beta)$.

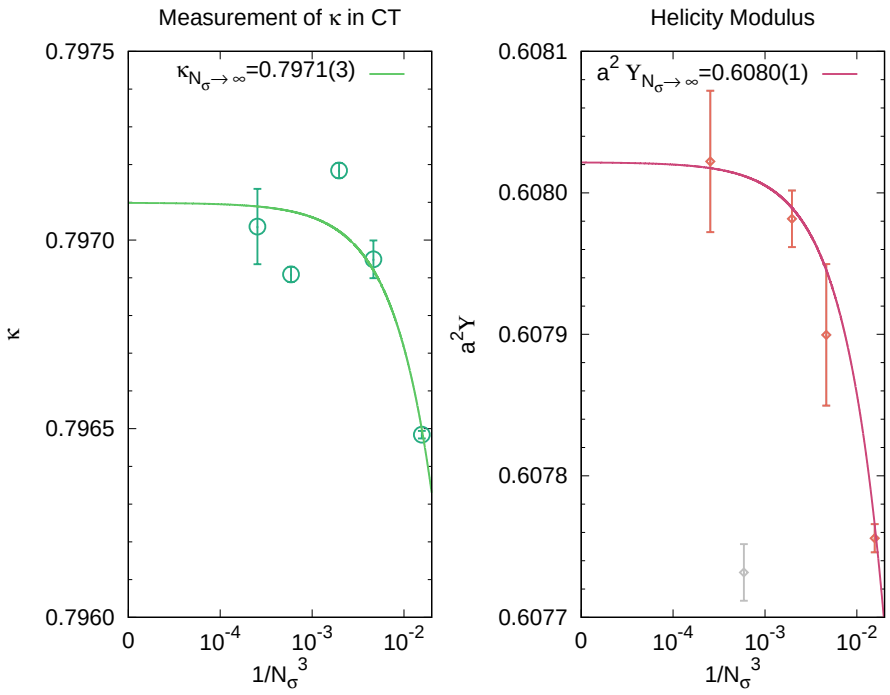

Figure 4.5: ***Left****: Thermodynamic extrapolation of the CT proportionality constant* κ *based on isotropic lattices with* $N_\sigma = 4, 6, 8, 12, 16$*. Note the overall precision in the data points.* ***Right****: Extrapolation of the helicity modulus which is of high interest for the measurement of the pion decay constant. The* $N_\sigma = 12$ *value is not considered in the fit. Both quantities are retrieved from the intersection point of the anisotropy calibration.*

4.3.2 Pion Decay Constant

In the chiral limit $m_q = 0$, lattice QCD with staggered fermions exhibits an exact $O(2)$ chiral symmetry (cf. Sec. 4.4.2). This symmetry is spontaneously broken at $T = 0$ but gets restored at high temperatures [56]. A finite-size scaling analysis gives rise to low-energy quantities such as the pion decay constant aF_π and the chiral condensate $a^3\Sigma \equiv a^3\langle\bar{\chi}\chi\rangle$.
The square of the pion decay constant is related to the helicity modulus via

$$a^2 F_\pi^2 = \lim_{N_\sigma \to \infty} a^2 \Upsilon, \tag{4.28}$$

which is in turn obtained from the variance of the conserved pion currents as [36, 46]

$$a^2 \Upsilon = \frac{1}{N_\sigma^2} \left\langle \mathfrak{M}^2 \right\rangle_0 . \tag{4.29}$$

Note that $\langle \mathfrak{M}^2 \rangle_0$ is the variance of the meson occupation number at the crossing point (see Eq. (4.27)) where the lattice is isotropic. Thus, the anisotropy calibration in CT is performed

on various volumes with results summarized in Tab. 4.1. The thermodynamic extrapolation of the helicity modulus is graphically shown in Fig. 4.5. Based on Eq.(4.28) the final result for the pion decay constant can be computed as

$$(aF_\pi)^{\mathrm{CT}} = 0.7797(1). \tag{4.30}$$

This result shows a 1% discrepancy from previous studies on DT lattices $(aF_\pi)^{\mathrm{DT}} = 0.78171(4)$ which is due to uncertainties in the ξ extrapolation of DT studies as discussed before.

4.3.3 Chiral Condensate

In a finite volume, the direct measurement of the chiral condensate $a^3\Sigma$ is proportional to the monomer density, which however vanishes in the chiral limit. Nevertheless, the chiral condensate can be extracted from Chiral Perturbation Theory (CPT) in a finite box by a large volume expansion in $1/V_\sigma^2$ [58]. As the chiral limit is considered, the correlation length diverges such that finite sized systems are necessarily be considered in the so-called ϵ-regime [59]. CPT predicts the finite-size scaling of the chiral susceptibility χ_σ, which is non-zero in a finite volume and contains the (infinite volume) chiral condensate as a contribution. The scaling reads [58, 60]

$$a^6\chi_\sigma \approx \frac{1}{2}a^6\Sigma^2 N_\sigma^4 \left(1 + \frac{\beta_1}{a^2F_\pi^2N_\sigma^2} + \frac{\alpha}{2a^4F_\pi^4N_\sigma^4}\right), \tag{4.31}$$

with the constant α being of the form

$$\alpha = \beta_1^2 + \beta_2 + \frac{1}{8\pi^2}\ln\frac{a\Lambda_\Sigma^2 N_\sigma}{\Lambda_M}. \tag{4.32}$$

The two constants $\beta_1 = 0.140461$ and $\beta_2 = -0.020305$ are the shape coefficients of the box and $\Lambda_\Sigma, \Lambda_M$ are two renormalization group invariant logarithmic scales [58]. Since aF_π is known from above, the chiral condensate $a^3\Sigma$ can be extracted by measurements of $a^6\chi_\sigma$ on various volumes $4^3 - 16^3$ (cf. Sec. 4.2) and fitting according to Eq. (4.31) (see Fig. 4.6). The volumes considered in this analysis are rather small, since simulations at low temperatures are required in order to keep the lattice isotropic (see Eq. (4.26)). The third term defining the constant α (cf. Eq. (4.32)) is considered to be a fit parameter as well. However, without a good estimate for the contribution $\frac{1}{8\pi^2}\ln\frac{a\Lambda_\Sigma^2 N_\sigma}{\Lambda_M}$, there is no benefit from considering this additional term. If the contribution of Eq. (4.32) is incorporated, the value for the chiral condensate follows as $(a^3\Sigma)^{\mathrm{CT}} = 1.306(6)$. However, the best result is achieved by neglecting the mentioned term which results in the final value

$$(a^3\Sigma)^{\mathrm{CT}} = 1.305(3). \tag{4.33}$$

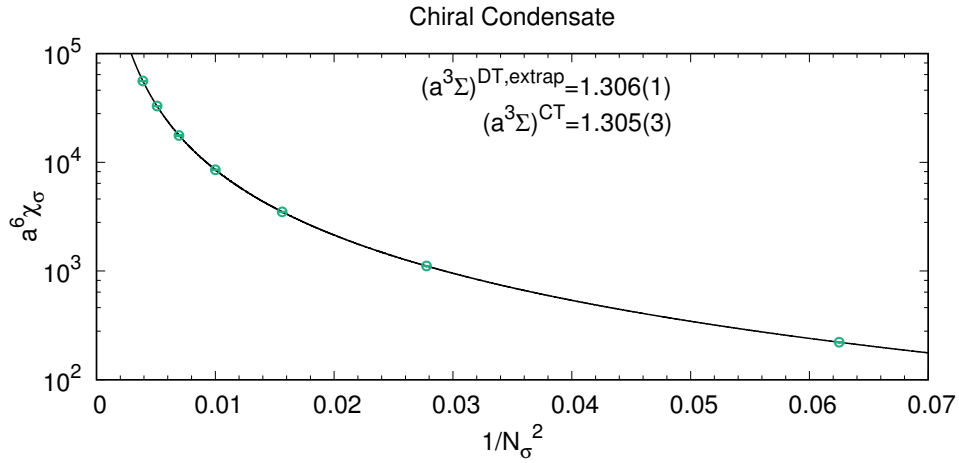

Figure 4.6: *Extraction of the chiral condensate via a fit of the chiral susceptibility $a^6\chi_\sigma$ according to Eq.* (4.31).

In contrast to other discussions on $T = 0$ observables, the obtained value coincides with the result from DT [36]. However, it is not possible to retrieve the same accuracy.

4.4 Phase Diagram

4.4.1 Pressure and Energy Density in the $\mu_B - T$ plane

With no sign problem present in the CT limit, the phase diagram for the pressure a^4p can be explored in the full $\mu_B - T$ plane (cf. Fig. 4.7). Since the pressure is proportional to the spatial dimer density n_{D_σ} according to Eq. (4.6) its temperature dependence is the same. It drops with increasing temperature and can almost be neglected above T_c. With respect to the chemical potential, the pressure vanishes below μ_c and obtains a finite value above. At low temperature there are unphysical thermalization effects. As discussed in [53] a discontinuous behavior of the pressure across the transition line is observed in the strong coupling limit of LQCD. Typically, these pressure gaps (or negative values in the pressure) arise due to perturbatively calculating anisotropy coefficients. Therefore, as presented in Sec. 2.1 a non-perturbative approach is chosen in the (continuous time) strong coupling limit. Nevertheless, the problem of a sudden increase in pressure at the transition line persists.

4.4.2 Determination of T_c

The imprint of the chiral transition on the chiral susceptibility (discussed in Sec. 4.2) is used in a finite size scaling analysis to determine the critical temperature at $\mu_B = 0$. In the chiral limit, the system undergoes a second order transition as temperature is increased. This

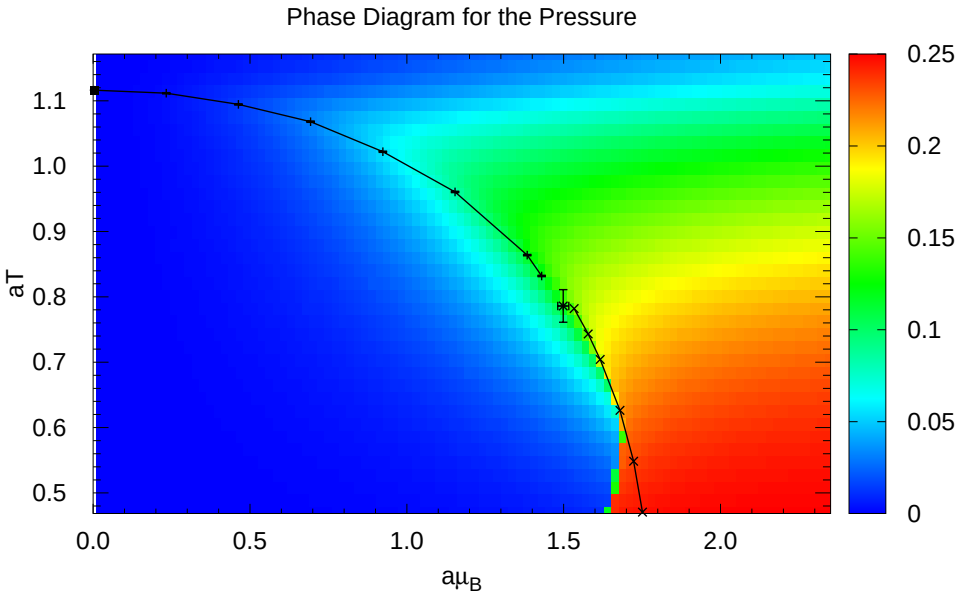

Figure 4.7: *Pressure a^4p in the finite bare density and temperature plane. The 2^{nd} and 1^{st} order phase transition in the chiral limit with its tri-critical point is depicted as well.*

transition belongs to the 3d $O(2)$ universality class with critical exponents [61]

$$\nu = 0.67155(27) \quad \text{and} \quad \gamma = 1.3177(5). \tag{4.34}$$

Note that ν is the critical exponent related to the correlation length by $\xi \propto |t|^{-\nu}$, with the reduced temperature defined as $t = 1 - T/T_c$. A critical behavior of $\chi \propto |t|^{-\gamma}$ is observed for the chiral susceptibility.

In the critical region the susceptibility is expected to scale as [12, 56, 62]

$$\chi_{\sigma,N_\sigma} = N_\sigma^{\gamma/\nu}\hat{\chi}(tN_\sigma^{1/\nu}) = N_\sigma^{\gamma/\nu}(a_0 + \mathcal{O}(tN_\sigma^{1/\nu})). \tag{4.35}$$

The rescaled susceptibilities $\chi_{\sigma,N_\sigma}/N_\sigma^{\gamma/\nu} = a_0$ yield the same value at T_c (i.e. $t = 0$) such that the intersection point of finite volume tuples $(N_{\sigma,i}|N_{\sigma,i+1})$ gives an estimate of the critical temperature (see Fig. 4.9 and Tab. 4.2). It is expected that $\chi_{\sigma,N_\sigma}/N_\sigma^{\gamma/\nu}$ collapses on a universal scaling function $\hat{\chi}(tN_\sigma^{1/\nu})$ when plotted as a function of $tN_\sigma^{1/\nu}$. Thus, an extrapolation according to

$$\chi_\sigma = a\mathcal{T}_c + a_0/N_\sigma^{1/\nu} \tag{4.36}$$

for successive volume tuples results in the final value $a\mathcal{T}_c^{\mathrm{CT}} = 1.4276(2)$ (Fig. 4.10).

The CT estimation of the critical temperature is different from previous studies deducing

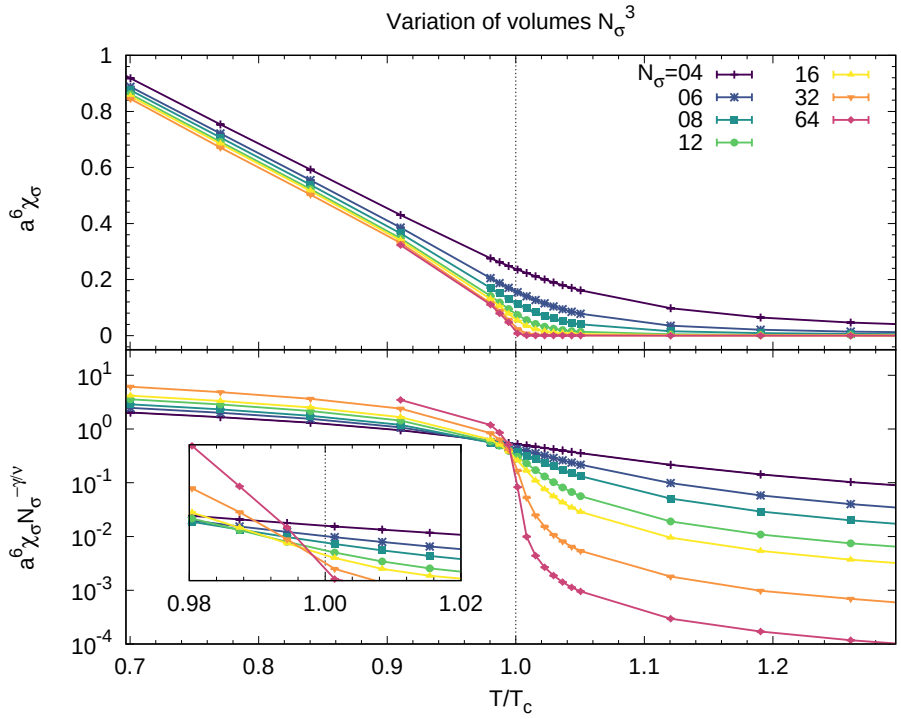

Figure 4.8: *Volume dependence of the chiral susceptibility. By rescaling χ_σ with $N_\sigma^{-\gamma/\nu}$ a crossing point emerges which indicates the critical temperature. The critical exponents are associated with the 3d $O(2)$ universality class. Note that the extrapolated value of $a\mathcal{T}_c = 1.4276(2)$ is already incorporated in both plots.*

a value of $a\mathcal{T}_c^{\mathrm{DT}} = 1.403(1)$ based on DT simulations with $N_\tau = 4$ lattices [12]. This again emphasizes the advantages of CT where no extrapolation in N_τ is required and calculations on lattices up to $N_\sigma = 64$ could be performed.

Summary Within this chapter dual observables are discussed, which includes an overview of discrete time observables and their formulation in continuous time. Among its many benefits, the CT framework thrives from its simple structured observables.

Crosschecks are performed for the most prominent observables where extrapolations in N_τ showed full agreement with the CT measurements.

At zero temperature $T = 0$ the proportionality factor κ is determined based on an anisotropy calibration. For CT this requires measurements of variances of spatial and temporal charges at certain temperatures far below T_c (cf. Eq. (4.26)). In this temperature regime CT simulations are limited to lattices with a spatial extent of $N_\sigma = 16$ due to the increasing numerical effort. However, this suffices as κ exhibits only small finite size effects. The crossing point encodes information not just about κ, but also gives rise to the helicity modulus. From latter follows the pion decay constant. In both κ and the pion decay constant aF_π a few percentage

Table 4.2: *Data for the determination of $a\mathcal{T}_c$ from the finite size scaling of the chiral susceptibility. Successive volume tuples are intersected. The crossing points are an estimate for $a\mathcal{T}_c$.*

$(N_1 \cdot N_2)^{1/2}$	$a\mathcal{T}_c$
$(4 \cdot 6)^{1/2}$	1.3654(5)
$(6 \cdot 8)^{1/2}$	1.3851(5)
$(8 \cdot 12)^{1/2}$	1.4041(1)
$(12 \cdot 16)^{1/2}$	1.41348(6)
$(16 \cdot 32)^{1/2}$	1.42029(3)
$(32 \cdot 64)^{1/2}$	1.424240(9)

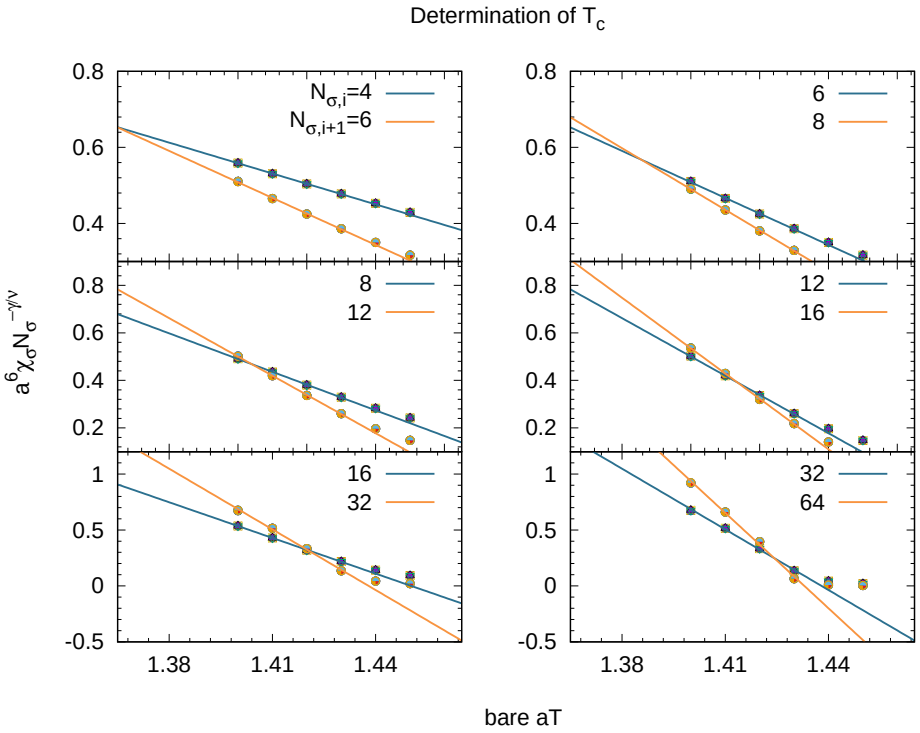

Figure 4.9: *Finite volume scaling of the chiral susceptibility. The crossing point of successive volumes is an estimate for $a\mathcal{T}_c$. A tight region around $a\mathcal{T}_c$ is chosen such that a linear approximation of the slope is feasible.*

mismatch was observed between DT and CT results. These differences are expected to arise when keeping in mind that DT results require an extrapolation in ξ. These are based on rather small values $\xi \leq 8$ and on a fit ansatz for the function ξ/γ^2. The respective systematic

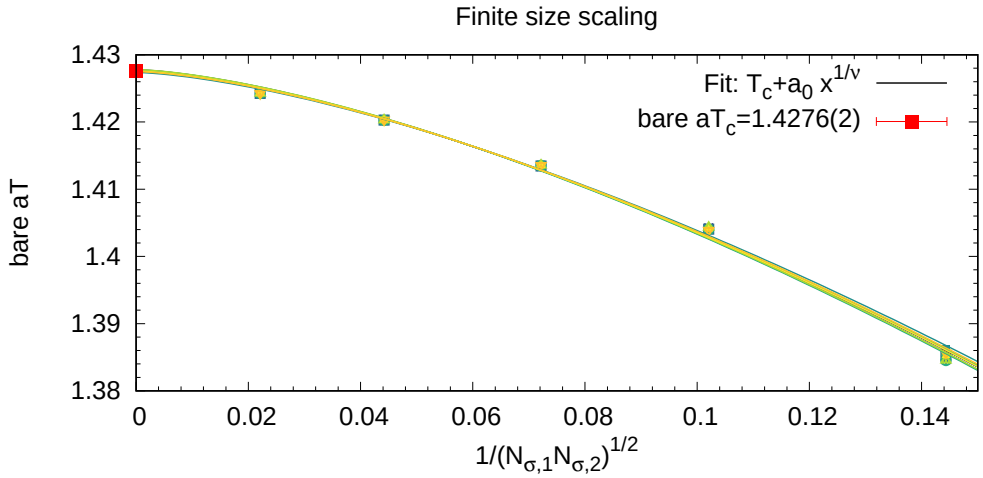

Figure 4.10: *Extrapolation of the finite volume critical temperatures $a\mathcal{T}_{c,(N_{\sigma,i}|N_{\sigma,i+1})}$ to the thermodynamic limit. Note that a jackknife analysis is performed for the error estimation. This yields the depicted* 10 *fits from which $a\mathcal{T}_c$ and the standard deviation can be calculated.*

error due to the choice of fit ansatz is unknown. As noted, the anisotropy calibration can also be performed at finite quark mass m_q and/or finite β. Additionally, the chiral condensate is extracted from CPT in a finite box by a large volume expansion in $1/V_\sigma^2$. The CT measurement agrees with results obtained from DT simulations.

Finally, the phase diagram of the pressure/energy density is obtained from finite temperature and density simulations. Based on a finite-size scaling analysis of the chiral susceptibility, the critical temperature is estimated which slightly deviates from values obtained so far in DT studies. This clearly stresses the necessity to have an algorithm performing directly in the CT limit in order to avoid inaccuracies due to extrapolations or anisotropy calibrations. In order to improve on the precision of T_c, more data points are required in a narrower range around T_c for the larger volumes $N_\sigma = 32, 64$ and beyond.

Within the last chapters 2-4 the continuous time limit is introduced with its partition function, an algorithm that samples respective configurations as well as observables of interest. The next two chapters will cover two major topics within the research area of lattice QCD. Firstly, temporal correlators are constructed at finite temperatures and densities and so-called pole masses will be investigated (see chapter 5). Secondly, the phase diagram of SC-QCD is explored with the Taylor expansion method (cf. chapter 6). Since the continuous time framework has no sign problem, the range of reliability is discussed by means of the radius of convergence and the reconstruction of the pressure.

Chapter 5

Temporal Correlators

Meson correlators allow to extract the ground state mass and possibly excited mesonic states. Typically, there is a focus on spatial correlators since large lattice extents are required to isolate the lowest excitation [63]. Here, temporal directions suffer from being limited by the inverse temperature. The respective masses of spatial (screening mass) and temporal correlators (pole mass) obtained from the exponential decay are not necessarily identical. However, they are related to the same spectral function which is a central tool for the study of transport properties of the quark-gluon plasma [63]. By means of the spectral function the dissolution of heavy quarks at high temperatures is studied in order to learn about the modifications of hadronic properties under extreme conditions.
Within this chapter, hadronic correlators projected to zero spatial momentum are constructed (Sec. 5.1). The focus is on temporal correlators as the CT algorithm is not hindered by an insufficiently large temporal lattice extent. Especially, staggered correlators are introduced which have a more complicated bilinear spin-taste structure (Sec. 5.2). The temporal correlators are discussed for discrete and continuous time (see Sections (5.3) and (5.4)). An extraction of corresponding pole masses is outlined by means of correlated fits performed on temporal correlators (Sec. 5.5). Many results are presented for the masses at various temperatures below, around and above T_c as well as at zero and finite baryon chemical potential (Sections (5.5) and (5.6)). Finally, methods for the calculation of transport coefficients are discussed, such as the Maximum Entropy method and the Schwinger-Keldysh contour (see Sec. 5.7).

5.1 Foundation of Hadron Correlators

For the construction of a hadron correlation function an arbitrary hadronic state $|h\rangle$ is taken into account with some associated quantum numbers that are discussed in Appendix (C). The interpolating operators $\mathcal{O}_{i,f}$ are considered which have a non-vanishing overlap with the state of interest $|h\rangle$ [28] and eventually also with its decay products

$$\langle 0|\mathcal{O}_{i,f}|h\rangle \neq 0. \tag{5.1}$$

The overlap with other states of the same quantum numbers is ideally minimal. With the initial state $\mathcal{O}_i(x)|0\rangle$ (source) creating the desired hadron state at $x = (\mathbf{x_0}, t_0)$ from the vacuum $|0\rangle$ and the final state $\mathcal{O}_f(y)|0\rangle$ (sink) annihilating it after some time t at $y = (\mathbf{y}, t)$,

the hadron correlation function is constructed as the expectation value

$$C(x-y) = \langle \mathcal{O}(y)\mathcal{O}^\dagger(x)\rangle. \tag{5.2}$$

An evaluation of this function will give rise to the energy levels corresponding to the eigenstates of $\mathcal{H}$. Due to translational invariance it is an options to choose $(\mathbf{x}_0, t_0) = (\mathbf{0}, 0)$ from here on

$$C(x) = \langle \mathcal{O}(x)\mathcal{O}^\dagger(0)\rangle. \tag{5.3}$$

The Heisenberg operators on a discrete Minkowski space-time with periodic boundary conditions can be written as

$$\mathcal{O}(x) = e^{ip(x-N_t)}\mathcal{O}(0)e^{-ipx} = e^{i\mathcal{H}(t-N_t)+i\mathbf{p}(\mathbf{x}-\mathbf{N}_\sigma)}\mathcal{O}(\mathbf{0},0)e^{-i\mathcal{H}t+i\mathbf{px}}. \tag{5.4}$$

For a discrete lattice extent $N = (\mathbf{N}_\sigma, N_t)$ in spatial and temporal direction, the discrete momentum is given as

$$\mathbf{p} = \frac{2\pi}{\mathcal{N}_\sigma}\mathbf{N}_\sigma, \quad \mathbf{N}_\sigma^i = 0, 1, \ldots, \mathcal{N}_\sigma - 1, i = 1, 2, 3. \tag{5.5}$$

In the following, the associated energy eigenstates to the Hamiltonian $e^{-i\mathcal{H}t}|n\rangle = e^{-iE_nt}|n\rangle$ will be ordered according to $E_0 \leq E_1 \leq E_2 \ldots$ with E_0 the vacuum energy and E_1 the energy state corresponding to the first excited state above the vacuum.
By using Eq. (5.4) in order to rewrite (5.3) and by inserting a complete set of eigenstates $\mathbb{1} = \sum_m |m\rangle\langle m|$ yields the expression

$$\begin{aligned}
C_M(\mathbf{x},t) &= \sum_{n,m}\langle n|\mathcal{O}(\mathbf{x},t)|m\rangle\langle m|\mathcal{O}^\dagger(\mathbf{0},0)|n\rangle \\
&= \sum_{n,m}\langle n|e^{ip(x-N)}\mathcal{O}(0)e^{-ipx}|m\rangle\langle m|\mathcal{O}^\dagger(0)|n\rangle \\
&= \sum_{n,m} e^{ip_n(x-N)}e^{-ip_mx}\langle n|\mathcal{O}(0)|m\rangle\langle m|\mathcal{O}^\dagger(0)|n\rangle \\
&= \sum_n e^{ip_n(x-N)}|\langle 0|\mathcal{O}^\dagger(0)|n\rangle|^2 + \sum_m e^{-ip_mx}|\langle m|\mathcal{O}^\dagger(0)|0\rangle|^2 + \ldots \\
&= \sum_n A_n(x)e^{ip_n(x-N)} + \sum_m A_m(x)e^{-ip_mx} + \ldots
\end{aligned} \tag{5.6}$$

In the last two lines the expectation values are expanded about the vacuum with $p_0 = 0$ [15] which is the reference point of choice such that energies are always measured with respect to the vacuum energy E_0. Furthermore, the abbreviations $A_n(x) = |\langle 0|\mathcal{O}^\dagger(0)|n\rangle|^2$ and $A_m(x) = |\langle m|\mathcal{O}^\dagger(0)|0\rangle|^2$ are used. In general, the amplitudes are related as $A_n(x) = \pm A_m(x)$ if the correlator $C(x)$ is even (odd) in temporal direction [64]. Finally, a Wick rotation is performed to proceed with Euclidean space-time $t \to -i\tau$ and the exponential is split up for

space and time-like momenta $p = (\mathbf{p}, p^\tau)$ such that

$$\begin{aligned} C_E(\mathbf{x},\tau) =& \sum_n A_n e^{\mathcal{H}(\tau-N_\tau)} e^{i\mathbf{p}_n(\mathbf{x}-\mathbf{N}_\sigma)} + \sum_m A_m e^{-\mathcal{H}\tau} e^{i\mathbf{p}_m\mathbf{x}} \\ =& \sum_m A_m e^{i\mathbf{p}_m\mathbf{x}} \left[e^{-E_m(\mathbf{p})\tau} + e^{-E_m(\mathbf{p})(N_\tau-\tau)} \right] \\ =& \sum_m A_m e^{i\mathbf{p}_m\mathbf{x}} \left[e^{-E_m(\mathbf{p})\frac{N_\tau}{2}} 2\cosh\left(E_m(\mathbf{p}) \left(\frac{N_\tau}{2} - \tau \right) \right) \right]. \end{aligned} \tag{5.7}$$

Due to the periodic boundary conditions, the contribution $e^{-E_m(\mathbf{p})(N_\tau-\tau)}$ corresponds to a particle propagating backward in temporal direction.

5.1.1 Zero momentum projection

Typically, when studying correlation functions the interpolating correlators are projected to have a definite momentum. When studying temporal correlators and their associated pole masses the corresponding momentum projection results in the spatial momentum $\mathbf{p} = 0$ to vanish. For spatial correlators the screening masses are obtained from the $\tilde{p} = (p_x, p_y, p_\tau) = 0$ projection [15]. In this case only the p_z component is non-zero. In order to get the correlation function in terms of momentum, a discrete Fourier transformation has to be performed

$$C(\mathbf{p},t)_M = \sum_{\mathbf{x}} e^{-i\mathbf{p}\mathbf{x}} \langle 0|\mathcal{O}(\mathbf{x},t)\mathcal{O}(\mathbf{0},0)^\dagger|0\rangle \tag{5.8}$$

$$\mathcal{O}(\mathbf{x},t) = \frac{1}{N_\sigma^{3/2}} \sum_{\mathbf{p}} e^{i\mathbf{p}\mathbf{x}} \mathcal{O}(\mathbf{p},t), \quad \mathcal{O}^\dagger(\mathbf{x},t) = \frac{1}{N_\sigma^{3/2}} \sum_{\mathbf{p}} e^{-i\mathbf{p}\mathbf{x}} \mathcal{O}^\dagger(\mathbf{p},t), \tag{5.9}$$

where the transformation of the discussed interpolation operators is given in the second line. Taking into account that a complete set of hadronic states reads $|n\rangle\langle n| \equiv \sum_{\mathbf{p}_n} \frac{|n,p\rangle\langle n,p|}{2(2\pi)^3 E_n}$, similar calculations as performed in Eq. (5.6) and Eq. (5.7) result in

$$C(\mathbf{p},\tau) = \sum_m \frac{|\langle m,\mathbf{p}|\mathcal{O}^\dagger(0)|0,\mathbf{0}\rangle|^2}{\mathcal{N}_\sigma^3 2E_m} \; e^{i\mathbf{p}_m\mathbf{x}} \left[e^{-E_m(\mathbf{p})\frac{N_\tau}{2}} 2\cosh\left(E_m(\mathbf{p}) \left(\frac{N_\tau}{2} - \tau \right) \right) \right]. \tag{5.10}$$

In particular, the zero momentum projection results in a simplified expression for the temporal correlator

$$C(\mathbf{p}=0,\tau) = C(\tau) \equiv \sum_m \tilde{A}_m \cosh\left(E_m(\mathbf{p}=\mathbf{0}) \left(\frac{N_\tau}{2} - \tau \right) \right). \tag{5.11}$$

5.1.2 Mass extraction

At finite momentum, correlators are usually noisier [65] and the explicit choice of zero spatial momentum (**p=0**) makes it possible to extract pole masses from the exponential decay of the

correlator due to energy and mass being directly related via the relativistic dispersion relation

$$\begin{aligned} E(\mathbf{p}) =& \sqrt{m_h^2 + \mathbf{p}^2}(1 + \mathcal{O}(\mathbf{p})), \\ E(\mathbf{p} = \mathbf{0}) =& E_h = M_h. \end{aligned} \tag{5.12}$$

Based on Eq. (5.11), a study of the large time behavior of a temporal correlator is beneficial for the mass extraction since

$$\begin{aligned} C(\tau) \overset{N_\tau \to \infty}{=} & \tilde{A}_1 \cosh\left(E_1 \left(\frac{N_\tau}{2} - \tau\right)\right) \left[1 + \frac{\tilde{A}_2}{\tilde{A}_1} \cosh\left((E_2 - E_1)\left(\frac{N_\tau}{2} - \tau\right)\right)\right] \\ = & \ \tilde{A}_1 \cosh\left(E_1 \left(\frac{N_\tau}{2} - \tau\right)\right) \left[1 + \mathcal{O}(\cosh((E_2 - E_1)\ldots))\right]. \end{aligned} \tag{5.13}$$

This means that the pole mass of the ground state can be obtained from the leading order decay of the hadron correlator describing the state of interest. Since Eq. (5.13) only holds in the limit $N_\tau \to \infty$, large temporal lattice extents are necessary in order to obtain a mass plateau corresponding to $E_1 = M_1$ without many excited states tampering the result. In practice, the ground state is often studied by defining the so-called effective mass in a range away from the center $N_\tau/2$, where the cosh-function can be approximated by an exponential [66]

$$\begin{aligned} M_{eff}(\tau) =& N_\tau \log\left(\frac{C(\tau)}{C(\tau + 1/N_\tau)}\right) \equiv N_\tau \log\left(\frac{\sum_n A_n e^{-M_n \tau}}{\sum_n A_n e^{-M_n(\tau + 1/N_\tau)}}\right), \\ \Rightarrow \lim_{N_\tau \to \infty} & \left(N_\tau \log\left(e^{M_1/N_\tau} \underbrace{\frac{1 + \sum_n \frac{A_n}{A_1} e^{-(M_n - M_1)\tau}}{1 + \sum_n \frac{A_n}{A_1} e^{-(M_n - M_1)(\tau + 1/N_\tau)}}}_{=1 + \mathcal{O}(e^{-(M_2 - M_1)\tau})}\right)\right) = M_1. \end{aligned} \tag{5.14}$$

Finally, the fit of a constant to the effective mass gives rise to the ground state. Note that the sum over the excited state $|n\rangle$ consists of all states with the correct quantum numbers, thus, it is possible to also measure decay products instead of the desired quantum state[14].

5.2 Staggered Meson Correlators

So far, only general interpolating operators were considered. In the following, this is specified by incorporating the staggered formalism and by considering mesons only.
The staggered quark fields are introduced in Sec. 1.3.5 for which each flavor comes in a multiplet of four tastes [29]

$$\psi^{\alpha a}(y) = \frac{1}{8} \sum_s \Omega_s^{\alpha a} \chi_{2y+s}, \quad \bar{\psi}^{\alpha a}(y) = \frac{1}{8} \sum_s \Omega_s^{\alpha a} \bar{\chi}_{2y+s}, \tag{5.15}$$

with flavor index f, spinor index $\alpha = 0, \ldots, 3$ and taste index $\beta = 1, \ldots, 4$. In the latter equation it is summed over all sixteen corners of the four dimensional hypercube with origin at $2y$. Moreover, the product of gamma matrices is denoted as

$$\Omega(s) = \gamma_0^{s_0}\gamma_1^{s_1}\gamma_2^{s_2}\gamma_3^{s_3}. \tag{5.16}$$

which follows some useful properties

$$\frac{1}{4}\mathrm{Tr}\left[\Omega^{(s)\dagger}\Omega^{(s')}\right] = \delta_{ss'} \quad \text{and} \quad \frac{1}{4}\sum_s \Omega^{(s)\dagger}_{\alpha a}\Omega^{(s)}_{\beta b} = \delta_{\alpha,a}\delta_{\beta,b}. \tag{5.17}$$

The taste component complicates the construction of staggered interpolating operator since adding only a Dirac spin kernel $\Gamma_D \in (\mathbb{1}, \gamma_5, \gamma_\mu, \gamma_{\mu\nu}, \gamma_{\mu 5})$, with sixteen different choices depending on the particle class, in between two staggered fields $\langle \mathcal{M}(x)\Gamma_D\mathcal{M}^\dagger(0)\rangle$ is not sufficient. Rather staggered bilinears have to be considered with another sixteen taste choices that come with each $q\bar{q}$ pair. Thus, a staggered mesonic interpolating operator $\mathcal{M}_{\text{stagg}}$ is built by a bilinear structure called Dirac-Taste kernel. The final operator reads

$$\begin{aligned}
\mathcal{M}_{\text{stagg}} =& \bar{\psi}(y)\Gamma_H\psi(y) = \bar{\psi}(y)(\Gamma_D^{\alpha\beta}\otimes\Gamma_T^{ab})\psi(y) \\
=& \frac{1}{64}\cdot\sum_{s,s'}\bar{\chi}_{(2y+s)}\Omega^{(s)\dagger}_{a\alpha}(\Gamma_D^{\alpha\beta}\otimes\Gamma_T^{ab})\Omega^{(s')}_{\beta b}\chi_{(2y+s')} \\
=& \frac{1}{64}\cdot\sum_{s,s'}\mathrm{Tr}[\Omega^{(s)\dagger}_{a\alpha}\Gamma_D^{\alpha\beta}\Omega^{(s')}_{\beta b}\Gamma_T^{ab;\dagger}]\bar{\chi}_{(2y+s)}\cdot\chi_{(2y+s')} \\
=& \frac{1}{16}\cdot\sum_{s,s'}\zeta(s,s')\bar{\chi}_{(2y+s)}\cdot\chi_{(2y+s')}
\end{aligned} \tag{5.18}$$

In the last equality, the phase factor $\zeta(s, s')$ is defined as [29]

$$\zeta(s,s') = \frac{1}{4}\mathrm{Tr}[\Omega^{(s)\dagger}_{a\alpha}\Gamma_D^{\alpha\beta}\Omega^{(s')}_{\beta b}\Gamma_T^{ab;\dagger}] \tag{5.19}$$

which encodes all information about the meson particle. The four-vector s labels the 2^4 sites of the hypercube with components $s_\mu \in (0, 1)$. The factor in Eq. (5.19) is typically simplified in order to avoid considering two different spatial locations within the hypercube. Thus, a diagonal Dirac-Taste basis with $\Gamma_D^{\alpha\beta} = \Gamma_T^{ab}$ is chosen, i.e. Dirac spin and Taste are evaluated at the same point within the hypercube which means that local bilinears are studied with a simplified phase

$$\zeta(s,s') = \zeta(s)\cdot\delta_{s,s'}, \quad \text{with} \quad \zeta(s) = \frac{1}{4}\mathrm{Tr}[\Omega^{(s)\dagger}\Gamma_D\Omega^{(s)}\Gamma_T^\dagger]. \tag{5.20}$$

Table 5.1: *List of particle classes with their associated Dirac-Taste basis encoding the quantum numbers of the respective particle as well as the phase factor. Related operators are assumed to be diagonal in their respective basis.*

Particle Class	$\Gamma_H = \Gamma_D \otimes \Gamma_T$	$\zeta(s)$
Scalar (S)	$\mathbb{1} \otimes \mathbb{1}$	1
Pseudo-Scalar (PS)	$\gamma_5 \otimes \gamma_5^*$	$(-1)^{s_1+s_2+s_3+s_0}$
Vector (V)	$\gamma_\mu \otimes \gamma_\mu^*$	$(-1)^{s_\mu}$
Axial-Vector (A)	$(\gamma_\mu\gamma_5) \otimes (\gamma_\mu\gamma_5)^*$	$(-1)^{s_1+s_2+s_3+s_0-s_\mu}$
Tensor (T)	$(\gamma_\mu\gamma_\nu) \otimes (\gamma_\mu\gamma_\nu)^*$	$(-1)^{s_1+s_2+s_3+s_0-s_\mu-s_\nu}$

Hence, the staggered meson operator is given as

$$\mathcal{M}_{\text{stagg}} = \frac{1}{16}\sum_s \zeta(s)\bar{\chi}_{(2y+s)}\chi_{(2y+s)}. \tag{5.21}$$

It is important to keep in mind that studying local correlators is a choice which simplifies the evaluation of the equations above, however, it is not a necessity. In fact, non-local correlators – which connect two different points within the hypercube – have some improved parity properties [15]. For the full taste multiplet both types of operators are required. Nevertheless, within this dissertation the focus is on local operators only.

5.2.1 Staggered Phase Factors

In the following, a calculation of phase factors for the different classes of particles is performed as presented in Tab. 5.1.

The simplest phase factor is derived in case of a **scalar** particle for which $\Gamma_H = \mathbb{1} \otimes \mathbb{1}$. It trivially follows

$$\zeta(s) = \frac{1}{4}\text{Tr}\left[\Omega^{(s)\dagger}\mathbb{1}\Omega^{(s)}\mathbb{1}\right] = 1. \tag{5.22}$$

While no substantial calculation is necessary for scalar particles, for **pseudoscalars** it is helpful to recall $\gamma_5\gamma_\mu = -\gamma_5\gamma_\mu$ which makes the following very simple

$$\begin{aligned}
\zeta(s) =& \frac{1}{4}\text{Tr}\left[\Omega^{(s)\dagger}\gamma_5\Omega^{(s)}\gamma_5\right] \\
=& \frac{1}{4}\text{Tr}\left[\Omega^{(s)\dagger}\left(\gamma_5\right)\left(\gamma_1^{(s_1)}\gamma_2^{(s_2)}\gamma_3^{(s_3)}\gamma_0^{(\tau)}\right)\gamma_5^\dagger\right] \\
=& \frac{1}{4}\text{Tr}\left[\Omega^{(s)\dagger}\Omega^{(s)}(-1)^{s_1+s_2+s_3+\tau}(\gamma_5)^2\right] \\
=& (-1)^{s_1+s_2+s_3+\tau}.
\end{aligned} \tag{5.23}$$

When particles transforming as **axialvectors** are studied, the Dirac-Taste structure of $\Gamma_H =$

Table 5.2: *Mesonic operators for staggered fermions that are diagonal in the spin-taste basis $\Gamma^D \otimes \Gamma^T$ and the corresponding physical states. The oscillating and Non-Oscillating channels corresponding to the same $\zeta(s)$ are distinguished. The J^{PC} representation is discussed in Appendix* (C)

$\zeta(s)$	$\Gamma_D \otimes \Gamma_T$		J^{PC}		Physical states	
	NO	O	NO	O	NO	O
1	$\mathbb{1} \otimes \mathbb{1}$	$\gamma_0\gamma_5 \otimes (\gamma_0\gamma_5)^*$	0^{++}	0^{-+}	σ_S	π_A
$(-1)^{s_i}$	$\gamma_i\gamma_5 \otimes (\gamma_i\gamma_5)^*$	$\gamma_i\gamma_0 \otimes (\gamma_i\gamma_0)^*$	1^{++}	1^{--}	a_A	ρ_T
$(-1)^{s_j+s_k}$	$\gamma_j\gamma_k \otimes (\gamma_j\gamma_k)^*$	$\gamma_i \otimes \gamma_i^*$	1^{+-}	1^{--}	b_T	ρ_V
$(-1)^{s_i+s_j+s_k}$	$\gamma_0 \otimes \gamma_0^*$	$\gamma_5 \otimes (\gamma_5)^*$	0^{+-}	0^{-+}	$-_V$	π_{PS}

$(\gamma_\mu\gamma_5) \otimes (\gamma_\mu\gamma_5)$ has to be taken into account. It follows

$$\begin{aligned}\zeta(s) =& \frac{1}{4}\mathrm{Tr}\left[\Omega^{(s)\dagger}\Omega^{(s)}(-1)^{s_1+s_2+s_3}(-1)^{s_1+s_2+s_3+\tau}(\gamma_0)^2(\gamma_5)^2\right] \\ =& (-1)^{s_\mu}.\end{aligned} \tag{5.24}$$

where the simplification $(-1)^{s_1+s_2+s_3}(-1)^{s_1+s_2+s_3+\tau} = (-1)^{2s_1+2s_2+2s_3+\tau} = (-1)^\tau$ is applied. In an analogous calculation it can be shown that for $\Gamma_H = (\gamma_i\gamma_5) \otimes (\gamma_i\gamma_5)^*$ it follows that $\zeta(s) = (-1)^{s_i}$. For **vector** and **tensor**-class particles the respective factors are listed in Tab. 5.1.

5.2.2 Staggered Correlation Function

Based on Eq. (5.21) with phase factors from Sec. 5.2.1, the formulation for local staggered meson operators yields the temporal staggered correlation function [29]

$$C_{\mathrm{stagg}}(2\tau) = -\frac{1}{16^2}\sum_y \sum_{s,s'} \zeta(s,s')\langle\bar{\chi}(2y+s)\chi(2y+s)\bar{\chi}(s')\chi(s')\rangle. \tag{5.25}$$

This correlation function is local in space, but occupies two adjacent time slices. It is far more practical to restrict to single-time-slice operators when studying the temporal decay of correlation functions.

In order to achieve that, it can be enforced that the Dirac-Taste bilinear is replaced as [29]

$$\Gamma_D \otimes \Gamma_T \to \Gamma_D \otimes \Gamma_T \pm \Gamma_D\gamma_0\gamma_5 \otimes (\Gamma_T\gamma_0\gamma_5)^*. \tag{5.26}$$

The plus-minus sign cancels one of the two time slice contributions – either the $s_0 = 0$ or $s_0 = 1$ – inside the hypercube and the correlation function is independent of the choice of the temporal location [29]. Furthermore, this leads also to a modification of the phase factor

according to

$$\zeta(s) \to \zeta(s)(1 \pm (-1)^\tau) \tag{5.27}$$

because according to Eq. (5.24) the associated phase of $\gamma_0\gamma_5$ is $(-1)^\tau$. The change in kernel introduces a new contribution, an oscillating state which is measured alongside with the current Non-Oscillating state. It has opposite spin, parity and taste content. Thus, this oscillating state is called the **parity partner**. Fixed to a single time slice it is not possible for the staggered correlator to exhibit the full parity properties, thus, it is parity degenerated. Finally, the incorporation of the new finding leads to the staggered correlation function fit ansatz

$$\begin{aligned} C(\mathbf{p},\tau) = &\sum_n A_{NO,n}(\mathbf{p}) \cosh[E_{NO,n}(\mathbf{p})(N_\tau/2-\tau)] \\ &\pm(-1)^\tau \sum_n A_{O,n}(\mathbf{p}) \cosh[E_{O,n}(\mathbf{p})(N_\tau/2-\tau)]. \end{aligned} \tag{5.28}$$

Since calculations are performed on a discrete lattice the oscillating prefactor is typically expressed as $(-1)^\tau = \cos(\pi\tau)$. In Tab. 5.2 all states measured by the worm algorithm are summarized. All states within a single line are measured simultaneously. As discussed in [29] there is no parity partner for the single time slice correlator of the Goldstone pion constructed by $\gamma_5 \otimes \gamma_5 \pm \gamma_0 \otimes \gamma_0$. The reason is that for degenerate quark masses $\gamma_0 \otimes \gamma_0$ is the density for a conserved charge and in case of the zero momentum projection $\mathbf{p} = 0$, it is the charge itself which does not excite states from the vacuum, thus there is no parity partner [29].

5.3 Discrete Time Mesonic Correlators

When measuring histograms in discrete time, the substantial difference to continuous time calculations is the fixed discretization in temporal direction. The finite temporal lattice extent N_τ determines the fineness of the discretization. For a $N_\sigma^3 \times N_\tau$ lattice the correlator can be symmetrized due to the axial-symmetry of the cosh-function. Hence, it is feasible to construct histograms with just $N_\tau/2 + 1$ entries.

Discrete time histogram data are fitted according to Eq. (5.28), where the sign in between the taste partners is chosen such that the amplitude is positive. For a first qualitative analysis of a temporal correlator, a simple four-parameter fit-ansatz is sufficient

$$\begin{aligned} C_{\mathrm{DT}}(\tau) &= C_{\mathrm{NO}}(\tau) - (-1)^\tau C_{\mathrm{O}}(\tau) \\ &= A_{\mathrm{NO}} \cosh[a_\tau M_{\mathrm{NO}}(N_\tau/2-\tau)] - (-1)^\tau A_{\mathrm{O}} \cosh[a_\tau M_{\mathrm{O}}(N_\tau/2-\tau)]. \end{aligned} \tag{5.29}$$

The energy is already substituted by the corresponding mass measured in DT as $a_\tau M$. In Sec. 5.5 excited states are accounted and a systematic approach is presented to choose the

most reasonable number of states.

A fit according to Eq. (5.29) describes the complete data set at once (see Fig. 5.1). However, due to its oscillating prefactor $(-1)^\tau = \cos(\pi\tau)$ it is challenging to choose first estimates of the parameters such that the fit converges. Therefore, it is helpful to notice that the contributions to the histograms for even τ can be fitted separately from the odd part:

$$\begin{aligned} C_{\mathrm{Even}}(\tau) =& C_{\mathrm{NO}}(\tau) - C_{\mathrm{O}}(\tau) \\ =& A_{\mathrm{NO}} \cosh[a_\tau M_{\mathrm{NO}}(N_\tau/2-\tau)] - A_{\mathrm{O}} \cosh[a_\tau M_{\mathrm{O}}(N_\tau/2-\tau)] \\ C_{\mathrm{Odd}}(\tau) =& C_{\mathrm{NO}}(\tau) + C_{\mathrm{O}}(\tau) \\ =& A_{\mathrm{NO}} \cosh[a_\tau M_{\mathrm{NO}}((N_\tau/2-\tau)] + A_{\mathrm{O}} \cosh[a_\tau M_{\mathrm{O}}(N_\tau/2-\tau)]. \end{aligned} \tag{5.30}$$

The oscillating factor vanishes trivially since for even sites $(-1)^{\tau_{\mathrm{Even}}} = (-1)^{2\tilde{\tau}} = +1$ and for the histogram data at odd τ the sign is opposite $(-1)^{\tau_{\mathrm{Odd}}} = (-1)^{2\tilde{\tau}+1} = -1$. This means that the pole masses for the Non-Oscillating and Oscillating contribution can be measured by either performing a fit according to Eq. (5.29) with an oscillating prefactor, or according to Eq. (5.30). The latter ansatz avoids the prefactor $\cos(\pi\tau)$. It is sufficient to perform the fit for either the even or the odd data set and reconstruct the respective other. Note that a four-parameter fit is required either way. However, the fit-ansatz according to Eq. (5.29) contains twice the data points and should therefore yield better accuracy.

Finally, the correlators corresponding to the Non-Oscillating and the Oscillating state can be formulated as

$$\begin{aligned} C^{\mathrm{DT}}_{\mathrm{NO}}(\tau) =& A_{\mathrm{NO}} \cosh(a_\tau M_{\mathrm{NO}}(N_\tau/2-\tau)) = \frac{1}{2}(C_{\mathrm{Even}}(\tau) + C_{\mathrm{Odd}}(\tau)), \\ C^{\mathrm{DT}}_{\mathrm{O}}(\tau) =& A_{\mathrm{O}} \cosh(a_\tau M_{\mathrm{O}}(N_\tau/2-\tau)) \quad = \frac{1}{2}(C_{\mathrm{Even}}(\tau) - C_{\mathrm{Odd}}(\tau)). \end{aligned} \tag{5.31}$$

These correlators can only be constructed based on a simultaneous fit of the data set according to Eq. (5.29) or Eq. (5.30). This construction is summarized in Fig. 5.1. The correlator for the Oscillating channel can only be reasonably depicted in case the data set is shifted to be located at around zero, as the magnitude of $C_{\mathrm{O}}(\tau)$ is given by the difference of $C_{\mathrm{Even}}(\tau)$ and $C_{\mathrm{Odd}}(\tau)$. In contrast, by definition $C_{\mathrm{NO}}(\tau)$ is positioned in between the even and odd correlator data.

For temperatures below T_c the spatial dimer emission and thus, also the worm length is large. Due to the tight connection between chiral susceptibility and temporal correlators (cf. Eq. (4.10)), the amplitude of correlators associated with the phase factor $\zeta(s) = 1 = (-1)^{s_1+s_2+s_3+\tau}$ increases with decreasing temperature and vice versa (cf. Fig. 5.2).

Discrete time calculations have to be performed for multiple temporal discretizations N_τ's. At fixed temperature $T = 0.35\,T_c$ several correlators are constructed with increasing temporal extent and for various channels according to Tab. 5.1. A temperature far below T_c is

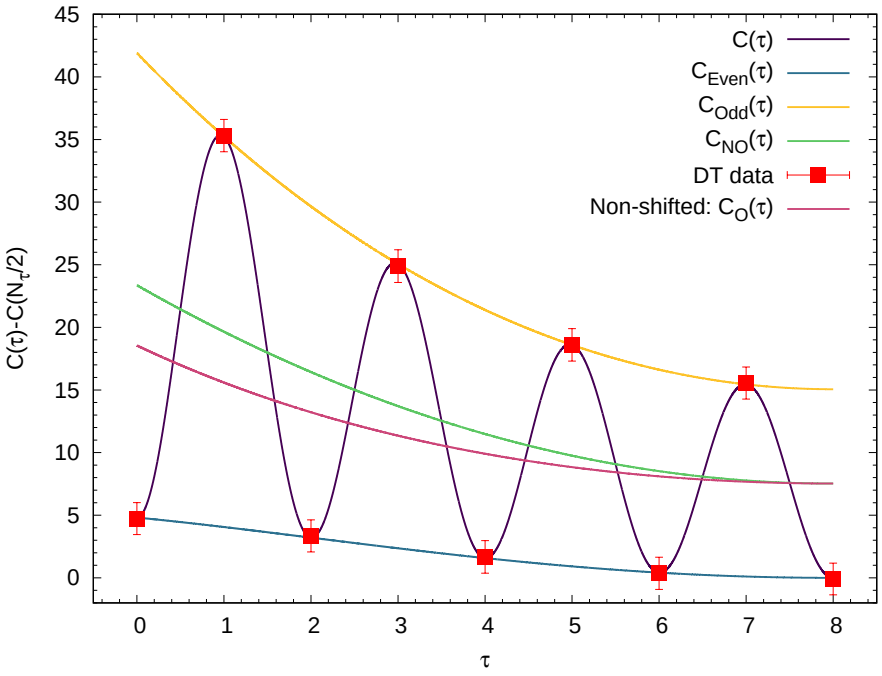

Figure 5.1: *Discrete time histogram data for a $N_\sigma^3 \times N_\tau = 4^3 \times 16$ lattice. The data set is shifted to agree with zero at $N_\tau/2$. $C(\tau)$ is extracted from the full Oscillating data fit, while $C_{Even}(\tau)$ and $C_{Odd}(\tau)$ are fitted separately to the respective data set. $C_{NO}(\tau)$ and $C_O(\tau)$ are the resulting constructed correlators.*

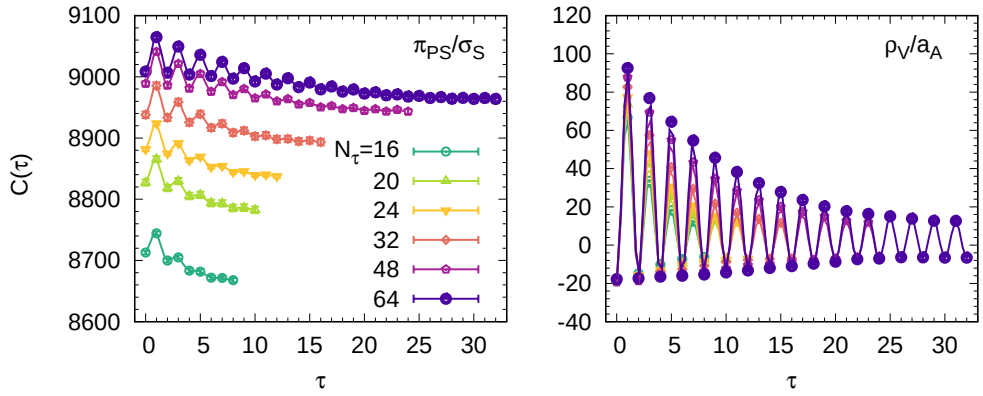

Figure 5.2: *Temporal Correlators for two different channels π_{PS}/σ_S and ρ_V/a_A at a fixed temperature of $T = 0.35\,T_c$ and various $N_\tau \in (16, \ldots, 64)$.*

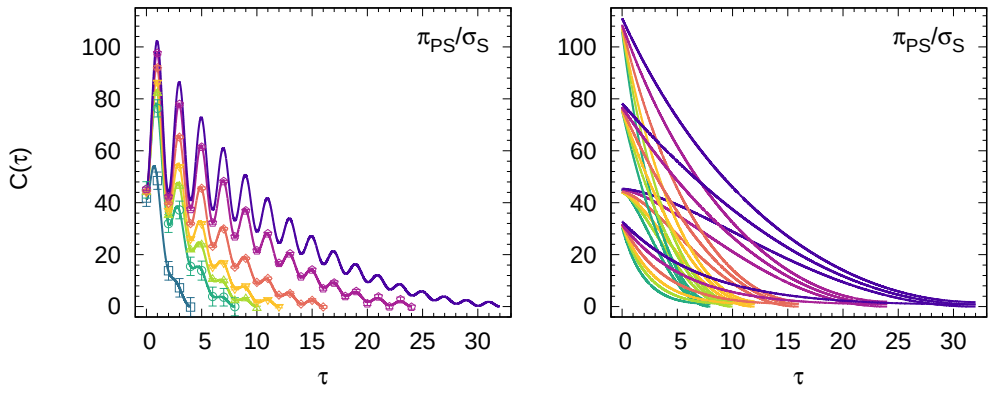

Figure 5.3: *Temporal correlator fits for the π_{PS}/σ_S channel. The fits are shifted such that the $N_\tau/2$ data point coincides with 0.* ***Left:*** *A simultaneous fit of the even and odd histogram data points.* ***Right:*** *Individual fits of even and odd histogram data as well as the reconstructed Non-Oscillating and oscillating correlators.*

chosen to distinguish between the different correlators without much overlap. In Fig. 5.2:Left such correlators are depicted corresponding to the channel π_{PS}/σ_S. With increasing N_τ the worm length and therefore, the correlator value increases. However, this effect becomes less prominent for larger temporal extents. On the other side, temporal correlators associated with the channel ρ_V/a_A (cf. Fig. 5.2:Right), corresponding to $\zeta(s) = (-1)^{s_i} = (-1)^{s_j+s_k+\tau}$, are funnel-shaped by showing a maximum width at $\tau = 0$ and are damped in amplitude as τ gets larger. For small N_τ the drop is more intense.

Again, further interesting features are observed by shifting the correlators by $C(N_\tau/2)$ as shown in Fig. 5.3. All correlators $C(\tau)$ coincide at the point $\tau = 0$ which lies necessarily on $C_{\text{Even}}(\tau)$ (cf. Fig. 5.3:Left). The oscillation covers a larger range as N_τ is increased and there are no intersection points between correlators at all. Finally, for the same channel the different correlators $C_{\text{Even}}(\tau), C_{\text{Odd}}(\tau)$, $C_{\text{NO}}(\tau)$ as well as $C_{\text{O}}(\tau)$ start each at the same position for $\tau = 0$ and merge as τ is increased (cf. Fig. 5.3:Right).

5.4 Continuous Time Meson Correlators

In the following, temporal correlators are constructed from histograms obtained by performing computations with a continuous time worm algorithm. In contrast to the discrete time analysis, there is no alternating structure since the continuous time histograms are continuously incremented during the Poisson process. Thus, the histogram data yield immediately the Non-Oscillating and Oscillating part of the full correlator such that a single two parameter fit is sufficient to extract the ground state of the corresponding particle. Nevertheless, the even and odd histogram structure is also recovered in continuous time. However, note that it is not related to the artificial discretization which is necessarily introduced in CT to store the

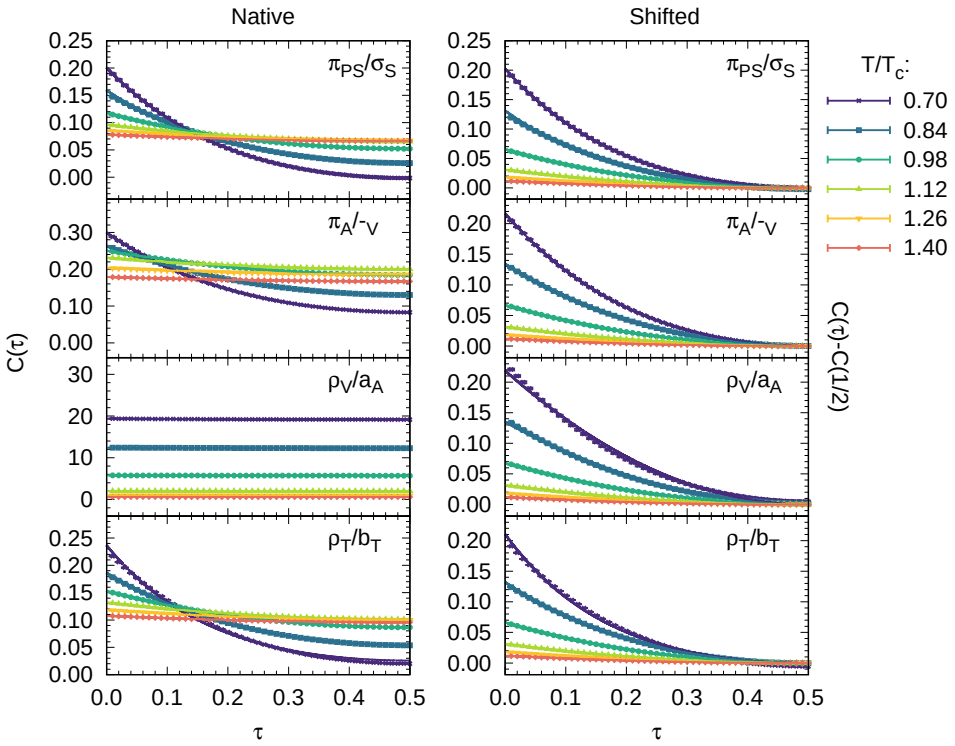

Figure 5.4: *Continuous time correlators for various channels covering a broad temperature range around $a\mathcal{T}_c = 1.4276(2)$. All correlators are fitted with a 4-parameter ansatz.* ***Left:*** *"Native" correlators as directly extracted from the incremented histograms.* ***Right:*** *Correlators shifted to match $C(1/2) = 0$.*

results. An even (odd) histogram is continuously incremented whenever the worm Head and Tail have an odd (even) spatial separation and an opposite parity. Thus, if Head and Tail have matching parities, there will be no contribution to the even histogram and vice versa.

The Non-Oscillating and Oscillating meson correlators are obtained in CT via

$$\begin{aligned} C_{\mathrm{NO}}^{\mathrm{CT}}(\tau) = A_{\mathrm{NO}} \cosh(M_{\mathrm{NO}}/T(\tau - 1/2)) &= \frac{1}{2}\left(C_{\mathrm{Odd}}\,(\tau) + C_{\mathrm{Even}}(\tau)\right), \\ C_{\mathrm{O}}^{\mathrm{CT}}(\tau) = A_{\mathrm{O}} \cosh(M_{\mathrm{O}}/T(\tau - 1/2)) &= \frac{1}{2}\left(C_{\mathrm{Odd}}(\tau) - C_{\mathrm{Even}}(\tau)\right). \end{aligned} \tag{5.32}$$

The temporal correlators constructed by the even and odd histogram contributions are depicted in Fig. 5.4. Each subplot contains correlators measured at temperatures covering a range around T_c. As the temperature is increased the curves show a successively softer falloff. For different channels the correlators are scattered around different ranges (cf. Fig. 5.4:Left) while the overall shape of the correlation functions is very similar independently of the associated channel (see Fig. 5.4:Right).

5.5 Pole Masses from Correlated Fits

The previous two sections offered a formulation of temporal correlators in DT and CT. The fits performed on the data assumed a single ground state for the respective taste partners excluding any excited states. Discrete time correlator data exhibit large scale oscillations (see Fig. 5.1 or 5.2) such that the Non-Oscillating and Oscillating contributions can't be addressed individually. A combined four parameter fit is required according to Eq. (5.29) or (5.30). On the contrary, continuous time correlators show no oscillations since the averaging of even and odd site contributions is necessarily incorporated in a CT algorithm. The correlators for the taste partners can be addressed individually and are reasonably good described by a two-parameter fit. This corresponds to a ground state fit of either the Non-Oscillating or Oscillating channel.

These approaches already yield promising results and follow the data even at short distances. Nevertheless, it is of high interest to include additional states. These will separate the ground state signal from the leading order excited contributions. However, by involving more states into the fit makes it highly dependent on the initial guess which is necessary in order to stabilize it, and will most likely increase the error on the individual results (cf. Fig. 5.6). Thus, a good balance between number of states and reasonable signal is of crucial importance.

To account for correlated data sets is one main challenge when dealing with correlators in lattice calculations. These data sets carry less information compared to uncorrelated data. Correlations between neighboring lattice points necessarily arise because the worm performs local updates. During these elementary worm steps histograms are accumulated such that correlations arise. Latter can be minimized by performing many global updates. A measure for the correlation of data is the autocorrelation time which can be obtained from Eq. (1.87) as the largest τ_i in the series of exponentials [14]

$$\frac{C_{\mathcal{O}}(t)}{C_{\mathcal{O}}(0)} \sim \sum_i A_i e^{-t/\tau_i}. \tag{5.33}$$

Mesonic correlators are specifically affected by correlations since they are evaluated typically along some lattice axis. For temporal correlators it is the time direction where neighboring points are correlated and this also affects successive histogram entries. Typically, the statistical errors of such observables are underestimated by not compensating for the lack of information. Therefore, correlated fits are performed in order to get a reasonable error handling and to choose the number of states involved in the fit.

For the pole mass extraction, a fitting routine is used which is described in detail in [14]. Within this work a concise overview of the main features is given.

5.5.1 Construct estimators

When fitting a data set X, it is of interest to study functions of some form $f(X, \theta)$ that approximate the data obtained from measurement best. The parameter θ is unknown. It is adjusted according to some methods such as the maximum likelihood method or the least squares method. These try to approximate the real value θ_0.
For a correlated data set the χ-squared to be minimized reads [14, 51]

$$\chi^2 = \sum_{i,j=1}^{N} \left(\frac{\bar{y}_i - f(\theta, x_i)}{\sigma_i} \right) (X)^{-1}_{ij} \left(\frac{\bar{y}_j - f(\theta, x_j)}{\sigma_j} \right) \tag{5.34}$$

$$\hat{L}(\theta) = \frac{1}{(2\pi)^{N/2}\sqrt{\det C}} \exp\left(-\frac{1}{2}\chi^2 \right), \tag{5.35}$$

with the definition of the likelihood function $\hat{L}$ in the second line. The main effort is encoded in the calculation and inversion of the correlation matrix X which is defined as

$$X_{ij} = \frac{C_{ij}}{\sigma_i \sigma_j}, \quad \text{with } C_{ij} = \frac{1}{N-1} \sum_{k=0}^{N} (y_{i,k} - \bar{y}_i)(y_{j,k} - \bar{y}_j). \tag{5.36}$$

Here, the covariance matrix with its elements C_{ij} is introduced. It contains information on how two quantities i and j fluctuate together with respect to their individual mean values. In fact, the correlation matrix is used which binds all entries to $X_{ij} \in$ `[-1:1]` [51] and reduces the condition number such that the matrix is expected to be less singular [14].
Several minimization algorithms are applied and the fit parameters are taken from the algorithm yielding the smallest χ^2. The covariance matrix for the errors of the fit parameters can be directly calculated from the errors of the data set [14]. Here, underestimated errors by not accounting for the quality of the fit are compensated for by multiplying the error with $\frac{\chi^2}{\text{d.o.f.}}$.

5.5.2 Multiple State Fits

The whole fitting procedure is more involved and requires several steps in order to assure the best possible outcome even when including excited states.
Each correlator corresponds to a certain channel and its taste partner. The selected bare correlator data are fitted according to the number of Non-Oscillating (*--nstates*) and Oscillating states (*--nstates-osc*) specified when calling the fitting program `./corrfitter.py` [14]

```
1 ./corrfitter.py $out -Nt $nt --nstates $nsN0 --nstates-osc $ns0 --
     corr --folder $write
```

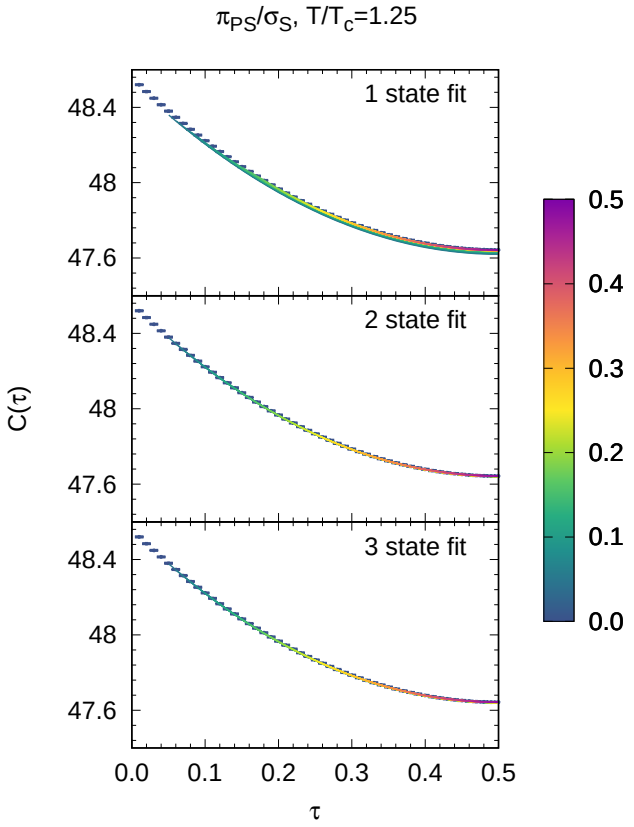

Figure 5.5: *Different multiple-state fits are performed on the same CT correlator at a temperature slightly above T_c and for the Goldstone pion channel π_{PS}. The color coding signals the value of the lower fit boundary. The blueish color tones correspond to fits on large intervals. Along the color spectrum the fit intervals are chosen smaller, with the smallest intervals associated with the color purple.*

which is discussed in detail in [14]. The option *--corr* ensures that **correlated fits** are performed. If the fit interval is not constraint, the fits are performed on all successive intervals

$$[1 : N_\tau/2], [2 : N_\tau/2], \ldots, [N_\tau/2 - P, N_\tau/2] \tag{5.37}$$

with P being the number of fit parameters (see Fig. 5.5). By changing only the lower bound but keeping the upper fixed at $N_\tau/2$ can improve on the quality of the correlation matrix. Even though the fits in Fig. 5.5 do not show a large impact by including additional states, the obtained ground state masses can change drastically (see Fig. 5.6). By including too many states the precision on all present states can get lost. It is simply not possible for the algorithm to estimate good start parameters for all fit parameters and thus, inaccuracy in some parameters have to be absorbed by others, thus, resulting in an overall loss in precision.

In order to assure a good choice of initial parameters, the following sequence of steps is

Table 5.3: *Different combinations of Non-Oscillating (NO) and Oscillating (O) states included in a correlator fit for DT as well as CT data sets. In DT simultaneous fits are required with contributions in both channels. In CT the considered states are either fully associated with the Non-Oscillating part or with the Oscillating part.*

DT:	NO	O
	1	{1,2,3}
	2	{1,2,3}
	3	{1,2,3}

CT:	NO	O
	{1,2,3}	0
	0	{1,2,3}

performed [14]:

1. Choose a small fit interval, roughly half of the correlator. Perform a one state fit on the even and odd sites separately to obtain the parameter sets $(A_{\mathrm{Even}}, M_{\mathrm{Even}})$ and $(A_{\mathrm{Odd}}, M_{\mathrm{Odd}})$ respectively.

2. Calculate initial parameters for the combined fit via $A_{\mathrm{NO},1} = (A_{\mathrm{Even}} + A_{\mathrm{Odd}})/2, A_{\mathrm{O},1} = (A_{\mathrm{Even}} - A_{\mathrm{Odd}})/2$ and $M_{\mathrm{NO},1} = M_{\mathrm{O},1} = (M_{\mathrm{Even}} + M_{\mathrm{Odd}})/2$.

3. Perform a full one state fit, i.e. with a single Non-Oscillating and Oscillating part according to Eq. (5.29).

4. Increase the fit interval. Introduce the next excited state in either the Even or Odd channel. Guess its initial mass by choosing arbitrarily $M_{\mathrm{Even,Odd}} = 5/4 \cdot M_{\mathrm{NO/O},1}$. Set the amplitude $A_{\mathrm{NO/O},2}$ to agree with the first point of the correlator within the fit interval.

5. Perform a fit including the higher states introduced so far. Parameters from *steps 3* and *4* are taken as initial guess.

6. Repeat *steps 4* and *5* until the desired number of states is included.

Note that *steps 1 and 2* correspond to the relations specified in Equations (5.31) and (5.32). The presented sequence of steps is good for noisy data sets. However, in principal it is of course possible to implement and try many variations of such a procedure and choose the one with the smallest χ^2 [14].

5.5.3 Mass plateau

For each possible fit range $n_\tau \in [1 : N_\tau/2 - P]$ various multiple state fits are performed. All combinations of states are listed in Tab. 5.3.
There are a couple of reasons why to include excited states in a correlator fit. Some fits might be spoiled by contributions from excited states as the total number of included fit-states is not sufficient, while others are bothered by larger errors due to overfitting. The notorious task

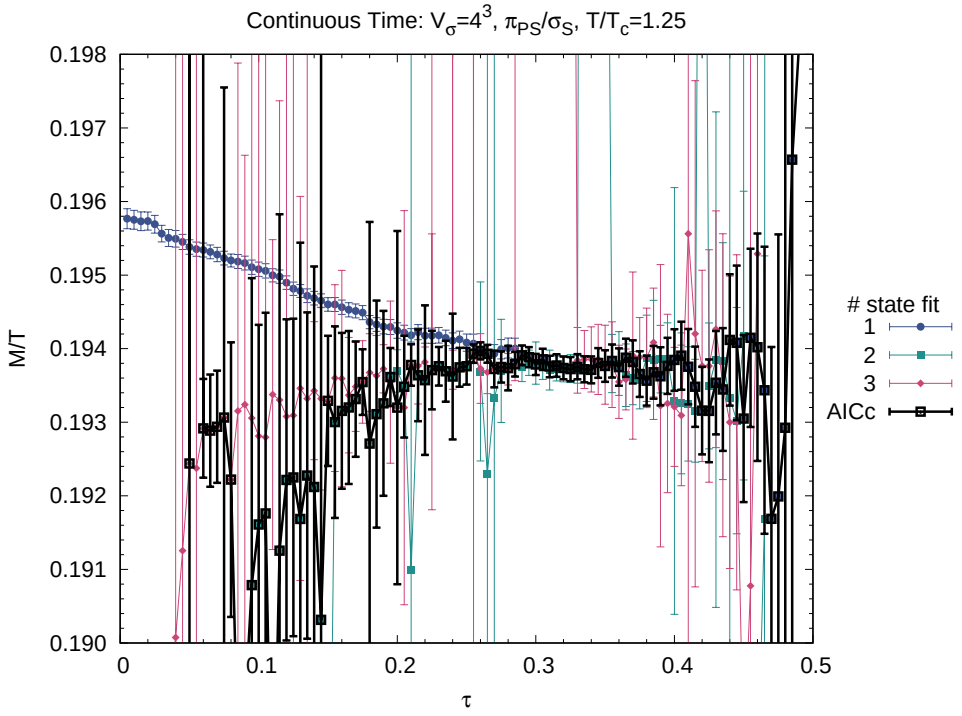

Figure 5.6: *Masses from continuous time mesonic correlators on a 4^3 volume. Various multi-state fits are used and a single value per τ is selected by AICc. The one state fit is dominant at large τ while the two and three state fits are preferred by the AICc at small τ.*

is to select the appropriate number of states for each fit-range. Here, the *Aikaike Information criterion* (AIC) is applied to find the balance between number of states and error. In fact, a modified version of the criterion is used, the *corrected* AIC (AICc) [67]

$$AICc = \underbrace{2P - \ln\left(\hat{L}\right)}_{\text{AIC}} + \frac{2P^2 + 2P}{N - P - 1} \tag{5.38}$$

with P the number of parameters, N the number of points within an interval and $\hat{L}$ the likelihood function as defined in Eq. (5.35). The corrected version of the AIC accounts for effects of overfitting whenever the number of fitted parameters P is a large fraction of the sample size N [67]. In the end, the smallest AICc value decides which fit values are considered for the determination of the mass plateau.

In order to obtain the meson pole mass for the considered channel, an averaging over the region of constant mass is performed. Since the masses are all extracted from fits based on the data set, it is not possible to choose standard statistical methods to evaluate the final values. By calling the `./find_plateau.py` function

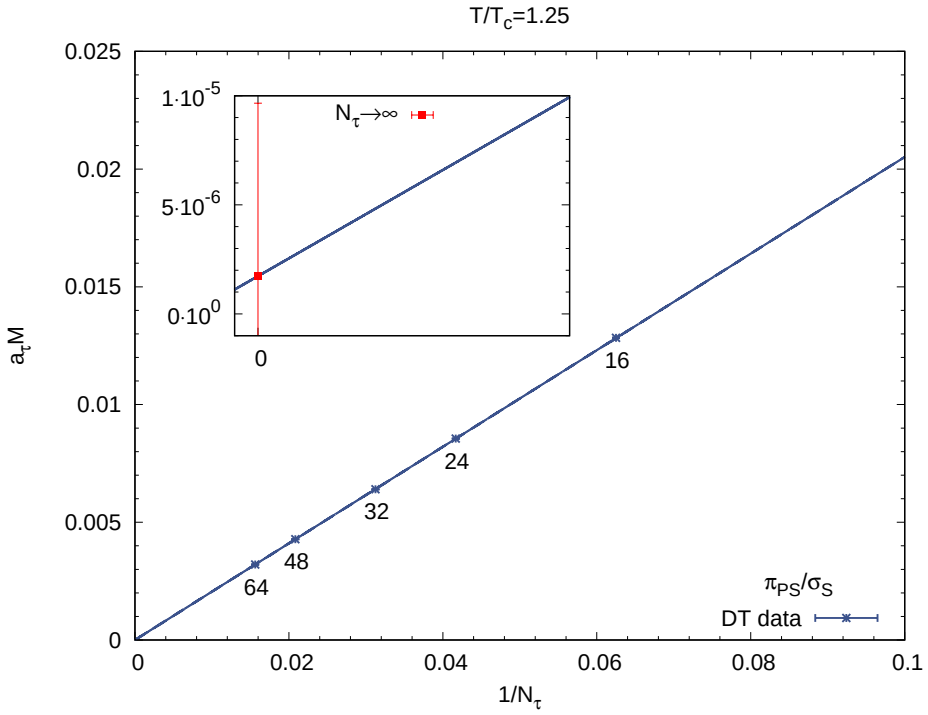

Figure 5.7: *Meson correlator masses obtained from discrete time simulations on $4^3 \times N_\tau$ lattices with $N_\tau = 16, 24, 32, 48, 64$. Since a_τ vanishes in the CT limit, so does $a_\tau M$. The extrapolation agrees with zero within errors.*

```
1 ./find_plateau.py $massFile
```

a Gaussian bootstrap method is used where the median will correspond to the final value and its error is estimates as the 68% percentile around the median [14].

5.5.4 Pole Masses from Discrete Time

For temporal correlator measurements in discrete time the binning is fixed by the number of sites in temporal direction N_τ. Simulations performed at various values of N_τ are required to extrapolate towards continuous time. The number of states considered for the fits are listed in Tab. 5.3. The meson correlator masses are measured as $a_\tau M$ which is reflected in the weaker decay as N_τ is increased (see Fig. 5.2). In the continuous time limit the quantity $a_\tau M$ has to vanish (cf. Fig. 5.7) because the lattice spacing $a_\tau \to 0$ vanishes and is not defined anymore. However, CT simulations yield finite masses which cannot match with discrete time results as these all extrapolate to zero. Since the temperature is the only parameter left, it follows that CT masses are measured as ratios M/T (cf. Eq. (5.32)). Thus, also discrete time masses

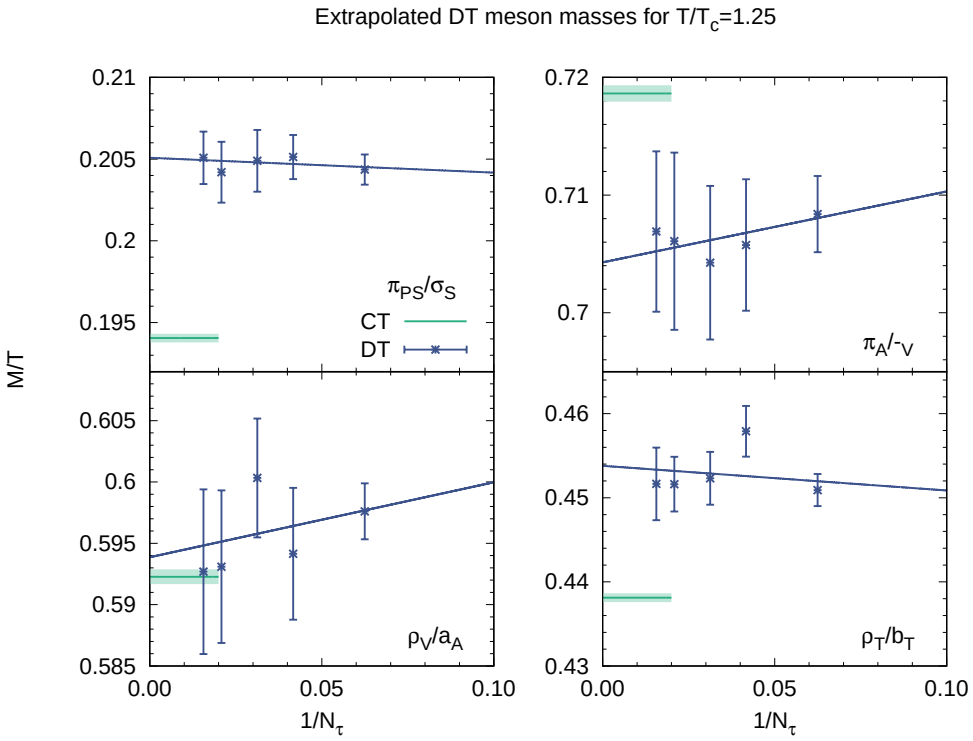

Figure 5.8: *Comparison of meson masses extracted from CT and DT worm simulations for three different channels and a fixed temperature of* $1.25\,T_c$*. The DT results at finite* N_τ *are extrapolated to compare with CT. All masses are located within the same* 5% *window.*

have to be measured accordingly (see Fig. 5.8) by the following conversion rule

$$M/T = N_\tau a_\tau M \tag{5.39}$$

$$aM = \kappa_{\mathcal{d}\mathcal{T}} M/T. \tag{5.40}$$

A comparison between mesonic correlator masses from extrapolated DT simulations as well as direct CT simulations shows a 5% discrepancy for the first two and the fourth channel (cf. Fig. 5.8). For the third channel the results match within errors. In fact, it cannot be expected for the results to coincide due to a variety of factors:

- It is necessary to have a large temporal extent to extract pole masses. This requirement is difficult to meet due to the computational effort with larger values of N_τ and the computational cost of many simulations at various N_τ. As an example, the $N_\tau = 16$ correlator is symmetrized and the lowest state fit contains four fit parameters in total. Thus, the mass plateau contains $8 - 4 = 4$ values only.

- A discrete time correlator encodes both, information on the Non-Oscillating and Oscillating channel. An averaging is required to reconstruct the respective correlator.

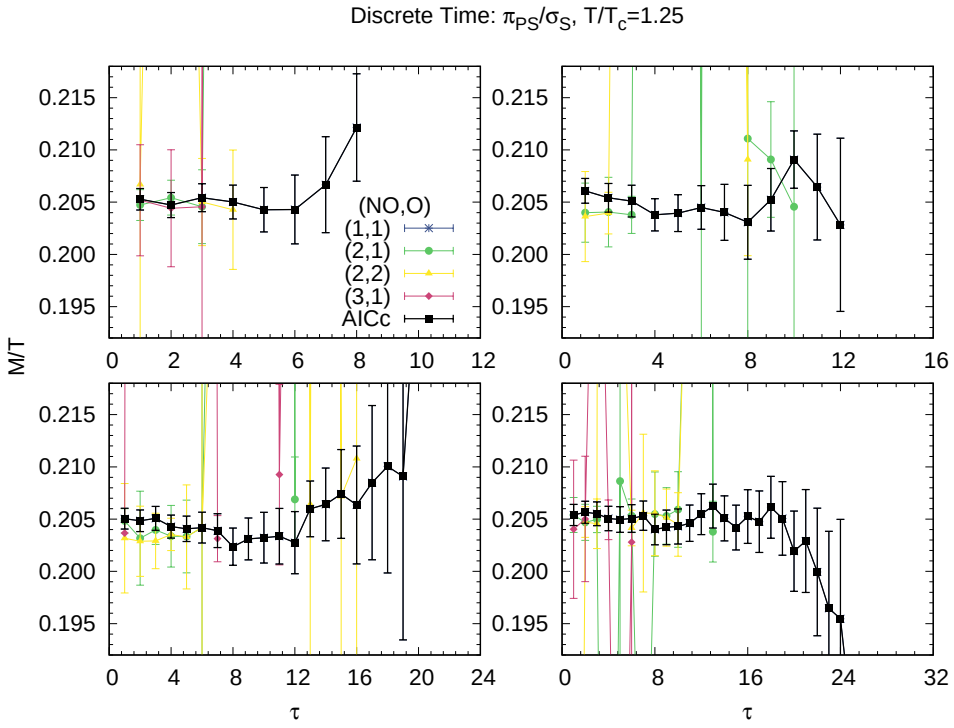

Figure 5.9: *Masses from discrete time mesonic correlators on a $4^3 \times CT$ volume for different temporal extents $N_\tau = 24, 32, 48, 64$. The correlators are symmetrized, thus, covering maximally half the range minus the number of fit parameters. Fits with contributions in both, Non-Oscillating and Oscillating channel (NO, O) have to be considered.*

This averaging yields better results for large N_τ. In CT the "added" correlator data yield the Non-Oscillating channel while the subtracted data give rise to the Oscillating contribution. The averaging is already incorporated in the algorithm such that the respective channels can be fitted independently.

Both points are stressed when studying the location of the mass plateau. In DT the plateau is located at short distances where excited states contribute the most (cf. Fig. 5.9). Lattices with a larger temporal extent N_τ have to be studied in order to improve on the averaging which should result in a shift of the mass plateau. In contrast, in CT the mass plateau is commonly positioned at intermediate or large distances (see Fig. 5.6).

5.5.5 Pole Masses from Continuous Time

As motivated in the previous section, meson masses are studied in CT for various kernels, temperatures and volumes. A first analysis is performed at zero chemical potential (see Fig. 5.10). Each degenerate pair leads to meson masses that are clearly distinguishable in magnitude from the other pairs for temperatures below and around T_c. The largest masses

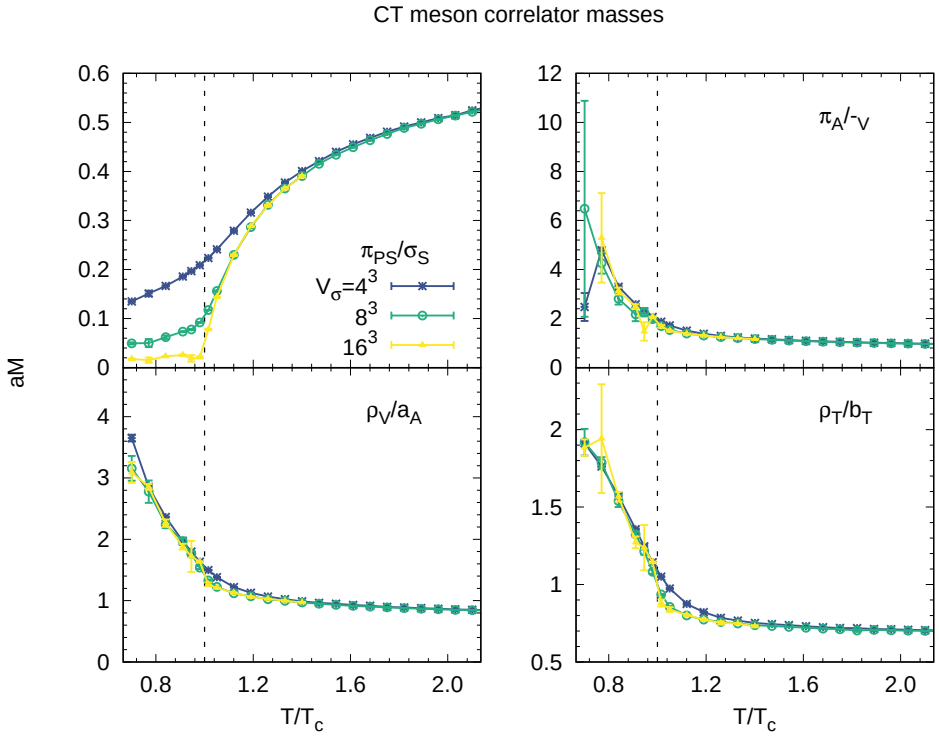

Figure 5.10: *Meson masses measured in CT for four different degenerated meson operators, three different volumes $V_\sigma = 4^3, 8^3, 16^3$ at zero baryon chemical potential.*

are obtained for the $\pi_A/-_V$ pair while by far the lowest masses are measured for the π_{PS}/σ_S kernel. Three meson operators show a similar temperature and volume dependence and it is the Goldstone pion channel which has a significantly different behavior. Below T_c the mass $M_{\pi_{PS}}/T$ decreases as the volume is increased. In fact, it is expected that the Goldstone pion mass is zero in the continuum limit at small temperatures due to spontaneous symmetry breaking and suddenly obtains a finite mass when crossing T_c. An imprint of such a behavior is already visible in the $V_\sigma = 16^3$ data set.

At large temperature all channels have similar masses and the same high temperature behavior (see Fig. 5.11). The masses expressed as aM no longer tend towards zero but approach a constant value of $aM_{T\to\infty} = 0.361(1)$ which is identical for all channels (see Fig. 5.12). The meson masses do not diverge according to

$$M = \sqrt{\Omega^2 + m_{\text{tot}}^2}, \tag{5.41}$$

since there is no thermal mass contribution from the lowest Matsubara frequency $\Omega = 0$. The mesons are still subject to periodic (bosonic) boundary conditions as they do not separate into quarks above T_c in the strong coupling limit. In case of baryon correlators, a thermal mass

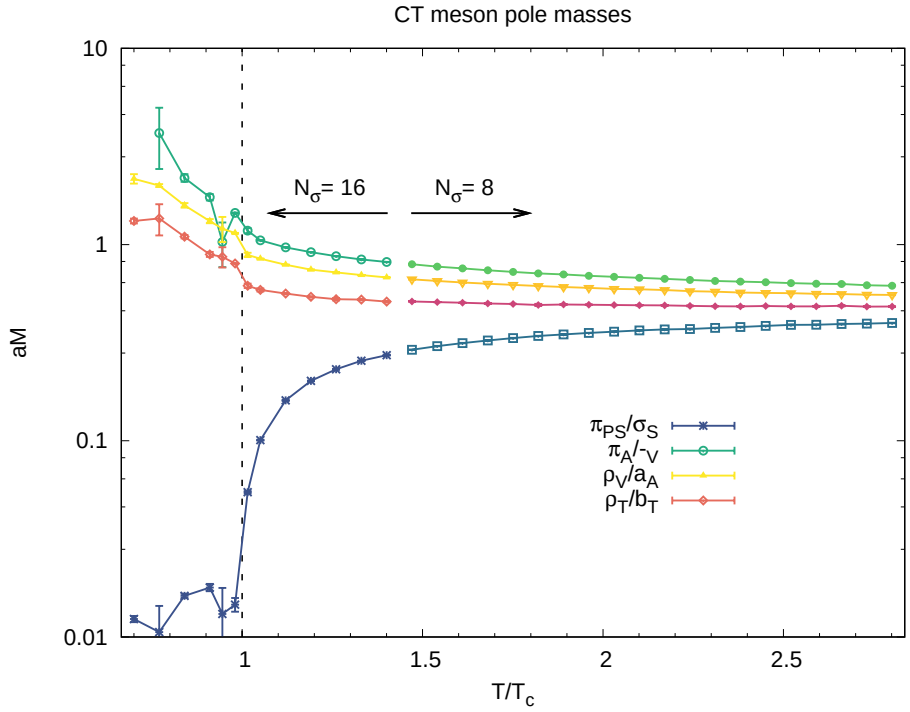

Figure 5.11: *Meson pole masses from CT correlators at zero density for the $16^3 \times CT$ volume at small temperatures and for the $8^3 \times CT$ volume at larger temperatures. Masses for the channels discussed in Tab. 5.2 are shown. The Goldstone pion channel has a distinctively different mass dependence below T_c. The high-temperature limit is independent of the considered channel.*

contribution $\Omega = \pi T$ results in diverging masses [68]. Whether this value is N_c dependent or sensitive to the lattice dimension is not known so far and may be subject to future studies.

5.5.6 Variation of Bins

In order to obtain the best possible signal from a temporal correlator, large extents in time direction are necessary. Despite the fact that a CT correlator has a continuous temporal extent, an artificial discretization has to be introduced in order to measure the correlators (see Fig. 4.1). However, this binning only affects the measurement of the histograms, not the propagation of the worm. Thus, it is more cost-efficient to double the number of bins in contrast to increase N_τ by a factor of two.

Due to an increase in the binning, the amplitude of the correlator is expected to drop (see Fig. 5.13). As each bin is incremented by

$$\frac{f(T)}{\#\text{bins}} = \frac{V_{\text{CT}}}{2a\mathcal{T}\#\text{bins}} \tag{5.42}$$

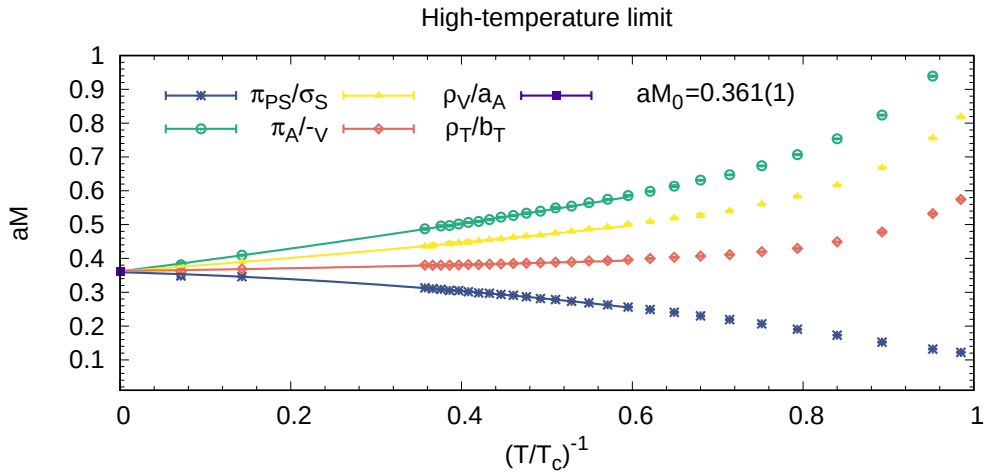

Figure 5.12: *Extrapolation of aM for the different channels on a $4^3 \times CT$ volume via a quadratic fit anzatz. Indeed, a single high-temperature value is approached.*

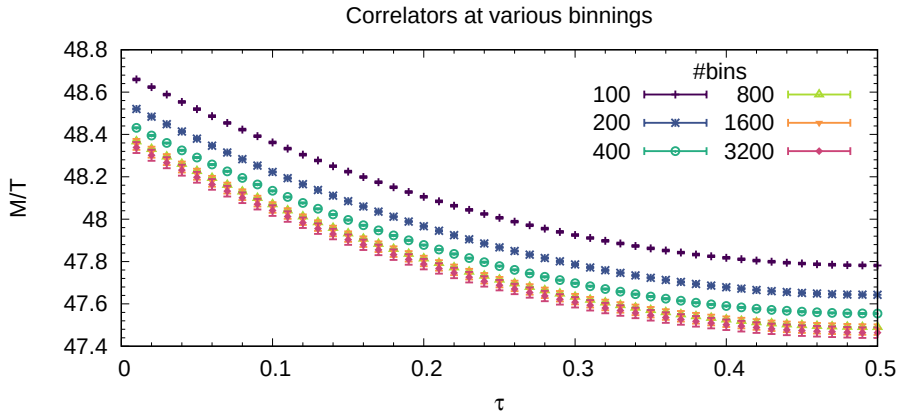

Figure 5.13: *Variation in the number of bins used in temporal direction for the same mesonic correlator corresponding to the Goldstone pion channel $\pi_{PS}\sigma_S$ at a temperature of $T/T_c = 1.25$. The slight drop in amplitude is an effect due to the finite binning. Note that not all data points are depicted here for the larger #bins.*

with $f(T)$ according to Eq. (3.16), there is some overhead coming from the two bins covering the locations of worm Head and Tail respectively (cf. yellowish area in Fig. 4.1). This contribution can be minimized by increasing the total number of bins. This leads to a reduction in the bin size which has the desired effect. Note that the bin at location $L_\tau = 0$ is always incremented. Therefore, it is excluded from all analyses.

Mesonic masses are not changed by the binning since the curvature of the correlator does not change (see Fig. 5.13). The plateau region fluctuates with the number of bins (Fig. 5.14) and estimates on the plateau location for the $4^3 \times$ CT lattice and the $\pi_{\mathrm{PS}}/\sigma_{\mathrm{S}}$ channel are given in Tab. 5.4. A larger binning yields a better precision for the mass M_{plt} extracted from

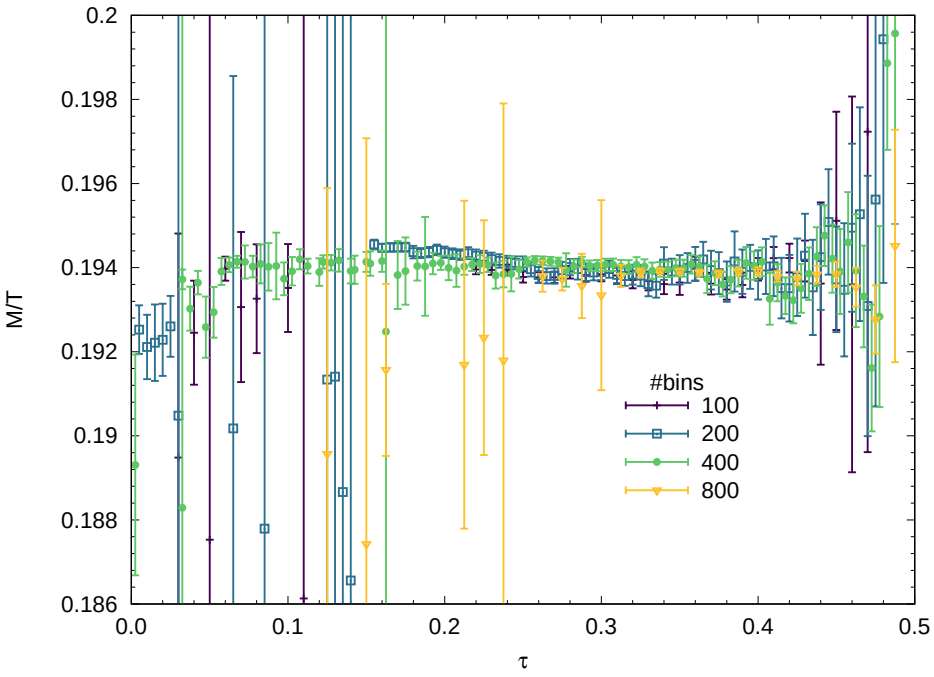

Figure 5.14: *Meson masses obtained for the channel π_{PS}/σ_S on a $4^3 \times CT$ lattice at various binnings. The plateau region fluctuates with the number of bins.*

Table 5.4: *Plateau location in absolute and relative values and the corresponding mass. The error of M_{plt} becomes slightly smaller as the number of bins is raised.*

# bins	M_{plt}	$(x_{min}, x_{max})_{\text{abs}}$	$(x_{min}, x_{max})_{\text{rel}}$
100	0.1938(7)	$(22, 45)$	$(0.22, 0.45)$
200	0.1941(4)	$(34, 82)$	$(0.17, 0.41)$
400	0.1941(2)	$(49, 146)$	$(0.12, 0.37)$
800	0.1939(2)	$(200, 390)$	$(0.25, 0.49)$

the plateau. The plateau width stays almost unchanged. A larger binning is beneficial as more data points contribute to the plateau. However, it is computationally more expensive to evaluate all intervals for fine histograms such that intervals have to be skipped. Therefore, for example for a binning of $\#bins = 800$ only every 10^{th} interval is evaluated. Instead of increasing the number of bins in order to yield a slightly better accuracy as addressed in Tab. 5.4, it is of more interest to shift the plateau region to large τ as far as possible by investing in statistics. Latter means that the number of global worm updates should be

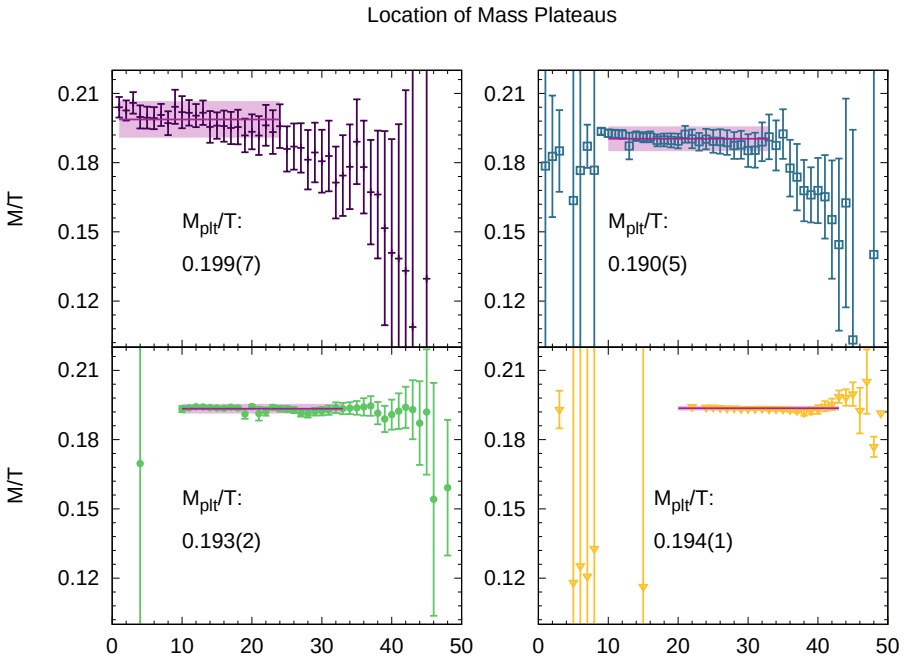

Figure 5.15: *Meson masses corresponding to the Goldstone pion π_{PS}/σ_S kernel at increasing statistics from left to right and top to bottom. Values fluctuate less, the plateau size stays constant but is shifted towards larger values.*

Table 5.5: *Critical chiral restoration bare temperatures for various bare baryon chemical potential values. Multiply with κ in order to convert to non-perturbative results.*

$a\mu_B$	aT_c
0.0	1.4276(2)
0.3	1.423(1)
0.9	1.367(1)
1.5	1.229(1)

maximized. This is successively done in Fig. 5.15, where the number of closed worm updates – initially set to 1000 – is raised by a factor of 10 for each subsequent plot.

5.6 Finite Chemical Potential

In the infinite coupling limit there are no restrictions concerning simulations at finite chemical potential. Instead, the chiral transition temperature decreases as $\mu_B = 3\mu_q$ gets larger (cf. Tab. 5.5). A clear imprint of this behavior is observed in the data set where results are shifted along the temperature axis with larger shifts corresponding to larger values of chemical potential (see Fig. 5.16). These shifts are directly connected to the critical

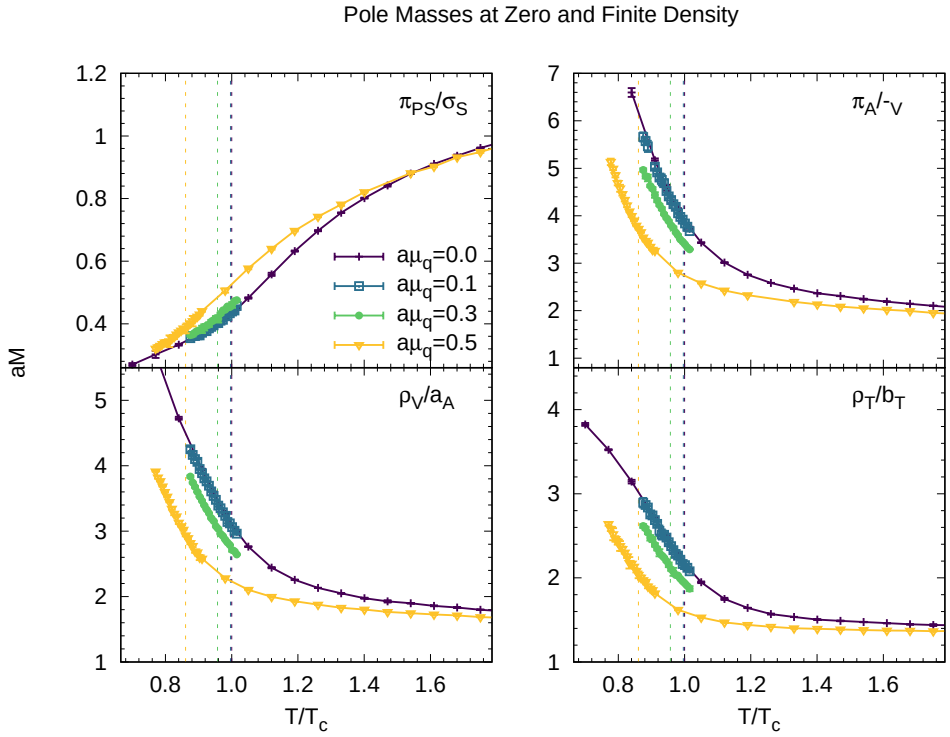

Figure 5.16: *Meson masses extracted from CT correlators on a $4^3 \times CT$ lattice at zero and finite chemical potential. The associated critical temperatures are highlighted by dashed vertical lines. Each subplot is devoted to one distinctive meson correlator channel. The large temperature behavior is studied for bare $a\mu_q = 0.0$ and 0.5.*

temperatures summarized in Tab. 5.5. All considered chemical potentials address the second order phase transition regime. Even though the tri-critical point (TCP) is approached with $a\mu_{B,\mathrm{TCP}} = 1.95(5)$, there is no impact due to its presence. So far no chemical potentials were considered which address the first order regime. Future studies should be performed to verify that a singularity is occurs at T_c when addressing chemical potentials beyond the tri-critical point.

5.7 Towards Transport Coefficients

The study of correlators is far more versatile and goes beyond the extraction of meson masses from the long-distance exponential decay. Firstly, their relation to the spectral function $\sigma(\omega, \mathbf{p})$ is explored which reads

$$G(\tau, \mathbf{p}) = \int_0^\infty d\omega \sigma(\omega, \mathbf{p}) K(\omega, \tau), \quad K(\omega, \tau) = \frac{\cosh(\omega(\tau - 1/2T))}{\sinh(\omega/2T)}, \tag{5.43}$$

with the associated kernel denoted as $K(\omega, \tau)$. The spectral function contains all the information about the considered bound state. Thus, the impacts of the surrounding thermal medium are imprinted on it. The spectral functions peak-like structure encodes the properties of the bound states at respective frequencies ω [69]

$$\sigma(\omega, \mathbf{p}) = |\langle 0|\mathcal{O}|h\rangle|^2 \epsilon(\omega)\delta(p^2 - M_h), \tag{5.44}$$

with M_h the hadron mass of the corresponding meson state and $\epsilon(\omega)$ the sign function. The dissolution of states is encoded in the width of the bound state peaks. Latter broaden and disappear at sufficiently high temperatures such that the large ω regime is described by the continuum [70].
A variety of transport coefficients can be extracted from the spectral function such as viscosities, conductivities, diffusion coefficients ... [69, 71–73]. For example, the heavy quark diffusion coefficient as well as the electrical conductivity are calculated from the spectral function for the $\Gamma = \gamma_i$ kernel. Both quantities are obtained from the zero-frequency limit as follows [71–73]

$$\begin{aligned} D =& \frac{\pi}{3\chi_\sigma} \lim_{\omega\to 0} \sum_{i=1}^{3} \frac{\sigma_{\gamma_i}(\omega, \mathbf{p} = \mathbf{0}, T)}{\omega} \\ \frac{\sigma_{\text{em}}}{T} =& \frac{C_{\text{em}}}{6} \lim_{\omega\to 0} \frac{\sigma_{\gamma_i}(\omega)}{\omega T}, \end{aligned} \tag{5.45}$$

with the quark number susceptibility χ_σ and the electromagnetic factor C_{em}.
As pointed out, the spectral function yields different transport coefficients and should therefore be studied in further detail. However, temporal correlators are measured in imaginary (Euclidean) time while the spectral function is real-valued. Thus, an analytic continuation from data in imaginary time to real frequencies is required. In the following, two methods are presented which tackle this problem.

Maximum Entropy Method

The extraction of the spectral function by inverting Eq. (5.43) is highly problematic since it is an ill-posed problem. There are far too many degrees of freedom compared to the temperature restricted number of temporal lattice points that can be offered. As there is an infinite number of possible solutions, a method is required to select the most suitable spectral function. Due to its non-negativity and normalizability, the spectral function can be treated as a probability density. In the Maximum Entropy Method (MEM) which is based on Bayesian probability theory, the conditional probability

$$P[\sigma|DH] = \frac{P[D|\sigma H]P[\sigma|H]}{P[D|H]} \propto \exp(-L + \alpha S) \tag{5.46}$$

is to be maximized given the correlator data D and some additional prior knowledge H. The same is achieved by minimizing the sum of likelihood function $\hat{L}$ (defined in Sec. 5.5.1) and Shannon-Jaynes entropy [73]

$$S = \int_0^\infty \frac{d\omega}{2\pi} \left[\sigma(\omega) - m(\omega) - \sigma(\omega) \ln \frac{\sigma(\omega)}{m(\omega)} \right], \tag{5.47}$$

which is the central element of the Maximum Entropy Method (MEM). Here, the default model $m(\omega)$ contains additional information in order to minimize correlations between data. Often, the relation $m(\omega) = m_0\omega^2$ is used with m_0 being a constant that is dependent on the choice of channel.

Schwinger-Keldysh contour

For the extraction of transport coefficients the Schwinger-Keldysh contour is of interest. A construction of this contour as depicted in Fig. 5.17 requires simulations at real Minkowski time where a sign problem is introduced. However, for the dual representation presented in this thesis the sign problem can be controlled when excluding dynamic baryons. The phase factor then only takes values of ± 1. Therefore, the CT limit with its feature of having static baryons is an interesting framework for studying the Schwinger-Keldysh contour.

Observables are defined through thermal averaged real time operators

$$\langle \mathcal{O}_1(t)\mathcal{O}_2(t') \rangle_\beta = \mathrm{Tr}\Big(e^{-\beta H} \mathcal{O}_1(t)\mathcal{O}_2(t') \Big). \tag{5.48}$$

The Schwinger-Keldysh formalism dictates how to express real time correlators in terms of a path integral [74]

$$\begin{aligned} \langle \mathcal{O}_1(t)\mathcal{O}_2(t') \rangle &= \mathrm{Tr}\Big[\mathcal{O}_1(t)\mathcal{O}_2(t') e^{-\beta H} \Big] \\ &= \mathrm{Tr}\Big[\mathcal{O}_1(0) e^{-iH(t-t')} \mathcal{O}_2(0) e^{iH(t-t'+i\beta)} \Big] \\ &= \frac{1}{Z} \int \mathcal{D}x e^{iS_{SK}[x]} \mathcal{O}_1(t)\mathcal{O}_2(t'), \end{aligned} \tag{5.49}$$

with the action $S_{SK} = \int_{\mathcal{C}} dt L[x]$ obtained from the original action S by analytical continuation of the time along values on the contour $\mathcal{C}$ (Fig. 5.17). The obtained correlator has a severe sign problem since the integrand is a pure phase but it is expected that this can be addressed by the CT limit of SC-LQCD as discussed before. A fit of the oscillating decay of the real-time correlator and a successive Fourier transformation gives rise to the spectral function. Also, for real time simulations large time extents are required in order to include as many frequencies as possible.

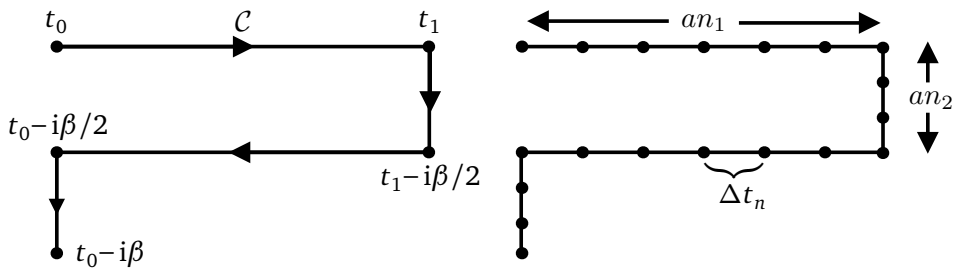

Figure 5.17: *Schwinger-Keldysh contour in its continuous (**Left**) and discretized form (**Right**). Within the complex time plane, there are two real time legs connected by a third, imaginary time segment of length $\beta/2$.*

5.8 Discussion

Based on the general fit ansatz formulated in Eq. (5.28), the construction of temporal correlators in discrete and continuous time was outlined. In one point the analysis is distinctly different: Discrete time correlators exhibit strong oscillations such that a four parameter fit is necessary. This fit averages the even and odd histogram contributions in order to extract the Non-Oscillating and Oscillating channel. Due to the alternating structure large N_τ are required such that the averaging is reasonably good. In contrast, this averaging of an alternating data structure is not required in CT. The histogram data allow to extract the Non-Oscillating and Oscillating channel independently via two parameter fits for the ground state extraction.

In order to incorporate excited states as well as for having a reasonable error estimation, correlated fits are performed. The strategy is outlined which should assure good initial fit parameters for fits with many states. In DT fits also include the oscillating part but suffer from being too complicated such that most fits including additional states fail (see Fig. 5.9). In contrast, in CT only exponential fits on the symmetrized correlator have to be performed where it seems easier to find good initial estimates. At long ranges (small τ) data can be qualitatively better described by incorporating additional states (see Fig. 5.5). However, the signal is not good enough to extract any excited states with a reasonable error estimate. Nevertheless, in these regions the AICc favors masses from multiple state fits (cf. Fig. 5.6).

Within the plateau region, mainly the ground state mass contributes and a comparison to DT calculations shows an offset by about 5% for various channels. It is motivated that the DT data are affected by strong inaccuracies due to the mentioned averaging as well as small N_τ. Even for simulations on a $4^3 \times 64$ lattice the mass plateau in DT is situated in the region most severely tampered by excited states even though good statistics is used. Here, the CT worm algorithm is by far superior as a better discretization can be chosen with statistics where the

mass plateau is shifted to rather small values of τ.
The Goldstone pion channel shows the expected mass dependence. In the infinite volume limit the mass vanishes below T_c, while at and above T_c a mass is acquired which rises and limits in a constant value. The other channels exhibit a constantly decreasing mass as temperature is increased. A limiting high-temperature value of 0.361(1) is obtained. The meson masses do not diverge since no thermal mass contribution is obtained from anti-periodic boundary conditions for fermions. An explanation of the exact value for the high-temperature mass limit is subject to future analysis.
The binning chosen for the CT correlators does not seem to have a distinct impact on the location of the mass plateau or on the accuracy of the final meson mass. In contrast, the included statistics affects the plateau greatly by shifting it to regions of interest (cf. Fig. 5.15).
As there is no sign problem in continuous time strong coupling QCD, also correlators were measured at finite densities. The results exhibited very slight changes according to their associated critical temperatures. Their overall features stayed the same compared to the $\mu_q = 0$ analysis.
Finally, it would be of great interest to use the insights on the correlator measurement not just for mass extraction. A business of high significance is the extraction of transport coefficeints. Several methods were outlined where in particular the Schwinger-Keldysh contour is investigated more thoroughly in the future.

Chapter 6

Taylor Expansion

Phase diagrams are a common tool in physics to illustrate the state of a substance under different values of thermodynamic parameters such as temperature, pressure and chemical potential. The QCD phase diagram as presented in Fig. 1.2 exhibits a rich structure which is still in the focus of current research. One potential feature of the QCD phase diagram is of great interest for the theoretical [16, 75–79] and experimental [80–82] physics community: the existence of a critical end point (CEP) and its location $(\mu_{B,\mathrm{CEP}}, T_{\mathrm{CEP}})$ in the $\mu_B - T$ plane. Such a point would separate a first order line originating from the cold and dense regime and a crossover region leading towards $\mu_B = 0$.

On the theoretical side, great efforts towards overcoming the finite density sign problem are undertaken, but so far none can access the region of interest and pinpoint the potentially location of the CEP (for reviews see Ref. [83, 84], for instance). Nevertheless, various methods offer a solution (Reweighting, Taylor expansion, Imaginary chemical potential, ... [31, 78, 85–87]) to circumvent the complex phase problem. By using these methods, the finite density plane can be accessed at least for small values of chemical potentials. The most established approach [16–18] is based on a Taylor expansion of thermodynamic variables in powers of μ_B/T about $\mu_B = 0$. Calculations are performed either at zero or purely imaginary baryon chemical potential μ_B, such that no fermionic sign problem occurs. Due to computational effort the Taylor series is limited to a finite order n (current state of the art [17, 18, 83, 88] is $n \leq 6$ for HISQ and $n \leq 8$ for unimproved staggered fermions), and thus, limiting the range of reliability. In the end, the full Taylor series would be required to locate the CEP exactly. Moreover, a breakdown of the Taylor expansion in some thermodynamic variable, such as pressure and its derivatives, is necessary in the presence of a CEP due to their non-analytic behavior. Such a finite radius of convergence of a Taylor series can be taken advantage from. The position of a CEP [89] can be probed as the radius of convergence specifies the distance from the series' origin to the nearest non-analytic point.

In the following, a Taylor expansion is performed in the continuous time limit based on the dual formulation of strong coupling lattice QCD (see Sec. 6.1). In this regime an expansion from zero baryon density is not required in order to gain access to the finite $\mu_B - T$ plane as no sign problem is present. However, since the Taylor expansion method is

the most prominent procedure in full QCD, the continuous time simulations can provide a framework in which the range of reliability is tested. The implemented method is validated with an exact enumeration of the partition function for QCD in two dimensions (cf. Sec. 6.2). Various methods for measuring baryon number fluctuations are presented (see Sec. 6.3). This results in a histogram-based method which has the best signal-to-noise ratio and allows a measurement of Taylor coefficients up to c_{12} for a $N_\sigma^3 = 10^3$ volume and c_8 for volumes of 16^3 and 32^3 respectively. The volume dependence of different order cumulants in a tight range around T_c is explored (Sec. 6.4). Furthermore, the chiral phase transition is mapped from the radius of convergence and an imprint of the TCP possibly emerges (see Sec. 6.5). Finally, the reconstruction of the pressure is performed by dropping the homogeneity condition and measuring Taylor coefficients based on the spatial dimer density weighted by the baryon density fluctuations (Sec. 6.6).

6.1 Taylor Expanding the Pressure

Thermodynamic quantities such as pressure and energy density are of great interest due to their most prominent role governing the expansion of the QGP in the early universe as well as in heavy ion collisions. Both quantities are very closely related in the chiral limit of SC-LQCD (see Sec. 4.1.1). In fact, they only differ by a factor of three which is also expressed in terms of the vanishing interaction measure (cf. Eq. (4.9)). Latter is the equation of state (EOS) for relativistic, massless, non-interacting particles.
Under the assumption that the considered system is homogeneous, the pressure is related to the partition function via

$$a^4 p = -a^3 \kappa \frac{a\mathcal{T}}{V} \ln(\mathcal{Z}) \quad \text{and} \quad a^4 \epsilon = -a^3 \kappa \frac{a\mathcal{T}}{3V} \ln(\mathcal{Z}), \quad V = a^3 N_\sigma^3. \tag{6.1}$$

This expression is most helpful since no volume derivative has to be considered as in the fundamental definition of the pressure $a^4 p = -a^3 \kappa a\mathcal{T} \frac{\partial}{\partial V} \ln(\mathcal{Z})$.
Based on the homogeneity condition, the pressure by itself is a thermodynamic potential and in general should be continuous along phase transitions. Thus, in the large density and small temperature regime, where a first order phase transition occurs, the pressure should match as the two phases coexist at the first order line (cf. discussion in Sec. 4.4). On the other hand, the energy density between the phases is different which is denoted by the latent heat [90]. As the interaction measure vanishes, pressure and energy density will behave in the same fashion for the studies presented here.
An important aspect to be analyzed is the homogeneity condition that is enforced for lattice calculations (cf. Eq.(6.1)). In fact, this condition only holds in the continuum and will make it impossible to reconstruct the pressure from strong coupling Monte Carlo simulations by means of a Taylor expansion of Eq. (6.1). Therefore, it will be required to perform an expansion in

terms of the spatial dimer density which will give rise to a slightly more complicated structure (see Sec. 6.6). Nevertheless, since the homogeneity approximation is mostly considered in literature, the analysis of the expansion coefficients as well as the radius of convergence will be based on Eq. (6.1).

The Taylor expansion of the pressure about $(T, \mu_B = 0)$ is given as [17],[31]

$$\begin{aligned} p = -\frac{T}{V} \ln \mathcal{Z} =& p(T, \mu_B = 0) - \frac{T}{V} \sum_{n=1}^{\infty} \frac{1}{n!} \left(\frac{\mu_B}{T}\right)^n \frac{\partial^n \ln \mathcal{Z}}{\partial(\mu_B/T)^n} \\ =& p(T, \mu_B = 0) - \frac{T}{V} \sum_{n=1}^{\infty} \frac{1}{(2n)!} \left(\frac{\mu_B}{T}\right)^{2n} \frac{\partial^{2n} \ln \mathcal{Z}}{\partial(\mu_B/T)^{2n}}\bigg|_{\mu_B=0} \\ =& p(T, \mu_B = 0) - \sum_{n=1}^{\infty} c_{2n} \left(\frac{\mu_B}{T}\right)^{2n} \end{aligned} \tag{6.2}$$

The second line already incorporates the fact that the thermodynamic potential $\Omega(T, \mu, V)$ is an even function of the baryon chemical potential μ_B due to reflection symmetry $\mathcal{Z}(T, \mu_B) = \mathcal{Z}(T, -\mu_B)$ (see e.g. [88]) and thus, $P(T, \mu_B) = P(T, -\mu_B)$ as well. Within the last line the Taylor coefficients are defined as

$$c_{2n} = \frac{T}{V} \frac{1}{(2n)!} \frac{\partial^{2n} \ln \mathcal{Z}}{\partial(\mu_B/T)^{2n}}\bigg|_{\mu_B=0} \tag{6.3}$$

with $\frac{\partial^{2n} \ln \mathcal{Z}}{\partial(\mu_B/T)^{2n}}$ being the essential contribution to be studied in the following.

Cumulants and Moments From statistical physics it is known that the grand-canonical partition function is the exponential or moment generating function $\exp(\mu_B/T\, X)$ of the baryon density moments $X = \Omega_B/V_\sigma$ ([51, 91],[92]). The volume is given as $V_\sigma = N_\sigma^3$. It follows

$$\begin{aligned} \mathcal{Z}(T, \mu_B, V_\sigma) = M(t \equiv \mu_B/T) = \langle e^{tX} \rangle =& 1 + t\langle X \rangle + \frac{t^2 \langle X^2 \rangle}{2!} + \ldots \frac{t^r \langle X^r \rangle}{r!} + \ldots \\ =& 1 + t\mu_1 + \frac{t^2 \mu_2}{2!} + \ldots \frac{t^r \mu_r}{r!} + \ldots \\ =& \sum_{r=0}^{\infty} \mu_r \frac{t^r}{r!}, \end{aligned} \tag{6.4}$$

with μ_r being the r^{th} raw moment. By differentiating the moment generating function $M(t)$ a total of r times with respect to t (at the origin), the r^{th} raw moment reads

$$\mu_m = \frac{d^m M}{dt^m}\bigg|_{t=0} = \langle X^m \rangle = \left\langle \left(\frac{\Omega_B}{V_\sigma}\right)^m \right\rangle = \langle \omega^m \rangle. \tag{6.5}$$

As there is no favoring between the baryon and anti-baryon sector at zero baryon chemical potential $\mu_B = 0$, the odd baryon density moments vanish ($m = 2n + 1, n \in \mathbb{N}$).
Based on the moment generating function, the so-called cumulant generating function is defined as

$$K(t) = \ln(M(t)) = \sum_{r=0}^{\infty} \kappa_r \frac{t^r}{r!}. \tag{6.6}$$

By inserting Eq. (6.4) into Eq. (6.6) and matching coefficients allows to express the cumulants in terms of the moments $\mu_n(\omega) = \langle \omega^n \rangle$:

$$\begin{aligned}
\kappa_1(\omega) &= \mu_1 \\
\kappa_2(\omega) &= \mu_2 - \mu_1^2 \\
\kappa_3(\omega) &= \mu_3 - 3\mu_2\mu_1 + 2\mu_1^3 \\
\kappa_4(\omega) &= -6\mu_1^4 + 12\mu_1^2\mu_2 - 3\mu_2^2 - 4\mu_1\mu_3 + \mu_4 \\
&\dots
\end{aligned} \tag{6.7}$$

Note that another elegant way to calculate the cumulants is based on the initial condition

$$\frac{\partial \ln \mathcal{Z}}{\partial(\mu_B/T)} = \langle \omega \rangle, \tag{6.8}$$

and a recursion relation which makes it possible to relate successive orders of moments by enforcing [93]

$$\frac{\partial}{\partial(\mu_B/T)} \langle \omega^n \rangle = \langle \omega^{n+1} \rangle - \langle \omega^n \rangle \langle \omega \rangle. \tag{6.9}$$

Therefore, derivatives $\frac{\partial^{2n}}{\partial(\mu_B/T)^{2n}}$ of arbitrary order n can be applied to Eq. (6.8) and by inserting Eq. (6.9) it can be concluded that the partition function $\mathcal{Z}$ is related to the cumulants via

$$\frac{\partial^{2n} \ln \mathcal{Z}}{\partial(\mu_B/T)^{2n}} = \kappa_{2n}(\Omega_B) = \kappa_{2n}(\omega) \cdot V_\sigma^{2n}. \tag{6.10}$$

As the thermodynamic potential is a function of even orders, this leads to less complex higher order cumulants κ_{2n}:

$$\begin{aligned}
\kappa_2(\omega) &= \mu_2 \\
\kappa_4(\omega) &= -3\mu_2^2 + \mu_4 \\
\kappa_6(\omega) &= 30\mu_2^3 - 15\mu_2\mu_4 + \mu_6 \\
\kappa_8(\omega) &= -630\mu_2^4 - 35\mu_4^2 + 420\mu_2^2\mu_4 - 28\mu_2\mu_6 + \mu_8 \\
&\dots
\end{aligned} \tag{6.11}$$

Table 6.1: *Static limit results for the Taylor coefficients discussed in the following. At high temperatures the Taylor coefficients have to converge towards their respective limit.*

$\kappa_2(\Omega_B)/V_\sigma$	$\kappa_4(\Omega_B)/V_\sigma$	$\kappa_6(\Omega_B)/V_\sigma$	$\kappa_8(\Omega_B)/V_\sigma$	$\kappa_{10}(\Omega_B)/V_\sigma$	$\kappa_{12}(\Omega_B)/V_\sigma$
$\frac{1}{3}$	0	$-\frac{2}{9}$	$\frac{10}{9}$	$-4\frac{6}{9}$	$-3\frac{1}{3}$

This reduces the expression for the Taylor expansion of the pressure to

$$\begin{aligned}\Delta p = p(T,0) - p(T,\mu_B) =& \frac{T}{V}\sum_{n=1}^{\infty}\frac{1}{(2n)!}\left(\frac{\mu_B}{T}\right)^{2n}\kappa_{2n}(\Omega_B) \\ =& \sum_{n=1}^{\infty} c_{2n}(\Omega_B)\left(\frac{\mu_B}{T}\right)^{2n}, \quad c_{2n}(\Omega_B) = \frac{T}{(2n)!}\frac{\kappa_{2n}(\Omega_B)}{V}\end{aligned} \tag{6.12}$$

with the Taylor coefficients $c_{2n}(\Omega_B)$. By measuring the baryon density moments

$$\langle n_B^m \rangle = \langle \omega^m \rangle = \mu_m \tag{6.13}$$

via a CT worm algorithm, the cumulants $\kappa_n(\omega)$ are constructed. Based on the cumulants, a Taylor expansion of the pressure for a homogeneous system can be composed.

Cumulants in the High Temperature Limit In Sec. 1.4.2 the high temperature limit is explored which features static mesons and baryon lines. Based on the one-dimensional QCD partition function Eq.(1.80) at vanishing baryon chemical potential $\mu_B = 0$, the moments calculated by Equations (6.8) and (6.9) yield the same static limit value

$$\mu_{2n}^{\text{static}} = \frac{1}{3}, \tag{6.14}$$

Note that aside from being independent of the order n, there is also no volume dependence present in the static moment definition. By inserting Eq. (6.14) into Eq. (6.11) results in the static limit values for $\kappa_{2n}(\Omega_B)/V_\sigma$ summarized in Tab. 6.1. These values are of great interest as a crosscheck for all further calculations. Interestingly, the limiting values are in close proximity of $\sim \pm 1$ for all cumulants up to $\kappa_{12}(\Omega_B)/V_\sigma$. Beyond that the high temperature limit results seem to diverge.

6.2 Exact enumeration in two dimensions

An exact evaluation of the partition function, whether it is in discrete ($\mathcal{Z}_{\text{DT}}$) or continuous time ($\mathcal{Z}_{\text{CT}}$), is only manageable on small lattices where the number of possible configurations is under control. Nevertheless, such crosschecks are crucial in order to verify that measurements work properly.

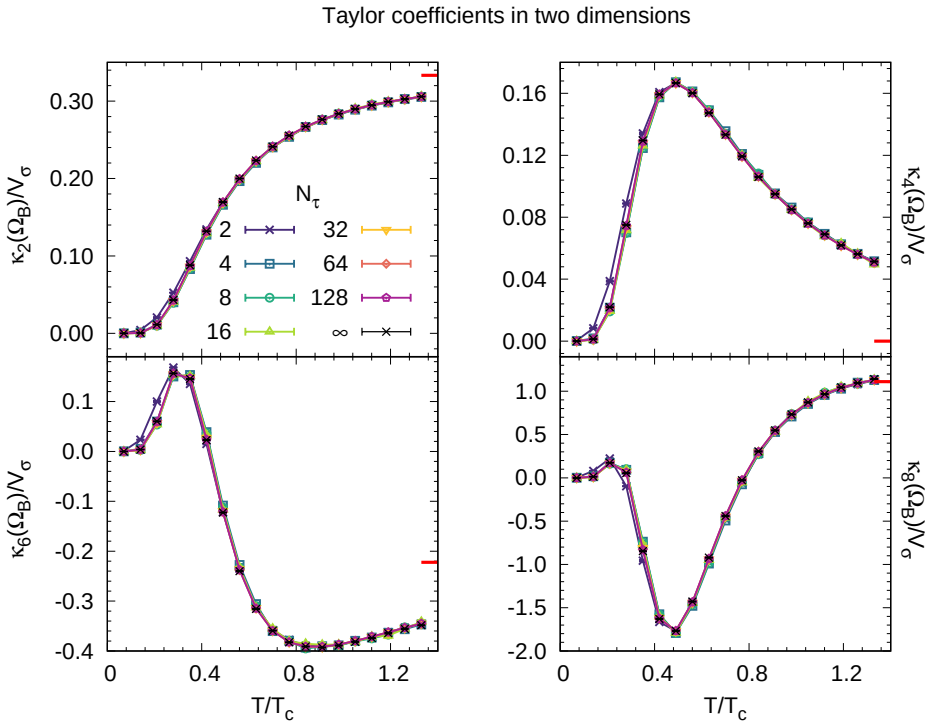

Figure 6.1: *Discrete time simulations of the first four Taylor coefficients $\kappa_{2\ldots8}(\Omega_B)/V_\sigma$ on a $2 \times N_\tau$ lattice. Noticeable deviations are visible for $N_\tau = 2$ results, while larger temporal extends converge smoothly towards the continuous time simulation results $N_\tau \to \infty$. The exact numeration results for $N_\tau = 2$ and 4 agree perfectly with the same colored data points.*

Details on the analytic derivation of the exact partition function on a 2×2 lattice is given in [53]. Its generalization to $2 \times N_\tau$ only changes the multiplicity in the bare anisotropy

$$\begin{aligned} \mathcal{Z}^{\mathrm{DT}}_{2\times N_\tau} = \gamma^{6N_\tau} &\left(2\cosh(2\mu_B/T) + 16(\cosh(\mu_B/T)+1) + 2\right) \\ &+ \frac{400}{9}\left(\gamma^{4N_\tau} + \gamma^{2N_\tau}\right) + 4. \end{aligned} \tag{6.15}$$

For the CT limit such an expression can only be derived approximately, as spatial dimer can be placed arbitrary tight and thus, an infinite number of terms contributes. The starting point is the static limit as discussed for a one-dimensional system in Sec. 1.4.2. In general, the partition function can be structured into sectors which are characterized by the winding number

$$\mathcal{Z}_{\mathrm{CT,static}} = \sum_{\Omega_B=-V_\sigma}^{V_\sigma} \mathcal{Z}_{\Omega_B}. \tag{6.16}$$

No spatial meson hoppings can be present for configurations with a baryon winding number

$\Omega_B \neq 0$. A lattice that is fully saturated with (anti)-baryons is associated with winding numbers ($\Omega_B = -V$) $\Omega_B = V$ while lattices partly occupied with (anti)-baryons take integer valued numbers in between ($-V_\sigma \leq \Omega_B \leq V_\sigma$). As (anti)-baryons carry a weight of $\exp(\pm\mu_B/T)$, contributions to the purely baryonic sectors $\mathcal{Z}_{\Omega_B=\pm 2}$ add up to

$$\mathcal{Z}_{\Omega_B=2} + \mathcal{Z}_{\Omega_B=-2} = 2\cosh(2\mu_B/T). \tag{6.17}$$

For the mixed sectors $\mathcal{Z}_{\Omega_B=\pm 1}$ there are $N_c + 1$ combinations to put a static (anti)-baryon and a static meson line on a $2 \times \mathrm{CT}$ lattice. Therefore, the weight is given by

$$\begin{aligned} \mathcal{Z}_{\Omega_B=1} + \mathcal{Z}_{\Omega_B=-1} &= 2(N_c+1)(\exp(\mu_B/T)+1) + 2(N_c+1)(\exp(-\mu_B/T)+1) \\ &= 16(\cosh(\mu_B/T)+1). \end{aligned} \tag{6.18}$$

Finally, the largest number of configurations are gathered in the $\Omega_B = 0$ sector. There are two ways of putting a baryon/anti-baryon on a $2 \times \mathrm{CT}$ lattices with $\Omega_B = 0$ which yields a weight of $2\exp(\mu_B/T)\exp(-\mu_B/T)|_{\mu_B=0} = 2$. In total, the static partition function on a $2 \times \mathrm{CT}$ lattice reads

$$\mathcal{Z}_{CT,static} = \mathcal{Z}_{2\times\mathrm{CT}} = 2\cosh(2\mu_B/T) + 16\,(\cosh(\mu_B/T)+1) + 2. \tag{6.19}$$

Note that this static contribution is part of the first term in Eq. (6.15).

In discrete time the number of configurations remains finite and only grows with a larger temporal extend N_τ. As mentioned before, this is very different for CT configurations. Since an arbitrary number of sets of oppositely oriented spatial dimers can be included in a configuration, there is in fact no upper limit for the number of vertices that can be included. Thus, infinitely many configurations can be constructed. However, at bare temperatures $a\mathcal{T} > 1/2$, contributions with larger spatial dimer number k are suppressed more and more. According to Eq. (2.28) the partition function including the corrections to the static limit reads

$$\mathcal{Z}_{2\times\mathrm{CT}} = \mathcal{Z}_{\mathrm{CT,static}} + \sum_{k\in 2\mathbb{N}} c_k \left(\frac{1}{2a\mathcal{T}}\right)^k, \quad c_k = \sum_{\mathcal{G}\in\Gamma_n^{V_\sigma}} v_{\mathbf{T}}^{N_{\mathbf{T}}(\mathcal{G})}. \tag{6.20}$$

The coefficients c_k contain the contributions of the spatial dimer vertices as discussed in Sec. 2.3. Thus, by adding order-by-order c_k's the overall static limit contribution is corrected. Higher order c_k are necessary to be included at temperatures below T_c where multiple spatial dimers per site are very common. However, the process of tabulating the v_T-multiplicities beyond $k \geq 10$ is sophisticated. It is most crucial to avoid configurations where the number of emission and absorption events attached to a spatial site does not match, thus violating the Grassmann Constraint at the boundaries. Alternatively, the GC can be violated by

Table 6.2: *Number of spatial dimers and the associated multiplicities of* **T***-shaped vertices with their non-trivial weight* $v_T = \frac{2}{\sqrt{3}}$. *For* n *spatial dimers there are* $0 \dots 2n$ *vertices. Only even multiplicities occur and every second column has only one non-zero entry, namely for the* $\#D$ *row and* $v_T^{\#D}$ *column. A symmetry factor of* 8 *is factored out from the whole table.*

#D	$\boldsymbol{v_T^0}$	$\boldsymbol{v_T^2}$	$\boldsymbol{v_T^4}$	$\boldsymbol{v_T^6}$	$\boldsymbol{v_T^8}$	$\boldsymbol{v_T^{10}}$	$\boldsymbol{v_T^{12}}$	$\boldsymbol{v_T^{14}}$	$\boldsymbol{v_T^{16}}$
2	4	4	1	–	–	–	–	–	–
4	4	0	12	0	1	–	–	–	–
6	4	0	9	16	6	0	1	–	–
8	4	0	16	0	52	0	8	0	1

raising (lowering) the meson state occupation number above (below) N_c (0). In Tab. (6.2), the first four correction terms c_2, c_4, c_6 and c_8 are listed including their multiplicities in v_T. Note that a symmetry factor motivated by Fig. 6.2 of $2 \cdot 4 = 8$ is factored out. With the

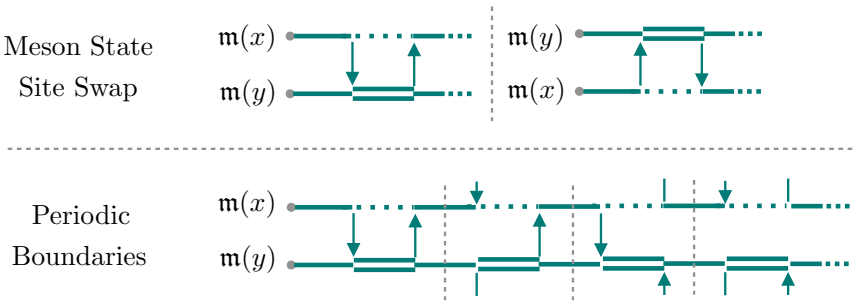

Figure 6.2: *Configurations of the same weight. Due to the depicted symmetries only* $\frac{1}{8}^{th}$ *of all possible configurations have to be calculated.*

strategy elaborated in Appendix (A.1), it is easily possible to compute multiplicities up to c_{28}. Moreover, correlations between the multiplicities of v_T and v_L vertices and the total number of spatial dimers k can be found. Without a proof, the contributions to Eq. (6.20) can be written down to arbitrary order in k (see Appendix (A.2)).

Finally, it needs to be discussed to what order it is necessary to include spatial dimer contributions and when a truncation is reasonable. At temperatures above T_c meson hoppings are suppressed and no significant deviations between calculations based on different truncated partition functions are obtained (see Fig. 6.3). This is very different for temperatures below T_c where spatial hoppings are very common. While clear deviations are visible for coefficients κ_2 and κ_4, good agreement is obtained for $k \geq 6$ and the analytic curve describes the continuous time worm simulation results perfectly. Therefore, at least for the $2 \times \mathrm{CT}$ test case the listing in Tab. 6.2 is sufficient.

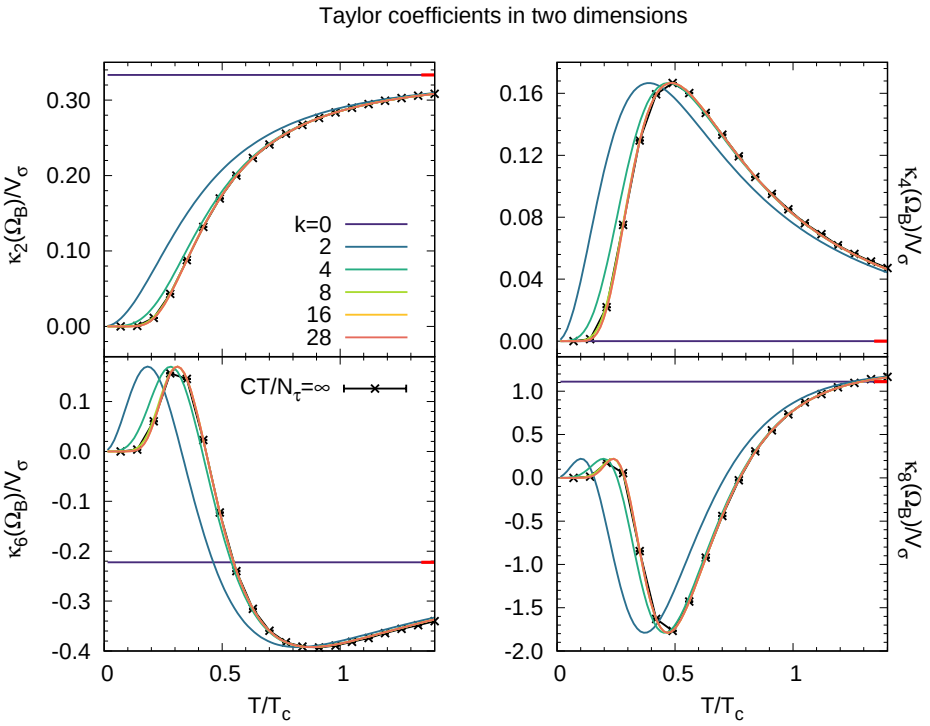

Figure 6.3: *Continuous time results for the first four Taylor coefficients* $\kappa_{2\ldots8}(\Omega_B)/V_\sigma$ *on a* $2\times$ *CT lattice obtained respectively by a CT worm simulation and the truncated partition function Eq.* (6.20)*. Analytic results up to* $k = 28$ *spatial dimers are considered.*

6.3 Taylor coefficients in 3+1 dimensions

The previous sections strongly support that the method for extracting Taylor coefficients based on the baryon number density is well established and is ready to be applied to larger lattices in $3 + 1$ dimensions. Calculations on various lattice sizes provide insights on the cumulants behavior in the vicinity of T_c as the thermodynamic limit is approached.

6.3.1 Naïve approach

Recent studies based on DT lattices of size $10^3 \times 4$ at finite quark mass $am_q = 0.1$ already failed to extract the fourth order cumulant with sufficient accuracy [53]. It is expected that the CT data are significantly less noisy due to the continuous time feature of having static baryon lines which keeps the cumulants under control especially at temperatures above T_c where baryon/anti-baryon fluctuations are rare. To verify that this is not a quark mass dependent effect, the simulations in discrete time are repeated for $m_q = 0$.
Worm simulations for a $10^3\times$CT lattices are performed. A comparison of cumulants $\kappa_2(\Omega_B)/V_\sigma$ and $\kappa_4(\Omega_B)/V_\sigma$ from both DT and CT calculations is given in Fig. 6.4. For the second order

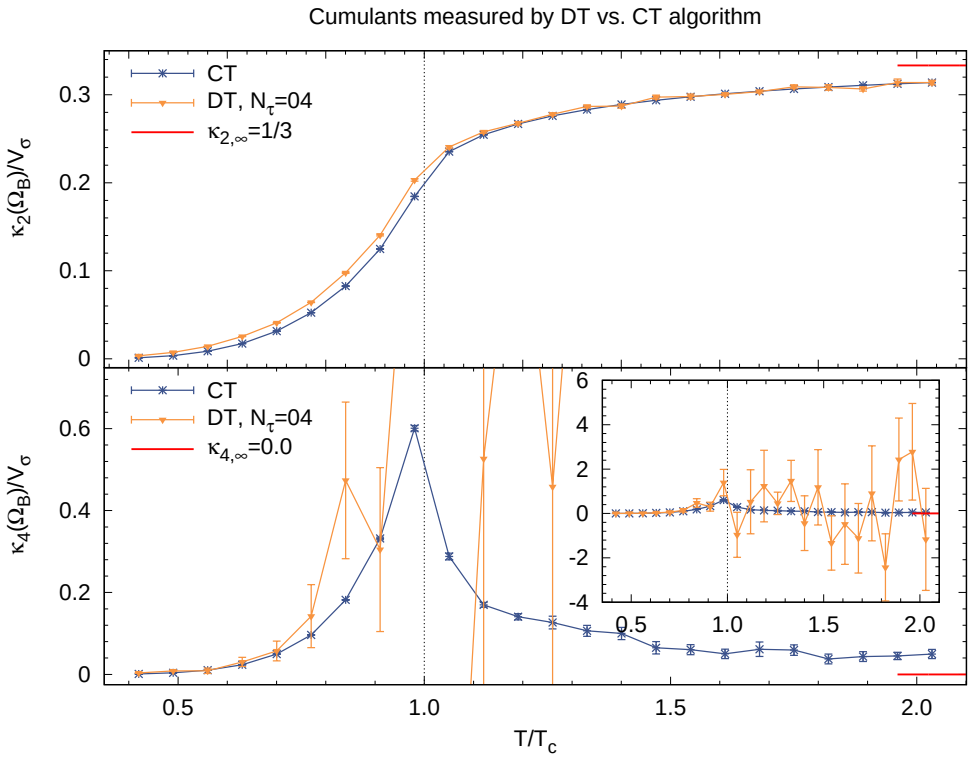

Figure 6.4: *Measurement of the cumulants $\kappa_2(\Omega_B)/V_\sigma$ and $\kappa_4(\Omega_B)/V_\sigma$ on a discrete time lattice with $N_\tau = 4$ and on a continuous time lattice. The offset below T_c in $\kappa_2(\Omega_B)/V_\sigma$ between the results is a finite size effect as discussed for $2 \times N_\tau$ simulations. discrete time results start to become noisy for $\kappa_4(\Omega_B)/V_\sigma$ below T_c whereas the CT results show a smooth and well-defined behavior.*

cumulant an overall match is observed, except for temperatures below T_c where the finite size effects discussed in Fig. 6.1 contribute to a small offset. This offset cannot be observed in the fourth order cumulant, since data are already too noisy for DT simulations below T_c.

Note that both data sets are based on the same statistics. A total of 10^8 worm updates were performed to obtain a hundred averaged values for the baryon density. Subsequently, a jackknife analysis (details in Sec. 1.5.2) was performed on these data sets. This is approximately a factor four less statistics compared to the results for finite $m_q = 0.1$ in [53] which is also why the errors here are larger by about the same factor. Hence, it is even more impressive that the continuous time method has a superior performance just due to its native feature of static baryon lines.

In general, the noise in the baryon density will be lowest at small temperatures where configurations are dominated by spatial meson hoppings such that there is no space for static degrees of freedom on the lattice. This state of baryon loop suppression does not hold anymore around T_c and above. As the baryon density increases, the calculation of high-order cumulants becomes demanding since with each order more moments contribute to a single cumulant (cf.

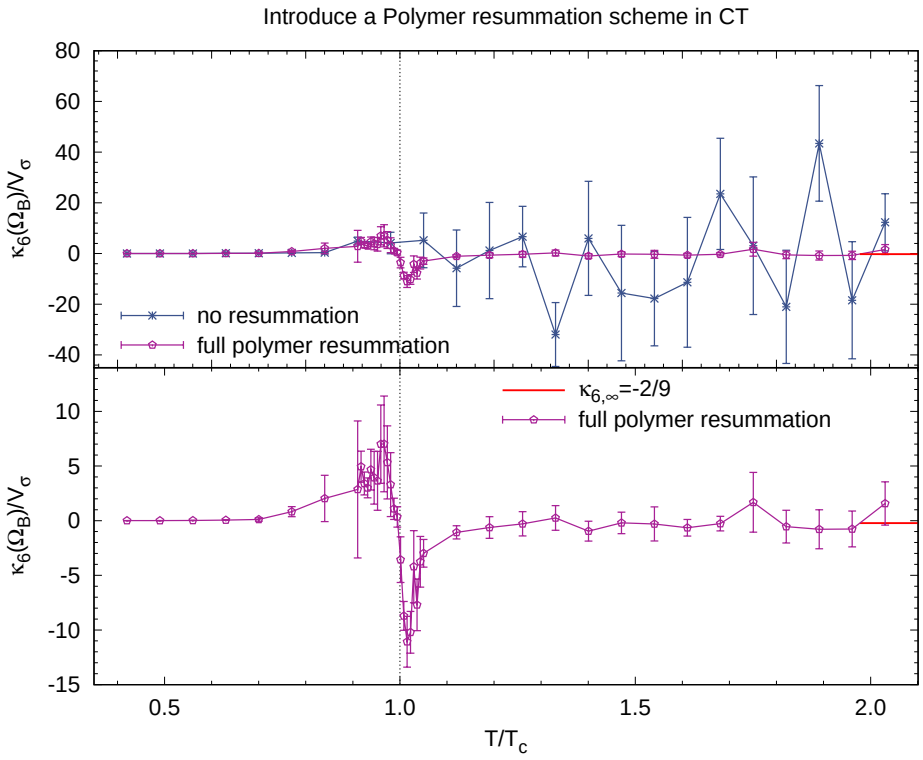

Figure 6.5: *Measurement of the cumulant $\kappa_6(\Omega_B)/V_\sigma$ with and without a resummation scheme. A resummation of static objects reduces the errors such that the structure of κ_6 close to T_c can be studied.*

Eq. (6.11)). It needs high precision to compensate for these new contributions which become more and more sensitive to variations as higher orders are considered.

6.3.2 Polymer resummation

The application of the CT algorithm results in a reasonable improvement compared to the latest discrete time studies. However, the wiggles in Fig. 6.4 above T_c also highlight that no major improvement over several orders of cumulants was achieved so far. Thus, the sixth order cumulant k_6 is calculated based on a polymer resummation scheme in order to reduce fluctuations. Static meson state chains as well as (anti)-baryons are treated the same during the worm evolution and the individual contributions are extracted based on the probabilities stated in Eq. (6.21). A clear improvement can be achieved as seen in Fig. 6.5. Without a full resummation, the noise is extreme and destroys the imprint of the chiral transition completely, while the imprint is visible with a full polymer resummation. Nevertheless, the errors are still large, even though it should be manageable to reconstruct at least $k_6(\Omega_B)/V_\sigma$ with more statistics. In order to get some additional benefit from this analysis in the strong coupling limit, it is most crucial to be able to go beyond the sixth order which can also be addressed

in full QCD [18]. Thus, the next section introduces the final method which allows to extract decent results up to $\kappa_{12}(\Omega_B)/V_\sigma$.

6.3.3 Histograms in the Polymer Number

In the following, a method based on a histogram in the winding number density is presented which boosts the accuracy in the reconstructed Taylor coefficients. This method depends on the Polymer resummed algorithm in order to incorporate these benefits as well. This resummation scheme treats static meson lines and (anti-)baryons as the exact same object, a polymer. At zero baryon chemical potential $\mu_B = 0$ the probability of interpreting a polymer $Q \in \{B, A, D\}$ as a static meson D or (anti-)baryon $P = B + A$ is given as

$$\mathcal{P}_D = \frac{N_c + 1}{\mathcal{Z}_{1d}} = \frac{2}{3}, \qquad \mathcal{P}_P = \frac{2\cosh(\mu_B/T)}{\mathcal{Z}_{1d}} = \frac{1}{3}, \tag{6.21}$$

with $N_c = 3$ and $\mathcal{Z}_{1d}$ from Eq. (1.80). Now, instead of distinguishing between the different types of static lines at the very end of every single worm update, histograms $H_{V,T/\mu_B}(Q)$ are accumulated in the polymer number Q and normalized such that each histogram corresponds to a probability distribution (see Fig. 6.6:Top). Moments and cumulants are reconstructed based on such a histogram. At low and high temperatures, the histogram structure is narrow and peaked. While almost no static lines are present at $0.5\,T_c$, there are almost no non-static lines at $2.0\,T_c$. As T_c is approached, the probability of single polymeric sites Q decreases. This is compensated by a broadening of the distribution. At T_c the histograms peak is located in the vicinity of $V_\sigma/2$, as this temperature highlights the transition from a dynamic regime (at low temperatures) with almost only non-static sites to a regime with almost only static polymer sites (large temperatures).

Starting from the histograms in the fully resummed polymer number Q (cf. Fig. 6.6:Top), a binomial transformation is applied which yields a histogram in P:

$$\begin{aligned}\tilde{H}_{V,\mu_B/T}(P) &= \sum_Q H_{V,\mu_B/T}(Q) \underbrace{\binom{Q}{P} \left(\frac{N_c+1}{\mathcal{Z}_{1d}}\right)^{Q-P} \left(\frac{2\cosh(\mu_B/T)}{\mathcal{Z}_{1d}}\right)^{P}}_{q_{\mu_B/T}(Q,P)} \\ &= \sum_Q H_{V,\mu_B/T}(Q) \binom{Q}{P} \left(\frac{2}{3}\right)^{Q-P} \left(\frac{1}{3}\right)^{P}.\end{aligned} \tag{6.22}$$

In the second line the function $q_{\mu_B/T}(Q,P)$ is evaluated for $N_c = 3$

$$q_{\mu_B/T}(Q,P)\Big|_{\mu_B=0} = \binom{Q}{P} \left(\frac{2}{3}\right)^{Q-P} \left(\frac{1}{3}\right)^{P}, \tag{6.23}$$

where the weights introduced in Eq. (6.21) are recovered. The temperature dependence of the

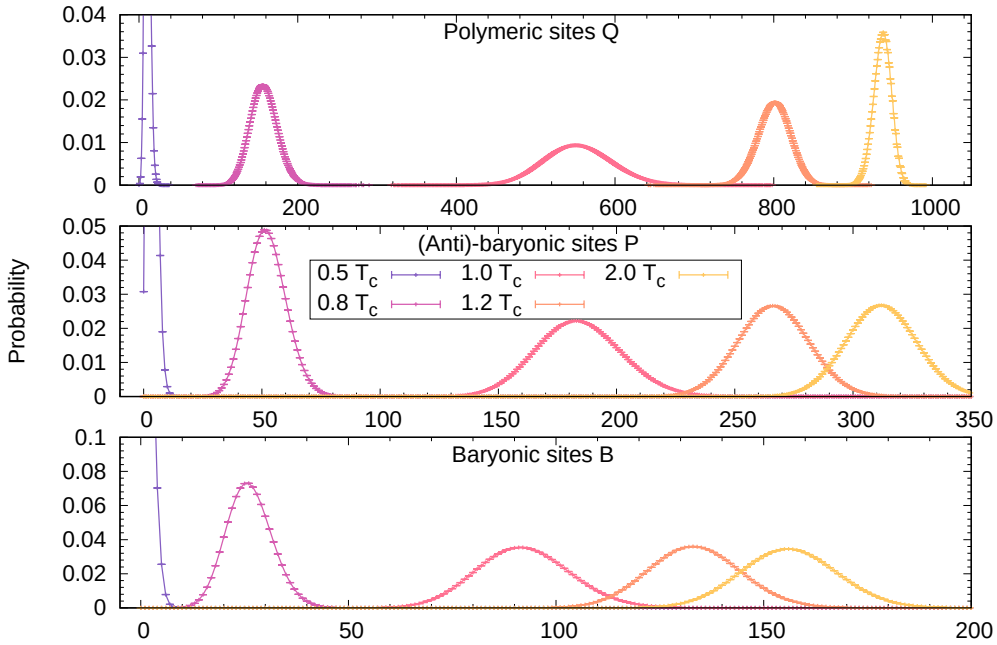

Figure 6.6: *Histograms used for an accurate calculation of cumulants. The histograms in the polymer number Q are obtained from CT worm simulations on $V = 10^3$ lattices while all others are derived completely analytically.*

histograms $H_{V,\mu_B/T}(P)$ is shown in Fig. 6.6:Center. Since the probability of (anti)- baryonic sites is $\frac{1}{3}$, the data points are no longer distributed over the whole V_σ-range but located within $\sim \frac{V_\sigma}{3}$. Above T_c static sites dominate and no saturation occurs which would result in a narrow, peaked structure since only Q feels the saturation due to the finite volume but P can vary and be spread out. The amplitude stays rather constant since Q can be interpreted as $\frac{2}{3}$ static dimer sites and $\frac{1}{3}$ static (anti-)baryon sites. Another transformation is necessary to differ between antibaryonic and baryonic sites. At zero μ_B none of the two is favored and the distribution will be exactly the same. For the same reason all odd moments of the baryon density vanish. In analogy to Eq. (6.22) it follows that

$$\begin{aligned}\tilde{\tilde{H}}_{V,\mu_B/T}(B) &= \sum_P \tilde{H}_{V,\mu_B/T}(P) \binom{P}{B} \frac{e^{\mu_B/T \cdot B}}{(2\cosh(\mu_B/T))^B} \frac{e^{-\mu_B/T(P-B)}}{(2\cosh(\mu_B/T))^{P-B}} \\ &= \sum_P \tilde{H}_{V,\mu_B/T}(P) \underbrace{\binom{P}{B} \left(\frac{1}{2}\right)^P}_{\tilde{q}_{\mu_B/T}(P,B)}\end{aligned} \tag{6.24}$$

In the last line it is used that at $\mu_B = 0$ the chance of interpreting a polymer site P as

a baryon or antibaryon is identical. Due to this fifty-fifty chance of having a baryon or antibaryon, histograms in the baryon number are constrained to an interval of $\sim (V_\sigma/3)/2$ (see Fig. 6.6:Bottom). A complete similar structure to the previous histograms in the polymer number emerges. Since the baryon histograms are constraint to a narrower region, less data points build up the peak structure with a raise in amplitude in order to keep the normalization fixed to one.

The analysis can be shortened by skipping the intermediate step of having a histogram in P and hence, combining both binomial transformations in a single trinomial distribution

$$D^{QB}_{\mu_B/T}(Q,B) = \sum_{P=|B|}^{Q} \binom{Q}{\frac{P+B}{2}, \frac{P-B}{2}, Q-P} \frac{e^{B\mu_B/T}(N_c+1)^{Q-P}}{w_Q(\mu_B/T)^Q}. \tag{6.25}$$

This distribution is used to transform histograms in the fully resummed polymer number Q into histograms in B:

$$H^B_{V_\sigma,\mu_B/T}(B) = \sum_{Q=P}^{V_\sigma} D^{QB}_{\mu_B/T}(Q,B)\, H^Q_{V_\sigma,\mu_B/T}(Q). \tag{6.26}$$

Finally, a certain raw moment μ_m can be extracted fully analytically by weighting a function in the required (anti)-baryon number $f(B) = B^m$ with the before mentioned histogram

$$\langle f(B) \rangle = H^B_{V_\sigma,\mu_B/T}(B)\, f(B). \tag{6.27}$$

Since the histograms in baryon and antibaryon number are the same at $\mu_B = 0$, a function in $(B-A)^m$ can be selected to shorten the process.

In the following, final results on the extraction of cumulants are presented. The moments of n_B are calculated by applying Eq. (6.27) to a suitable function in the baryon and antibaryon number. In Fig. 6.7:Left results up to the eighth order are shown in a close range around T_c. In this range the data are well-behaved even for the larger volumes and the emergence of local extrema with each two orders in κ_{2n} becomes evident. The peaks closest to T_c are the ones that are strongest. While the $16^3 \times$ CT and $32^3 \times$ CT data already converge pretty well at the low- and high-temperature borders of the depicted range, there are clear finite size scaling effects in the vicinity of T_c. At larger orders of κ_{2n} the high temperature behavior cannot be featured precisely. The data is clearly dominated by noise for the $16^3 \times$ CT volume at κ_8 but also fails for the $10^3 \times$ CT simulations. The problem is that with each order in the cumulants a factor of V_σ pushes down the signal which has to be compensate for by tuning up the precision by the same factor. At some point this is not manageable anymore with a serial algorithm. In the vicinity of T_c the corrections due to finite size effects become stronger with the order of κ_{2n}. Higher order cumulants show a divergence of the amplitude also for the $10^3 \times$ CT volume as depicted in Fig. 6.8. Since κ_{10} and κ_{12} are well behaved around T_c

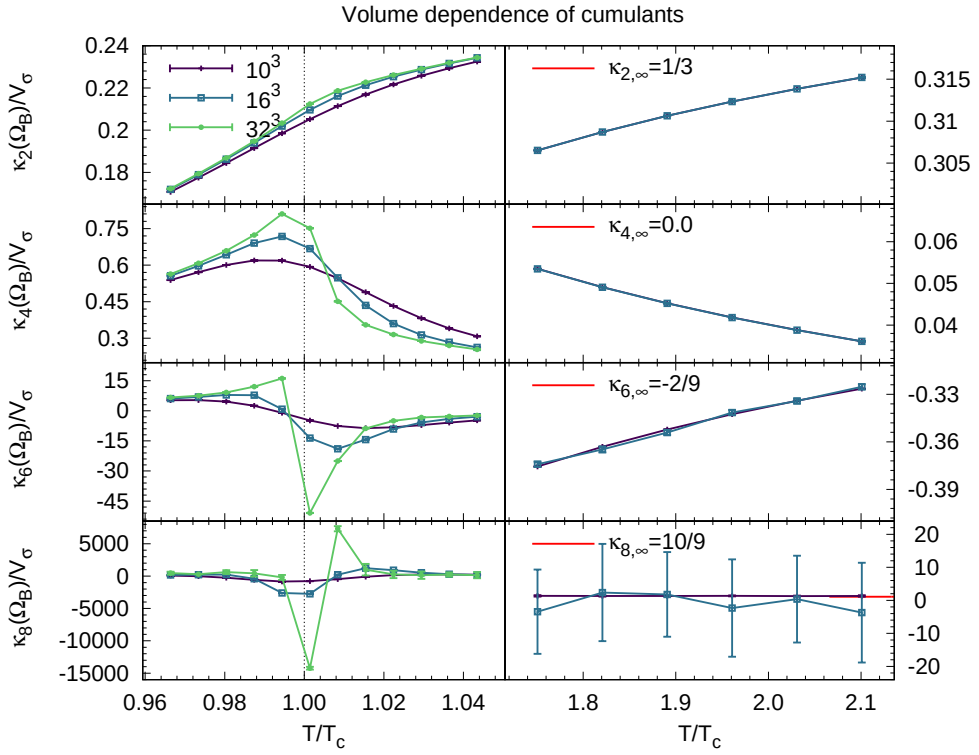

Figure 6.7: *Cumulants up to order 8 obtained from histograms in the polymer number Q for various volume sizes.* ***Left****: Temperature dependence in close vicinity to T_c.* ***Right****: Temperature dependence towards the static limit.*

such that the expected behavior can be studied, these two orders will also be considered in the following analysis.

The location of maxima and the shape of the cumulant function is further investigated in the next section.

6.4 Inflection Points

When studying the different orders of cumulants, several systematics can be observed such as new maxima arising with every two orders and hence inflection points with each order in κ_{2n}. Similar structures for cumulants are obtained in [87],[93],[94]. To qualitatively narrow down the locations of minima, maxima and inflection points more precisely the coarse simulation data are cubic spline interpolated in order to raise the number of available data points by a factor of 10. The resampling is performed on an interval $d\mathcal{T}$ = `[1.30:1.50]` around T_c with 200 bins. A larger number of bins is not reasonable and would lead to possible oscillations introduced by the spline interpolation. At constant volume the location of maxima and minima as well as the position of inflection points are reasonably good distributed symmetrically

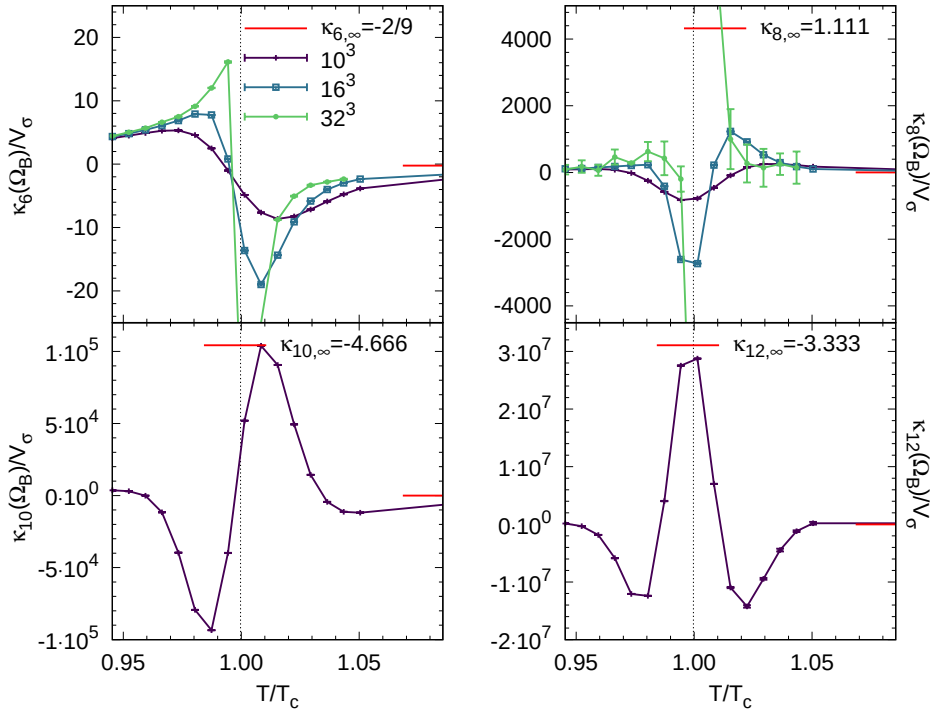

Figure 6.8: *Higher order cumulants in a close range around T_c. For $10^3 \times CT$ simulations the 10^{th} and 12^{th} order are shown with reasonable errors which allow to observe the increasingly complex structure around T_c with diverging amplitudes already for this small volume.*

around T_c (see Fig. 6.9). Based on the results it can be assumed that exactly at T_c there is in alternating order (1) an inflection point with negative sign change (κ_2), followed by (2) a maximum (κ_4), (3) an inflection point with positive sign change (κ_6) and (4) a minimum (κ_8). This behavior is quite reasonable when looking at the slope of κ_n and comparing it to κ_{n+2} as depicted in Fig. 6.10 for κ_2 and κ_4. The shape of the two functions is similar and in particular the position of the maximum agrees. Nevertheless, they totally differ in amplitude and in low- and high-temperature behavior since the derivative of κ_n is expected to vanish in both limits. If the volume dependence of the cumulants is taken into account there are two main observations (see Fig. 6.11):

1. With increasing volume the locations of peaks are narrowed down to successively smaller intervals around T_c,

2. and the amplitude diverges.

Eventually, in the thermodynamic limit it can be expected that poles will emerge. Away from T_c no volume effects arise. Table (6.3) sums up the different locations and in Fig. 6.12 an extrapolation towards the thermodynamic limit is performed. For the two lowest order

Table 6.3: *Temperature locations of Maxima, Minima (*left*) and inflection points (*right*) from the analysis of the four lowest order cumulants and for three different volumes.*

$T_{\text{Min/Max}}$	$\mathbf{10^3}$	$\mathbf{16^3}$	$\mathbf{32^3}$	$T_{\text{Inflection}}$	$\mathbf{10^3}$	$\mathbf{16^3}$	$\mathbf{32^3}$
κ_2	–	–	–	κ_2	1.409	1.418	1.422
κ_4	1.415	1.419	1.423	κ_4	1.382	1.400	1.413
					1.448	1.437	1.435
κ_6	1.386	1.405	1.416	κ_6	1.362	1.399	1.412
	1.451	1.438	1.431		1.422	1.424	1.424
					1.473	1.448	1.436
κ_8	1.369	1.395	1.415	κ_8	1.359	1.384	1.411
	1.423	1.425	1.429		1.406	1.415	1.422
	1.474	1.450	1.441		1.440	1.435	1.435
					1.494	1.458	1.446

cumulants the extrapolations agree very well with the critical temperature obtained from the chiral susceptibility scaling (see Sec. 4.2). On the contrary, extrapolation results are far more scattered for the higher order cumulants since these exhibit more complex structures which cannot be resolved as good by the sparsely distributed simulation data. Therefore, the cubic spine interpolation is affected by larger uncertainties for higher order cumulants as well as for larger volumes where peaks and inflection points are located in a narrower range about T_c.

6.5 Radius of Convergence

In the chiral limit of strong coupling LQCD the phase diagram exhibits a first order transition line at densities around $\mu_q \sim 0.77$ and low temperatures. This line ends in a tricritical point (TCP), which is located at $(a\mu_{B,\text{TCP}}, aT_{\text{TCP}}) = (1.95(5), 1.005(25))$. For smaller densities the phases of low and high temperatures are separated by a 2^{nd} order phase transition. By measuring the radius of convergence r_n, the chiral transition can be tested. A finite r_n indicates the position of the nearest critical point with respect to the center of the expansion. It is not possible to have a series expansion that crosses the non-analyticity to describe the phase transition in the adjacent phase.

For a general power series expansion

$$\sum_{n=1}^{\infty} a_n = \sum_{n=1}^{\infty} c_n (x-b)^n \tag{6.28}$$

the radius of convergence r is a nonnegative, real number which specifies that the series in Eq. (6.28) is convergent if $|x-b| < r$. It is estimated from successive ratios of the expansion

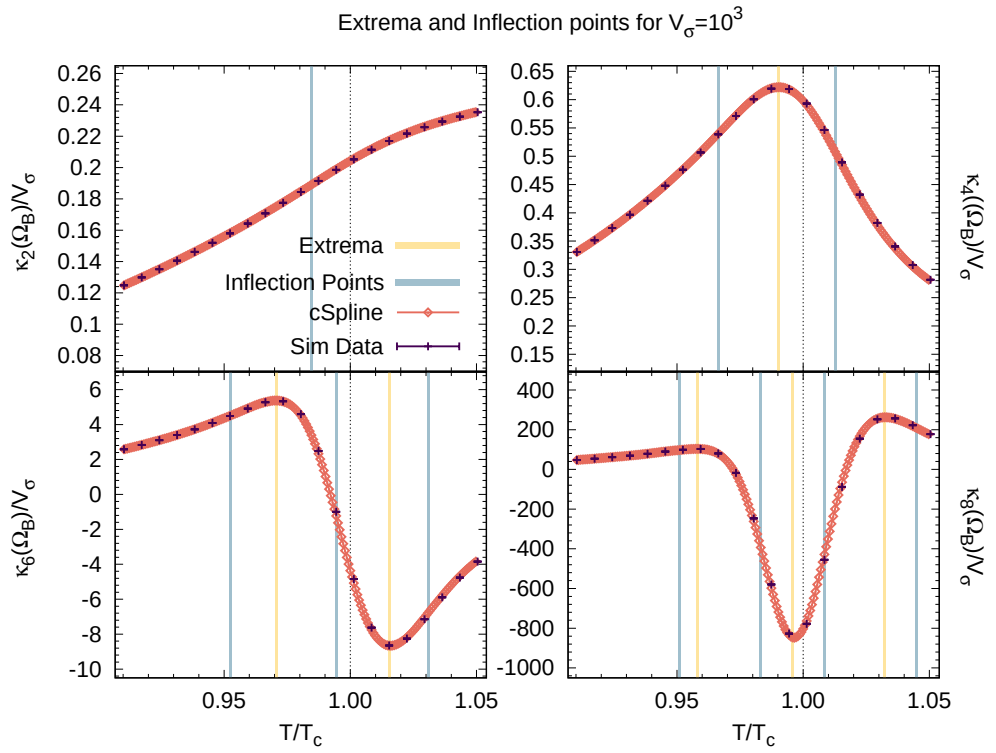

Figure 6.9: *First four cumulants for a $10^3 \times CT$ volume with the pointed out location of maxima, minima and inflection points on a narrow interval around T_c. Simulation data are spline interpolated and resampled. $T/T_c = 1.0$ is also depicted as a dashed line for reference.*

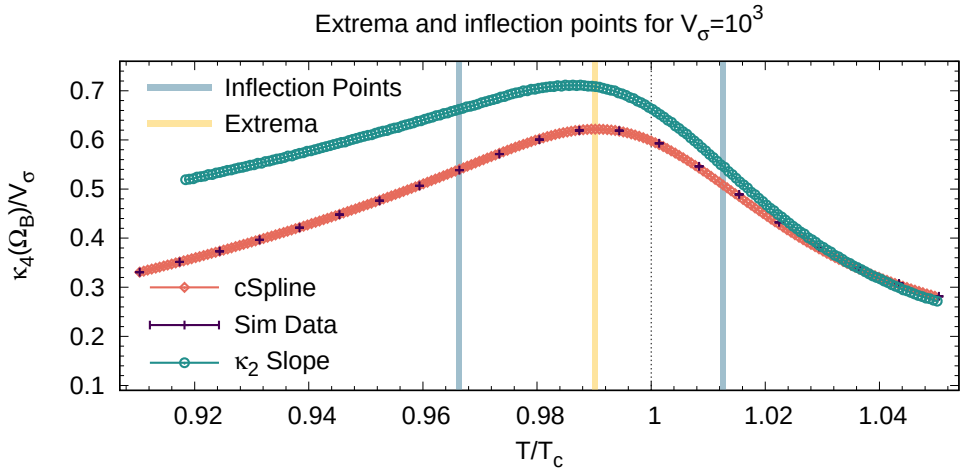

Figure 6.10: *Comparison of $\kappa_4(\Omega_B)/V_\sigma$ simulation data with the first derivative of $\kappa_2(\Omega_B)/V_\sigma$. Both data sets are spline interpolated and resampled as described in Sec. 6.4. The similarity motivates the sequence of Minima, Maxima and inflection points with different sign changes arising at T_c for consecutive $\kappa_n \to \kappa_{n+2}$.*

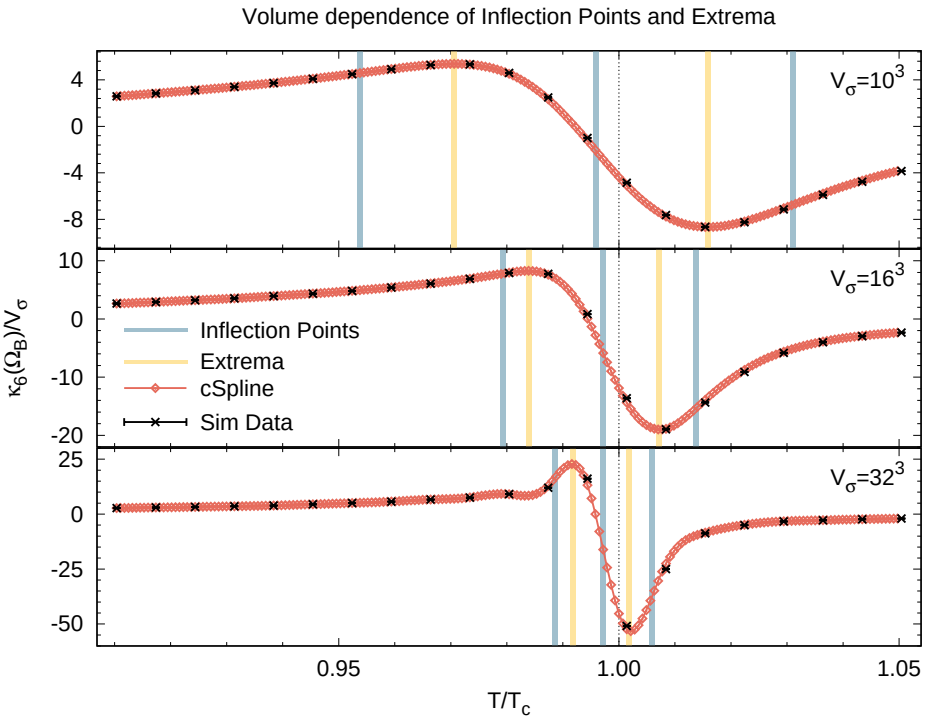

Figure 6.11: *Volume dependence of cumulant $\kappa_6(\Omega_B)/V_\sigma$. Extreme points move towards T_c and diverge in amplitude. The range away from T_c is unaffected by change in volume. Note that for the $V_\sigma = 32^3$ volume the simulation data are very sparsely distributed in the region of interest.*

coefficients and by performing the limit

$$r_\alpha = \lim_{n\to\infty} \sqrt{\left|\frac{c_n}{c_{n+2}}\right|} = \lim_{n\to\infty} \sqrt{\left|\alpha_x(n)\frac{\kappa_n}{\kappa_{n+2}}\right|}. \tag{6.29}$$

The square-root comes from the fact that the Taylor expansion is performed in $(\mu_B/T)^2$ rather than in μ_B/T [94]. The constant $\alpha_x(n)$ in Eq. (6.29) depends on which kind of observable is Taylor expanded. So, for the pressure a^4p or the baryon number susceptibility $a^6\chi_B$ the corresponding coefficients are [16]

$$\begin{aligned} \alpha_p(n) &= \sqrt{(n+2)(n+1)} \\ \alpha_{\chi_B}(n) &= \sqrt{(n-1)n}, \end{aligned} \tag{6.30}$$

and therefore, different r_n are obtained at finite n for different observables. In fact, the estimates for the radius of convergence for the baryon density r_{χ_B} can be directly related to

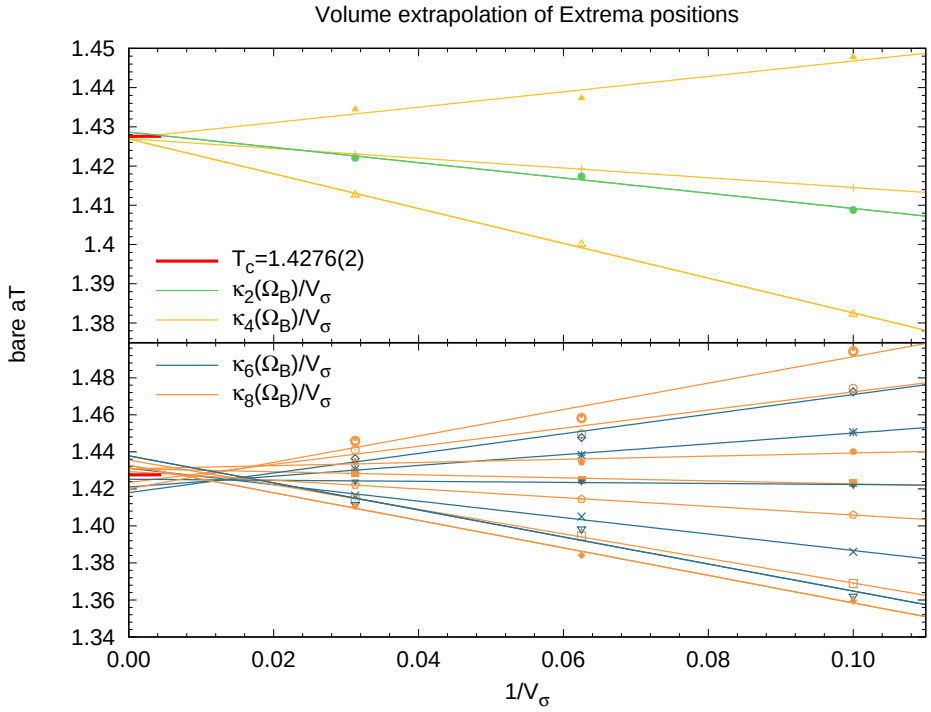

Figure 6.12: *Thermodynamic limit extrapolation of the Minima, Maxima and inflection point locations and comparison to T_c obtained from the chiral susceptibility scaling.*

the radius of convergence for the pressure [78]

$$r_{2n}^{\chi B} = r_{2n}^{p} \sqrt{\frac{2n(2n-1)}{(2n+2)(2n+1)}}. \tag{6.31}$$

Although there is a difference at finite n, they all agree in the $\lim_{n\to\infty}$ limit. For the pressure the constant directly follows from the definition of the Taylor coefficients c_{2n} in Eq. (6.12). As discussed before, the determination of Taylor coefficients does not allow yet to measure arbitrary high order coefficients. In fact, it is already extremely difficult to get a reasonable good signal-to-noise ratio for the low ordered coefficients as the system becomes more complex. For the $10^3 \times$ CT Taylor coefficients, the results for the radii of convergence are shown in Fig. 6.13. The phase transition lines connected by the TCP are obtained from CT SC-LQCD simulations. With increasing orders, the ratios of Taylor coefficients approach the transition line from the high density region. A similar behavior was discussed in [95] for an effective $N_f = 2 + 1$ flavour Polyakov-quark-meson model. For the low order ratios, a strong back-bending towards low densities is obtained which sets in at successively lower temperatures as higher orders are considered. Furthermore, the ratio $\frac{\kappa_{10}}{\kappa_{12}}$ is noisy below T_c due to a dramatic increase in simulation runtime at low temperatures. However, at temperatures slightly above

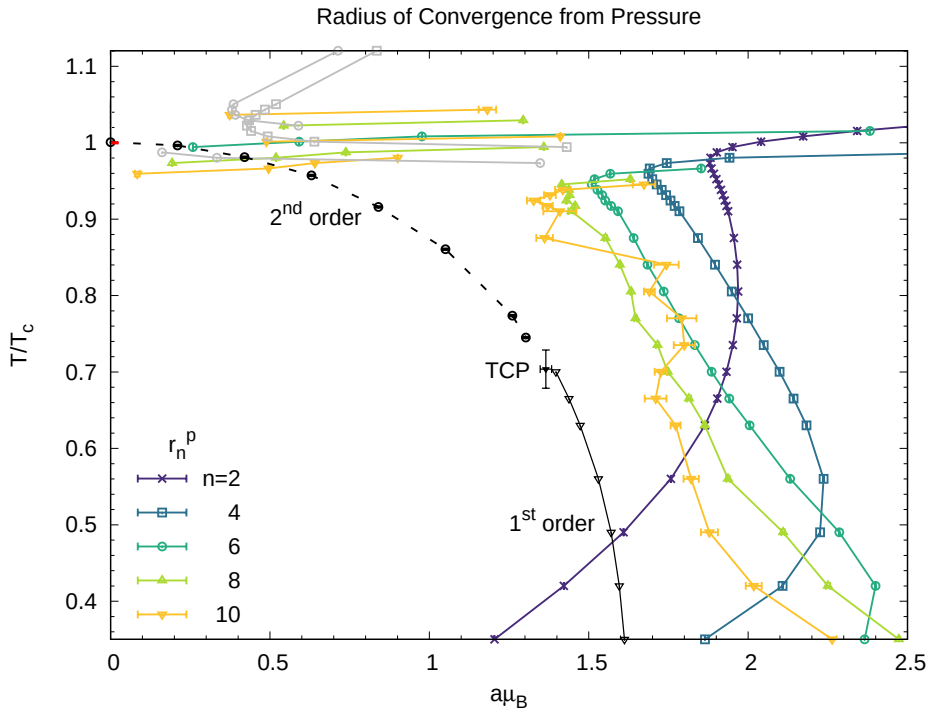

Figure 6.13: *Phase diagram in temperature and baryon chemical potential for the pressure with the numerical results from CT simulations depicted in black and the radii of convergence in color. Negative results indicating the presence of non-analyticities in the complex plane are shown in grey.*

T_{TCP} there is a slight bending towards higher densities which could be an impact of higher order ratios reacting on the presence of the TCP. On the other hand, this could also indicate that insufficient statistics is included in the construction of κ_{12}.

The same plot can be obtained when Taylor expanding the baryon susceptibility

$$\chi^B_{2n} = \frac{\partial^2 p}{\partial(\mu_B/T)^2} = \sum_{n=2}^{\infty} n(n-1)c^p_{2n}\left(\frac{\mu_B}{T}\right)^{2n-2}. \tag{6.32}$$

This expansion requires no new measurements as it is completely based on the Taylor expansion of the pressure with the respective coefficients c^p_{2n}. As susceptibilities diverge at non-analyticities, they have a stronger dependence on the transition line which should result in a faster convergence ([16],[95]). This is strongly supported by Fig. 6.15. The overall behavior in the finite $\mu_B - T$ plane matches between $r_{\chi_B}(2n)$ and $r_p(2n)$. However, Eq. (6.32) yields a "shift" such that the results for $r_{\chi_B}(2n)$ almost agree with the transition line for $n \geq 8$.

Below T_c the radius of convergence is positive and therefore sensitive towards the nearest singularity in the real $\mu_B - T$ plane [96]. In close proximity to $a\mathcal{T}_c = 1.4276(2)$ the ratios are

oscillating between positive and negative values. Here, the number of zeros increases with each order of $\frac{\kappa_n}{\kappa_{n+2}}$. From the previous discussion on the location of inflection points and extrema, it is evident that with increasing volume the locations of zeros are spread narrower around T_c. For $V_\sigma \to \infty$ the ratios $n \geq 4$ are positive below T_c and negative above, while at T_c there is a singularity. As the radius of convergence resembles the location of the closest singularity, it is expected that above T_c the ratios will react to a singularity in the complex plane since above T_c no phase transition takes place for real μ_B. However, in this temperature regime no mutual convergence towards some transition line is observed whatsoever.

Based on the finite r_n results, an extrapolation for fixed temperature will locate the position of the nearest non-analyticity. As studies in [95] show, a peaked behavior at small n followed by a decay towards the desired $r_{n\to\infty}$ value can be expected. This agrees with the behavior observed for small temperatures well below T_c for the baryon density as well as the associated susceptibility (Fig. 6.14). While at $0.75\,T_c$ a sudden rise occurs, which could be an imprint of the TCP or an indication of insufficient statistics, this bulky part will eventually vanish as T_c is approached. The results for the susceptibility nicely agree with the large n numerical value. At $0.95\,T_c$ a merely decaying behavior in r_p and a constant increase in r_{χ_B} is observed. Based on the shown convergence, a transition would be expected to take place at twice the numerical value.

Especially the plot for the last temperature stresses the necessity to incorporate many more higher order coefficients in order to meaningful approach and extrapolate towards $r_{n\to\infty}$.
As discussed before, higher order Taylor coefficients are difficult to obtain in non-toy models. In order to reliably extrapolate from the finite set of expansion coefficients towards $n \to \infty$ there are various methods to choose from. A usual approach is comprised in the Domb-Sykes Plot ([94],[97]), where the estimates for the radius of convergence $1/r_{n-1}^2$ are plotted versus $1/n$. The data points are then extrapolated linearly towards $1/n \to 0$ and the radius of convergence can be extracted. Note that it is required for the expansion coefficients to be asymptotically of the same sign or to alternate in the sign [94]. There are estimators which deal better with an irregular asymptotic structure. Typically, these estimators are not used since an increasing number of Taylor coefficients is involved in their calculations. As the histogram method in the polymer number gives rise to the first six orders of coefficients, this should allow to address more complex estimators. One such estimator which works best for non-analyticities away from the real axis was proposed by Mercer and Roberts [96]

$$\begin{aligned} r_n^{(MR)} &= \left| \frac{c_{n+1}c_{n-1} - c_n^2}{c_{n+2}c_n - c_{n+1}^2} \right|^{\frac{1}{2}} \\ &= \left| \frac{c_{n+2}c_{n-2} - c_n^2}{c_{n+4}c_n - c_{n+2}^2} \right|^{\frac{1}{4}} , \end{aligned} \tag{6.33}$$

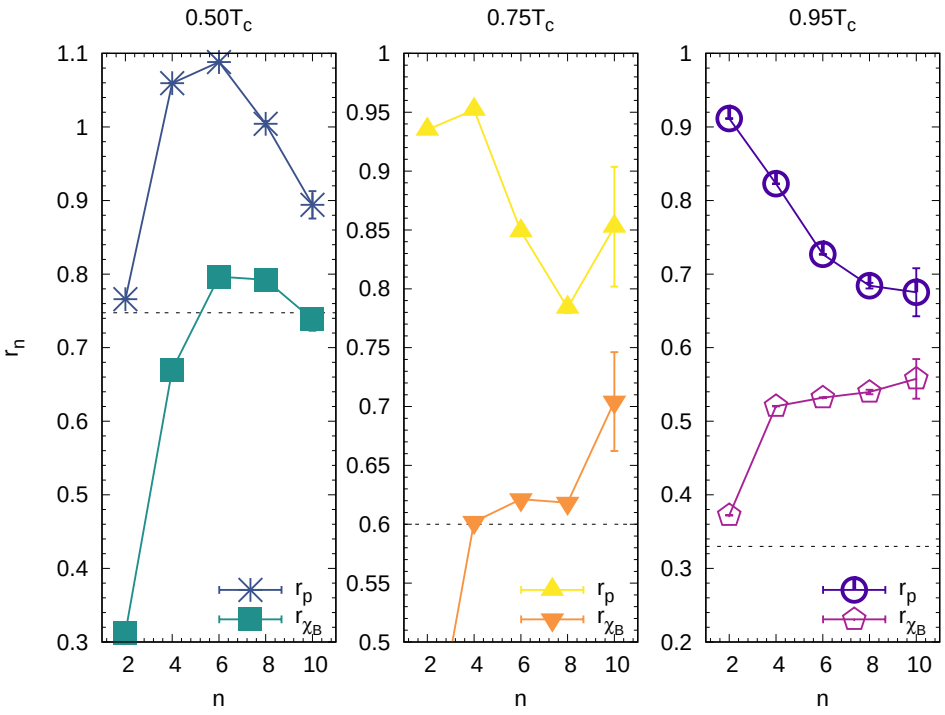

Figure 6.14: *Convergence of the radius of convergence towards the chiral transition line for three temperatures below T_c. The radii are obtained from expansions in the baryon density as well as the baryon susceptibility.*

and even more complex, modified versions (MMR) are proposed as presented in [98]

$$\begin{aligned} r_n^{(MMR)} &= \left| \frac{(n+1)(n-1)c_{n+1}c_{n-1} - n^2c_n^2}{(n+2)nc_{n+2}c_n - (n+1)^2c_{n+1}^2} \right|^{\frac{1}{2}} \\ &= \left| \frac{(n+2)(n-2)c_{n+2}c_{n-2} - n^2c_n^2}{(n+4)nc_{n+4}c_n - (n+2)^2c_{n+2}^2} \right|^{\frac{1}{4}} . \end{aligned} \tag{6.34}$$

A great variety of estimators is also presented in [99]. The radius of convergence $r_n^{(\mathrm{MR})}$ based on Eq. 6.33 shows strong imprints of some of the radii incorporated in its more complex structure (see also Fig. 6.16). It seems obvious that $r_4^{\chi_B,(\mathrm{MR})}$ is spoiled by the unphysical behavior of $r_2^{\chi_B}$ while $r_8^{\chi_B,\mathrm{MR}}$ shows large imprints of $r_{12}^{\chi_B}$. So, in case more Taylor coefficients were available it would be reasonable to exclude these mentioned results from an analysis with the MR estimator.

A descent analysis based on the Domb-Sykes Plot is not possible with the limited data set. In the end, the standard estimator for the Baryon susceptibility shows a better convergence towards the transition line while for the Mercer-Roberts estimator no real trend can be

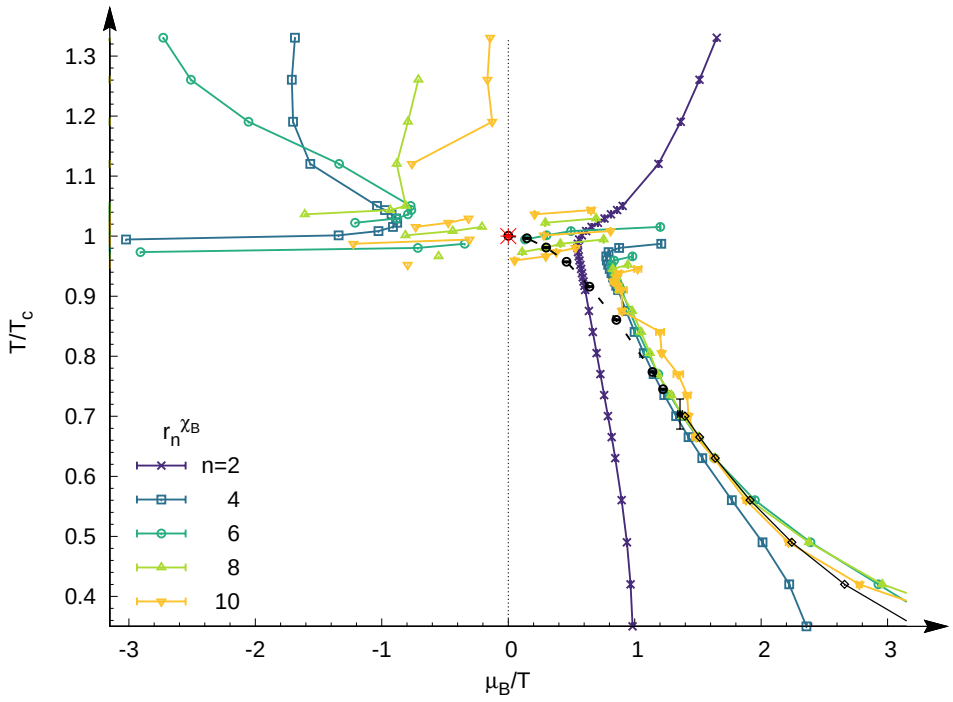

Figure 6.15: *Phase diagram in χ_B for real and imaginary chemical potentials.*

observed.

6.6 Reconstruction of the Pressure

Finally, it is of interest to reconstruct the pressure via the Taylor expansion method. As discussed in Sec. 6.1, a reconstruction according to Eq. (6.12) does not work as the Taylor expansion is based on the assumption of having measured the pressure on a homogeneous system. Most certainly this is not the case for the pressure obtained from calculations on a discrete lattice.

The starting point for the discussion is the definition of the pressure in terms of the spatial dimer density $a^4 p = -\frac{dT}{3}(C - \langle n_{D_\sigma} \rangle)$. Instead of an expansion in baryon density moments, the pressure for an inhomogeneous system is sensitive to a Taylor expansion in the spatial dimer density

$$\Delta p = \frac{1}{3} \sum_{n=0}^{\infty} \frac{1}{(2n)!} \left(\frac{\mu_B}{T} \right)^{2n} \frac{\partial^{2n} \langle n_{D_\sigma} \rangle}{\partial (\mu_B/T)^{2n}} \bigg|_{\mu_B = 0} . \tag{6.35}$$

The derivatives with respect to μ_B/T of $\langle n_{D_\sigma} \rangle$ are more involved as the expectation value of

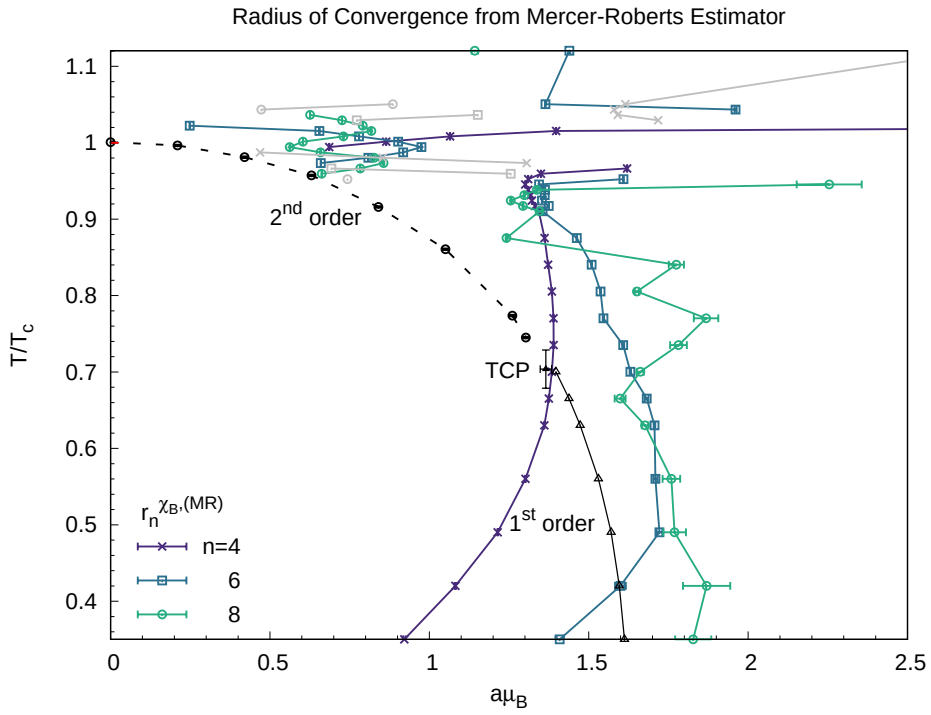

Figure 6.16: *Reconstruction of the chiral transition line in the phase diagram for the baryon susceptibility based on the Mercer-Roberts estimator.*

the spatial dimer density is given by

$$\langle n_{D_\sigma} \rangle = \frac{\sum_{\mathcal{C}} W(\mathcal{C}) n_{D_\sigma}}{\mathcal{Z}}, \tag{6.36}$$

where it is summed over all configurations $\mathcal{C}$. So, with each expansion order n, an additional factor in the winding number density emerges from the derivative of $\mathcal{Z}$. In particular, this leads to mixed terms $\langle n_{D_\sigma} \omega^{2n} \rangle$ to be evaluated. In the end, this whole problem can be scaled down to a simple recursion relation [93] similar to the one of Eq. (6.9):

$$\frac{\partial \tilde{\mu}_n}{\partial(\mu_B/T)} = \tilde{\mu}_{n+1} - \tilde{\mu}_n \mu_1 \quad \text{and} \quad \frac{\partial \ln\langle n_{D_s} \rangle}{\partial(\mu_B/T)} = \tilde{\mu}_1. \tag{6.37}$$

The modified moments $\tilde{\mu}_m$ are the before mentioned combinations of the spatial dimer density n_{D_σ} and the winding number density ω from previous studies

$$\tilde{\mu}_m = \langle n_{D_\sigma} \omega^m \rangle. \tag{6.38}$$

Finally, the modified cumulants are constructed by applying Eq. (6.37) [93]

$$\begin{aligned}
\tilde{\kappa}_0(n_{D_s}) =& \langle n_{D_s} \rangle = \tilde{\mu}_0 \\
\tilde{\kappa}_2(n_{D_s}) =& \frac{\partial^2 \langle n_{D_s} \rangle}{\partial(\mu_B/T)^2}\bigg|_{\mu_B=0} = (\tilde{\mu}_2 - \tilde{\mu}_0\mu_2) \\
\tilde{\kappa}_4(n_{D_s}) =& \frac{\partial^4 \langle n_{D_s} \rangle}{\partial(\mu_B/T)^4}\bigg|_{\mu_B=0} = (\tilde{\mu}_4 - 6\tilde{\mu}_2\mu_2 - \tilde{\mu}_0\mu_4 + 6\tilde{\mu}_0\mu_2^2) \\
\tilde{\kappa}_6(n_{D_s}) =& \frac{\partial^6 \langle n_{D_s} \rangle}{\partial(\mu_B/T)^6}\bigg|_{\mu_B=0} \\
=& (-90\mu_2^3\tilde{\mu}_0 - \mu_6\tilde{\mu}_0 + 90\mu_2^2\tilde{\mu}_2 - 15\mu_4\tilde{\mu}_2 + 15\mu_2(2\mu_4\tilde{\mu}_0 - \tilde{\mu}_4) + \tilde{\mu}_6) \\
\tilde{\kappa}_8(n_{D_s}) =& \frac{\partial^8 \langle n_{D_s} \rangle}{\partial(\mu_B/T)^8}\bigg|_{\mu_B=0} \\
=& (2520\mu_2^4\tilde{\mu}_0 + 70\mu_4^2\tilde{\mu}_0 - \mu_8\tilde{\mu}_0 - 2520\mu_2^3\tilde{\mu}_2 - 28\mu_6\tilde{\mu}_2 - 420\mu_2^2(3\mu_4\tilde{\mu}_0 - \tilde{\mu}_4) \\
& - 70\mu_4\tilde{\mu}_4 + 28\mu_2(2\mu_6\tilde{\mu}_0 + 30\mu_4\tilde{\mu}_2 - \tilde{\mu}_6) + \tilde{\mu}_8).
\end{aligned} \tag{6.39}$$

A far more sophisticated structure emerges here with significantly more terms that mix contributions from different moments. The Taylor expansion in terms of these defined coefficients reads

$$\begin{aligned}
\Delta p =& \frac{1}{3}\sum_{n=0}^{\infty} \frac{1}{(2n)!}\left(\frac{\mu_B}{T}\right)^{2n} \tilde{\kappa}_{2n}(N_{D_\sigma}) \\
=& \frac{1}{3}\sum_{n=0}^{\infty} \left(\frac{\mu_B}{T}\right)^{2n} \tilde{c}_{2n}(N_{D_\sigma}),
\end{aligned} \tag{6.40}$$

with the Taylor coefficients $\tilde{c}_{2n}(N_{D_\sigma})$ depending on the spatial dimer number, $N_{D_\sigma} = n_{D_\sigma} V_\sigma$.

The moments in Eq. (6.39) can be evaluated in a similar fashion to the homogeneous analysis. However, more histograms are required. In addition to the histogram in the polymer number, it is necessary to also measure a histogram in the spatial dimer density as well as in all different mixed contributions $n_{D_\sigma}\omega^{2n}$. The crucial difference is, that the new histograms are not limited in their number of entries since the CT limit allows infinite many spatial dimers. Therefore, a fixed and finite limiting value is set for the histogram size.

Within the scope of this thesis, results for the reconstruction of the pressure are limited to a non-histogram simulation but including a polymer resummation (see Fig. 6.17). The reconstruction of the pressure is analyzed for four different temperatures in the range of $0.56\,T_c$ up to $\sim T_c$. The lowest temperature ratio is slightly below T_{TCP}. As discussed in Fig. 4.7 the pressure shows an almost immediate jump from ~ 0 to a finite value at the phase transition. For temperatures $T_{\mathrm{TCP}} < T < T_c$ the transition is 2^{nd} order in the chiral limit and the jump in the pressure becomes smoother. A reconstruction of the pressure in the temperature regime $T < T_c$ is only possible from the series' origin to the nearest non-analytic

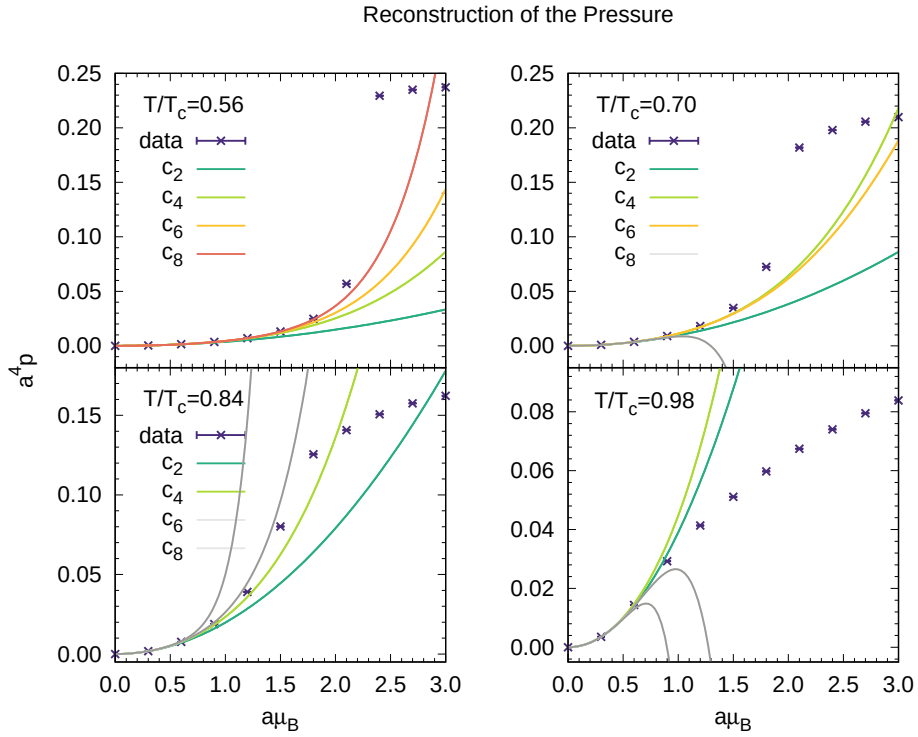

Figure 6.17: *Reconstruction of the pressure a^4p based on Taylor coefficients extracted from moments in the spatial dimer and baryon number density as well as mixed contributions on a 10^3 volume. A polymer resummation scheme is used for the calculation of the baryon number densities. At successively larger temperatures the coefficients $\tilde{\kappa}_6$ and $\tilde{\kappa}_8$ have large errors and should not be considered for a Taylor expansion. The respective expansions are shown in grey color.*

point. Beyond that the series expansion fails.

Since no histograms are used, only low order Taylor expansion coefficients can be considered. In the Appendix Fig. D.2 depicts the modified cumulants obtained by simulations with and without enforcing a polymer resummation scheme. Based on this as well as the observations made in Fig. 6.4 and 6.5, it can be expected that $\tilde{\kappa}_2$ and $\tilde{\kappa}_4$ reproduce the pressure while $\tilde{\kappa}_6$ and $\tilde{\kappa}_8$ can only be incorporated for low temperatures $T/T_c < 0.7$. Due to the more complex structure of the new coefficients, it can also be assumed that the order of the highest Taylor coefficient to be extracted with reasonable errors is lower. The polymer resummation scheme only affects the baryon number density while the spatial dimer density and combinations of these observables are afflicted by larger uncertainties.

6.7 Discussion

The Taylor expansion method is a powerful tool in QCD to access and learn about the finite density region. However, Taylor expansions in full QCD are typically restricted to just a

few low order coefficients. Therefore, often some QCD like models are chosen to discuss a wider range of Taylor coefficients as well as the radius of convergence. The SC limit is such a model which shares many important properties of QCD. It also provides the opportunity to go beyond the strong coupling limit and include β corrections.

In SC-LQCD, it is not necessary to use a Taylor expansion method as the sign problem is so mild that simulations can already be performed at finite μ_B, pinpointing the location of the TCP to $(a\mu_{B,\mathrm{TCP}}, a\mathcal{T}_{\mathrm{TCP}}) = ((1.95(5), 1.005(25)))$ in the chiral limit. However, in order to learn about the features of the expansion coefficients and to study the radius of convergence, a Taylor expansion was performed for the CT limit within the SC-LQCD framework. The analysis is based on an expansion of the pressure by assuming the system to be homogeneous. Crosschecks worked out well and showed agreement concerning an extrapolation in N_τ as well as with the static limit. In two dimensions with $N_\sigma = 2$ it is possible to formulate the partition function analytically and again the correctness of the extraction of the Taylor coefficients was emphasized.

Simulations in $3+1$ dimensions were performed on a $10^3 \times \mathrm{CT}$ lattice in order to compare with literature results for a discrete time analysis on a $10^3 \times 4$ lattice. Clearly, the CT limit performed better but not beyond κ_4. Apart from the polymer resummation, a histogram method was presented which allowed an analysis for $16^3 \times \mathrm{CT}$ and $32^3 \times \mathrm{CT}$ lattices up to κ_8. For the smaller $10^3 \times \mathrm{CT}$ volume also κ_{10} and κ_{12} are under control.

The volume dependency of the cumulants was analyzed. A larger volume leads to fluctuations in κ_{2n} to be in close vicinity to T_c and in the thermodynamic limit these narrow down to a single singularity at T_c. Additionally, each order in Taylor coefficients introduces a more complex structure with an increasing number of inflection points.

Based on the obtained Taylor coefficients for the $10^3 \times \mathrm{CT}$ study, the radius of convergence was constructed. Due to the number of available κ_{2n}, more complex estimators were used for the analysis. Interestingly, the radius of convergence for the baryon number density approaches the numerical transition line from large chemical potentials and clearly showed signs of convergence. An even better approximation of the transition was obtained for an expansion based on the baryon number susceptibility. In general, it is expected that susceptibilities are a better indicator for a chiral transition as they diverge at the respective location. At imaginary μ_B no transition can be observed from the data. The reconstruction of the phase transition in the chiral limit is very fruitful but also showed that κ_{12} should not be used due to increasing errors and uncontrolled behavior. Therefore, it is not possible to say whether there is an imprint of the TCP in κ_{12} and maybe also in all orders beyond that.

Finally, for the reconstruction of the pressure it was necessary to reformulate the Taylor

expansion in terms of the spatial dimer density. The respective Taylor coefficients become more complex but clearly reconstruct the pressure measured on the CT lattice. It is assumed that the Taylor expansion will reconstruct the data until the inflection point below T_c and completely above T_c. In order to see a possible imprint of the TCP and thus, to pinpoint the location of the TCP by means of the reconstruction of the pressure, it is necessary to perform a histogram analysis. So far, the polymer resummation scheme can only lead to improvements for measurements of moments in the baryon number density. A histogram method would most certainly yield for higher order expansion coefficients. However, due to the more complex Taylor coefficients it is challenging to reasonably measure expansion coefficients up to $\tilde{\kappa}_{12}$ or to go even beyond.

Chapter 7

Conclusion and Outlook

Within this thesis, the *continuous time limit* was explored for lattice QCD in the strong coupling limit based on a dual formulation. The examination of this distinct limit involved the derivation of the continuous time partition function $\mathcal{Z}_{\mathrm{CT}}$ (chapter 2), the formulation of an algorithm that samples the respective function and an extensive study of the features (chapter 3). Various crosschecks were performed and first measurements yielded results on the critical temperature T_c, the pion decay decay constant F_π and the chiral condensate Σ (chapter 4). Based on this formulation, two key research areas within lattice QCD were addressed:

1. The study of temporal correlation functions at zero and finite density (chapter 5),
2. and the inspection of the finite density phase diagram of QCD by means of the Taylor expansion method (chapter 6).

In chapter 2 the continuous time partition function was derived fully analytically based on the discrete time formulation of SC-LQCD and the simultaneous limit of $\gamma \to \infty$ and $N_\tau \to \infty$. The key observation was that spatial hopping are strongly affected by the CT limit. Baryonic hoppings are completely suppressed for $N_c \geq 3$ such that baryons are static while mesonic hoppings are strongly restricted. This restriction is encoded in the meson state raising and lowering operators which are the essential building blocks of the Hamiltonian. These operators restrict the possible changes in the meson state to one unit $\mathfrak{m} \to \mathfrak{m}' = \mathfrak{m} \pm 1$. The derived partition function expressed by a Quantum Hamiltonian has the desired structure in order to work towards the $N_f = 2$ formulation. For such a future study mainly the meson state raising and lowering operators have to be adjusted accordingly (see [46]). Additionally, a quark mass dependence can be incorporated in the CT limit [100].
Based on the formulation of the continuous time partition function a respective algorithm was implemented and described in detail in chapter 3. In order to sample Eq. (2.35) a worm type algorithm was used. The key characteristic of the algorithm is the use of a Poisson process to distribute spatial hoppings evenly in time without any dependence on previous emission events. Other properties such as the interplay of Absorption and Emission Updates are general features of a worm type algorithm. Its many advantages compared to discrete time analyses make it a highly interesting formulation in future studies. However, the flexibility of

the algorithm has to be strongly improved as it is constraint so far to the chiral and strong coupling limit with one flavor. This is an essential part to work on and fix in the near future.

Finally, CT worm simulation were performed, followed by an analysis of the results in chapter 4. The obtained data sets for various dual observables were checked with simulations on DT lattices as well as with literature. For this crosscheck it was most helpful that dual observables in the CT limit have a much simpler structure with no anisotropy calibration required. For various observables it was graphically pointed out that the CT results match extrapolations from DT simulations. The determination of the critical temperature $a\mathcal{T}_c^{\mathrm{CT}} = 1.4276(2)$ at $\mu_B = 0$ led to a reasonable correction compared to studies for $a\mathcal{T}_c^{\mathrm{DT}}$ from literature. This discrepancy was also observed for the measurement of the continuous time specific proportionality factor κ as well as for the pion decay constant F_π. Again, this strongly supports that extrapolations in N_τ or ξ should be avoided if the analysis can be performed in the CT framework. It is important to notice that previous error estimations were unable to predict such a high inaccuracy as pointed out in this work for the mentioned observables. Altogether, the accuracy in κ, T_c or F_π could still be improved, although, the focus should be on including gauge corrections such that results could possibly be meaningfully related to studies at finite gauge coupling β.

In chapter 5 the extraction of pole masses from temporal meson correlation functions was discussed. For DT simulations a combined fit considering states in both the Non-Oscillating and Oscillating sector is necessary. Since there is a finite resolution in temporal direction, an alternating structure emerges which requires an averaging in order to reconstruct the correlators associated with the taste partners. In contrast, in continuous time there is an "infinite resolution" such that the averaging is already incorporated in the data and Non-Oscillating and Oscillating correlators are obtained directly from the histogram measurement. Therefore, it is possible to perform separate fits for the two taste partners. Based on a correlated fit analysis presented in [14] the pole masses were extracted and the anaysis revealed that mainly the ground state contributed to the mass plateau. No such plateau was obtained for excited state contributions. A possible reason for an unsatisfying signal of excited states could be the simulation temperature. It might be helpful to perform further analysis at temperatures below T_c where the worm length increases significantly due to the higher spatial dimer density. Therefore, the signal in the region of expected excited states should get stronger and possibly the associated masses can be restored. It was observed that the meson masses for all kernels yield the same (finite) high-temperature limit. In the strong coupling limit, the mesons do not split up into quarks in the deconfined phase and are still subject to bosonic boundary conditions. Therefore, there is no thermal mass contribution and the meson masses remain finite. Finally, it is expected that the sign problem for real-time worm simulations is under control in the strong coupling limit. Thus, the Schwinger-Keldysh Contour can be constructed which would allow the extraction of transport coefficients.

The final chapter of this thesis explored the Taylor expansion method performed for the pressure (see chapter 6). Based on the homogeneous definition of the pressure the Taylor coefficients were reconstructed by measurements of baryon density moments. The static baryon feature of the CT formulation was already helpful for obtaining distinctly better results for $\kappa_4(\Omega_B)/V_\sigma$ compared to DT studies in literature. However, in order to address significantly higher orders it was required to apply a polymer resummation scheme as well as a histogram method giving rise to Taylor coefficients up to order 12. The histogram method is a powerful tool to improve on accuracy and enhance variability since arbitrary baryon density moments are reconstructed fully analytically. The Taylor coefficients revealed the expected behavior of additional fluctuations emerging in the vicinity of T_c as the order in κ_{2n} is increased. The determination of the radius of convergence is helpful to get a first estimate on the location of the transition line when based on the baryon density. A Taylor expansion in the baryon susceptibility was very promising as results for orders ≥ 8 are partly identical with the transition line around T_c. Even though the Mercer-Roberts estimator did not yield a great improvement in the results for the baryon susceptibility, it might be of interest for future studies to investigate further improved estimators as well as to go to larger volumes. The reconstruction of the pressure required a Taylor expansion in the spatial dimer density. The pressure at strong coupling is that of an inhomogeneous system and thus, it cannot be obtained from a Taylor expansion as performed before. Even though the structure of the expansion gets more involved with a contribution mixing spatial dimer density and baryon density moments, it is clearly possible to reconstruct the pressure based on Taylor coefficients up to order four. Obviously, a histogram method is also required for this analysis. However, it might be more challenging to obtain the same accuracy compared to the expansion for a homogeneous system because the spatial dimer number is not limited. Therefore, it requires some cut-off in order to fit into a finite sized histogram. Especially at temperatures in the vicinity of T_c or below this cut-off is severe.

The CT limit with its many assets served to be versatile and worth to study. Several important quantities were verified or corrected by the direct measurements in the CT limit. It was possible to construct temporal correlators at zero and finite density. Pole masses were studied at finite temperature associated with various channels. Finally, a powerful method for the construction of Taylor coefficients for the pressure was set up. These coefficients were used to reconstruct the first order transition line down to $T/T_c = 0.5$ in the finite density plane of SC-LQCD in the chiral limit.

Bibliography

[1] D. Bes. *Quantum Mechanics: A Modern and Concise Introductory Course*. Springer-Verlag Berlin Heidelberg, 2012.

[2] Max Planck. "Zur Theorie des Gesetzes der Energieverteilung im Normalspektrum. (German) [On the Theory of Distribution of Energy in the Normal Spectrum]". German. In: *VERH-DTSCH-PHYS-GES* 2.17 (Dec. 1900). English translation in [103]. In this paper, Planck introduces a formula for the blackbody radiation law, and also derives estimates of Loschmidt's number L (proportional to Avogadro's number), the Boltzmann–Drude constant α, and the electron charge, e., pp. 237–245.

[3] Albert Einstein. "Concerning an heuristic point of view toward the emission and transformation of light". In: *Annalen Phys.* 17 (1905), pp. 132–148.

[4] Ernest Rutherford. "The Building up of Atoms". In: *Engineering (London, UK)* 110 (1920), pp. 382–382.

[5] J. Chadwick. "Possible Existence of a Neutron". In: *Nature* 129 (1932), p. 312.

[6] Murray Gell-Mann. "Symmetries of baryons and mesons". In: *Phys. Rev.* 125 (1962), pp. 1067–1084.

[7] Murray Gell-Mann. "A Schematic Model of Baryons and Mesons". In: *Phys. Lett.* 8 (1964), pp. 214–215.

[8] G. Zweig. "An SU(3) model for strong interaction symmetry and its breaking. Version 2". In: *DEVELOPMENTS IN THE QUARK THEORY OF HADRONS. VOL. 1. 1964 - 1978*. Ed. by D.B. Lichtenberg and Simon Peter Rosen. Published in 'Developments in the Quark Theory of Hadrons'. Volume 1, 1964, pp. 22–101.

[9] David J. Gross and Frank Wilczek. "Ultraviolet Behavior of Non-Abelian Gauge Theories". In: *Phys. Rev. Lett.* 30 (26 1973), pp. 1343–1346.

[10] Helmut Satz. "The Quark-Gluon Plasma: A Short Introduction". In: *Nucl. Phys.* A862-863 (2011), pp. 4–12.

[11] Kenneth G. Wilson. "Confinement of quarks". In: *Phys. Rev. D* 10 (8 1974), pp. 2445–2459.

[12] Philippe de Forcrand et al. "Lattice QCD Phase Diagram In and Away from the Strong Coupling Limit". In: *Phys. Rev. Lett.* 113.15 (2014), p. 152002.

[13] Wolfgang Unger and Philippe de Forcrand. *Continuous Time Monte Carlo for Lattice QCD in the Strong Coupling Limit*. 2011.

[14] Hauke Sandmeyer. "Hadronic correlators from heavy to very to very light quarks". In: (2019).

[15] Anthony Francis. "Improved Staggered Lattice Meson Operators - A study of wall, fuzzed and coulombic meson operators in staggered 2 and 2+1 flavour lattice QCD at zero and finite temperature". MA thesis. Universität Bielefeld, 2008.

[16] R. V. Gavai and Sourendu Gupta. "QCD at finite chemical potential with six time slices". In: *Phys. Rev.* D78 (2008), p. 114503.

[17] S. Ejiri et al. "The Isentropic equation of state of 2-flavor QCD". In: *Phys. Rev.* D73 (2006), p. 054506.

[18] A. Bazavov et al. "The QCD Equation of State to $\mathcal{O}(\mu_B^6)$ from Lattice QCD". In: *Phys. Rev.* D95.5 (2017), p. 054504.

[19] Wikimedia Commons. *File:Standard Model of Elementary Particles.svg — Wikimedia Commons, the free media repository*. [Online; accessed 11-February-2020]. 2020.

[20] Heinz J. Rothe. *Lattice Gauge Theories: AN Introduction (third Edition)*. World Scientific Publishing Co. Pte. Ltd., 2005.

[21] Walter Greiner and Stefan Schramm. *Quantum chromodynamics*. Springer-Verlag, 2007.

[22] Christof Gattringer and Christian B. Lang. "Quantum chromodynamics on the lattice". In: *Lect. Notes Phys.* 788 (2010), pp. 1–343.

[23] Manfried Faber and Roman Höllwieser. "Chiral symmetry breaking on the lattice". In: *Progress in Particle and Nuclear Physics* 97 (2017), 312–355.

[24] M. Tanabashi et al. "Review of Particle Physics". In: *Phys. Rev. D* 98 (3 2018), p. 030001.

[25] Patrick Steinbrecher. "The QCD crossover at zero and non-zero baryon densities from Lattice QCD". In: *Nuclear Physics A* 982 (2019), 847–850.

[26] Vladimir G. Ivancevic and Tijana T. Ivancevic. *Natural biodynamics / Vladimir G. Ivancevic, Tijana T. Ivancevic*. English, xxxiii, 1001p. :

[27] Michael E. Peskin and Daniel V. Schroeder. *An Introduction to quantum field theory*. Reading, USA: Addison-Wesley, 1995.

[28] Zoltan Fodor and Christian Hoelbling. "Light hadron masses from lattice QCD". In: *Reviews of Modern Physics* 84.2 (2012), 449–495.

[29] Thomas DeGrand and Carleton E. Detar. *Lattice methods for quantum chromodynamics*. World Scientific Publishing Company, 2006.

[30] Michael Fromm. "Lattice QCD at strong coupling thermodynamics and nuclear physics". PhD thesis. ETH Zurich, 2010.

[31] Gert Aarts. "Introductory lectures on lattice QCD at nonzero baryon number". In: *Journal of Physics: Conference Series* 706 (2016), p. 022004.

[32] Giuseppe Gagliardi and Wolfgang Unger. "New dual representation for staggered lattice QCD". In: *Phys. Rev. D* 101.3 (2020), p. 034509.

[33] Pietro Rossi and Ulli Wolff. "Lattice QCD With Fermions at Strong Coupling: A Dimer System". In: *Nucl. Phys.* B248 (1984), pp. 105–122.

[34] Ulli Wolff. "Baryons in Lattice QCD at Strong Coupling". In: *Phys. Lett.* 153B (1985), pp. 92–96.

[35] F. Karsch and K. H. Mutter. "STRONG COUPLING QCD AT FINITE BARYON NUMBER DENSITY". In: *Nucl. Phys.* B313 (1989), pp. 541–559.

[36] Philippe de Forcrand, Wolfgang Unger, and Hélvio Vairinhos. “Strong-coupling lattice QCD on anisotropic lattices”. In: *Phys. Rev. D* 97 (3 2018), p. 034512.

[37] N. Metropolis et al. “Equation of state calculations by fast computing machines”. In: *J. Chem. Phys.* 21 (1953), pp. 1087–1092.

[38] M. H. Quenouille. “Approximate Tests of Correlation in Time-Series”. In: *Journal of the Royal Statistical Society. Series B (Methodological)* 11.1 (1949), pp. 68–84.

[39] J.W. Tukey. “Bias and Confidence in Not-quite Large Samples”. In: *Ann. Math. Statist.* 29.2 (June 1958), pp. 614–623.

[40] A. Cameron and Pravin Trivedi. *Microeconometrics Using Stata*. Vol. 5. College Station, Tex. : Stata Press, Jan. 2010.

[41] Michael Chernick. *Bootstrap Methods: A Guide for Practitioners and Researchers, Second Edition*. Wiley-Interscience, Jan. 2008.

[42] Rupert G. Miller. “The Jackknife–A Review”. In: *Biometrika* 61.1 (1974), pp. 1–15.

[43] B. Efron. “Bootstrap Methods: Another Look at the Jackknife”. In: *The Annals of Statistics* 7.1 (1979), pp. 1–26.

[44] J. Shao and D. TU. *The Jackknife and Bootstrap*. Springer, 1995.

[45] Neven Bilic, Frithjof Karsch, and Krzysztof Redlich. “Flavor dependence of the chiral phase transition in strong-coupling QCD”. In: *Phys. Rev. D* 45 (9 1992), pp. 3228–3236.

[46] M. Klegrewe and W. Unger. “Strong Coupling QCD in the Continuous Time Limit”. In: - (2020).

[47] B. B. Beard and U. J. Wiese. “Simulations of discrete quantum systems in continuous Euclidean time”. In: *Phys. Rev. Lett.* 77 (1996), pp. 5130–5133.

[48] Emanuel Gull et al. “Continuous-time Monte Carlo methods for quantum impurity models”. In: *Reviews of Modern Physics* 83.2 (2011), 349–404.

[49] Nikolay Prokof’ev and Boris Svistunov. “Worm Algorithms for Classical Statistical Models”. In: *Physical Review Letters* 87.16 (2001).

[50] Nikolay Prokof’ev, B. Svistunov, and Igor Tupitsyn. “"’Worm"’ algorithm in quantum Monte Carlo simulations”. In: *pla* 238 (Feb. 1998), pp. 253–257.

[51] Frederick James. *Statistical methods in experimental physics*. World Scientific, 2006, 2006.

[52] David H. Adams and Shailesh Chandrasekharan. “Chiral limit of strongly coupled lattice gauge theories”. In: *Nuclear Physics B* 662.1-2 (2003), 220–246.

[53] Dennis Bollweg. “The Equation of State of lattice QCD in the strong coupling limit”. MA thesis. Bielefeld University, 2018.

[54] G. Burgers et al. “QCD ON ANISOTROPIC LATTICES”. In: *Nucl. Phys.* B304 (1988), pp. 587–600.

[55] Frithjof Karsch. “SU(N) gauge theory couplings on asymmetric lattices”. In: *Nuclear Physics, B* 205.2 (1982), pp. 285–300.

[56] Shailesh Chandrasekharan and Fu-Jiun Jiang. “Chiral limit of strongly coupled lattice QCD at finite temperatures”. In: *Phys. Rev. D* 68 (9 2003), p. 091501.

[57] W. Unger, Dennis Bollweg, and Marc Klegrewe. “Thermodynamics at Strong Coupling on Anisotropic Lattices”. In: *PoS* LATTICE2018 (2018), p. 181.

[58] P. Hasenfratz and H. Leutwyler. “Goldstone Boson Related Finite Size Effects in Field Theory and Critical Phenomena With O(N) Symmetry”. In: *Nucl. Phys.* B343 (1990), pp. 241–284.

[59] J. Gasser and H. Leutwyler. “Thermodynamics of Chiral Symmetry”. In: *Phys. Lett.* B188 (1987), pp. 477–481.

[60] Philippe de Forcrand and Massimo D’Elia. *Continuum limit and universality of the Columbia plot*. 2017.

[61] Massimo Campostrini et al. “Critical behavior of the three-dimensionalXYuniversality class”. In: *Physical Review B* 63.21 (2001).

[62] John Kogut and D. Sinclair. “Evidence for O(2) universality at the finite temperature transition for lattice QCD with 2 flavors of massless staggered quarks”. In: *Physical Review D - PHYS REV D* 73 (Apr. 2006).

[63] F. Karsch and E. Laermann. *Thermodynamics and in-medium hadron properties from lattice QCD*. 2003.

[64] Ines Wetzorke. “Lattice QCD Calculations of Hadron Spectra and Spectral Functions in the Vacuum and in a Thermal Heat Bath”. PhD thesis. Universität Bielefeld, 2001.

[65] M. C. Tichy and P. Faccioli. *The Scalar Glueball in the Instanton Vacuum*. 2007.

[66] Johannes Weber et al. *An introduction to lattice hadron spectroscopy for students without quantum field theoretical background*. 2013.

[67] CLIFFORD M. HURVICH and CHIH-LING TSAI. “Regression and time series model selection in small samples”. In: *Biometrika* 76.2 (June 1989), pp. 297–307.

[68] G. Boyd et al. “Spatial and temporal hadron correlators below and above the chiral phase transition”. In: *Zeitschrift für Physik C Particles and Fields* 64.2 (1994), 331–338.

[69] ÁGNES MÓCSY, PÉTER PETRECZKY, and MICHAEL STRICKLAND. “Quarkonia in the quark gluon plasma”. In: *International Journal of Modern Physics A* 28.11 (2013), p. 1340012.

[70] Alexei Bazavov et al. *Hot-dense Lattice QCD: USQCD whitepaper 2018*. 2019.

[71] H.-T. Ding et al. “Thermal dilepton rate and electrical conductivity: An analysis of vector current correlation functions in quenched lattice QCD”. In: *Physical Review D* 83.3 (2011).

[72] H-T Ding et al. “Heavy quark diffusion from lattice QCD spectral functions”. In: *Journal of Physics G: Nuclear and Particle Physics* 38.12 (2011), p. 124070.

[73] Gert Aarts et al. “Electrical conductivity and charge diffusion in thermal QCD from the lattice”. In: *Journal of High Energy Physics* 2015.2 (2015).

[74] Andrei Alexandru et al. “Monte Carlo Study of Real Time Dynamics on the Lattice”. In: *Physical Review Letters* 117.8 (2016).

[75] Frank R. Brown et al. “On the existence of a phase transition for QCD with three light quarks”. In: *Phys. Rev. Lett.* 65 (20 1990), pp. 2491–2494.

[76] Sean Gavin, Andreas Gocksch, and Robert D. Pisarski. "QCD and the chiral critical point". In: *Phys. Rev.* D49 (1994), R3079–R3082.

[77] Yoshitaka Hatta and Takashi Ikeda. "Universality, the QCD critical and tricritical point, and the quark number susceptibility". In: *Physical Review D* 67.1 (2003).

[78] Philippe de Forcrand. "Simulating QCD at finite density". In: *PoS* LAT2009 (2009), p. 010.

[79] M. A. Stephanov. *QCD phase diagram: an overview*. 2006.

[80] T. Anticic et al. "Search for the QCD critical point in nuclear collisions at the CERN SPS". In: *Phys. Rev.* C81 (2010), p. 064907.

[81] Anton Andronic et al. "Decoding the phase structure of QCD via particle production at high energy". In: *Nature* 561.7723 (2018), pp. 321–330.

[82] D. Cebra and STAR Collaboration. "Studying the Phase Diagram on QCD Matter at RHIC". In: *APS Division of Nuclear Physics Meeting Abstracts*. Sept. 2014, FJ.001.

[83] Heng-Tong Ding. "Lattice QCD at nonzero temperature and density". In: *PoS* LATTICE2016 (2017), p. 022.

[84] Lorenzo Bongiovanni. "Numerical methods for the sign problem in Lattice Field Theory". PhD thesis. Swansea U., 2015.

[85] Christof Gattringer. "New developments for dual methods in lattice field theory at non-zero density". In: *PoS* LATTICE2013 (2014), p. 002.

[86] Owe Philipsen. "Lattice QCD at non-zero temperature and baryon density". In: *Modern perspectives in lattice QCD: Quantum field theory and high performance computing. Proceedings, International School, 93rd Session, Les Houches, France, August 3-28, 2009*. 2010, pp. 273–330.

[87] Szabolcs Borsanyi et al. "Higher order fluctuations and correlations of conserved charges from lattice QCD". In: *JHEP* 10 (2018), p. 205.

[88] Saumen Datta, Rajiv V. Gavai, and Sourendu Gupta. "Quark number susceptibilities and equation of state at finite chemical potential in staggered QCD with Nt=8". In: *Phys. Rev.* D95.5 (2017), p. 054512.

[89] Mark Abraao York and Guy D. Moore. *Exploring the Phase Diagram with Taylor Series: Epic Voyage or Just Another Bad Trip*. 2011.

[90] Mizuki Shirogane et al. "Latent heat at the first order phase transition point of SU(3) gauge theory". In: *Phys. Rev. D* 94 (1 2016), p. 014506.

[91] G. Grimmett, D.J.A. Welsh, and D. Welsh. *Probability: An Introduction*. Oxford University Press. Clarendon Press, 2014.

[92] Michael George Bulmer. *Principles of statistics*. 2. ed. Cambridge, Mass.: M.I.T. Press, 1967. VII, 252.

[93] C. R. Allton et al. "Thermodynamics of two flavor QCD to sixth order in quark chemical potential". In: *Phys. Rev.* D71 (2005), p. 054508.

[94] Volodymyr Vovchenko et al. "Cluster expansion model for QCD baryon number fluctuations: No phase transition at μ_B/T<π". In: *Phys. Rev. D* 97 (11 2018), p. 114030.

[95] F. Karsch et al. “Towards finite density QCD with Taylor expansions”. In: *Physics Letters B* 698.3 (2011), 256–264.

[96] G. Mercer and A. Roberts. “A Centre Manifold Description of Contaminant Dispersion in Channels with Varying Flow Properties”. In: *Siam Journal on Applied Mathematics - SIAMAM* 50 (Dec. 1990).

[97] C. Domb and M. F. Sykes. “On the Susceptibility of a Ferromagnetic above the Curie Point”. In: *Proceedings of the Royal Society of London. Series A, Mathematical and Physical Sciences* 240.1221 (1957), pp. 214–228.

[98] M. Giordano and A. Pásztor. “Reliable estimation of the radius of convergence in finite density QCD”. In: *Physical Review D* 99 (June 2019).

[99] C. Domb and J. L. Lebowitz. *PHASE TRANSITIONS AND CRITICAL PHENOMENA. VOL. 13*. London: Academic Press, 1989.

[100] Timo Kaya. “Analysis of Critical Behavior in Strong Coupling QCD with an improved Worm algorithm’”. MA thesis. Universität Bielefeld, 2019.

[101] David Griffiths. *Introduction to elementary particles*. John Wiley & Sons, 2008.

[102] C. A. Meyer and Y. Van Haarlem. “Status of exotic-quantum-number mesons”. In: *Physical Review C* 82.2 (2010).

[103] Max Planck. “On the Theory of the Energy Distribution Law of the Normal Spectrum”. In: *The Old Quantum Theory*. The Commonwealth and international library. Selected readings in physics. English translation of [2]. Oxford, UK: Pergamon Press, 1969, pp. 82–90.

List of Figures

List of Tables

Appendix

A "Exact" Continuous Time Partition Function for $2 \times$ CT Lattice.

The two-dimensional continuous time partition function (6.20) is structured in two contributions, a static and a dynamic part. Latter contains all the corrections to the static limit due to meson and baryon hoppings. As it has been pointed out it is sufficient to include the first three non-zero contributions to get accurate results on a $2 \times$ CT lattice. Nevertheless, for larger N_σ and dimensions the corrections to the static limit are expected to get more complex and higher orders will be required. Therefore, it is useful to formulate the $2 \times$ CT partition function to whatever order is possible.

A.1 Numeric approach

Instead of checking for the fulfillment of the Grassmann constraint with pen and paper, it is strongly recommended to transfer the problem to a computer. The task is to generate all combinations of n spatial dimers attached to a site, where $n/2$ indistinguishable emission and absorption sites are distributed respectively. These sets of absorption and emission sites must not violate the Grassmann constraint. Thus, the meson states have to be kept in a range ≥ 0 or $\leq N_c$. There are $\binom{n}{n/2}$ possible configurations which then have to be checked for the GC. Most approaches run into the problem of generating $n!$ configurations and sorting out the duplicates on the run. Almost all standard build in functions will therefore fail for $n > 16$. Let's say $k = 6$ spatial dimers are considered. All combinations of three emission and absorption sites distributed in a row have to be found which are a total of $\binom{6}{3} = 20$. Instead of generating $6! = 720$ configurations and removing the duplicates it is far more efficient to only generate the required 20. This is done by shifting blocks of different sizes. The initial setup is a sorted array

$$i) \quad 1 \quad 2 \quad 3 \quad 4 \quad 5 \quad 6. \tag{A.1}$$

As a first step, blocks of size $n/2$ ($\boxed{1\ 2\ 3}$) are shifted from left to right:

$$\begin{aligned} ii) \quad & 4 \quad \boxed{1 \quad 2 \quad 3} \quad 5 \quad 6 \\ iii) \quad & 4 \quad 5 \quad \boxed{1 \quad 2 \quad 3} \quad 6 \\ iv) \quad & 4 \quad 5 \quad 6 \quad \boxed{1 \quad 2 \quad 3} \end{aligned} \tag{A.2}$$

As a next step the size of the block is reduced by one such that a block containing the last $(n/2 - 1 = 2)$ elements is shifted from left to right. There will be three new combinations for

i), two new ones ii) and one for iv):

$$\begin{array}{rcccccc}
i) \rightarrow v) & 1 & 4 & \boxed{2} & \boxed{3} & 5 & 6 \\
vi) & 1 & 4 & 5 & \boxed{2} & \boxed{3} & 6 \\
vii) & 1 & 4 & 5 & 6 & \boxed{2} & \boxed{3} \\
ii) \rightarrow viii) & 4 & 1 & 5 & \boxed{2} & \boxed{3} & 6 \\
ix) & 4 & 1 & 5 & 6 & \boxed{2} & \boxed{3} \\
iii) \rightarrow x) & 4 & 5 & 1 & 6 & \boxed{2} & \boxed{3}
\end{array} \tag{A.3}$$

This step is repeated until a single element is left in a block. For this specific example a shift of the last element in the box ($\boxed{3}$) yields the combinations:

$$\begin{array}{rcccccc}
i) \rightarrow xi) & 1 & 2 & 4 & \boxed{3} & 5 & 6 \\
xii) & 1 & 2 & 4 & 5 & \boxed{3} & 6 \\
xiii) & 1 & 2 & 4 & 5 & 6 & \boxed{3} \\
ii) \rightarrow xiv) & 4 & 1 & 2 & 5 & \boxed{3} & 6 \\
xv) & 4 & 1 & 2 & 5 & 6 & \boxed{3} \\
iii) \rightarrow xvi) & 4 & 5 & 1 & 2 & 6 & \boxed{3} \\
v) \rightarrow xvii) & 1 & 4 & 2 & 5 & \boxed{3} & 6 \\
xviii) & 1 & 4 & 2 & 5 & 6 & \boxed{3} \\
vi) \rightarrow xix) & 1 & 4 & 5 & 2 & 6 & \boxed{3} \\
ix) \rightarrow xx) & 4 & 1 & 5 & 2 & 6 & \boxed{3}
\end{array} \tag{A.4}$$

With this approach all possible configurations with up to $k = 28$ spatial dimers can be analyzed within minutes. Results are listed in Table A.1. It is only a question of memory whether all combinations can be stored such that it is also possible to go beyond $k = 28$. Here, the creative mind can improve by already evaluating configurations with boxes that are completely shifted through and then dropping these out of the memory while keeping the ones which still have to considered.

Table A.1: *Number of configuration with* $\#\boldsymbol{D}$ *spatial dimers that contain n* $\mathcal{T}$*-shaped vertices* (v_T^n)*. A symmetry factor of* 8 *is factored out.*

#D	v_T^0	v_T^2	v_T^4	v_T^6	v_T^8	v_T^{10}	v_T^{12}	v_T^{14}	v_T^{16}	v_T^{18}	v_T^{20}	v_T^{22}	v_T^{24}	v_T^{26}	v_T^{28}	v_T^{30}	v_T^{32}	v_T^{34}
2	4	4	1	–	–	–	–	–	–	–	–	–	–	–	–	–	–	–
4	4	0	12	0	1	–	–	–	–	–	–	–	–	–	–	–	–	–
6	4	0	9	16	6	0	1	–	–	–	–	–	–	–	–	–	–	–
8	4	0	16	0	52	0	8	0	1	–	–	–	–	–	–	–	–	–
10	4	0	25	0	50	64	35	0	10	0	1	–	–	–	–	–	–	–
12	4	0	36	0	105	0	240	0	54	0	12	0	1	–	–	–	–	–
14	4	0	49	0	196	0	294	256	210	0	77	0	14	0	1	–	–	–
16	4	0	64	0	336	0	672	0	1172	0	352	0	104	0	16	0	1	–
18	4	0	81	0	540	0	1386	0	1782	1024	1287	0	546	0	135	0	18	0
20	4	0	100	0	825	0	2640	0	4290	0	6052	0	2275	0	800	0	170	0
22	4	0	121	0	1210	0	4719	0	9438	0	11011	4096	8008	0	3740	0	1122	0
24	4	0	144	0	1716	0	8008	0	19305	0	27456	0	32944	0	14688	0	5814	0
26	4	0	169	0	2366	0	13013	0	37180	0	63206	0	68952	16384	50388	0	25194	0
28	4	0	196	0	3185	0	20384	0	68068	0	136136	0	176358	0	187808	0	94962	0

#D	v_T^{36}	v_T^{38}	v_T^{40}	v_T^{42}	v_T^{44}	v_T^{46}	v_T^{48}	v_T^{50}	v_T^{52}	v_T^{54}	v_T^{56}
2	–	–	–	–	–	–	–	–	–	–	–
4	–	–	–	–	–	–	–	–	–	–	–
6	–	–	–	–	–	–	–	–	–	–	–
8	–	–	–	–	–	–	–	–	–	–	–
10	–	–	–	–	–	–	–	–	–	–	–
12	–	–	–	–	–	–	–	–	–	–	–
14	–	–	–	–	–	–	–	–	–	–	–
16	–	–	–	–	–	–	–	–	–	–	–
18	1	–	–	–	–	–	–	–	–	–	–
20	20	0	1	–	–	–	–	–	–	–	–
22	209	0	22	0	1	–	–	–	–	–	–
24	1520	0	252	0	24	0	1	–	–	–	–
26	8645	0	2002	0	299	0	26	0	1	–	–
28	40964	0	12397	0	2576	0	350	0	28	0	1

A.2 Combinatorial approach

There are various systematics arising when taking a closer look at Table A.1. The first column v_T^0 always takes the value 4, while the last value of each line is a 1. The column v_T^4 contains only square numbers $\left(\frac{\#D}{2}\right)^2$ except for $\#D = 4$. There is an additional contribution from the diagonal $v_T^{\#D}$ which takes values of $2^{\#D/2+1}$ such that $\frac{4}{2}^2 + 2^{4/2+1} = 4 + 8 = 12$. There are further prominent features which finally lead to a generalization that holds for all columns with $n \pmod 4 = 0$ and $n > 0$:

$$C(\#D, n) = \#D \frac{\prod_{k=-n/4+1}^{n/4-1} (\#D/2 + k)}{(2\frac{n}{4})!} = \#D \frac{(\#D/2 + n/4 - 1)!}{(\#D/2 - n/4)!(n/2)!}. \tag{A.5}$$

Note that this equation is based on observations and does not provide a solid proof.

B Grassmann Integration

The quark fields represent fermions which have to behave according to Fermi statistics. These fields anti-commute with each other. This can be expressed in terms of Grassmann numbers which form an algebra with $2N$ generators $\eta_i, \bar{\eta}_j, i = 1, 2, \ldots, N$ that anti-commute [22]

$$\eta_i \eta_j = -\eta_j \eta_i, \quad \bar{\eta}_i \bar{\eta}_j = \bar{\eta}_j \bar{\eta}_i, \quad \bar{\eta}_i \eta_j = -\eta_j \bar{\eta}_i. \tag{B.1}$$

It follows that these numbers are nilpotent. A Grassmann variable being squared $\eta_i^2 = 0$ yields zero. Assuming that the Grassmann variables transform as

$$\eta'_j = \sum_{k=1}^{N} M_{jk} \eta_k, \tag{B.2}$$

the respective integration measure gives rise to the fermion determinant

$$d^N \eta \equiv d_N \eta \ldots d_1 \eta = \det[M] d^N \eta'. \tag{B.3}$$

The basic integration rules when dealing with Grassmann numbers are

$$\int d^N \eta \eta_1 \eta_2 \ldots \eta_N = 1, \quad \int d\eta_i 1 = 0, \quad \int d\eta_i \eta_i = 1. \tag{B.4}$$

Combing the insights from above gives rise to the Matthews-Salam formula

$$\mathcal{Z}_F = \int d\eta_N d\bar{\eta}_N \ldots d\eta_1 d\bar{\eta}_1 \exp\left(\sum_{i,j=1}^{N} \bar{\eta}_i M_{ij} \eta_j \right) = \det[M], \tag{B.5}$$

with M being a complex $N_c \times N_c$ matrix.

For the generating functional for fermions it is found that

$$W[\theta,\bar{\theta}] = \det(M)\exp\left(-\sum_{x,y}^{N}\bar{\theta}_x(M^{-1})_{xy}\theta_y\right) \tag{B.6}$$

with θ and θ' being Grassmann variables as well, which are not integrated over and serve as source terms. This functional is used to derive Wicks's theorem

$$\langle\eta_{i_1}\bar{\eta}_{j_1}\dots\eta_{i_n}\bar{\eta}_{j_n}\rangle_F = \frac{1}{\mathcal{Z}_F}\int\prod_{k=1}^{N}d\eta_k d\bar{\eta}_k d\eta_{i_1}d\bar{\eta}_{j_n}\dots i_n\exp\left(\sum_{l,m=1}^{N}\bar{\eta}_l M_{lm}\eta_m\right) \tag{B.7}$$

$$= (-1)^n\sum_{P(1,2\dots n)}\mathrm{sign}(P)(M^{-1})_{i_1 j_{P_1}}(M^{-1})_{i_2 j_{P_2}}\dots(M^{-1})_{i_n j_{P_n}}, \tag{B.8}$$

which is a fundamental formula for the discussion of fermion expectations values $\langle\dots\rangle_F$. The expectation value on the left-hand side of Eq. (B.7) is a n-point function which requires an equal number of η_i and $\bar{\eta}_j$ to be different from zero.

C Quantum Numbers

Particles are characterized and identified by their intrinsic quantum numbers. In the following those quantum numbers of interest for studying meson states are discussed [24],[66]:

- Total Angular Momentum J. Bosons take integer values ($J = 0, 1, \dots$), fermions half-integer values $J \in (\frac{1}{2}, \frac{3}{2}, \dots)$. Mesons and force carriers are all bosons.

- Flavor quantum numbers
  - Isospin I, $I_z \in (-I, -I+1, \dots I-1, I)$ and $I_z = \frac{1}{2}(n_u - n_d) \to +\frac{1}{2}(u), -\frac{1}{2}(d)$. Number of particles in multiplet is given by $2I+1$. I_z is related to the charge of a particle by Gell-Mann-Nishijima formula $Q = I_z + \frac{1}{2}(B+S)$.
  - Strangeness $S = -(n_s - n_{\bar{s}}) \to -1(s), +1(\bar{s})$
  - Charm $C = n_c - n_{\bar{c}} \to +1(c), -1(\bar{c})$
  - Bottomness $B = -(n_b - n_{\bar{b}}) \to -1(b), +1(\bar{b})$
  - Topness $T = n_t - n_{\bar{t}} \to +1(t), -1(\bar{t})$

  The mentioned quantum numbers are all additive.

- Parity $P = \pm 1$. While the parity of a boson particle agrees with its anti-particle, the parity of a fermion must be opposite to its counterpart. Thus, quarks q are often chosen to have positive parity. It is worth to mention that parity is a multiplicative quantum number. For compound meson states an extra factor of $(-1)^L$ (with L being the orbital angular momentum) occurs in determining the parity while for baryons its $(-1)^{L_{12}+L_3}$

Table C.1: *Behavior of different particle classes under the parity transformation.*

Scalar	$P(s) = s$
Pseudo-Scalar	$P(p) = -p$
Vector	$P(\mathbf{v}) = -\mathbf{v}$
Axial-Vector	$P(\mathbf{a}) = \mathbf{a}$

- Charge Conjugation $C = \pm 1$. Converts particles into anti-particles by changing the sign of all "internal" quantum numbers. Keeps spin, mass, energy and momentum fixed [101]. For meson states $q\bar{q}$ only electrically neutral states can be eigenstates of C. Typically, a G-parity is introduced to describe all states independent of their charge [102].

- Electrical Charge is not accounted for.

Meson states which have quantum numbers in accordance with the previous discussed ones are considered: J, I, P, C and G. Particles are referenced by shortly writing $(I^G)J^{PC}$ or just J^{PC} [24]. Latter will be used to describe the meson states constructed by the discussed temporal correlation functions. The lightest meson states (made up from u, d and s quark combinations) are depicted in Fig. C.1 where they are arranged according to their quantum numbers Strangeness S and Isospin I_z. Both diagrams contain a meson octet and a singlet contribution, the η' for pseudo-scalar mesons and the ω for vector-mesons. Since the C-parity is only relevant for neutral mesons, it is dropped here. The Kaons all contain a s-quark or $\bar{s}$-anti-quark, thus, $S \neq 0$. Additionally, η, η' and the ϕ also contain combinations of strangeness which adds up to zero. Meson states on a single horizontal line lie within the same multiplet. For better visualization the center states corresponding to $(I_z, S) = (0, 0)$ are depicted a bit offset.

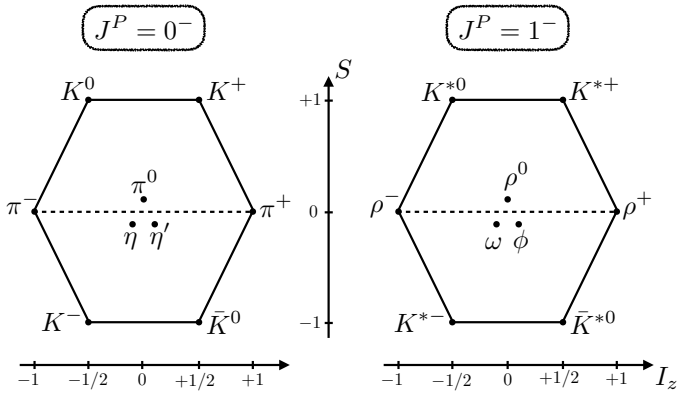

Figure C.1: *Lightest pseudo-scalar (left) and vector (right) meson states combined in a nonet. Horizontally states are separated according their isospin quantum numbers while vertically they have different strangeness.*

D Miscellaneous Plots

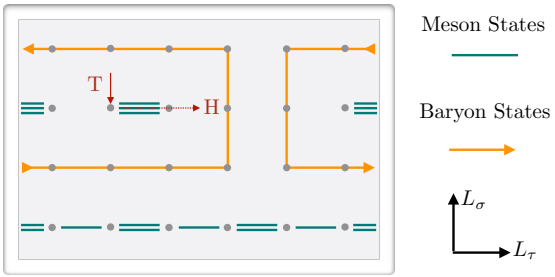

Figure D.1: *A two-dimensional discrete time lattice configuration. For such systems with non-static baryons, mesonic lines can be trapped by baryons. This requires the worm to backtrack, i.e. to choose the incoming direction as outgoing direction.*

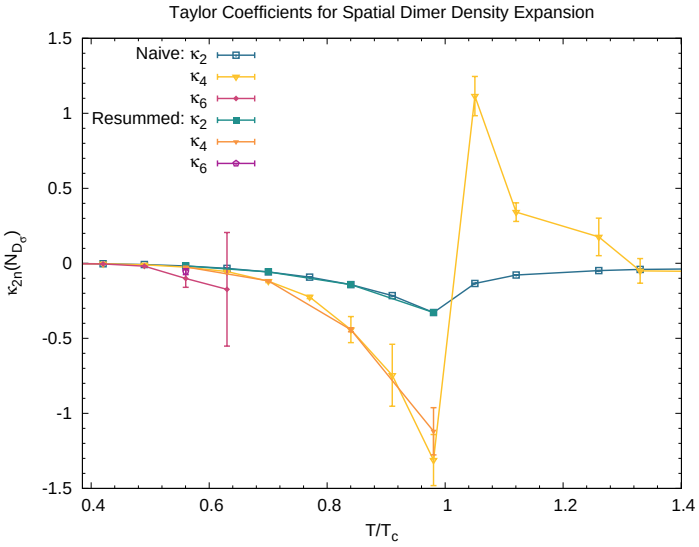

Figure D.2: *Taylor coefficients based on the modified cumulants for an expansion of the spatial dimer density. Data points with an error larger than $\Delta\kappa_{2n} > 0.5$ are not plotted. The polymer resummation scheme leads to reasonable error reduction which is nevertheless not good enough to consider higher order cumulants.*

Eigenständigkeitserklärung

Hiermit erkläre ich, dass ich die vorliegende Arbeit selbstständig verfasst und gelieferte Datensätze, Zeichnungen, Skizzen und graphische Darstellungen selbstständig erstellt habe. Ich habe keine anderen Quellen als die angegebenen benutzt und habe die Stellen der Arbeit, die anderen Werken entnommen sind — einschließlich verwendeter Tabellen und Abbildungen – in jedem einzelnen Fall unter Angabe der Quelle als Entlehnung kenntlich gemacht.

Bielefeld, 4. Mai 2020

Marc Andre Klegrewe